

# Reservoir analogue and fluid characterization of travertine carbonate in Acquasanta Terme, Italy

**Nick JANSSENS**

Supervisor: Prof. Dr. R. Swennen

Mentors: *H. Claes, J. Soete, M. Erthal*

Thesis presented in fulfillment of  
the requirements for the degree of  
Master of Science in Geology  
(Ghent – Leuven)

Academic year 2014-2015



© Copyright by KU Leuven

Without written permission of the promotor and the authors it is forbidden to reproduce or adapt in any form or by any means any part of this publication. Requests for obtaining the right to reproduce or utilize parts of this publication should be addressed to KU Leuven, Faculteit Wetenschappen, Geel Huis, Kasteelpark Arenberg 11 bus 2100, 3001 Leuven (Heverlee), Telephone +32 16 32 14 01.

A written permission of the promotor is also required to use the methods, products, schematics and programs described in this work for industrial or commercial use, and for submitting this publication in scientific contests.







# Preface

Travertine has grown to a major field of study since the discovery of the Lula (Tupi) oil field in the Santos basin in Brazil, in 2006. The oil field is discovered in the pre-salt deposits of the deep offshore. Oil wells are drilled to a depth of over 5 km (Beasley et al., 2010). The pre-salt hydrocarbon plays form a combination of several types of carbonate deposits. The deposits are related to the creation of sag basins upon cooling of the lithosphere after the breakup of Pangea. The deposits are often termed “lacustrine coquina” (Borsato et al., 2012) or brackish stromatolites (Borsato et al., 2012; Lottaroli et al., 2012). Sharp et al. (2012) noted the presence of both pre- and post-salt travertine deposits in the African part of the Atlantic Ocean. Both these observations and the petrographic description given by Terra et al. (2010) indicate the possibility that travertine deposits are present in the pre-salt of both Brazil and Africa (Angola). This makes them good targets for oil exploration, but knowledge about the sedimentation and diagenetic processes that affect reservoir properties in these continental carbonates is only limited. For comprehension on how these deposits behave as hydrocarbon reservoirs research of reservoir analogues is required (Borsato et al., 2012).

The research in this thesis has three main objectives:

- The first objective is to reconstruct a three-dimensional (3D) reservoir analogue. For this study, a description of the different travertine textures is integrated with detailed field data and petrophysical measurements. The final result should provide information on the porosity and permeability distribution in a travertine body and analyse possible challenges in reservoir exploitation to ultimately give advice on the reservoir variability.
- The second objective is a characterization of the fluids involved in the creation and post-depositional alteration of the travertine body. The provenance analysis of the primary spring fluids should allow to determine fluid migration paths. This study can prove to be interesting from an exploration point-of-view. Fluids that precipitate travertine must have dissolved carbonate in the subsurface, generating additional secondary porosity, which could generate additional reservoirs.
- The third objective is the reconstruction of the depositional history. Through differentiating different lithofacies and linking them to environmental settings, the precipitation processes can be chronologically analysed. This objective should result in an interpretation of the change of parameters, influencing travertine deposition in the Acquasanta system through time.

I have been helped by a lot of people throughout this research and I am grateful towards all of them.

To start off with, I am greatly indebted to my promotor prof. Rudy Swennen for giving me the opportunity to study such a challenging and interesting subject but also for helping me by commenting on the text I wrote for this thesis. I also want to thank his collaborators: Hannes Claes, Jeroen Soete, Benjamin Lopez and Marcelle Erthal for both guiding me during the field study and the constructive comments during my research. I am also very grateful towards Dr. Enrico Capezzuoli for the interesting discussions we have had, both during the field work and during the lapse of my thesis. Prof. Philippe Muchez has given me a lot of guidance with the fluid inclusion study and he was always prepared to answer my questions concerning fluid inclusions, for which I am certainly grateful.

I would like to thank Herman Nijs for the careful preparation of the thin sections and wafers that I have used for this research. My gratitude also goes towards Dr. Elvira Vassilieva, whom has both guided me during the sample preparation of the ICP-OES analyses and performed these analyses. I would also like to thank prof. Michael Joachimski (Friedrich-Alexander Universität Erlangen-Nürnberg) and his laboratory for the stable oxygen and carbon analysis and prof. Rob Ellam (Scottish Universities Environmental Research Centre, Glasgow) and his laboratory for analysis of the strontium isotopes. Of course I would also like to thank my parents, my family and my girlfriend, Babette, for supporting me throughout my five years of studying. More importantly I would like to thank them for supporting me throughout my thesis and to sometimes get my mind off working! Thanks a lot!

I would like to thank every one of my classmates and more especially Joke, Steven, Frédéric and Stef for spending countless hours together in the microscopy classroom while writing our theses. I would also like to thank Nicolas for the supporting messages he has send while he was on Erasmus in Spain.

Vorrei ringraziare tutti i lavoratori della cava per la loro gentilezza durante la mia ricerca sul campo. Mi hanno sempre aiutato volentieri, ovunque potessero e sono stati così gentili da condividere con noi la loro cucina e i loro pasti durante le giornate di pioggia. Non dimenticherò mai le divertenti conversazioni che abbiamo avuto durante queste pause pranzo, durante le quali la barriera linguistica diventava un ostacolo minimo.

Grazie di cuore!

# Abstract

Research on continental carbonates was sparked by the discovery of the Lula (Tupi) hydrocarbon field in 2006 in the Pre-salt deposits in the deep offshore of Brazil. The discovery of these continental carbonates led to the realization that the knowledge about these complex carbonates was limited. Since then, a lot of reservoir analogue studies have been performed to describe the sedimentary setting and diagenetic features as well as the complexity of the deposits. This thesis provides the characterization of such a reservoir analogue at high detail, performed with high resolution field observations, petrographical analysis (classical and fluorescence microscopy) and petrophysical characterization of the rocks. The fluids related to the travertine deposits are characterized through cathodoluminescence microscopy (CL), fluid inclusion analysis, stable isotopes and trace element analysis by Inductively Coupled Plasma Optical Emission Spectroscopy (ICP-OES). Finally, a depositional model is proposed.

Travertine deposits can be characterized as dense deposits with fine and irregular layering, which are mainly formed by inorganic or microbial processes, for which a morphological classification is proposed in this research. The spring waters that precipitate such deposits usually have a deep origin and high temperature ( $> 25\text{ }^{\circ}\text{C}$ ).

The area of study is Acquasanta Terme, which is located on the border of the Abruzzi and Marche regions, central Italy. A combination of different tectonic styles present in the area is the result of the Apennine orogeny. Strike-slip faulting was recently ongoing in this area. Three levels of travertine deposits have been generated during Pleistocene and Holocene, with still some active thermal sources remaining.

A reservoir model of this field analogue is constructed from a set of detailed field observations and is separated into ten different lithotypes, which all have petrophysical measurements linked to them. The measurements also indicate the variation of both porosity and permeability within just one lithotype. The reservoir model concludes that only 0.21 % of the exposed travertine is of very good reservoir quality, 5.42 % and 20.61 % is of good and fair reservoir quality, respectively, leaving another 73.77 % to be non-reservoir quality rocks. Cementation only had a minor influence on most lithotypes with the exception of erosional horizons. A banded travertine vein, which is impermeable, cuts through the travertine body and compartmentalizes it into two hydrologically unconnected sectors.

Characterization of the fluids, especially relies on the analysis of fluid inclusions. The analysis of two samples from the same vein discerns six different types of fluid inclusions, both monophasic and two-phase. Two different fluids are recorded, of which the first one had a  $T_{fm}$  between  $-0.4\text{ }^{\circ}\text{C}$  and  $-0.7\text{ }^{\circ}\text{C}$  and a  $T_m$  of  $0.0\text{ }^{\circ}\text{C}$  to  $-0.5\text{ }^{\circ}\text{C}$ , resulting in salinities between 0.0 and 0.8 eq. wt% NaCl. These fluid inclusions record meteoric fluids, which have undergone some fluid-rock interactions during subsurface

transport by gravitationally driven fluid flow. The second fluid has a  $T_{fm}$  of  $-48.9\text{ }^{\circ}\text{C}$ , a  $T_{m,HH}$  of  $-30.5\text{ }^{\circ}\text{C}$  and a  $T_{m,ice}$  between  $-29.7$  and  $-28.8\text{ }^{\circ}\text{C}$ . The fluids have a salinity between 25.5 and 26.5 wt% and indicate a  $\text{H}_2\text{O}-\text{NaCl}-\text{CaCl}_2$  system. The salinity data in combination with  $\delta^{18}\text{O}$  of  $-12.07\text{ }_{\text{‰}}$  and the  $T_H$  indicates that the fluids are deeply circulating fluids with a meteoric origin, that have infiltrated through faults to the Burano Fm. (Triassic) which contains anhydrite layers. The travertine body has a  $^{87}\text{Sr}/^{86}\text{Sr}$  ratio of 0.70791 on average and the veins record  $\delta^{13}\text{C}_{fluid} = -1.26\text{ }_{\text{‰}}$ . These measurements indicate thermal decarbonation and dissolution of Triassic carbonates at a temperature  $> 90^{\circ}\text{C}$ . The spring fluids at the near-surface had temperatures varying between  $29.1$  and  $65\text{ }^{\circ}\text{C}$ , based on calculations from stable isotopes and from the  $T_H$  of two highly saline inclusions, which indicates cooling during the rise of the fluids.

After emergence from the springs, the main processes influencing the fluids are cooling and degassing, which is recorded in a small difference of stable isotopes between vein and layered travertine samples ( $\Delta\delta^{18}\text{O} = 1.08\text{ }_{\text{‰}}$  and  $\Delta\delta^{13}\text{C} = 0.43\text{ }_{\text{‰}}$ ). Diagenesis was only of minor importance and the most important fluid in cement generation were the spring waters themselves, which flow through the deposits after they formed, causing variable reducing and oxidizing conditions as seen from CL.

The depositional history is reconstructed from analysis of lithofacies distribution. Six different lithofacies are described and their environmental characteristics are inferred. The most important lithofacies are: (i) the sloping lithofacies, recording subaerial deposition from a thin sheet of water, (ii) the flat lithofacies, deposited subaqueously in water at high temperatures and high dissolved  $\text{H}_2\text{S}$ , (iii) the microbial laminites, indicating shallow pans and (iv) the erosional horizons that mark periods in which subaerial processes altered the deposits. The other lithofacies are of minor importance, they are: (v) terrace and (vi) waterfall lithofacies. Throughout the depositional history, two main build-up phases are recognised. The first phase marks fluids derived from two different fluid paths, which could be two alternately active primary flow paths or two separate point-sources. The deposits grade from subaerial to subaqueous deposits. The second phase marks the activity of a fissure ridge system, of which the fissure is exposed in the quarry walls.

# Glossary

- **Autobrecciation:** Decay of the earlier precipitated travertine. The decay results in blocks, which are transported. These blocks can be incorporated in other sediments.
- **CL:** Cathodoluminescence
- **Effective porosity:** This is the open porosity, the pores that can actually be reached by fluids. The effective porosity is equal to the total porosity – closed porosity. The closed porosity are the pores which are occluded by the fabrics of the rock or be cementation. The effective porosity is the porosity parameter, which is actually important in a reservoir model.
- **e.g.:** exempli gratia = for example
- **FIA:** Fluid Inclusion Association (Goldstein & Reynolds, 1994)
- **i.e.:** it est
- **Lithofacies:** This links a lithotype or an association of lithotypes to environments of formation. (e.g.: *Sloping facies* comprises following lithotypes: *bacterial mats*, *crystalline shrubs* and *peloidal micrite*).
- **Lithotype:** A deposit that is defined by its characteristics in the quarry. These characteristics are mainly based on porosity and morphology. A link is made to descriptions in literature to add an explanation to how the lithotype is formed (e.g.: bacterial mats morphologically look like a vacuolar framestone).
- **MDC:** Micritic Dendrite Crust
- **MM I:** Type I microbial mats
- **MM II:** Type II microbial mats
- **Phytoclastic:** “a rock containing plant fossils”. In the quarry this is mainly remnants of reed or leaves. Also imprints of grass occur. In all cases, the original organic material has decayed and nothing but an imprint remains.
- **PM:** Peloidal Micrite
- **PP:** Parallel Polars (in microscopy)
- **Primary flow path:** This is the path that is followed by the largest volume of spring water. This path is characterized by the smallest drop in temperature on a given distance (Fouke et al., 2000). The primary flow path often shifts due to damming in the preceding path or due to shifting of vents.
- **Shrub:** This term is purely a morphological description when mentioned throughout the work. They also occur as a lithotype, which is separately discussed. The lithotype is also based on the morphology of these structures. The structures start off with a small base and branch upwards. This name is often used because of the similarity with bushes (shrubs) in nature. The branching is an important characteristic to get described as a shrub.

- **Spherulite:** these features look similar to axial figures and are represented by a black cross. These features are observed in thin sections, made from cores from the Lula field in Brazil. Their origin is unknown. In the thermal veins, in this example they are probably created by the very thin crystals from the carbonate needles, growing in a fan.
- $T_H$  = Homogenization temperature
- $T_{fm}$  = Temperature of first observed melt
- $T_m$  = Temperature of final melt
- **Transpressional fault:** Faults with a compressive and transform component.
- **Transtensional fault:** Faults with an extensional and a transform component.
- **XP:** Crossed Polars (in microscopy)

# Contents

Chapter 1:	Introduction.....	1
Chapter 2:	Travertine: definition and classification.....	3
2.1.	Travertine precipitation mechanisms and CO <sub>2</sub> sources .....	6
2.1.1.	Microbial precipitation mechanisms.....	7
2.2.	Travertine classification .....	8
2.2.1.	Classification based on the morphology of deposits .....	8
2.2.2.	Note on the internal architecture of fissure ridges.....	14
2.3.	Travertine lithofacies models.....	15
Chapter 3:	Setting of Acquasanta Terme travertine .....	19
3.1.	Geographical setting .....	19
3.2.	Geological setting.....	20
3.2.1.	Geological evolution in Italy.....	20
3.2.2.	Regional geology .....	22
3.2.3.	Travertine in Acquasanta Terme and the rest of Italy .....	24
Chapter 4:	Methodology .....	29
4.1.	Fieldwork.....	29
4.1.1.	Lithologs .....	29
4.1.2.	Linedrawings .....	29
4.1.3.	Sampling.....	30
4.2.	Petrography.....	30
4.2.1.	Thin sections.....	30
4.2.2.	Classical microscopy.....	31
4.2.3.	Cold CathodoLuminescence (CCL).....	32
4.2.4.	Fluorescence microscopy .....	32
4.3.	Image analysis .....	33
4.4.	Petrophysics: porosity and permeability .....	33
4.5.	X-Ray Diffraction (XRD) .....	36
4.6.	Geochemistry .....	37
4.6.1.	Stable isotopes .....	37
4.6.2.	Inductively Coupled Plasma-Optical Emission Spectroscopy (ICP-OES).....	40
4.7.	Fluid inclusion analysis .....	41
4.8.	3D – model .....	42
4.9.	Upscaling approach .....	42
Chapter 5:	Results .....	45



5.1. Petrography .....	45
5.1.1. Micritic dendrite crust .....	45
5.1.2. Peloidal micrite (PM) .....	48
5.1.3. Microbial mats .....	48
5.1.4. Erosional horizons .....	52
5.1.5. Microbial laminites .....	54
5.1.6. Crystalline crust .....	58
5.1.7. Banded travertine.....	58
.....	60
5.1.8. Exotic lithotypes .....	61
5.1.9. Fossil cave fill .....	66
5.1.10. White cements .....	69
5.2. Travertine architecture.....	69
5.2.1. Lithologs and image analysis .....	69
5.2.2. Linedrawings, lithotype variation and lithofacies .....	69
5.2.3. Structural data .....	74
5.3. Three-dimensional analogue reservoir characterization .....	74
5.4. Geochemistry and mineralogy .....	78
5.4.1. XRD-analysis .....	78
5.4.2. Stable oxygen and carbon isotopes.....	80
5.4.3. Stable strontium isotopes.....	81
5.4.4. ICP-OES .....	81
5.5. Fluid inclusions .....	85
5.5.1. Petrography .....	85
5.5.2. Microthermometry data.....	88
5.5.3. Salinity of fluids .....	90
Chapter 6: Discussion .....	93
6.1. Three-dimensional reservoir model .....	93
6.2. Fluid characterization .....	97
6.2.1. Spring water .....	97
6.2.2. Fluid evolution after emergence from the spring .....	103
6.2.3. Diagenetic fluids .....	104
6.2.4. Fossil cave fluids .....	104
6.3. Depositional history.....	105
Chapter 7: Conclusion .....	111

Chapter 8:	Future research .....	113
Chapter 9:	References.....	115



# Chapter 1: Introduction

The discovery of the Lula (Tupi) oil field in the pre-salt deposits, in offshore Brazil led to a bloom in the research for continental carbonate deposits. Prior to the discovery of the Lula oil field, there was not a lot of research on travertine and complex continental carbonates, in general. Even though travertine deposits are still labelled as a geological curiosity, they are found across the entire globe proving that their fossil equivalents might provide interesting hydrocarbon targets. Only a few of these examples include Turkey, in the Denizli basin (Claes, 2011; De Filippis et al., 2012 & 2013b; Özkul et al., 2002; Soete, 2011) and Rapolano Terme, Tivoli and Acquasanta in Italy (Brogi et al., 2014; De Filippis et al., 2013a; Guo & Ridin (Boni & Colacicchi, 1966)g, 1998 and 1999; Honlet, 2013; Madonna et al., 2005; Minissale et al., 2002), Hungary (Kele et al., 2008), Plitvice in Croatia (Ford & Pedley, 1996), the Huanglong province in China (Lu et al., 2000), Mammoth Hot Springs at Yellowstone, Wyoming, USA (Fouke, 2011; Fouke et al., 2000) and a lot of other deposits, worldwide.

Reservoir analogue models are required to assess the complexity in both sedimentological and diagenetic characteristics of complex carbonates. This study presents such an analogue reservoir characterization. In addition to this, the fluids that precipitate the travertine are analysed through a fluid inclusion and stable isotope analysis to define the provenance of these fluids. Ultimately, a depositional model, based on field observations is constructed. A multidisciplinary approach in which detailed field work, petrography, petrophysics, geochemistry and fluid inclusions are integrated, is adapted to tackle the three objectives of this research.

The present study is performed at Acquasanta Terme, in Italy which is a small village with three stratigraphic levels of travertine precipitation. The upper level, which is excavated by Eurobuilding at the Cava San Pietro or “San Pietro quarry”, is studied in this research.



## Chapter 2: Travertine: definition and classification

Travertine and tufa belong to a family of continental carbonates that dominantly precipitate under subaerial conditions from solutions rich in bicarbonate, occurring in a variety of depositional and diagenetic environments (Capezzuoli et al., 2014).

The initial terminology comes from Greek and Roman times, when travertine and tufa were both used in construction. The term travertine originally comes from the Roman name “Lapis Tiburtinus”, which means “Rock of Tibur” (Pedley, 2009). Tibur is the original name of Tivoli, a village close to Rome, where a lot of travertine is quarried for monuments in Rome (Pentecost, 2005). Active travertine precipitation is ongoing in Tivoli (Chafetz & Folk, 1984; De Filippis et al., 2013b). The Roman name for tufa is “tophus” and was used by Pliny the Elder for white, crumbly rocks and was used for both volcanic tuff and tufa, the latter containing micro- and macrophytes (Ford & Pedley, 1996; Pedley, 2009).

Travertine and tufa are both complex rock types in sense of textures, porosity and depositional processes. Definitions of travertine and tufa changed throughout time, due to the accumulation of new knowledge. Pentecost (2005) visited several definitions and criticizes how they often fail to focus on formational mechanisms. Older definitions (e.g.: from encyclopaedia) are often generalizing. Travertine is defined as “a partly porous deposit of springs or rivers, usually consisting of calcite, but of aragonite when precipitating from hot spring water” (Schieferdecker, 1959) or “formed by evaporation of spring and river waters” (Mitchell, 1985). Preceding definitions of travertine do not consider the formational mechanism of the travertine. Tufa is generally seen as a porous, friable deposit of calcium-carbonate that precipitates around leaves or plants (Lapides, 1978; Schieferdecker, 1959). Speleothems are often classified as travertines (Bates & Jackson, 1987; Mitchell, 1985; Pentecost, 2005). Even in recent studies, the term “travertine” is sometimes still used as a general term for continental deposits. For example Fouke et al. (2000) apply the definition of travertine as “all non-marine carbonate precipitates near terrestrial springs, rivers, lakes and caves”. The best known example is Pentecost (2005) in which the term “travertine” is used for continental carbonates in general. A different prefix, indicating the source of the depositing waters, is used for differentiation between travertine and tufa (Pentecost, 2005). Recent publications tend to distinguish between all types of continental carbonates (Pedley, 2009).

Definitions of continental carbonates focus on an entire range of factors, like temperature, textures, formational mechanisms, source of CO<sub>2</sub> (e.g.: Pentecost, 1995) and the influence of microbial organisms. It is important to realise that travertine and tufa systems are very complex, both in terms of a huge variety of different textures and in different porosity types in one body. It is difficult to

differentiate between tufa and travertine, let alone distinguishing them from the rest of the continental carbonate family. Koban and Schweigert (1993) place travertine in the midst of a continuum of continental carbonates (Figure 2-1). The figure illustrates that the focus for the distinction between the different continental carbonates, relies on the influence of organisms, on depositional environment and

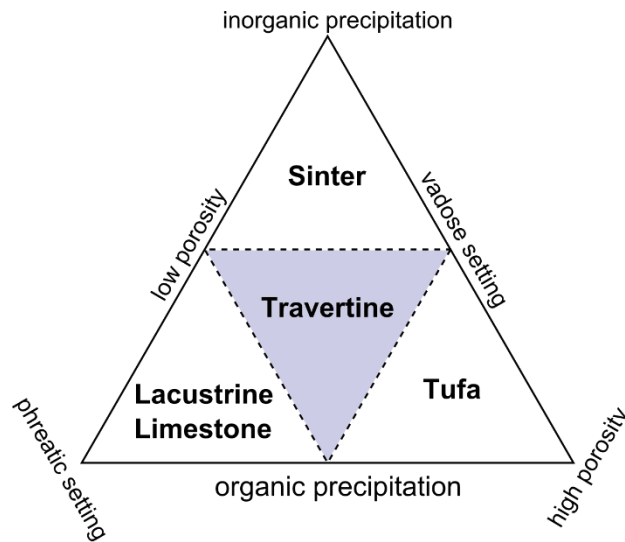


Figure 2-1: Classification illustrating that a continuum between different types of continental carbonate exists (Koban & Schweigert, 1993).

on the porosity of the rock. Even though this diagram is an elegant solution for differentiating between different continental carbonates, it is not applicable in classifying fossil deposits. This is because the defining parameters could not always be uniquely determined from the fossil deposits. In all definitions there is bias concerning the scale of observation. An important definition is given by Pentecost (2005):

*“A **chemically-precipitated** continental limestone formed around seepages, springs and along streams and rivers, occasionally in lakes and consisting of **calcite or aragonite**, of low to moderate **intercrystalline porosity** and often high **mouldic or framework porosity** within a **vadoso or occasionally shallow phreatic** environment. Precipitation results primarily through the transfer of carbon dioxide from or to a groundwater source leading to **calcium carbonate supersaturation**, with nucleation/crystal growth occurring upon a submerged surface.”* (Pentecost, 2005)

No biogenic influence is mentioned in this definition, even though it can be a significant process, as is indicated by Chafetz and Folk (1984), Kandianis et al. (2008) and Fouke (2011). Pentecost distinguishes meteogene and thermogene travertine, based mainly on the origin of the CO<sub>2</sub> that is dissolved in the precipitating fluids. Pedley and Rogerson (2010) also make a link to the origin of the fluids (Figure 2-2) and they also show that tufa could also be formed from cooled thermal waters distally of travertine deposits. These deposits are called “travitufa” by Capezzuoli et al. (2014), as it is difficult to pinpoint the exact difference between travertine and tufa in such conditions.

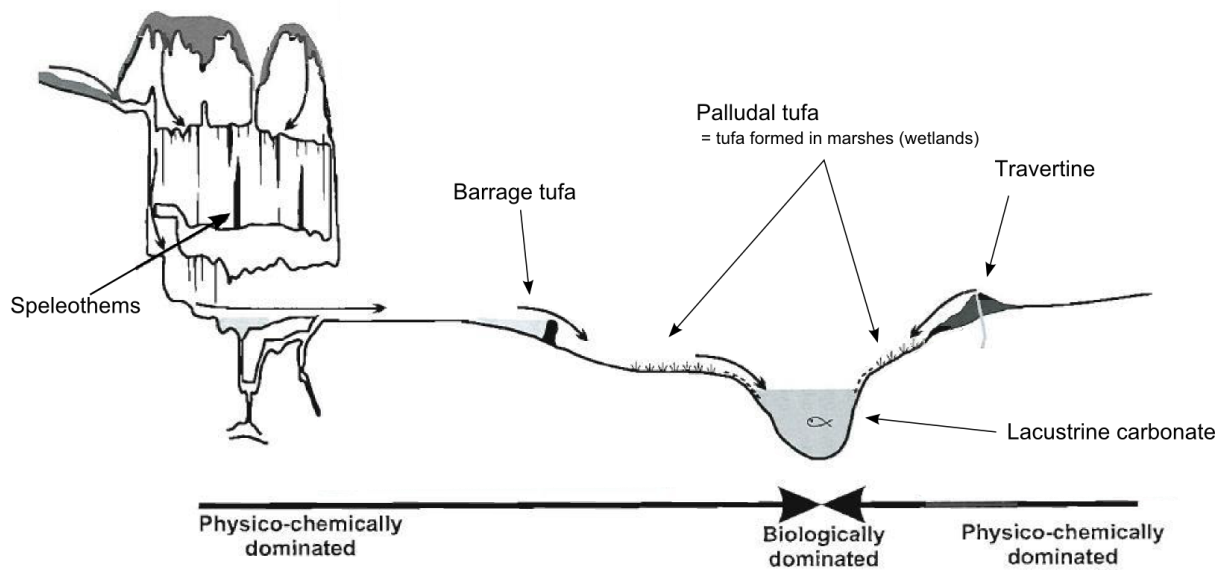


Figure 2-2: Classification scheme for freshwater carbonates showing the relation between several continental deposits and with the origin of the fluids. Fluids forming tufa could either come from karstic dissolution of carbonates (shallow origin) or could come from the cooling down of thermal fluids that form travertines. These thermal fluids come from deep circulation of water with subsequent dissolution of carbonates that are present in the sedimentary sequence (adapted from Pedley and Rogerson (2010)).

Complete definitions of travertine and tufa are difficult to come up with, as a lot of different factors influence the structure and texture of the deposits. The most important difference is the source of the fluids, which was already recognized by Pentecost (1995, 2005). A generic definition of both deposits is proposed, mainly based on Pentecost (2005), Claes (2011), Soete (2011) and Capezzuoli et al. (2014).

- Travertine is a white to creamy coloured limestone, characterized by dense deposits with low porosity, consisting of either aragonite or calcite. The deposits are generally finely and often irregularly laminated and are mostly of inorganic origin, caused by the evasion of  $\text{CO}_2$ . The organic influence is limited to microbial activity due to hostile conditions of spring waters which sometimes tend to reach high temperatures and a high  $\text{H}_2\text{S}$  content. The spring waters have a deep-seated origin, typically marked by a high  $\delta^{13}\text{C}$  (positive or slightly negative) signature. The deposits are usually linked to active tectonics.
- Tufa is a cream- to dark coloured deposit, characterized by highly porous deposits in which porosity is chiefly biomouldic, caused by the plants and other micro- and microphytic organisms involved in  $\text{CO}_2$ -uptake and deposition of  $\text{CaCO}_3$ , which is mainly calcite. The spring

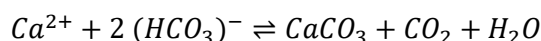


waters are characterized by an ambient temperature and have a low  $\delta^{13}\text{C}$  signature, linked to shallow origin of the waters, which is usually linked to karstic regions.

## 2.1. Travertine precipitation mechanisms and $\text{CO}_2$ sources

The deposition of travertine ( $\text{CaCO}_3$ ) is caused by a variety of processes, both inorganic and organic. Precipitation is controlled by parameters like spring water chemistry, physical processes (temperature change, degassing, boiling, evaporation and dilution), hydrology and the amount of biotic activity (Fouke, 2011).

Spring waters are supersaturated with regard to  $\text{CaCO}_3$  and precipitation is mostly caused by removal of  $\text{CO}_2$  according to the following chemical equation (Brasier, 2011; e.g.: Fouke, 2011; Pentecost, 2005):



This chemical equation presents a reversible reaction. The spring waters have to contain dissolved  $\text{CO}_2$  as  $\text{HCO}_3^-$  and  $\text{Ca}^{2+}$  to enable travertine precipitation.  $\text{CO}_2$  is removed from the system causing the reaction equilibrium to shift to the right, initiating  $\text{CaCO}_3$ -precipitation (Dreybrodt et al., 1996).  $\text{CaCO}_3$  can be precipitated as calcite and aragonite (e.g.: Fouke et al., 2000) or as vaterite, as seen in Chinese travertines of the Huanglong province (Lu et al., 2000).

$\text{HCO}_3^-$  can have a lot of different origins. Depending on the origin, travertine or tufa is precipitated (or thermogene and meteogene travertine, respectively, sensu Pentecost (1995; 2005)). When  $\text{CO}_2$  is originating from deeper sources like mantle degassing, metamorphism and decarbonation of limestone, oxidation of reduced carbon, etc., travertine is precipitated (Claes et al., 2015; Ford & Pedley, 1996; Pentecost, 2005). Tufa (or meteogene travertine) is precipitated when the  $\text{CO}_2$  is soil-derived by organic decay (Pentecost, 2005).  $\text{CO}_2$ -rich fluids are acidic and act aggressively towards carbonates in the subsurface. Upon dissolving  $\text{CO}_2$ , the reaction equilibrium of the chemical equation provided above will shift to the left, dissolve  $\text{CaCO}_3$  and load the fluids with  $\text{Ca}^{2+}$ . The  $\text{CO}_2$  source can be inferred from stable isotopes and the source of  $\text{Ca}^{2+}$  can be inferred from stable strontium isotopes.

The following list sums up some of the inorganic precipitation mechanisms for  $\text{CaCO}_3$ :

1. Degassing of  $\text{CO}_2$  is the primary mechanism for precipitation of  $\text{CaCO}_3$  during travertine deposition. Degassing is caused by pressure drop at the spring orifice or by turbulence of the water. The pressure drop is efficient for  $\text{CO}_2$ -degassing as the  $\text{pCO}_2$  in the water is higher than can be dissolved at atmospheric pressure. Turbulent flow can cause additional degassing as a result of a sudden increase of flow velocity at terrace rims or on steep irregular surfaces. Vigorous degassing is also possible at boiling springs at which a vapour phase is generated from

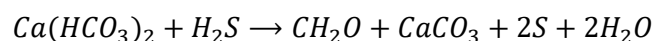
the spring water, which efficiently degasses CO<sub>2</sub> (Brasier, 2011; Ford & Pedley, 1996; Pentecost, 2005; Pentecost & Viles, 1994).

2. Evaporation is another mechanism that causes precipitation. The remaining ions would be concentrated in the solution. Deposition caused by evaporation is rare and is only expected in terrace deposits (Guo & Riding, 1994; Lapidés, 1978).
3. Mixing of Ca<sup>2+</sup>-rich waters with alkaline surface waters (e.g. lakes) also could cause precipitation at lacustrine springs (Pentecost, 2005; Wright, 2012).
4. Other processes include: the common-ion effect (Brasier, 2011) and the mixture of alkaline groundwater with atmospheric CO<sub>2</sub> (Pentecost, 2005). These processes are not expected in typical subaerial travertines but rather in subsurface carbonate precipitation.
5. In cold regions, the freezing out process could cause precipitation upon severe cooling of the spring water. Freezing a fraction of the water would cause supersaturation in the remaining water, which causes precipitation (Brasier, 2011). This process is not relevant for this research.

### 2.1.1. Microbial precipitation mechanisms

Another important factor in travertine precipitation is organic or microbial travertine precipitation. Microbial processes are an important agent as they sometimes tend to contribute to a large fraction of the deposits (Chafetz & Folk, 1984; Chafetz & Guidry, 1999; Fouke, 2011; Guo & Riding, 1999, 1994; Kandianis et al., 2008; Pentecost, 2005). The presence of microbes in active systems is usually seen by bacterial mats (Fouke, 2011) or shrub growth (Chafetz & Folk, 1984).

Microbial influence on travertine deposits has been mentioned in early literature, but Chafetz and Folk (1984) were the first authors to provide a detailed description of the role of bacteria and to prove their influence on travertine precipitation. They consider black micritic lumps to be of bacterial origin, based on SEM observations, in which rod shapes and filaments are found, indicating the former presence of bacteria. These micritic lumps or bacterial clumps are “the elementary building blocks” (Figure 2-3A; Chafetz & Folk, 1984). According to the estimations of Chafetz and Folk (1984), up to 90% of a thermal spring carbonate deposit could be created by the direct or indirect influence of bacteria. Microbial influence on carbonate generation is caused by several processes, depending on the type of organisms. Phototrophic micro-organisms (bacteria, cyanobacteria, blue-green algae, etc.) in an aerobic environment would locally take up CO<sub>2</sub>, decreasing alkalinity and thus creating the perfect situation for precipitation. Anaerobic conditions could host heterotrophic organisms, which generate suitable conditions for precipitation through different processes (Riding, 2000). The following chemical equation indicates a mechanism for the precipitation of CaCO<sub>3</sub> due to the influence of photosynthetic oxidation of sulphur by bacteria (Chafetz & Folk, 1984; Krumbein, 1979):



This chemical equation presents an endergonic irreversible reaction, for which the required energy is derived from sunlight. Experiments by Kandianis et al. (2008) relate an increase in the rate of  $\text{CaCO}_3$  precipitation to a mediating effect of increased biomass through decrease of the nucleation energy of calcite. Extracellular Polymeric Substances (EPS) are created by organisms and create a micro-environment which is suitable for mineral precipitation and sediment trapping (Riding, 2000). This is an example of the efficient mediating function of biological substances.

Shrubs (Figure 2-3B-D) are commonly associated with bacteria (Chafetz & Folk, 1984; Chafetz & Guidry, 1999; Fouke, 2011). The shrub morphologies are linked to flat pools and only minor shrub growths are recognized in travertine mounds, terraced systems or fissure ridges (section 1.3.2). The harsh environmental conditions with high temperatures and high dissolved  $\text{H}_2\text{S}$  in which only bacteria can thrive, are favourable for shrub growth (Chafetz & Folk, 1984; Chafetz & Guidry, 1999). The upward growth of shrubs is in accordance with phototrophic bacteria, which makes sense in these  $\text{H}_2\text{S}$ -rich pools.

Together with biological influence, an abiotic control is exerted on shrub deposition as well. Chafetz and Guidry (1999) notice a continuum between almost entirely biologically precipitated shrubs (bacterial shrubs; Figure 2-3C) and almost entirely inorganically precipitated shrubs (ray-crystals; Figure 2-3D). In between these two are the crystalline shrubs, which still contain clear bacterial clumps. More inorganic influence causes the shrub morphologies to display this crystal habit. The “leaves” will tend to have a more elongate shape, compared to the irregular shape of the bacterial clumps (Chafetz & Guidry, 1999). The most crystalline shrubs of this series are usually referred to as “crystalline crust” (Figure 2-3D; Gandin & Capezzuoli, 2014; Guo & Riding, 1998).

Up to now, only processes caused by micro-organisms are treated, but also larger organisms influence precipitation. Photosynthetic uptake of  $\text{CO}_2$  by plants, mosses or reed could, just like for microbial organisms, generate conditions in which  $\text{CaCO}_3$  precipitation will be favoured (Guo & Riding, 1998).

## 2.2. Travertine classification

### 2.2.1. Classification based on the morphology of deposits

Travertine is a general term and is sometimes interconnected in its use with tufa. Both deposit types have similar and distinct morphologies. Classification of travertine deposits is complex and is often based on a variety of characteristics of which morphology is an important one. Following morphologies are described in Pentecost (2005) and Pentecost and Viles (1994): spring mounds, fissure ridges, cascades and dams, fluvial crusts and lake deposits. A more recent classification by Capezzuoli et al. (2014) classifies travertines based on the morphologies of spring deposits and the slope deposits. The classification of Pentecost and Viles (1994), in which distinction is made between sources and other

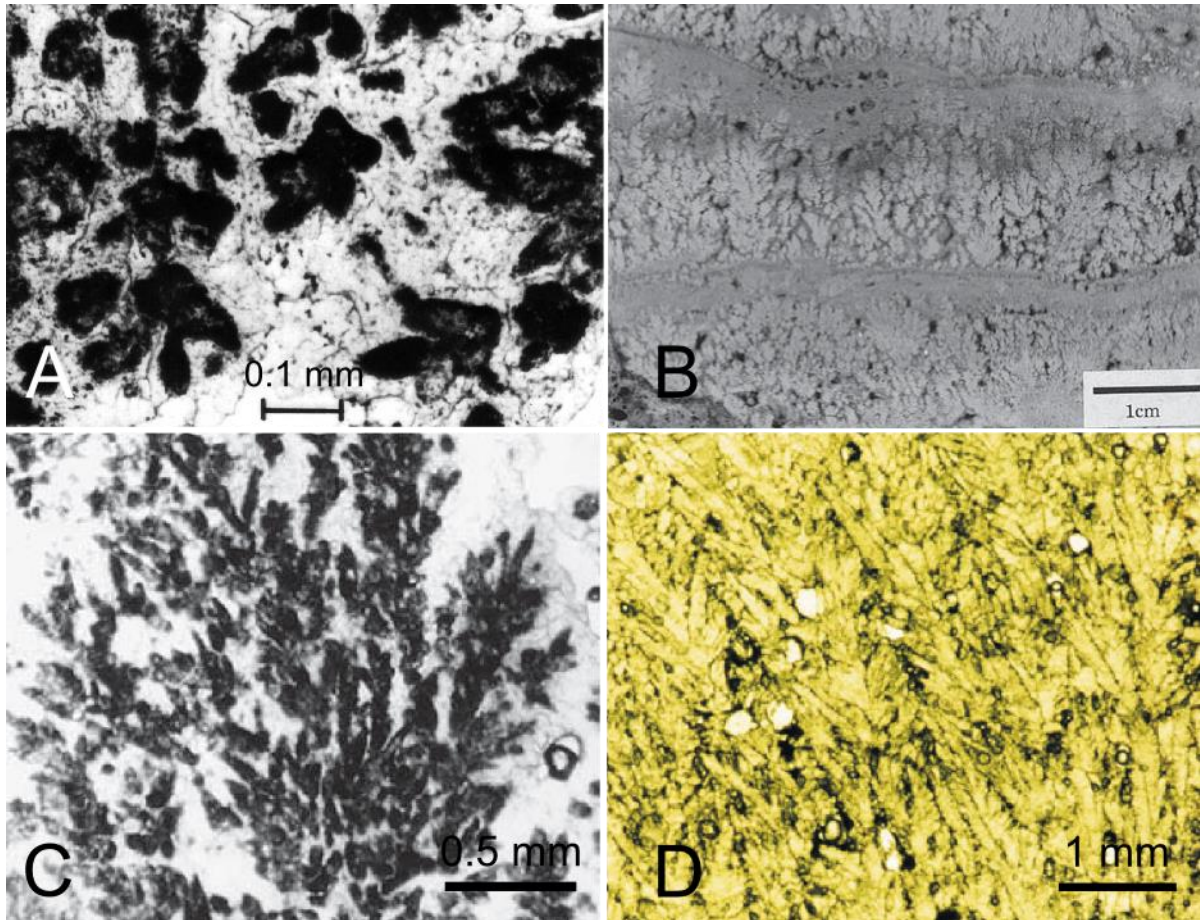


Figure 2-3: Bacterial influence recognized in bacterial clumps or shrubs. A. The black spots are “bacterial clumps” and are microporous zones that remain after the degradation of a dense accumulation of bacteria. Picture from: Chafetz and Folk (1984). B. Shrubs in outcrop. Picture from Chafetz and Guidry (1999). C. Bacterial shrubs, which are almost entirely build of bacterial clumps to form a lithology that morphologically looks like a shrub. The bacterial clumps are the “leaves” of the shrub. Picture from Chafetz and Guidry (1999). D. Ray-crystal shrubs (*sensu* Chafetz and Guidry (1999)) or plume-like crystals in abiotic crystalline crust (*sensu* Gandin and Capezzuoli (2014)). These shrubs are probably entirely abiotic, with maybe only a minor component of bacteria to initiate growth. Picture from Gandin and Capezzuoli (2014).

deposits, is partly adapted. In this section, the classification of travertine deposits will be based on the morphology of the deposits and whether spring deposits were formed subaerial or subaqueous.

Travertine deposits are characterized by a range of morphologies as there is a large variety of controlling factors (Figure 2-4). This causes morphologies to form a continuum between morphological end-members (travertine mound vs. fissure ridge and terraces vs. smooth slope). Factors influencing the morphology of travertine deposits are: substrate (consolidated rock or unconsolidated sediments), vegetation, local topography, structural setting, water turbulence, degree of  $\text{CaCO}_3$  saturation, water temperature and the location of the spring (on a slope, in a depression or subaqueous) (Capezzuoli et al., 2014; Chafetz & Folk, 1984; Guo & Riding, 1999, 1998; Hancock et al., 1999; Pentecost, 2005).



Setting	Subaerial - Spring water can freely flow	Depression - No drainage of water	Subaqueous - No flow structures - No facies differentiation
Spring deposits and related morphologies	 <p><b>Mound</b></p> <ul style="list-style-type: none"> <li>- Point source</li> <li>- Soft substrate</li> <li>- Low slope of deposit</li> <li>- Round, mound shape</li> </ul>  <p><b>Fissure ridge</b></p> <ul style="list-style-type: none"> <li>- Fissure source</li> <li>- Hard rock substrate</li> <li>- Low to steep slope</li> <li>- Lenticular, elongate</li> <li>- Crestal fissure/cones</li> </ul>	Shrub flats	Pinnacles Volcano-shaped cones Travertine reef Flats
Slope morphologies	<p>Smooth or sloping Terraced Composite</p> <ul style="list-style-type: none"> <li>- Large deposits with different lobes and varying slope morphology</li> </ul>	Shrub flats - no flow structures Paludal	No flow structures
Other morphologies	Self-built channels Fluvial crust Range-front travertine		Stromatolithic mounds

Figure 2-4: Morphological classification of travertine. Classification constructed from Capezzuoli et al. (2014), Guo and Riding (1998), Hancock et al. (1999) Pentecost and Viles (1994) and Pentecost (2005).

Based on the spring characteristics a first distinction can be made. They encompass point-sources and fissures. According to Capezzuoli et al. (2014), the point-sources would commonly result into circular domal and mound-like deposits (Figure 2-5A). These domes usually have low gradients and can be entirely round because by producing a small travertine dam at the spring orifice, distributing the water equally in all directions (Pentecost, 2005). A fissure source would result in fissure-ridge type of travertine (Figure 2-5B). These deposits have a lenticular, straight to curved appearance with dimensions of up to a few kilometres in length, 500 meters in width and up to 40 m high, with a typical height-to-width ratio of 0.2, based on 31 fissure ridges studied in Turkey (De Filippis et al., 2013b). An asymmetric profile can result from deposition on a slope. The downhill side will have low slope deposits, where the opposite side can develop slopes of 20° or can even become subvertical. In the latter case, travertine waterfall deposits are encountered (De Filippis et al. 2012; Figure 2-5C). A fissure ridge is usually marked by a crestal fissure or a series of small cones (Figure 2-5B & C). Guo and Riding (1999) remarked that the fissure is seen in the inactive part and the cones in the active part of the Rapolano Terme fissure ridge (Figure 2-5B). Fissures range from widths of a few millimetres up to widths of a few meters (Guo & Riding, 1998). The fluid mostly originates from smaller, local cones, as the fissure is rarely active over its entire length. Activation of the entire fissure would require a lot of fluid pressure. This is analogous to a volcanic fissure eruption, which ends in a series of cones when less pressure is exerted by the magma (e.g. Laki fissure eruption; Francis & Oppenheimer, 2004).



The spring morphology relates to the substrate on which the travertine is deposited. If loose sediments are on top of the fault feeding the system, the fluids will follow several pipe-like pathways, thus resulting in mound-shaped deposits. When the loose sediment is absent and there is only hard rock, the fracture will be more pronounced, resulting in a fissure ridge (Capezzuoli et al., 2014). Pentecost (2005) mentions that the transition from aligned mound deposits to a fissure ridge has been observed in Hungary. This process is also noted at Mammoth Hot Springs by Bargar (1978).

When the hydraulic head of the spring water is unable to keep up with the growth of the fissure ridges or the travertine mounds, the spring will become inactive. This could result in the growth of a new source downhill of the older spring location. The process of abandoning and creating springs over time at

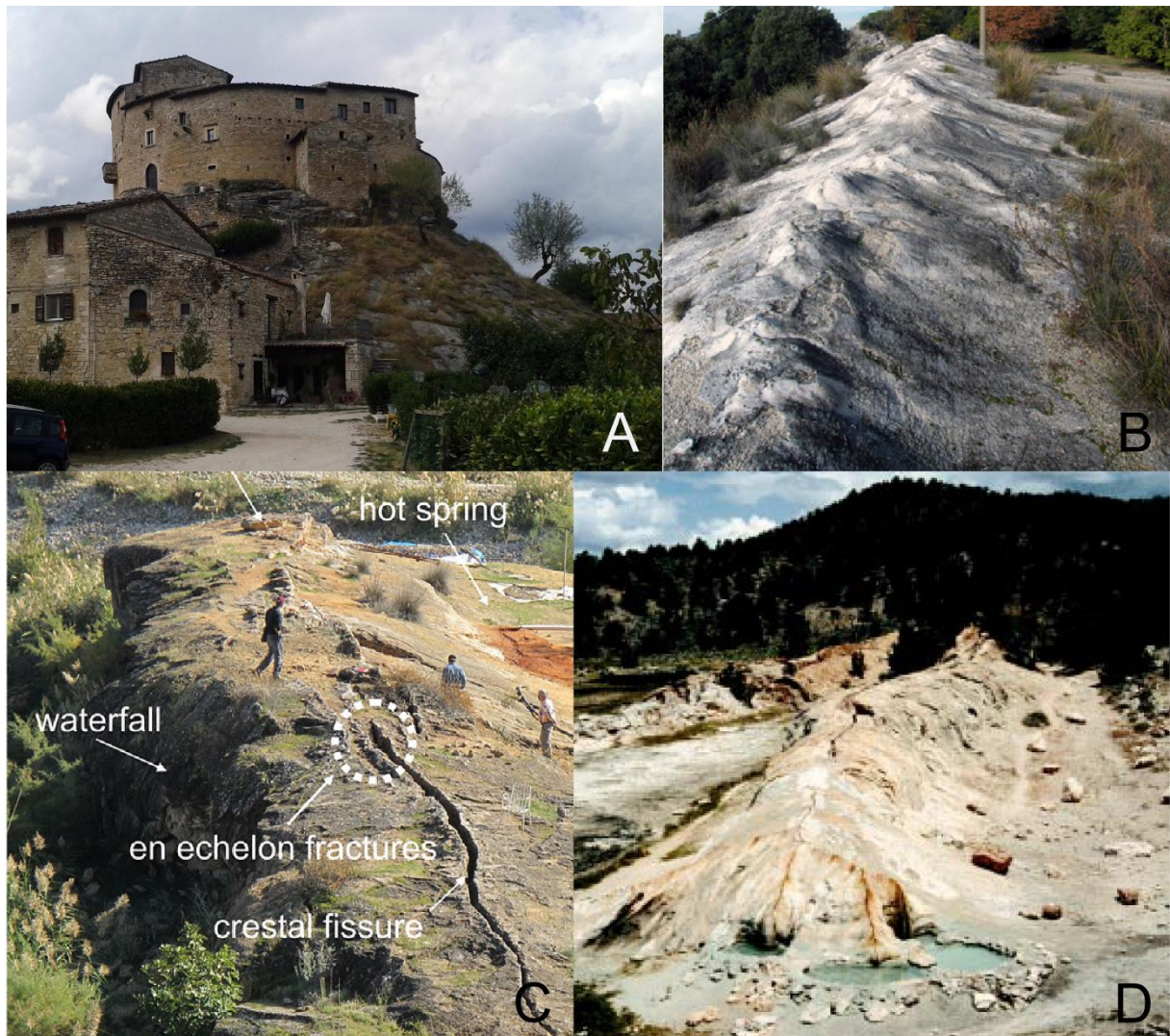


Figure 2-5: Morphologies related to different spring deposits. A. Travertine mound with a castle on top. Such a mount is the result of a point-source, along which the fluids emerge at the surface. Castel di Luco, Acquasanta Terme, Italy. B. Small travertine cones on top of a fissure at San Giovanni fissure ridge near Rapolano, Italy (Capezzuoli et al., 2014). According to Guo and Riding (1999) this indicates recent deposition. C. Crestal fissure of an inactive travertine deposit at Kamara, Turkey. Note the waterfall deposits on the left side of this fissure ridge (De Filippis et al., 2013b). D. Morphology of a 2 fissure ridges, which formed over larger distances, Bridgeport, California, U.S.A. (Hancock et al., 1999).

different locations in a travertine deposit can morphologically result into parasitic deposits (Pentecost, 2005).

Apart from the morphology of the spring deposits other distinctions can be made in subaerial travertine morphologies. The best known travertines in the world (e.g. Pamukkale, Turkey and Mammoth Hot Springs at Yellowstone, U.S.A.) are characterised by terraces (Figure 2-6A). Other travertine deposits have smooth slopes (Figure 2-5A). The names that are given to these two types of morphology on the surface of the travertine mound are respectively terraced mound travertine and sloping mound travertine (Chafetz & Folk, 1984; Guo & Riding, 1998). Guo and Riding (1998) explained that the underlying morphology and the resulting flow regime might play a role in which of these two systems will develop. The sloping mounds are favoured by laminar flow where terraced deposits result from turbulent flow. This implies that the slope of the morphology will be a determining factor (Guo & Riding, 1998). Both slope morphologies also occur at fissure ridges, which often contain small terraces or “terraces” (Figure 2-6D; Guo & Riding, 1999). It is suggested that slope morphologies should be classified apart from the spring deposits (Figure 2-4). Ford and Pedley (1996) note that large deposits have complex geometries and lobate sheets are formed away from the resurgence points, which implies alternating activity of different primary flow paths. This implies the possible presence of different slope types at the same altitudes. The name “composite slopes” is suggested for these deposits.

Apart from morphological groups that have previously been mentioned other, less common morphologies are described in other studies. Waterfall deposits are the first of these morphologies and are linked to (asymmetric) fissure ridges (Figure 2-5C; De Filippis et al., 2012), other travertine systems (Capezzuoli et al., 2014; Claes, 2011; Soete, 2011) or most commonly they occur in tufa deposits in rivers (e.g. Plitvice, Croatia; Figure 2-6B) (Ford & Pedley, 1996). In travertine systems they are rare, thus not included in a morphological classification but are considered a lithofacies (Guo & Riding, 1998 Section 1.3.3). Other characteristic morphologies are self-built channels (Figure 2-6C). These deposits are channels that built levees due to the turbulent flow of water. Fast vertical aggradation results in travertine aquaduct-like structures, which usually follow a sinuous path (Altunel & Hancock, 1993; Capezzuoli et al., 2014). In Pamukkale, Turkey these channels are often the result of anthropogenic influence (Altunel & Hancock, 1993). Less obvious morphologies are: fluvial crusts (Pentecost, 2005) and range-front travertine (Altunel & Hancock, 1993). Fluvial crusts occur when resurgence points are present in a river (Guo & Riding, 1999; Pentecost, 2005). Range-front travertine is only visible after erosion of travertine. Range-front travertine are calcite veins in a host rock that become visible after erosion of the travertine sheet (Altunel & Hancock, 1993).

Previously described deposits are present in subaerial settings, but resurgence points can also occur in depressions or subaqueous. Lakes can have a tectonic origin which increases the likelihood of subaqueous fractures that discharge fluids. The deposits have different morphologies compared to



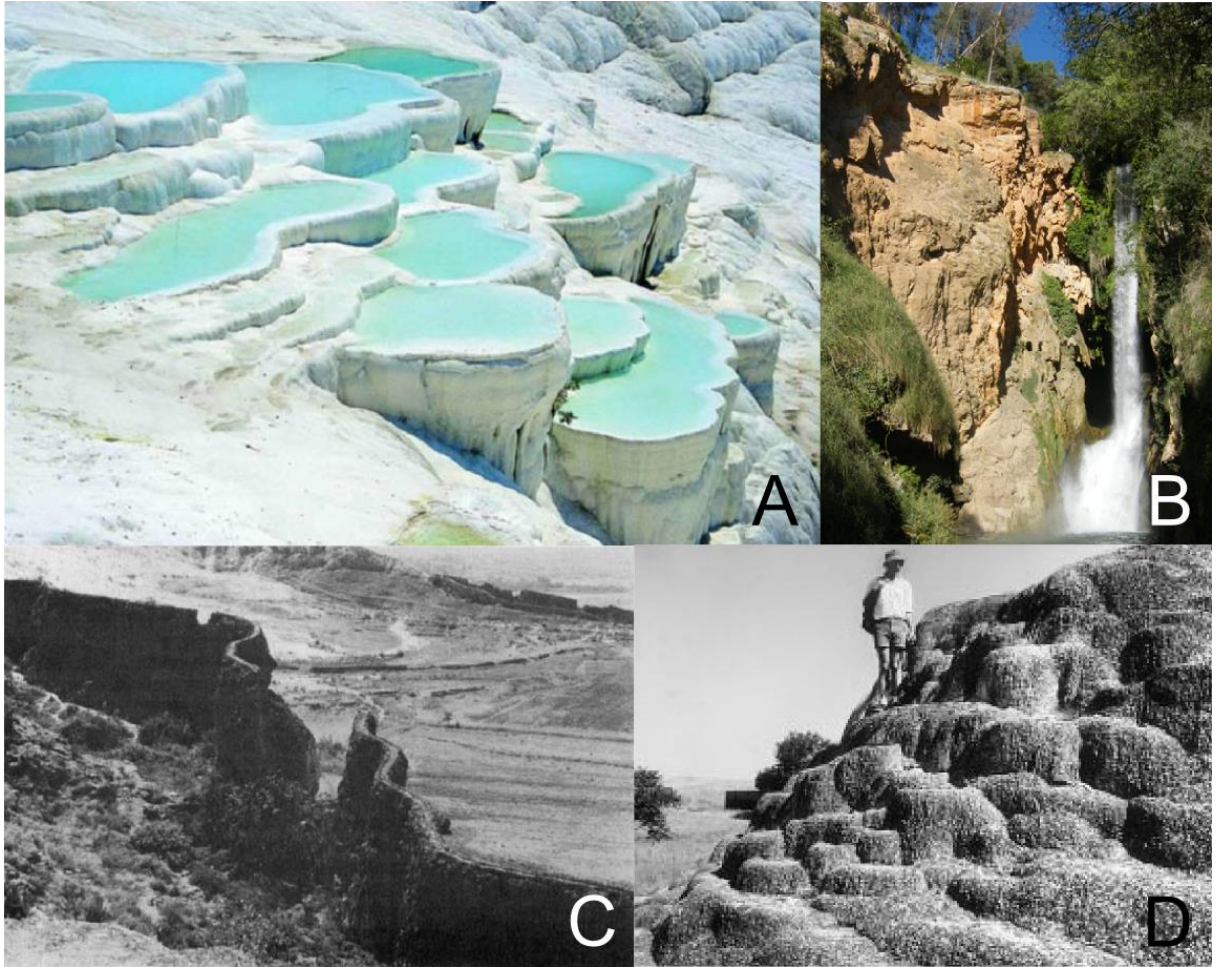


Figure 2-6: Different travertine morphologies. A: Terraces (or “terraces”) on a travertine mound at Pamukkale, Turkey (G20, 2015). B: Tufa waterfall deposit of 50m height. This deposit is present in a river at Monasterio de Piedra Natural Park (Zaragoza, Spain) (Capezzuoli et al., 2014). C: Self-built channel travertine, the channel is approximately 10m high and is ruptured, probably due to an earthquake. 200 m away from Çukurbag (Altunel & Hancock, 1993). D: Terracettes on a fissure ridge. The terrace dams are ornamented with microterraces, Rapolano Terme, Italy (Guo & Riding, 1999).

subaerial deposits, but more importantly, they are devoid of flow structures and facies differentiation (Wright, 2012).

A well-known subaqueous deposit is present at Tivoli, near Rome (Chafetz & Folk, 1984; Wright, 2012). Chafetz and Folk (1984) notice that the deposits of Tivoli are the result of sources emerging in a shallow lake or depression. A small lake is still present and bubbles indicate the presence of sources. The pool is possibly created by the thermal fluids themselves, emerging in a depression. De Filippis et al. (2013b) and Facenna et al. (2008) described the depositional environment more carefully as a low-energy environment, which possibly indicates pools or lakes of about 1 to 2 meters deep. The deposits at Tivoli are marked by flat, sometimes smoothly sloping benches of shrub travertine or micrite with regular intercalations of erosional horizons (De Filippis et al., 2013b; Pentecost, 2005; Wright, 2012). The



erosional horizons indicate episodic drying-up of the lake at the Tivoli travertine, which is possibly linked to meteoric parameters, like precipitation (Faccenna et al., 2008).

Another type of travertine or tufa deposits that occurs in depressions, distal of the spring, are paludal deposits (Pentecost, 2005) or “reed travertine” (Guo & Riding, 1998; Özkul et al., 2002). These deposits are created in depressions, with bad drainage, adjacent to or in between travertine deposits. They contain reed moulds, phytoclastic and detritic (non-travertinous) material as they are not solely influenced by the carbonate-precipitating system. These deposits resemble tufa and are classified as “travitufo” deposits as they are closely related to travertine deposits (Capezzuoli et al., 2014).

Morphologies resulting from subaqueous springs could form thin, high towers (pinnacles), stromatolitic mounds, volcano-shaped cones, travertine-like reefs or layered micritic and/or shrub-bearing flats (Guido & Campbell, 2012; Pentecost, 2005; Wright, 2012).

### 2.2.2. Note on the internal architecture of fissure ridges

Fissure ridges are a thoroughly studied subject in travertine research. This is because they prove to be interesting for paleoseismological studies (Altunel & Hancock, 1996; Hancock et al., 1999).

Fissure ridges are composed of two clearly distinguishable types of travertine, banded and layered travertine. The banded travertine is deposited in the vein that feeds the system and forms a dense crystalline precipitate. The layered travertine originates from degassing of the thermal water or from microbial activity and forms dense to porous textures, usually made up of crystalline crust, paper-thin rafts or microbial mats. The layered travertines slope down from where the banded travertines crosscut the surface (Figure 2-7A). This relationship can be more complex when several fissure phases are recognized in the deposits (Figure 2-7B; De Filippis et al., 2012). Further away from the ridge, the remaining water collects in a depression and forms reed travertine (paludal deposits) (De Filippis et al., 2012, 2013b; Guo & Riding, 1999).

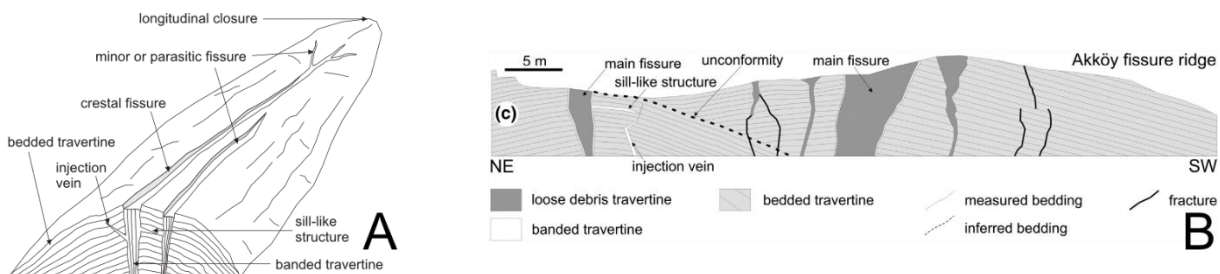


Figure 2-7: Schematic representation of fissure ridges. A: Layered travertine dips away from the central fissure. The other fissure does not show the same relationship, indicating that this fissure was of minor importance (after De Filippis et al., 2012). B: Akköy fissure ridge in Turkey with two depositional phases. Both phases are characterized by a main fissure indicated by banded travertine with layered travertine dipping away from it (after De Filippis et al., 2013b).

Fissure ridge activity often displays a relationship to seismological events (Brogi et al., 2014) or to climatic controls, like seasonally varying precipitation (De Filippis et al., 2013b & 2012). Brogi et al. (2014) suggests that seismological events create fluid pathways for spring waters, whereas De Filippis et al. (2012 & 2013b) link banded and layered travertine to dry and wet periods, respectively. Wet periods increase the water pressure which gradually opens the fracture. During the dry periods, there is insufficient pressure on the water to be expelled from the fissure, during which the banded travertine is precipitated.

## 2.3. Travertine lithofacies models

A lithofacies is defined as a set of characteristics of a sedimentary rock and is determined by several factors including: grain and crystal chemistry, mineralogy, texture, porosity, etc. A link between environmental conditions, which are thought to be present during precipitation, and a certain set of characteristic textures can be made (Veysey et al., 2008 and references therein). In travertine deposits these environmental conditions are mainly based on the thermal and chemical characteristics of the spring waters, their extent of mixing with meteoric water, water flux, surface morphology, etc. Downstream alteration of these characteristics will lead to lithofacies variations along the flow path. The resulting deposits could vary in crystal structure, framework, mineralogy, etc. Lithofacies have been described for both active (Fouke, 2011; Fouke et al., 2000) and fossil (Guo & Riding, 1998; Özkul et al., 2002) deposits. It proves to be difficult to exactly link facies types for different deposits, but Fouke (2011) mentions that the deposits at Mammoth Hot Springs, are characteristic for high temperature springs. Both the observed lithofacies sequences in active and fossil deposits are described below, explaining the differences in the two facies models.

The active deposits are described at Mammoth Hot Springs by Fouke et al. (2000) and Fouke (Fouke 2011). The lithofacies sequence is described from the vent to the distal parts and contains five lithofacies (Figure 2-8). The first lithofacies is the vent, which is a bowl-shaped depression of less than 5 m in diameter that is dammed by densely crystalline travertine. The spring orifice is present in this depression. This facies grades into the “apron and channel” lithofacies which are characterized by streamers which are coated microbial filaments, resulting in a tube-like deposit. The filaments act as a medium to nucleate crystals. This facies subsequently has a sharp contact with the downstream pond facies due to rapid deceleration of the water. The pond facies consists of terraces, with a pool and a dam, which are between 0.5 and 1.5 m high. The pond facies has a high temperature and pH gradient between the top and the bottom of the facies. The high temperature ponds ( $> 57\text{ }^{\circ}\text{C}$ ) will be filled with shrub deposits, whereas the lower-temperature ponds will contain calcite ice-sheets (or “paper-thin rafts” sensu Guo and Riding, (1998) and calcified bubbles (or “coated bubbles” sensu Guo and Riding, (1998). Downstream of the pond facies, at steeper slopes, the proximal slope facies begins, which is recognized by microterraces, which vary from well-defined terraces with a size of up to 1.5 m diameter to microterraces of 1 to 10

mm in diameter. These smallest terracettes also grow on the front of larger terraces, even in the pond facies. Finally, a gradual transition to the distal slope facies occurs and is marked by a transition from aragonite to calcite precipitation. This facies is recognized by a smooth slope and low-relief microterraces (Fouke, 2011; Fouke et al., 2000).

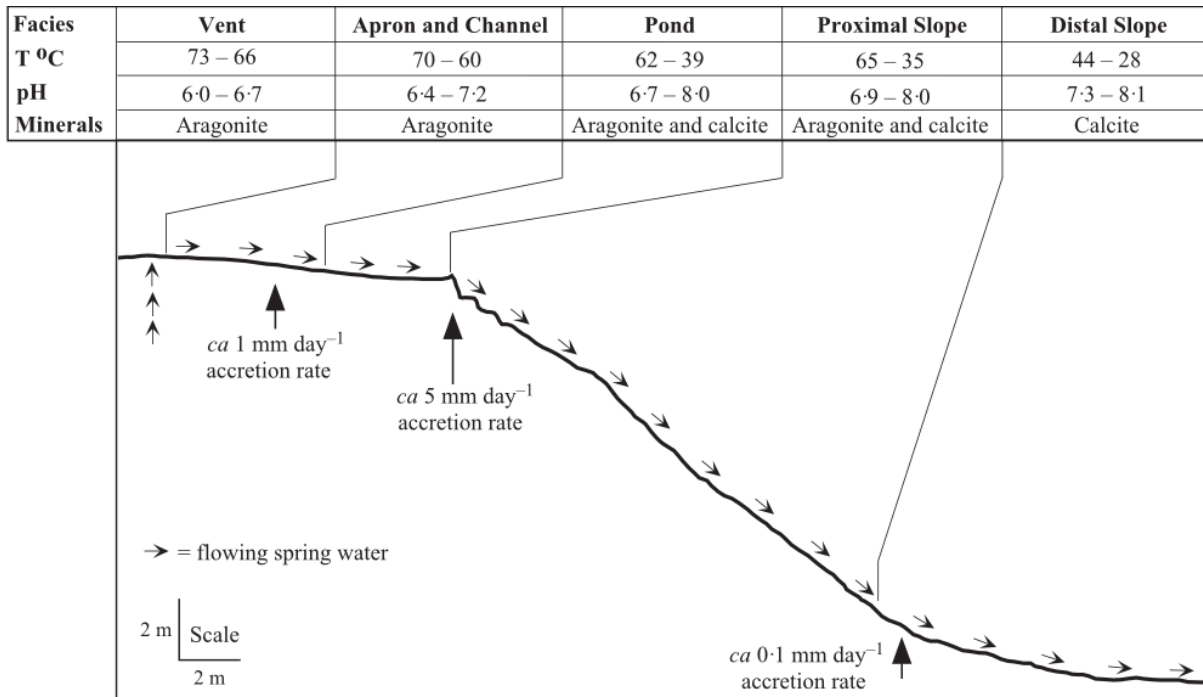


Figure 2-8: Facies variation at Mammoth Hot Spring (Fouke, 2011).

A fossil lithofacies sequence was described by Guo and Riding (1998) and a similar approach is adapted by Özkul et al. (2002). The main difference between the active and the fossil models is that the actual environments for certain deposits could be analysed in relation with the active system itself, whereas for the fossil systems only hints to the depositional environment are preserved in the structure of the deposits. The fossil sequence was reconstructed both at Rapolano Terme, Italy (Guo & Riding, 1998) and Denizli, Turkey (Özkul et al., 2002). The deposits are first classified in a depositional system. The defined Depositional Systems (DS) are: Slope (SDS), Depression (DDS) and Mound (MDS). Subsequently, the lithofacies are described. For the SDS, these are the terrace slope, smooth slope and the waterfall facies. For the DDS, these are shrub flats and marsh-pool facies. Finally, for MDS, these are the reed mounds and other types of mounds, which are fissure ridges, sloping mounds (smooth slopes) and terraced mounds, see section 2.2.1 (Guo & Riding, 1998; Özkul et al., 2002). A summary of the lithotypes and structures in each of the facies is given in Table 1. Two different types of springs can be defined from these depositional environments. The first is a spring on a slope, which would result in the slope depositional environment close to the spring which grades distally into the depression depositional environment. The other type of spring could occur in depressions and would result into extensive shrub flats (Guo & Riding, 1998).

Table 2-1: Summary of the different lithofacies in Guo and Riding (1998) and Özkul (2002). A similar table is presented in Honlet (2013).

DS	Lithofacies	Characteristics	Lithotypes
SDS	Terraced Slope	Terrace walls: height up to 2m	Crystalline crust (downward thinning)
		Terrace pools: dm – m diameter; depth < width	Shrubs, Pisoids, Micrite, Paper-thin rafts, Coated bubbles
		Terrace rims: slightly raised	Crystalline crust and brown micritic laminations
	Smooth Slope	Non-terraced, slope 10 – 40°	Crystalline crust
	Waterfall	Cut subvertical deposits, Subvertical with a short foot of 30 – 50°, rare in hot-springs	Crystalline crust; Angular breccia fragments (travertine)
DDS	Shrub flats	Thin layered, large lateral extent	Shrubs interlayered with fine-grained lithoclast deposits
	Marsh-pool	Horizontal to concave layers, with a lot of pedogenic effects	Lithoclast and Reed travertine
MDS	Reed mound	Wedge-shaped and lenticular units with a slope of 0 – 35°, up to 10m thick and 200m in length	Reed travertine, paper-thin rafts, coated bubble
	Fissure ridge		
	Sloping mound		
	Terraced mound		



## Chapter 3: Setting of Acquasanta Terme travertine

### 3.1. Geographical setting

This study focusses on one of a few travertine bodies at Acquasanta Terme, in Italy. Acquasanta Terme (Figure 3-1) is a small village, of about 138.3km<sup>2</sup>, located 20km off the city Ascoli Piceno. The village is situated to the east of the Adriatic Sea and on the eastern side of the Central-Apennines. Acquasanta Terme is located in the Marche region, close to the border with the Abruzzi region.

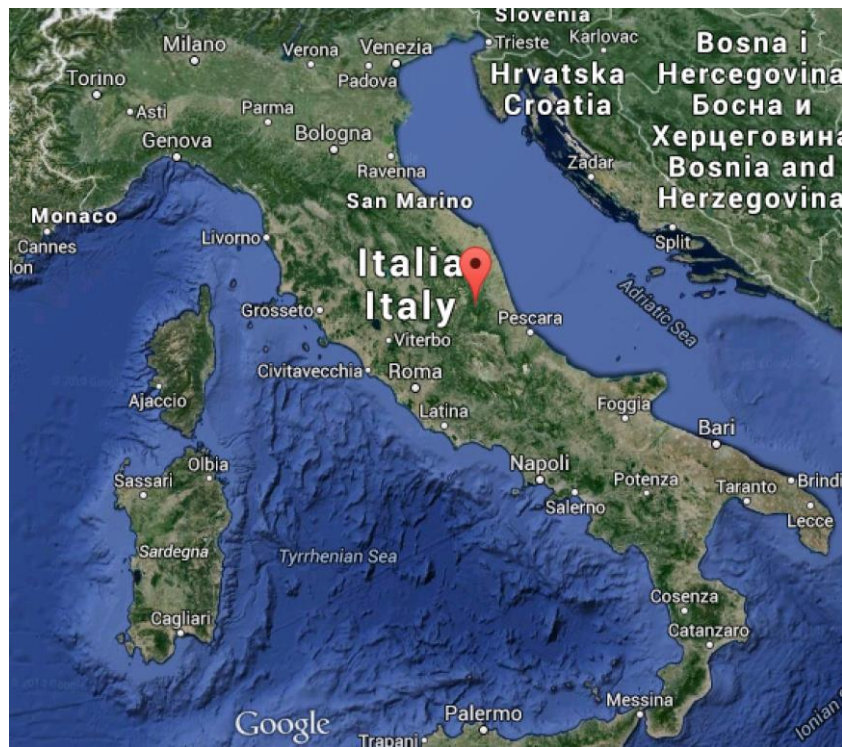


Figure 3-1: Geographical situating of Acquasanta Terme in Italy. Acquasanta Terme is indicated with the red dot. (Google Earth, 2015)

A topographic map of Acquasanta Terme is shown in figure 3-2. The main river, running through the village is the Tronto. This river is important for the geomorphology as its valley gives rise to the major topography variation at this location. The river marks the western boundary of the travertine occurrences at Acquasanta Terme. A few active thermal sources flow into the river. More detail on this will be given in the section 3.2.3. Topography controls travertine distribution in Acquasanta Terme, as different deposits occur at different altitudes. The height difference between the travertine body (581m) and the river (332m) is about 250m, based on the topographic map. The nearest hilltops near Acquasanta Terme reach heights up to 794.8m for Pizzo Murello and even 1070.5m for Monte Vicito.



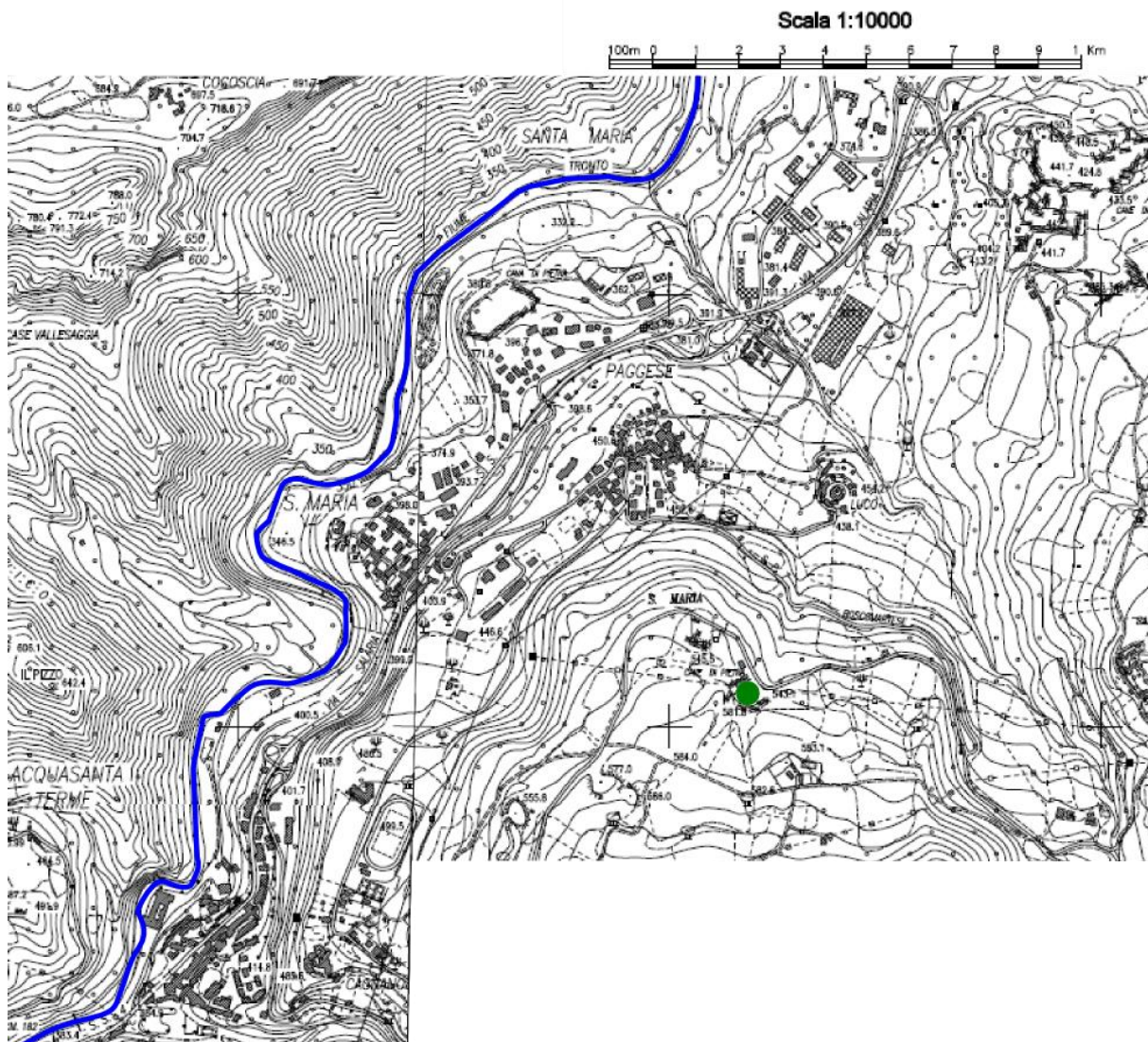


Figure 3-2: Situation of the studied quarry (green dot) on the topographic map, with Acquasanta Terme in the lower left corner. The blue line is the Tronto River. As this map shows, the travertine body is elevated, compared to the river.

## 3.2. Geological setting

The following sections will put the study area in a broader geological context. Section 3.2.1 covers the geological evolution of the Apennines. Section 3.2.2 treats the regional geology, in which the sedimentary sequence and the regional structures are analysed. The final section 3.2.3 will put the studied travertine body in the framework of both regional and other Italian travertine.

### 3.2.1. Geological evolution in Italy

The most relevant part of the geological evolution of Italy are the Apennines. Sani et al. (2004) describe the structure of the mountain chain as a thrust sheet complex, which is complicated by extensional and

strike-slip tectonics with both NE-SW and NNE-SSW trending principal stresses. The Apennines record a complex evolution varying from Mesozoic rifting (Cardello & Doglioni, 2015; di Francesco et al., 2010; Santantonio & Carminati, 2011) to subduction with related volcanism (Cardello & Doglioni, 2015; Royden et al., 1987) and a thrust-and-fold belt, caused by scraping of the lithosphere from the subsiding African plate (Capozzi et al., 2012; Cardello & Doglioni, 2015; di Francesco et al., 2010; Scisciani et al., 2002). This finally ended with post-shortening extension in the fold-and-thrust belt (Cardello & Doglioni, 2015; D'Agostino et al., 2009; Scisciani et al., 2014). Uncertainty remains whether thin- or thick-skinned tectonics prevailed in the Apennine mountain range. Thin-skinned tectonics would have a detachment level in the Triassic evaporates. Thick-skinned tectonics would result in deeper faults, where the evaporites are replaced by dolomite (Santantonio & Carminati, 2011). Scisciani et al. (2014) describes that both types of tectonics can be present. Another uncertainty is whether subduction is still ongoing or not. Even though Minissale et al. (2004) did not find evidence in literature that subductions was still ongoing, GPS measurements by Devoti et al. (2011) showed ongoing movement. Subduction is likely to be still occurring but it is certainly decaying (e.g.: Faccenna et al. 2004).

Extensional tectonics preceding the Apennine orogeny are related to paleomargins of the Triassic to Early-Jurassic opening of the Western limb of the Tethys ocean or the Liguria-Piemonte ocean, of which the oceanic crust outcrops in the Alps (Calamita et al., 2011; Manatschal & Bernoulli, 1999; Santantonio & Carminati, 2011). The generated normal faults are reactivated during later compressional phases during positive tectonic inversion (Artoni, 2013; Calamita et al., 2011; Scisciani et al., 2014, 2002). The compressive regime resulted from the collision of the Eurasian and the African plates starting from the Neogene to the recent (Calamita et al., 2011; Capozzi et al., 2012). This resulted in subduction of the oceanic crust of the western Adria plate below the Eurasian plate (Bigi et al., 2013). During the evolution of the subduction system a local extensional regime to the east of Italy resulted in the Liguro-Provençal back-arc basin (Faccenna et al., 2001). Most recent subduction resulted in the generation of the Tyrrhenian Sea where even oceanic crust has been created (Figure 3-3; Boccaletti et al., 1990; Capozzi et al., 2012; Faccenna et al., 2004, 2001; Gueguen et al., 1997; Royden et al., 1987). The other side of the fold-and-thrust belt is characterized by a foredeep basin in the Adriatic Sea, created by forces that the downgoing slab exerted on the overlying slab and gravitative force caused by the weight of the Apennine mountain chain (Royden et al., 1987). The subduction zone is retreating eastwards (Figures 3-3; Gueguen et al., 1997). Fast retreat of the subduction hinge gets the foredeep sediments continuously integrated in the mountain chain (Doglioni et al., 1999). The retreat of the subduction hinge is at a faster rate than the overlying plate follows. This resulted in cross-cutting of the Apennine accretionary prism by back-arc extension which generates Quaternary normal faults (Cardello & Doglioni, 2015). At present, uplift of the Apennine Mountains is still ongoing, with extension in the Apennine belt and compression east of the Apennines (Barchi & Mirabella, 2009; Devoti et al., 2011; Gulia & Wiemer,



2010). Activity of these tectonics are seen by the l'Aquila earthquake, which is of compressive origin (Walters et al., 2009).

The Apennine orogeny is linked to the travertine deposits at Acquasanta Terme as water flow is topographically or tectonically driven. The thrust faults, generated during the creation of the orogenic wedge, could be a possible permeable pathway for deep-seated fluids.

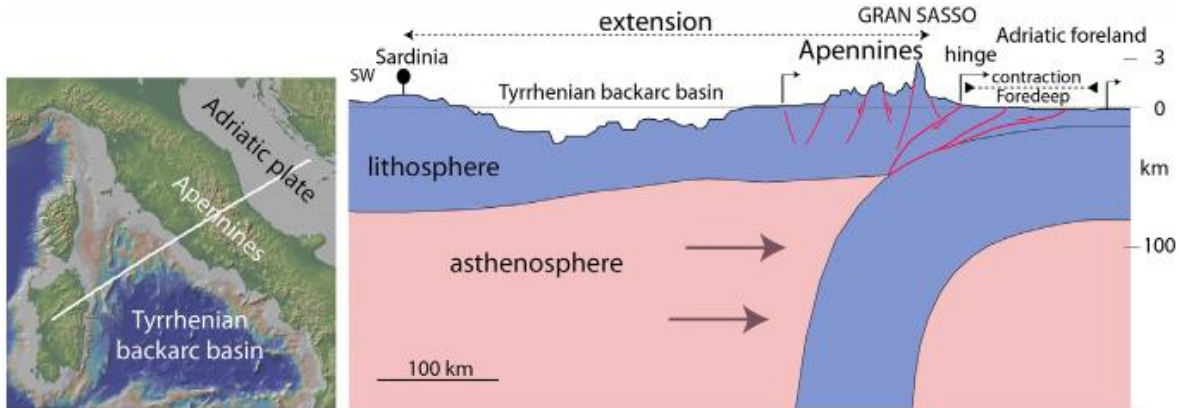


Figure 3-3: Westward subduction that is retreating towards the east, as indicated by the arrows. The Tyrrhenian basin is a back-arc basin created through subduction. The Apennine mountain chain is a fold-and-thrust belt created by scraping sediments of the subsiding slab. To the east of the mountain chain a foredeep basin is being generated and is caused by contractional forces (Cardello & Doglioni, 2015).

### 3.2.2. Regional geology

This section treats the geology proximal to the study area. First the sedimentary sequence is given, based on Koopman (1983) and more recent studies at the Acquasanta area. The second part of this section treats the local geological structures that could have influenced the creation of travertine in this area.

No actual sedimentary sequence at Acquasanta Terme has been described and most research focusses on the nearby mountain ranges. Due to lateral variation in the lithologies, only an estimate of the underlying stratigraphy can be given (Figure 3-4). Koopman (1983) has developed a detailed description of the stratigraphy of the Marche-Abruzzian area of the Central-Apennines, which was used as the basis of the stratigraphic sequence in figure 3-4. The oldest deposits in the sedimentary sequence are Triassic anhydrites, these are followed by a carbonate platform phase after which deepening occurred that generates marly sediments (Cardello & Doglioni, 2015; Koopman, 1983; Madonna et al., 2005; Menichetti, 2008). At Acquasanta Terme the marls and limestones of the Miocene Acquasanta Group are exposed in the core of the Acquasanta Anticline. More recent siliciclastic deposits of the Laga formation have eroded from the Acquasanta Anticline but are exposed in the nearby mountains (Galdenzi et al., 2010; Koopman, 1983). The marly units that are outcropped in the Acquasanta area form the regional aquiclude (Galdenzi et al., 2010).

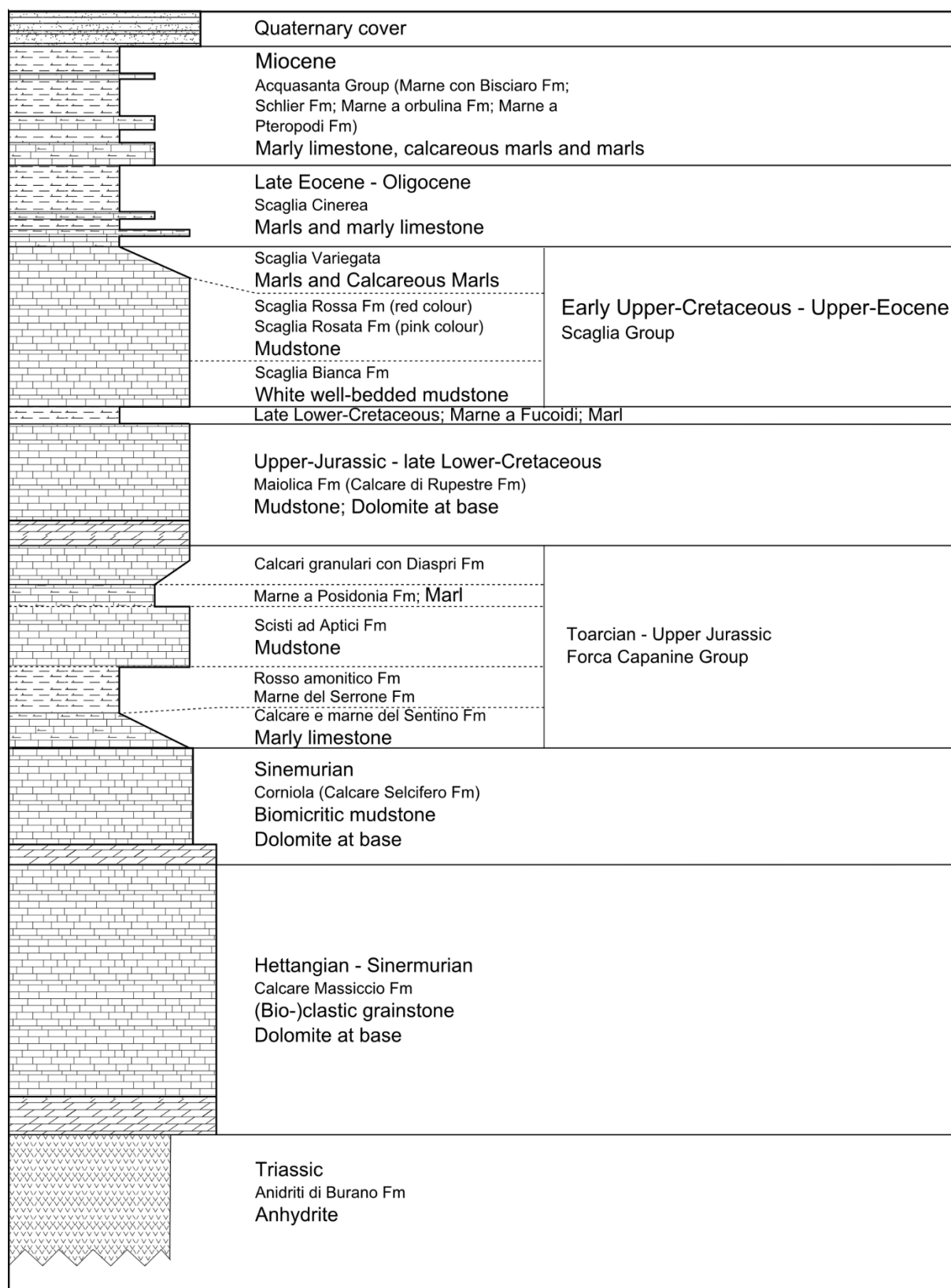


Figure 3-4: Stratigraphy at the Acquasanta Terme area compiled from descriptions of Koopman (1983); Madonna et al. (2005); Menichetti (2008), Galdenzi et al. (2010) and Cardello and Doglioni (2015). The Laga-formation on top of the Acquasanta group is not indicated in this column as it has been eroded in Acquasanta Terme. It is, however, present in the surrounding mountains. The Burano formation contains carbonates and anhydrite bedded in between them.

The Acquasanta anticline originated from Pliocene compressional forces in the area. The compressional phase of this region of the Apennines resulted in thrust nappes and folding of the rocks. In the area of Acquasanta Terme, this folding resulted in the Acquasanta anticline, which has thrust over the deposits of the Laga Formation by thrust activity of the Mt. Gorzano-Acquasanta thrust. The thrust has a throw of 2 km (Figure 3-5A; Bigi et al., 2011; Galdenzi et al., 2010; Menichetti, 2008).

The Acquasanta area is marked by local normal and transtensional faulting (Figure 3-6; Maggi et al., 2015; Menichetti, 2008). The cause of these transtensional faults is not given but is likely to be due to both eastward (thrust stacks of Apennine compressional stress) and northward (Gran Sasso Thrust) directed thrusting.

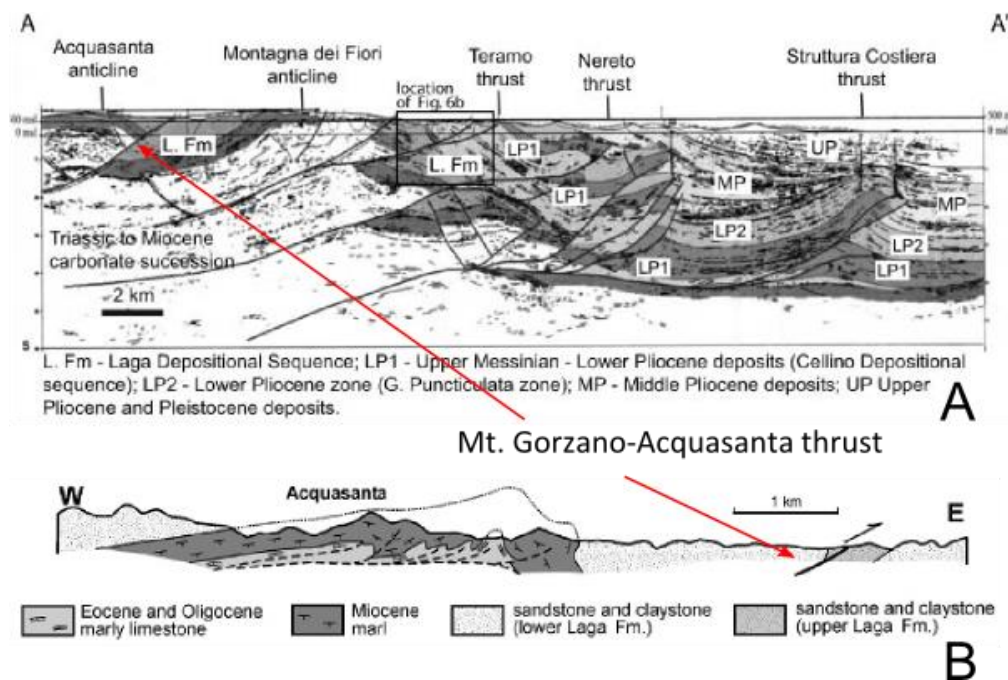


Figure 3-5: Acquasanta anticline and the associated thrust fault. A. Interpretation of a seismic section with the Acquasanta anticline shown in the left part. Picture from Bigi et al. (2011). B. Close-up sketch of the Acquasanta anticline. The core of the anticline shows the marly units of the Acquasanta Group (sensu Koopman, 1983). The sketch shows secondary folding. Picture from Galdenzi et al. (2010).

### 3.2.3. Travertine in Acquasanta Terme and the rest of Italy

As previously mentioned, the name travertine comes from Lapis Tiburtinus, the “Rock of Tivoli”. This already indicates that travertine has been of major importance in Italy and mainly the area around Rome (Tivoli is 20 km of Rome city centre). Travertine has indeed been used to construct buildings in a lot of cities throughout Italy (e.g.: Rome, Ascoli Piceno, etc.). Figure 3-7 indicates the distribution of fossil and actively depositing travertine. It provides a clear indication that travertine is mainly deposited to the

west of the Apennine mountain chain, related to back-arc extension (Minissale et al., 2002). Most of the travertine deposits are situated in the Northern Apennines (Ford & Pedley, 1996).

Travertine is mainly found in areas with an extensional regime. Upwelling of the calcium-saturated fluids is restricted to areas with increased permeability, usually created by faults in the bedrock. In extensional regimes, these faults are normal and transtensional faults (Brogi & Capezzuoli, 2009; Ford & Pedley, 1996). A relation with volcanic systems is often noted as increased temperatures could serve as a driver for a deep-seated hydrothermal system (Capezzuoli et al., 2014; Ford & Pedley, 1996; Minissale, 2004). Of the over hundred travertine and tufa deposits in Italy, both active and inactive, most are fed by meteoric or weakly to highly thermal waters, with temperatures sometimes as high as 64°C (Ford & Pedley, 1996). Based on  $\delta^{18}\text{O}$ -data, Minissale et al. (2002) proposed that the flow paths of the fluids that precipitated the travertine are shorter for the springs in the east of Italy (Acquasanta, Triponzo, ...), compared to the west (Viterbo, Tivoli, ...). The eastern springs lie topographically higher, in intramontane areas. In the area of Rome, the travertines occur in the Tiber valley. Also in the Central-Apennines, along the Ancona-Anzio line, several travertine springs occur (e.g.: Cotilia and Acquasanta).

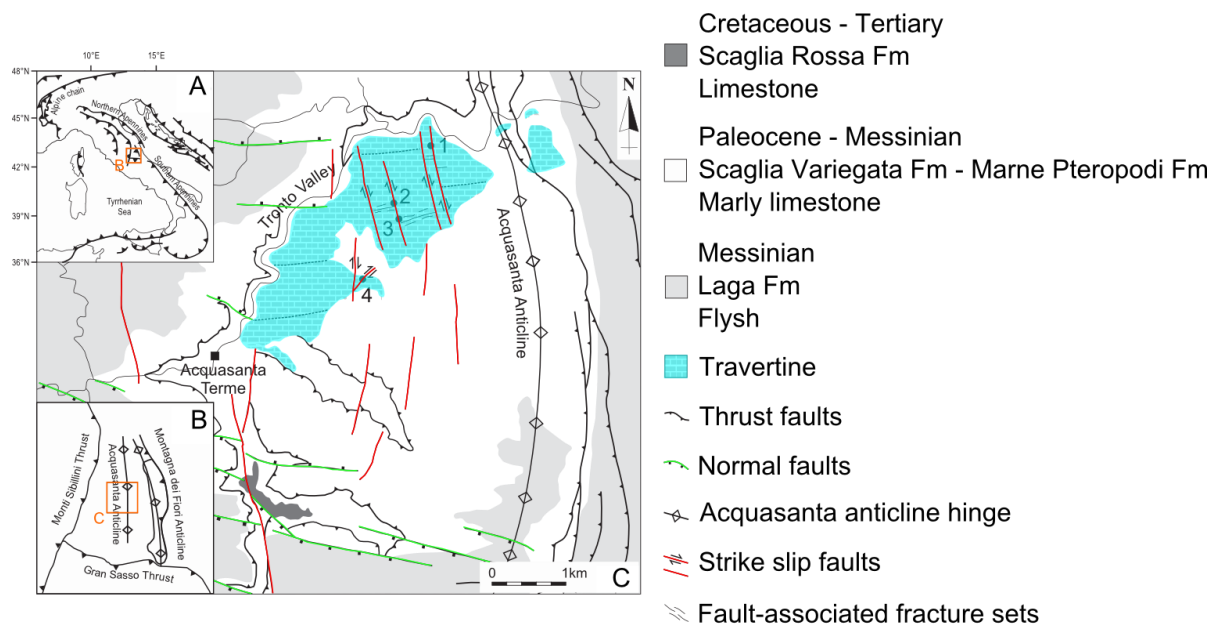


Figure 3-6: Small scale regional map of the Acquasanta area. The light blue colour indicates the travertine body. A lot of strike-slip faults are present in the area and a relation between the strike-slip faults can be assumed. The faults without travertine surrounding them are situated at higher altitudes, which could be the reason for the absence of travertine. The fluid pressure might not have been sufficiently high. A. Map of Italy. B. Situation of Acquasanta Terme area to other structures. C. Close-up geological map. Picture modified from Maggi et al. (2015)

The Ancona-Anzio line, which is a transpressional fault, separates two Mesozoic platform sequences, i.e. the Tuscan-Umbrian and the Abruzzese platform sequences to the North and the South, respectively (Minissale et al., 2002). The stratigraphy and the type of subsurface limestone deposits is different on both sides of the Ancona-Anzio line (Chiocchini & Cipriani, 1989; Minissale, 2004). The line separates



two zones of the Apennine mountain chain with a different amount of compression (Chiocchini & Cipriani, 1989).

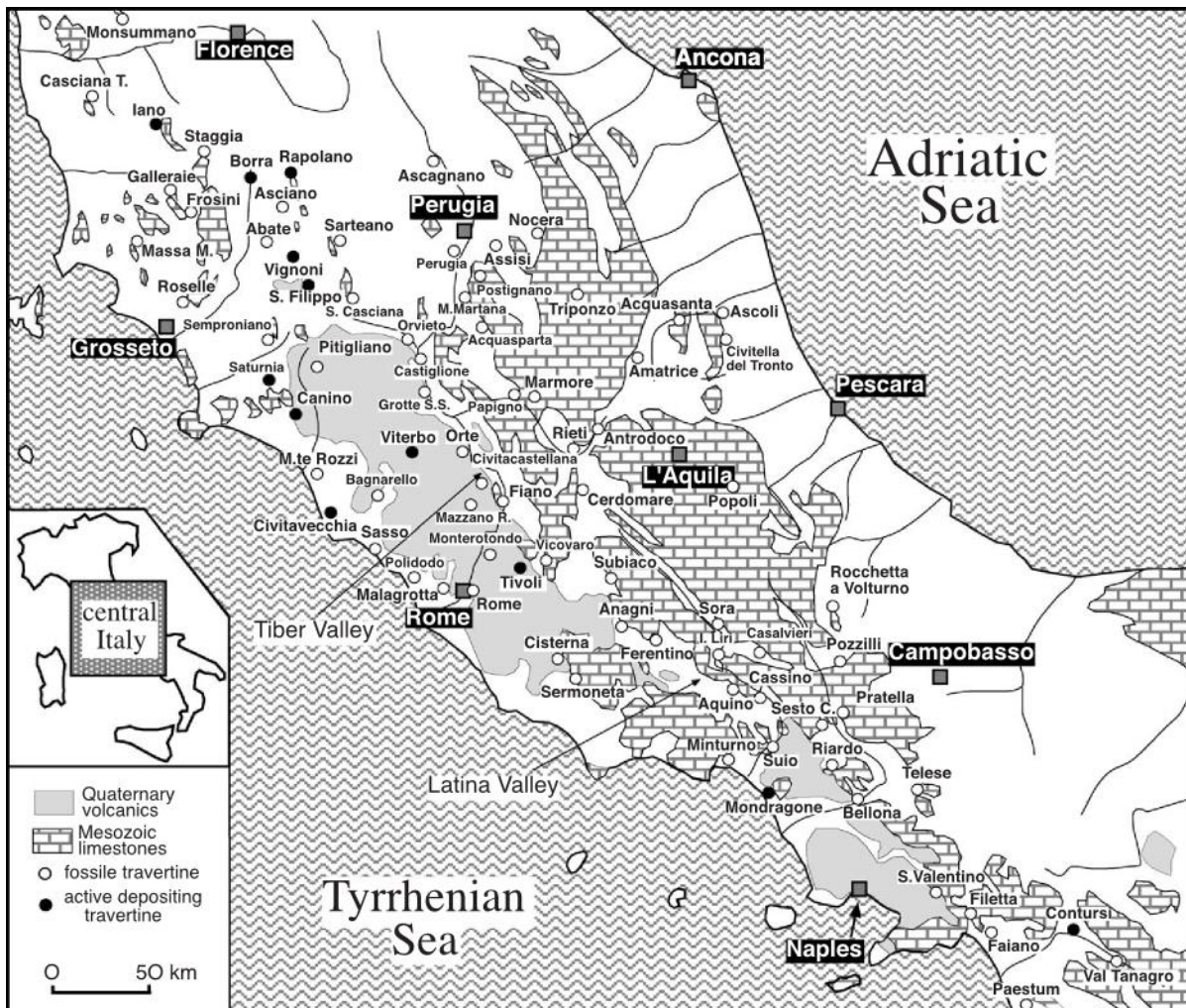


Figure 3-7: Distribution of both active and fossil travertine deposits. This figure shows that travertine mainly occurs to the west of the Apennine mountain chain and most are present in the Northern Apennines. This is likely to be related to volcanic activity in a back-arc basin. The area of study is situated in Acquasanta. Together with Ascoli and Civitella del Tronto, it forms a close cluster of travertine deposits to the east of the Apennines. Figure from Minissale (2004).

A lot of different spring carbonate systems are present in Italy (e.g.: plateau travertine, fissure ridges, tufa, etc.; Figure 3-7). The mostly studied deposits are the Tivoli plateau travertine near Rome (De Filippis et al., 2013b; Ford & Pedley, 1996), Rapolano Terme fissure ridge and mound deposits close to Siena (Brogi & Capezzuoli, 2009; Guo & Riding, 1999, 1998, 1994; Honlet, 2013), Viterbo in Lazio, near Rome, where hot springs ( $>60^{\circ}\text{C}$ ) are present (Di Benedetto et al., 2011; Pentecost, 1995), etc.

Only few travertine deposits are present to the east of the Apennines (Figure 3-7). The travertines in the area near Acquasanta Terme are one of those few locations. The travertine bodies nearby are not related to the same geological structures as the Acquasanta Terme deposits and have a different age. At Ascoli Piceno, 20 km of Acquasanta Terme, the older deposits of Colle San Marco, Monte Venna Rossa and la Zona di Rosara are deposited. Colle San Marco and Monte Venna Rossa are related to each other in their genesis (Boni & Colacicchi, 1966). Another deposit close to Acquasanta are the Civitella Del Tronto travertines (Boni & Colacicchi, 1966). These deposits are lacustrine and tufaceous deposits (own reconnaissance work). At Acquasanta Terme, three different levels or “terraces” of travertine are deposited (Figure 3-8; Boni & Colacicchi, 1966). The three terraces reflect a decreasing local hydraulic

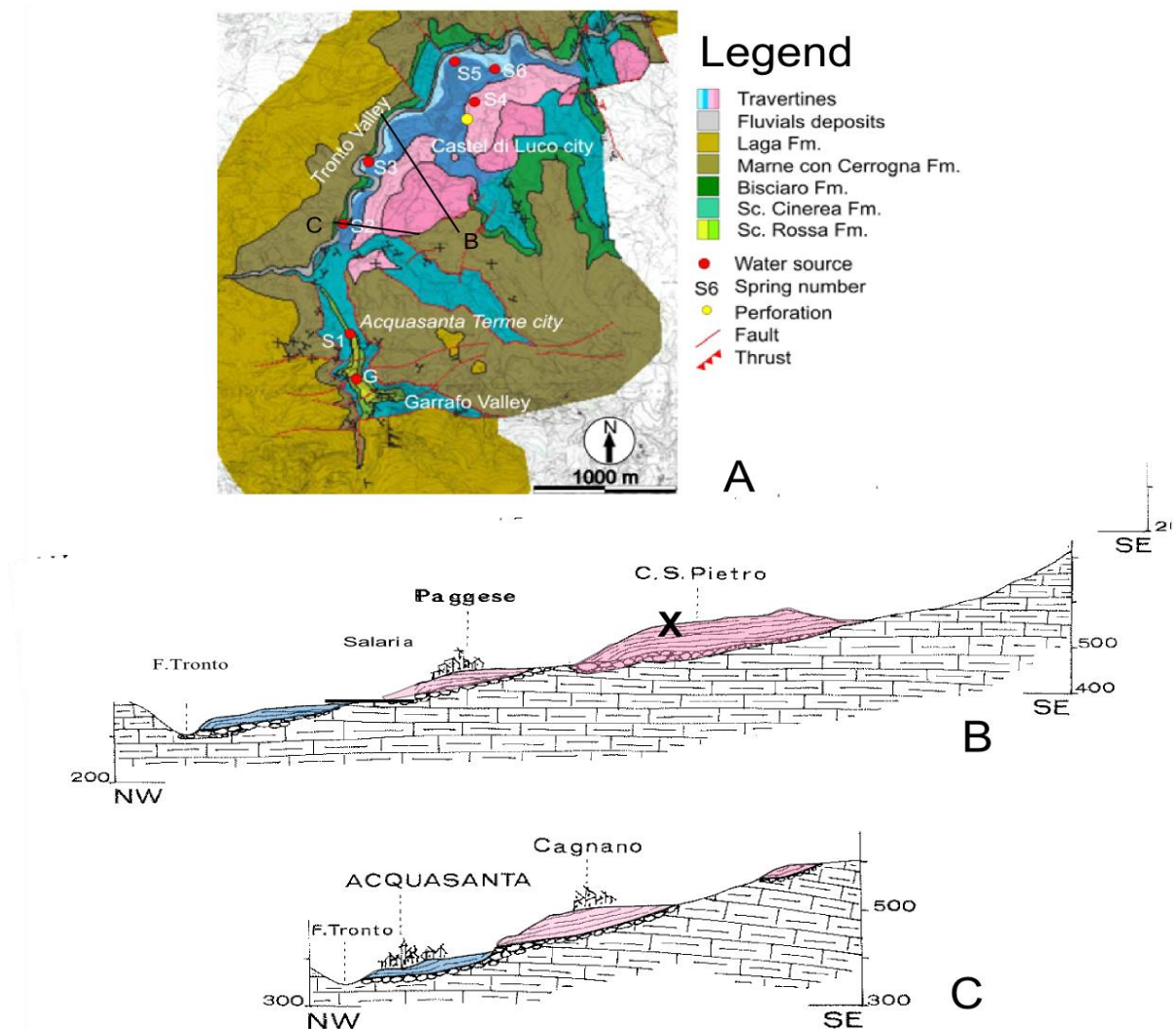


Figure 3-8: Three travertine terrace levels in Acquasanta Terme area. A. Map of the three travertine levels, a fourth level is indicated at the river. These are the recent travertine deposits. Map from Madonna et al. (2005). B and C. Cross sections, indicated by black lines in A. The black cross in B indicates the location of the analysed quarry. Pictures modified from Boni and Colacicchi (1966).

head, indicating that the oldest deposit is topographically at the highest level. The hydraulic head reaches lower altitudes due to a decrease in fluid pressure and abandons the upper level (Boni & Colacicchi, 1966; Madonna et al., 2005; Pentecost, 2005). Therefore a second travertine system at lower altitudes



developed. The continuing decrease in hydraulic head finally generated and abandons a third level. A decrease in the base level of the Tronto river is likely to be coinciding with a decreasing hydraulic head, which is why the river altitude is coincident with the depositing travertines. The presence of the Tronto river at the same altitude as the depositing travertine bodies is evidenced by the presence of fluvial conglomerates at the base of each travertine body (Figure 3-8 B&C; Boni & Colacicchi, 1966). All the travertine in the Acquisanta Terme area were deposited on the east bank of the Tronto (Figures 3-8 and 3-9A). At the present time, there is still activity of thermal springs in the Acquisanta area (Figure 3-9). The water is rich in  $H_2S$  and enters the Tronto river from caves at temperatures of up to  $44^\circ C$ . Seasonal fluctuation of the water temperature is present in each of the springs (Galdenzi et al., 2010; Madonna et al., 2005).

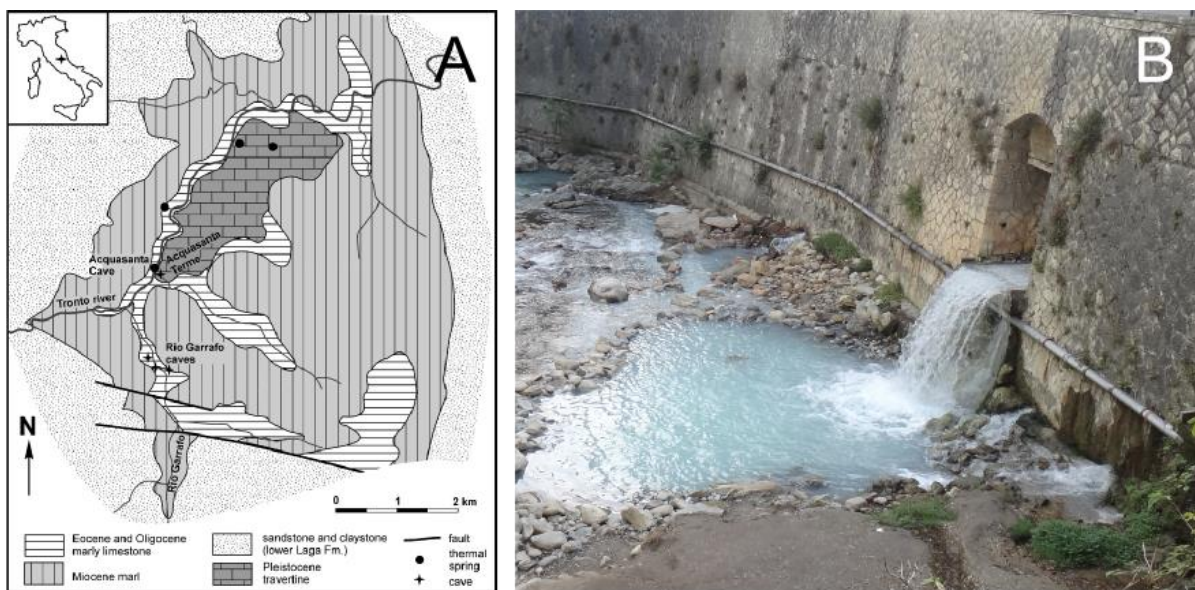


Figure 3-9: Thermal springs at Acquisanta Terme. A. Map of the Acquisanta Terme travertines and the surrounding geology. The black dots indicate the presence of present thermal springs. Picture from Galdenzi et al. (2010) B. A spring of thermal waters, which has been modified by anthropogenic activity to stimulate tourism. It is possible to enter this tunnel. A small cave is present there.

A bimodal origin of the spring waters is proposed by Menichetti (2008), Madonna et al. (2005) and Minissale et al. (2002). Deeply circulating and meteoric waters are mixed. The meteoric waters are provided by regional groundwater flow (Madonna et al., 2005; Minissale et al., 2002) or by direct infiltration of meteoric waters from the rivers (Galdenzi et al., 2010). The deep waters contain  $H_2S$ , sulphates and alkali chlorides and are the result of medium to deep circulation. They reached down to the Triassic evaporite sequence at the base of the Acquisanta anticline (Madonna et al., 2005; Menichetti, 2008; Minissale et al., 2002). Madonna et al. (2005) suggested volcanic influence in the deep thermal spring waters. The ratio of meteoric versus thermal waters is governed by climatological variations. Seasonal variation in water temperature and geochemistry suggests an alternating dominance of either deep thermal waters or shallow meteoric waters (Galdenzi et al., 2010; Madonna et al., 2005).

## Chapter 4: Methodology

This section describes the different methods used to achieve the objectives of this thesis. In this respect it is important to mention that one given method does not always provide unambiguous results and could only be interpreted in a correct way by combining the output of different methods. For example ICP-OES differentiates two lithotypes, thin section petrography is used to explain the differences in a qualitative way (e.g. based on the minerals that are present) and XRD-analysis provides quantitative results.

### 4.1. Fieldwork

Two weeks of fieldwork were conducted, from August 25<sup>th</sup> till September 5<sup>th</sup> 2015. The first part of the fieldwork consisted of getting acquainted to the diversity of different lithotypes and –facies in a travertine body. Together with this general introduction, some lithologs have been created. The second part of the fieldwork consisted of sampling and making linedrawings. Both the lithologs and the linedrawings are digitized in InkScape. The same colours are used for the lithotypes.

#### 4.1.1. Lithologs

Lithologs are made to consider vertical variation of the deposits throughout the travertine body. During digitization, the lithologs are combined with an estimated amount of porosity, complemented by a point-counting image analysis for a more quantitative approach. The scale of the lithologs drawn in the field is 1:50.

#### 4.1.2. Linedrawings

Linedrawings are sketches on which the deposits are indicated. They are used to correlate layers and deposits between different quarry walls to unravel the geobody architecture in three dimensions. Several features can be mapped in such linedrawings, e.g. erosional surfaces, onlap, offlap, downlap, karst features, etc. One of the most important features is to indicate layers that are onlapping, offlapping or downlapping as they indicate different moments in time or different flow directions. These features are often present near an erosional surface which form marker beds that can be followed over the quarry walls. They are very important in 3D-characterization of the geobody architecture.

The linedrawings are drawn on high quality merged pictures of the quarry walls (e.g.: Figure 4-1). One linedrawing has been sketched without a photo because the wall had been cut after printing of the photos.



After making linedrawings, the different lithotypes are indicated on them. This has been done to estimate facies variation throughout the geobody and to look at possible correlations related to the slope of the layers. These facies variations are later used in the depositional model. The lithotype mapping allows to get a detailed three-dimensional insight in the deposits and to construct a reservoir analogue.



*Figure 4-1: Example of a compiled picture of a quarry wall, used in linedrawings and lithofacies variations. Such pictures were available for most quarry walls.*

### 4.1.3. Sampling

Sampling during the field campaign was done by the use of two drilling machines. The first drill is a Stihl Pomeroy EZ Core Drill of the Model D261-C, equipped with a one inch core drill. This drill was used for in-situ sampling of plugs. The second drill is equipped with a four inch core (BS-4PRO Bit) and is a Pomeroy Model D026-GT10 drill. This drill was used for sampling of cores. This drill was dysfunctional from the second sampling day onward, so not a lot of cores could be taken.

## 4.2. Petrography

Petrographical analysis is the study of the textures, fabrics and porosity but also of post-depositional processes that affect the sediment fabrics and its porosity. The petrographical techniques are applied on thin sections, which will, in a first instance, be described by traditional microscopy. Fluorescence microscopy is performed on a set of thin sections to analyse especially micro-porosity. Finally cathodoluminescence will provide information on diagenetic processes which alter porosity and consequently also the permeability.

### 4.2.1. Thin sections

Thin sections form the base for classical microscopical analysis, cathodoluminescence and fluorescence microscopy. Before creation of thin sections, the samples are cut to a thickness of approximately 1 cm. Subsequently, they are doubly impregnated with a fluorescent, ultra-low viscosity resin, in a high vacuum, which causes the porosity to become more easily distinguishable from the rest of the fabrics. The chemicals added to this resin to ensure hardening are ERL 4206, n-Octenyl succinic anhydride, RD-

2 (epoxy-modifier) and S-1 accelerator. The impregnated resin fluoresces under light with a wavelength between 450 and 495 nm, which allows to use the thin sections for fluorescence microscopy. The remaining resin is cut off the sample and the sample is polished and attached on a frosted glass slide with a two-component glue (Epothin BUEHLER). The slab is subsequently cut to 1 mm thickness. In the following step, twelve rock slabs can be scraped to a thickness of 200  $\mu\text{m}$  in a G-BROT machine (version 1.03.12) and to 40  $\mu\text{m}$  with the BROT-machine (version 1.03.16), simultaneously. After this step the slabs are manually thinned to 30  $\mu\text{m}$ . As the final step, the thin sections are polished using a STUERS ROTOPOL (31, 35) and ROTOFORCE (4) on a MD DAC cloth with polycrystalline diamonds with a size of 1  $\mu\text{m}$ .

Scans of the thin sections are made by an EPSON Perfection 1240U scanner, supplied with an EPSON Film Adaptor B81317 to ensure light falling through the thin section. The photos are acquired by Corel PHOTO-PAINT 9 software, which allows to select the thin sections in the scanned image. An example of such a scan is shown in Figure 4-2. These scans are analysed by point-counting in J-MicroVision (Roduit 2002-2007).

In total, 42 thin sections are created of which 10 come from a fossil cave structure. The selection of the samples focussed on sampling all different lithotypes and textures and is based on the field description of the samples.

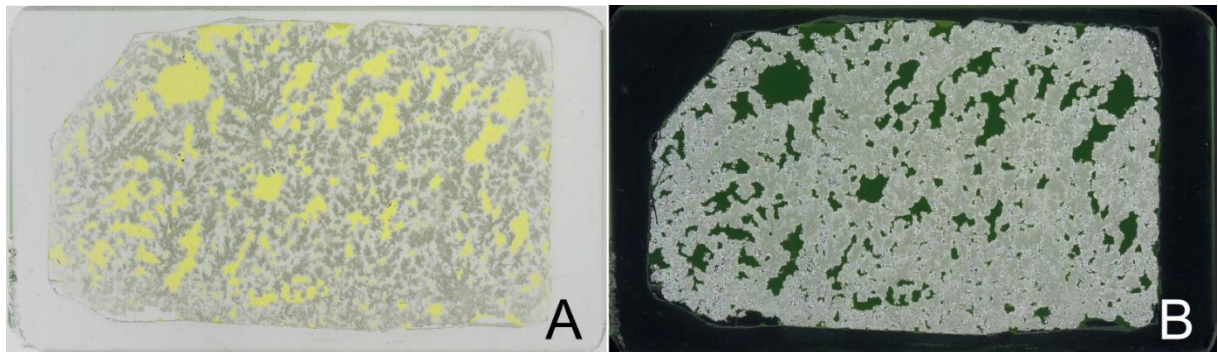


Figure 4-2: Example of a thin section scan of sample AS14NJ022. (a) shows a scan under parallel polars, (b) is the same thin section under crossed polars.

#### 4.2.2. Classical microscopy

Classical microscopy results in a reconnaissance analysis of textures and porosity in the samples. Thin sections are analysed for petrography by an Olympus BX60 microscope and photos are taken with a Jenapol microscope and photos of the thin sections are taken with an AxioCam MRc camera using the AxioCam software.

A short description of each thin section is made with special attention to existing textures, including the amount of micrite and sparite and the shapes under which they occur. Porosity and cementation are

addressed in the analysis as they are two important characteristics to be defined in a reservoir analogue study.

### 4.2.3. Cold CathodoLuminescence (CCL)

Cathodoluminescence (CL) is a technique commonly applied in sedimentary and diagenetic studies. This technique is combined with traditional microscopy and offers the additional benefit of visualisation of features, impossible to detect with traditional microscopy. CL, for example, often allows to visualise growth zones in crystals that would seem uniform under translucent light. Cathodoluminescence on carbonates could provide extra information on fundamental diagenetic relationships between grains and its relationship to the cements, porosity evolution and replacement reactions (Hiatt & Pufahl, 2014). More background on CL in Appendix 1. The cold cathodoluminescence equipment used for this study is a modified Techosyn Model 8200 MARK II. This microscope allows to observe and photograph the sample both under parallel polarized light and cathodoluminescence, induced by an electron beam. The thin sections on which the study is performed are inserted in a vacuum chamber with a low vacuum varying between 35 and 43 mTorr. The electron beam has a width of 5 mm and hits the sample under a shallow angle. The used voltage varies between 6 and 8 kV and the current changes between 350 and 500 mA. The camera's shutter time is set on 20 ms for photos of the sample under transmitted light and 10 s to photograph the luminescence. The long shutter time amplifies the weak light that is emitted from the cathodoluminescence.

Up to recently, not a lot of studies applied CL as an important technique in the determination of diagenetic processes in travertine. More and more recent studies on travertine apply cathodoluminescence to provide information about diagenesis, fluid origin, recrystallization, etc. (Brogi et al., 2014; Claes et al., 2015; Degros, 2013; Honlet, 2013; Smekens, 2013). Application of CL on continental carbonates is not always prone to provide extra information, due to uniform luminescence over all samples (Claes, 2011; Soete, 2011; Vandewijngaerde, 2012).

### 4.2.4. Fluorescence microscopy

Fluorescence microscopy allows to clearly distinguish pores as they are impregnated with a fluorescent resin. This resin illuminates when excited by fluorescent light, which is light filtered for a wavelength between 450 and 495nm. The fluorescence of the resin allows to give an estimate of pore interconnectivity and reveals microporosity and possible microfractures. Pore interconnectivity can be assessed by analysing which pathways are illuminating the most under fluorescent light. In fact, it is more common to analyse which pathways are blocked by e.g. cementation. The images are integrated with porosity and permeability data. The fluorescence analysis is done with a Leica DM LP microscope. The incident light is generated by a Leica 12V/100W light source and is filtered by a BP450-490/LP515 filter.

### 4.3. Image analysis

Image analysis is performed both on photos of the quarry walls and scans of thin sections with the program JMicroVision (Roduit, 2002 - 2007). The program is used for both point-counting and object extraction.

A point-counting analysis is always prone to small errors because: the analysis is done on a 2D thin section or field photograph while a 3D volume is analysed, it is user-dependent which results in small error and it follows a statistical approach. A random point on the image is indicated and identified. Because of the several sources of error, a standard deviation is identified for each phase identified in the point-counting analysis (Van Der Plas & Tobi, 1965), namely:

$$\sigma = \sqrt{\frac{P(100 - P)}{N}}$$

- $\sigma$  = standard deviation
- P = derived percentage of a given mineral by point-counting
- N = total number of points counted

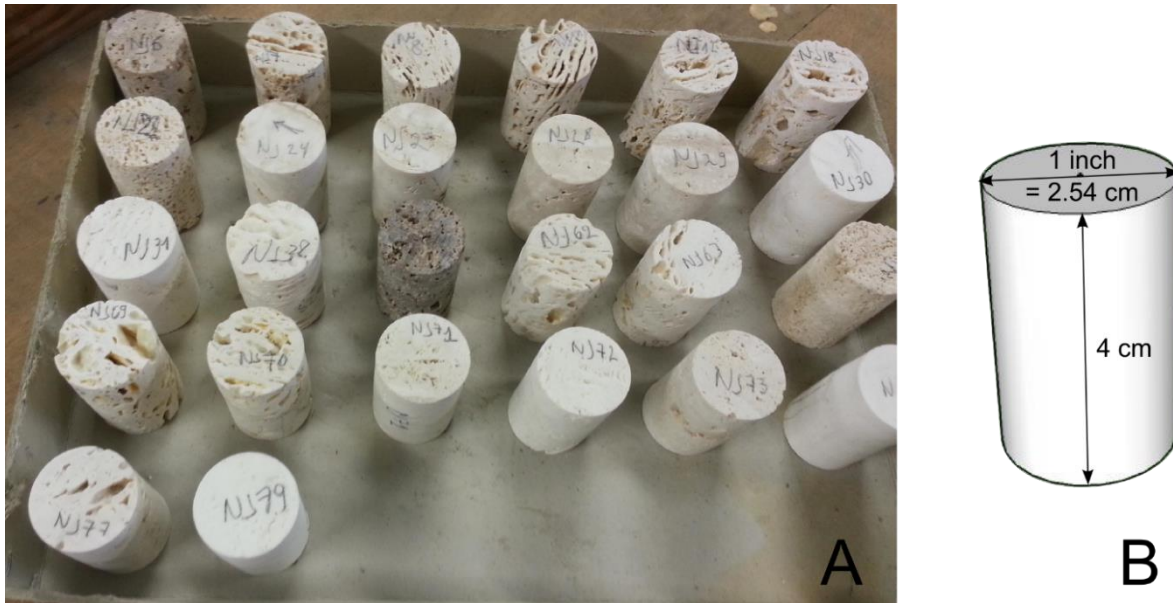
The standard deviation thus decreases with the amount of points counted. The percentage of phases present in the sample will influence the standard deviation. Analyses in this study are usually performed with 250 points counted, unless otherwise stated.

Image analysis is sometimes performed with the object extraction method. The dark green colour that the resin of the impregnated thin sections show under transmitted light scans, is taken as the colour threshold to select pores. The disadvantage of this technique is that small pores ( $< 20 \mu\text{m}$ ) and the rims of larger pores tend to be excluded from the selection. It is easy to over- or underestimate the porosity based on the followed approach.

### 4.4. Petrophysics: porosity and permeability

Constructing a petroleum reservoir analogue model is one of the goals of this study. Two of the most important characteristics for a reservoir model are the effective porosity and permeability. These parameters are determined by a petrophysical analysis, which was performed on 25 plugs from the different lithotypes (Figure 4-3). Some extra plugs are taken afterwards in the lab from larger blocks and cores with a HILTI DD 130 diamond core with plug diameter of one inch. The plugs are subsequently cut to a length of 4 centimetres and polished to make the ends flat and parallel. Plugs taken during the sampling campaign are all horizontal plugs. A small amount of plugs which are taken from blocks and cores are purposely selected to be perpendicular to the depositional layers to analyse the difference between horizontal and “vertical” permeability. This difference is important in a reservoir

analogue, especially in a complex system as travertine, in which vertical and horizontal variation is common. Indeed, flow of hydrocarbons during extraction would occur along and across the different layers, following the most permeable path.



**Figure 4-3:** A. (1 inch) plugs for analysis of petrophysics. B. Illustration of the dimensions of the plugs.

The analyses of the petrophysical properties of the samples have been outsourced to PanTerra Geoconsultants B.V., located in Leiderdorp, the Netherlands. The performed analyses are Helium Porosity and Specific Gas Permeability. Both measurements are non-destructive, allowing for repeated analysis for quality control.

Prior to the analysis, the samples are cleaned and dried according to a standard procedure. The cleaning makes use of solvents, which should be strong enough to remove unwanted components, like salts and water, but gentle enough to be harmless to the sample. The latter is very important as extra porosity generation would render the results useless. The used method to clean the samples is the refluxed Soxhlet treatment. The treatment with a cold Soxhlet extractor allows the samples to soak in the solvents. The used solvents to remove water, salts and oil are chloroform, methanol and toluene. The samples are subsequently placed in a fume hood to remove the vapours from the volatile solvents. The last step is drying in an oven at 95°C to evaporate remaining water. The sample is regularly weighed and once it reaches a constant weight, it is certain that all the remaining fluids have evaporated (AAPG, 2014; Andersen et al., 2013; Torsaeter & Abtahi, 2000).

Helium porosity is determined with a Helium expansion porosimeter, which allows for a precise calculation of the effective porosity. The porosimeter measures the grain volume ( $V_g$ ) by analysing the pressure change, according to Boyle's law, upon volume expansion in two connected chambers (Figure 4-4). One of the chambers is the reference chamber ( $V_1$ ) and the other is the sample chamber ( $V_2$ ). The

sample chamber contains the sample of which the bulk volume (BV) is calculated from the sample dimensions. The chambers are initially disconnected and the pressure is known in both vessels, being  $P_1$  and  $P_2$  for the reference and sample chamber, respectively. At this moment, the only unknown parameter is  $V_2$ . Opening the valve between the two chambers results in an equilibration of the pressure,  $P$ .  $V_2$  is calculated by the following formula (Dandekar, 2013):

$$V_2 = \frac{V_1(P_1 - P)}{(P - P_2)}$$

The porosity can be calculated from the  $V_2$  that has been directly inferred from the calculation of the measured data by (Dandekar, 2013):

$$\phi = \frac{V_2 - V_1 + BV}{BV}$$

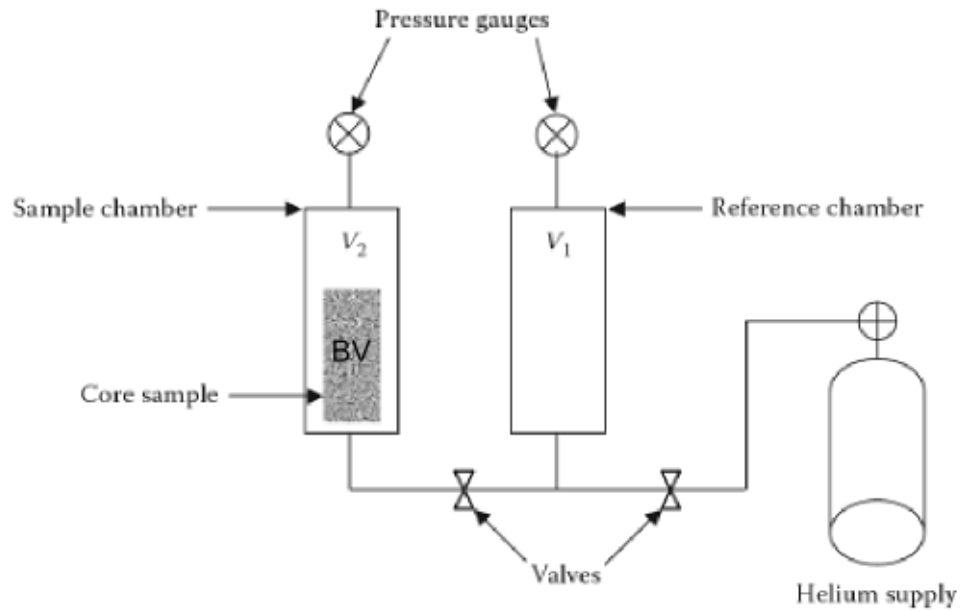


Figure 4-4: Workflow of the Helium expansion.  $V_1$  is the reference chamber,  $V_2$  is the sample chamber. They are initially disconnected with their own  $P_1$  and  $P_2$ , respectively. Opening the valves would connect the two chambers.

The specific gas permeability is measured with a steady state permeameter, which uses laminar gas flow. Permeability is the ability of a porous medium to transmit fluids. Nitrogen is used as an inert gas in this analysis. The sample is placed in an elastomer sleeve which ensures that no gas can flow along the sample and all gas goes through it (Figure 4-5A). In the case that large vugs are at the outer edge of the sample, they are often filled with Teflon. Darcy's law is applied to calculate the gas permeability from the measured flow rate and the pressure drop upon flowing through the sample. Three requirements have to be fulfilled for reliable results: (i) laminar flow, (ii) no reaction between the gas and the sample and (iii) the analyses have to be performed in a room with a constant temperature. Because a gas is used in



this method, corrections have to be made for the Klinkenberg effect which occurs due to turbulence when the capillary openings of the pores approach the mean free path of the gas. A variable permeability is measured when a different amount of pressure is exerted and when different gases are used. Measuring at different pressures and plotting the data points creates a line, which can be extrapolated to zero pressure conditions, giving the Klinkenberg corrected permeability (Figure 4-5B).

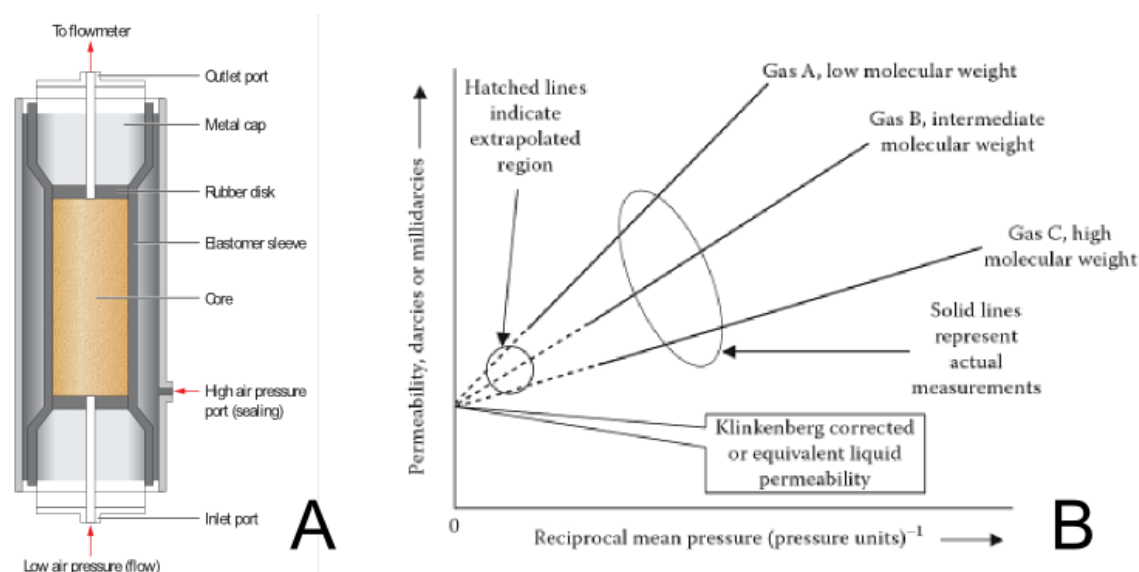


Figure 4-5: A. Conceptual sketch that indicates how the sample is trapped in an elastomer sleeve and how the gas flows through the sample (Andersen et al., 2013). B. This figure indicates how the Klinkenberg effect is different for different gasses and how the resulting permeability depends on the exerted pressure. By getting several measurements of the permeability at different pressures a line can be fit through the data points. This line has to be extrapolated to no pressure to get the “Klinkenberg corrected permeability”.

## 4.5. X-Ray Diffraction (XRD)

X-ray diffraction measurements are performed with powdered samples loaded on a sample holder and mounted into a device which can vary its angle during measurements. A beam of X-rays is sent to the sample and will hit the sample under the angle at which the holder is placed at that moment. The angle varies during the measurement from 5 to 70° and it is called the 2θ-angle. X-ray diffraction has been performed on 10 samples, representing several lithotypes in the deposit. The XRD-analysis is primarily done to discover whether aragonite or calcite dominates in the travertines. Focus was put on vein travertines and bright white cements, as those are expected to differ from the other travertine facies. This hypothesis will be tested. The theoretical background of XRD is provided in Appendix 1

The samples are prepared by grinding the rock with the mortar. After mortar-grinding, 2.7 g of the powder is weighed with 0.3 g of pure zincite to have 10% of zincite as a reference in the measurements.

The mixture of travertine and zincite powder is micronized with a McCrone Micronizing mill, with 5mL of ethanol for 7 minutes. After micronizing the samples, the pots and the corundum beads, with which the samples were crushed, are thoroughly rinsed with ethanol, to avoid the loss of sample material. The mixture of micronized sample and ethanol was collected in a porcelain cup. The ethanol was evaporated from the mixture under the fume hood. After evaporation of the ethanol, the sample is collected as a powder. The sample is subsequently disaggregated with an agate mortar as the sample had aggregated during evaporation of the ethanol. The powder was sieved to achieve grain sizes below 250  $\mu\text{m}$  and then loaded in a sample holder, using the back-loading technique. The powder was gently pushed in the holder, by streaking it with a small glass plate, to avoid preferential orientation and at the same time to ensure a good packing. This randomly oriented crystalline powder is analysed with X-rays.

The X-ray measurements are performed with a Philips PW 1830 diffractometer. An electric current of 30 mA heats a filament which releases electrons. These electrons are accelerated by a voltage of 45 kV and then hit a copper-anode. This anode radiates  $K\alpha$ -radiations with a wavelength ( $\lambda$ ) of 1.544 Å. The machine uses a graphite monochromator, a receiving slit of 0.1 mm and a divergence slit of 1°. The 2 $\theta$ -angle is varied between 5 and 70° with a step size of 0.02° and a count time of 2 seconds for each step.

The XRD-patterns are analysed both qualitatively and quantitatively. For the qualitative analysis, the EVA software is used. The qualitative analysis determines which mineralogies can be recognized from the XRD-pattern by comparing the peaks with high intensity to the EVA mineral database. The quantitative data is retrieved by a Rietveld analysis. The software used for this analysis is Topas (Academic V4.1), which generates an artificial XRD-diffractogram, then compares and fits this with the measured diffractogram. To insert the code in Topas, JEdit is used as a text-editor, which is linked to Topas Academic. The structural data of the minerals is retrieved from FindIt and is inserted in the JEdit code. Fitting of the two diffractograms (measured and artificial) can be optimized by refining the parameters of the minerals. The same incremental approach is used for each analysis. First, the background parameters are calculated, then the cell parameters are refined together with the crystallite size. This is done for each mineral one by one. Each mineral was only refined once and when a next mineral was added, only this new mineral is refined.

## 4.6. Geochemistry

### 4.6.1. Stable isotopes

Stable isotopes are analysed to determine the influence of certain processes (Figure 4-6). The stable C- and O-isotopes provide information on depositional and possible diagenetic processes and they are a powerful tool for fluid characterization in fossil travertine systems. Information about the depositional temperature, fluid origin, source of the  $\text{CaCO}_3$  and water-rock interactions can be obtained from the isotopes of only three different elements: O, C and Sr. Background on stable isotopes in Appendix 1.



Samples for the stable isotope analyses are taken with a Handdrill Dremel Multipro Model 225. The samples for oxygen and carbon isotopes are mainly bulk samples. Some samples have been selected to only represent cements to check for any different from the rest of the travertine deposits. Fourty samples are taken for the analysis of stable oxygen and carbon isotopes. For the analysis of Sr-isotopes, bulk samples are taken from, layered travertine, travertine veins and rocks representing the substrate rock (Miocene marly limestone). Eight samples are taken for Sr-isotopes.

#### 4.6.1.1. *Stable oxygen and carbon isotopes*

Oxygen has three different stable isotopes:  $^{16}\text{O}$  (99.759%),  $^{17}\text{O}$  (0.037%) and  $^{18}\text{O}$  (0.204%) (Harrison et al., 2010). Of these isotopes,  $^{16}\text{O}$  and  $^{18}\text{O}$  are analysed. Carbon has two stable isotopes  $^{12}\text{C}$  (98.89%) and  $^{13}\text{C}$  (1.11%) and an unstable isotope,  $^{14}\text{C}$ , which is often negligible due to the rapid decay. More background information in Appendix 1.

Isotopic compositions are expressed in the deviation of the values from a given standard and are expressed in permill (Equation for oxygen below; Baskaran, 2002). The laboratory standard for the carbonate fraction is the Vienna Pee Dee Belemnite (V-PDB) standard.

$$\delta^{18}\text{O}_{\text{sample}} = \frac{(^{18}\text{O}/^{16}\text{O})_{\text{sample}} - (^{18}\text{O}/^{16}\text{O})_{\text{standard}}}{(^{18}\text{O}/^{16}\text{O})_{\text{sample}}} * 1000$$

In a travertine system, a lot of different processes can be responsible for the fractionation of the stable isotopes (Figure 4-6). Common fractionation processes for oxygen ( $\delta^{18}\text{O}$ ) are degassing, caused by pressure drop at the spring or by turbulence of flowing water, by evaporation or by temperature-related fractionation during precipitation of the travertine (Chafetz & Folk, 1984; Pentecost, 2005). The stable carbon isotopes ( $\delta^{13}\text{C}$ ) vary through a variety of processes and  $\delta^{13}\text{C}$  can be used to determine the carbon source (Claes et al., 2015; El Desouky et al., 2015; Pentecost, 2005). The most important source of  $\text{CO}_2$  in travertine is usually thermal decarbonation of (marine) carbonates in the subsurface. Complementary analyses are often needed, e.g.: to prove a magmatic mantle origin, which gives a negative signal of -8 to -4 ‰ (Hoefs, 2009), additional data for  $^3\text{He}/^4\text{He}$  is required to provide certainty (Minissale, 2004). Other shifts in the  $\delta^{13}\text{C}$ -signature could be due to processes after the fluid emerged from the spring. Such processes include disequilibrium precipitation, degassing of  $\text{CO}_2$ , bacterial influence, atmospheric equilibration, etc. (Gonfiantini et al., 1968; Kele et al., 2011 and 2008; Panichi & Tongiorgi, 1976).

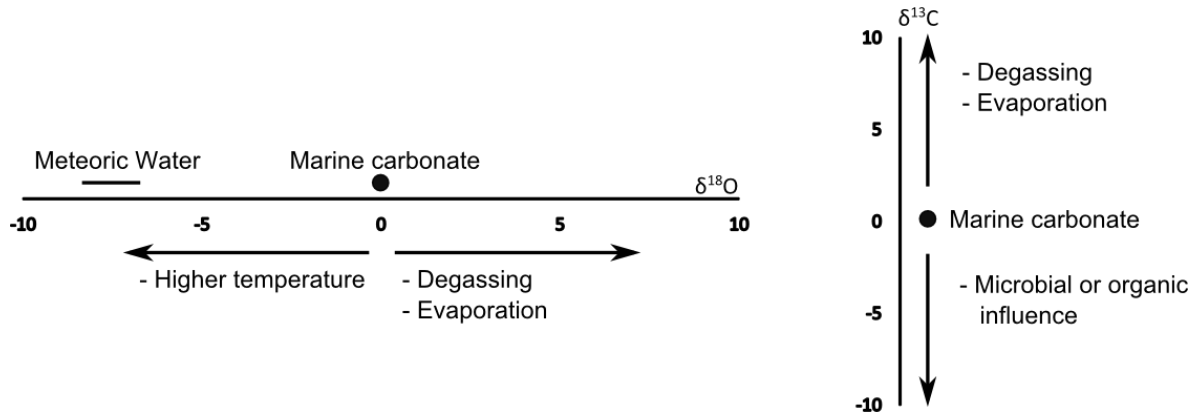


Figure 4-6: Variation in isotopic composition due to several processes. Note that only the surficial and most important processes for travertine are mentioned. The primary sources of the CO<sub>2</sub> are not included in this figure. The arrows indicate the direction in which the isotopic signal would move due to a certain processes, without any quantitative interpretation.

To analyse the actual isotopic composition of the precipitating waters, fractionation has to be taken into account. Fractionation is often calculated to be following equilibrium fractionation but for both  $\delta^{13}\text{C}$  and  $\delta^{18}\text{O}$  it is often assumed that non-equilibrium fractionation is present in travertine precipitation. This is often due to fast deposition rates caused by rapid CO<sub>2</sub>-degassing, due to which equilibration between HCO<sub>3</sub><sup>-</sup> and the travertine is impossible (Gonfiantini et al., 1968; Kele et al., 2011). For  $\delta^{13}\text{C}$ , the calculation of the original signature of the CO<sub>2</sub> in the spring water is given by the following formula (Panichi & Tongiorgi, 1976):

$$\delta^{13}\text{C}_{\text{CO}_2} = 1.2 * \delta^{13}\text{C}_{\text{trav}} - 10.5$$

Analysis of the samples is done at the Friedrich-Alexander-Universität (Erlangen-Nürnberg, Germany) under supervision of prof. M. Joachimski. The carbonate powders have reacted with 100% phosphoric acid at 70°C using a Gasbench II connected to a ThermoFinnigan Fave Plus mass spectrometer. Two laboratory standards are used, ERL-5 and Sol-1. The determined standard deviations are 0.6‰ ( $\delta^{13}\text{C}$  V-PDB) and 0.2‰ ( $\delta^{18}\text{O}$  V-PDB) for ERL-5 and 0.5‰ ( $\delta^{13}\text{C}$  V-PDB) and 0.04‰ ( $\delta^{18}\text{O}$  V-PDB) for Sol-1. During the sample preparation, there will be fractionation of the isotopes due to interaction with the acids, during dissolution. The extent of this fractionation will be dependent on the mineralogy of the sample. The samples contain calcite or aragonite. The fractionation due to dissolution is always calculated in respect of the mineralogy of the sample.

#### 4.6.1.2. Strontium isotopes

The strontium isotope ( $^{87}\text{Sr}/^{86}\text{Sr}$ ) analysis is carried out under supervision of Prof. Dr. R. Ellam at the Scottish Universities Environmental Research Centre. Strontium isotope analyses allow for determination of the source of the dissolved carbonate in the fluids, because the heavy Sr nucleides are not fractionated during chemical reactions. This indicates that the  $^{87}\text{Sr}/^{86}\text{Sr}$ -ratio remains unchanged

during dissolution of carbonates and during precipitation of in our case travertine. The source composition is reflected in the  $^{87}\text{Sr}/^{86}\text{Sr}$ -ratio (Leeman et al., 1977).

Nine samples are analysed for stable strontium isotopes. The powdered carbonate samples are digested in 2.5M HCl after being leached in 1M  $\text{NH}_4\text{Ac}$ . The Sr fraction is separated from the matrix into 2.5M HCl with a Bio-Rad AG50WX8 200-400 mesh cation exchange resin, which is Sr-selective. Prior to mass spectrometrical analysis with a VG Sector 54-30 multi-collector MS, the sample is loaded on Ta-filaments with 1M  $\text{H}_3\text{PO}_4$ . A  $^{88}\text{Sr}$  intensity of 1V ( $1 \times 10^{-10}\text{A}$ )  $\pm 10\%$  was maintained throughout the measurement. Correction of the  $^{87}\text{Sr}/^{86}\text{Sr}$  ratio for mass fractionation is done by applying Russel's law and the invariant  $^{86}\text{Sr}/^{88}\text{Sr}$  ratio of 0.1194 (Steiger & Jäger, 1977).

#### 4.6.2. Inductively Coupled Plasma-Optical Emission Spectroscopy (ICP-OES)

Inductively Coupled Plasma-Optical Emission Spectroscopy has been performed on 18 samples at the KU Leuven. This analysis allows for a multi-element analysis, which gives both the major and the trace elemental composition. The elemental composition of travertine deposits allows to interpret variation due to depositional processes, composition of the depositional fluid and diagenetic processes. Samples are selected to represent different stages in the evolution of the travertine body and to detect variations between different lithotypes.

The samples have been taken by cutting a small slab from the plugs. This slab is crushed into smaller pieces and pulverized with a pestle and mortar. The small particle size allows for easier dissolution in acids.

Before the analysis, the samples are dissolved with four acids digestion to allow for dissolution of silicates which could be present in some of the samples due to detrital influx. For the dissolution, 166 g of sample was weighed and put into Teflon beakers. The four acids used for digestion of the sample are  $\text{HNO}_3$  (14M or 65%, subboiled),  $\text{HClO}_4$  (70%, pro analyse Sigma Aldrich), HF (48%, subboiled) and HCl (2.5M). The digestion of the sample in the acids is done on two hotplates. Every plate contains 16 Teflon beakers, with a total of 32 beakers that are digested simultaneously. The acids are added in a certain order, while the beakers are on the hotplate. In the following order 3 mL  $\text{HNO}_3$  is added, followed by 3 mL of  $\text{HClO}_4$ , 3mL HF and finally 7 mL HCl is added. Between each step a certain time is allowed for the acid to evaporate and to digest the sample. All samples are entirely dissolved and no residue is remaining, so no filtering is required. In the final step, the sample solution is diluted up to 25 mL with MilliQ water. The digested samples are analysed with a VARIAN ICP-OES spectrometer of the 700 series of which the workflow is presented in Annex.

To determine the detection limit and the analytical accuracy, two reference samples and two empty beakers (one per hot-plate) are added to the digestion and measurement. Double digestion and measurement is performed for three samples, which is 10% of the amount of beakers.

The data of the ICP-OES measurements is analysed with statistical techniques by the statistical language R with the program RStudio. The data is transformed by a log or log-centred function to obtain a normal distribution of the data. A cluster analysis has been done, with the amount of clusters based on a function in R (nbclust). All the data has been put in a scatterplot-matrix and a correlation-coefficient-matrix. Finally a principal component analysis has been performed on the data to analyse which elements explain variation in the data.

## 4.7. Fluid inclusion analysis

Fluid inclusion analysis is performed on six samples from crystalline carbonates in the travertine body. The wafers have a thickness of 120  $\mu\text{m}$ , which is chosen to make the samples more translucent, without compromising the fluid inclusions. Four of the six selected samples are from actual veins, another is related to cement and the last sample shows crystals that grow within the bedded travertine. Pictures of the wafers are taken with a Leica DM LP microscope, using DeltaPix software.

Wafers with large crystals are broken in chips of 5 x 5 mm. These samples are studied with an Olympus BX60 microscope. The heating and cooling was done with a Linkham THMS 600 cooling/heating stage, mounted on an Olympus BX60 microscope. For the cooling phase, liquid nitrogen was used.

Each piece of a wafer is checked for the presence of fluid inclusions. The pieces without any visible inclusions are discarded. Sketches of the fluid inclusions associations (Goldstein & Reynolds, 1994) before analysis allow for assessment of fluid inclusion distribution and the possible growth of vapour bubbles due to stretching of the inclusion on the freezing phase.

Before the actual start of the measurements, the temperature of the cooling/heating stage had to be calibrated. The calibration is only done for negative temperatures with four different synthetic inclusions. The actual melting temperature of these inclusions is accurately known. The expected and measured melting temperature are plotted against each other to derive a formula to apply to the measurements.  $\text{CO}_2$  inclusions are expected to melt at  $-56.6^\circ\text{C}$ , the first melt of  $\text{H}_2\text{O}$ -NaCl inclusions at  $-21.1^\circ\text{C}$ , melt of  $\text{H}_2\text{O}$ -KCl inclusions at  $-10.7^\circ\text{C}$  and finally the  $\text{H}_2\text{O}$  inclusions at  $0.0^\circ\text{C}$ .

The first step in the microthermometry analysis was to find one or two two-phase inclusions per sample and to heat it up to  $110^\circ\text{C}$  to check for homogenization of the bubble and the liquid. No higher temperatures are analysed as this would increase the risk of leaking of inclusions. The heating step is performed before freezing to avoid artificial stretching, which would render data for homogenization temperatures useless. After one or two inclusions were analysed for  $T_h$ , the freezing stage is initiated.

Freezing is done up to  $-115^{\circ}\text{C}$  to overcome metastability of highly saline fluids. Cooling of the inclusions was done at a rate of  $40^{\circ}\text{C}/\text{min}$ . The first heating phase when a new sample was studied was done at a  $20^{\circ}\text{C}/\text{min}$  up to  $-60^{\circ}\text{C}$  and  $3^{\circ}\text{C}/\text{min}$  up to  $0^{\circ}\text{C}$  until a melting temperature was determined. Afterwards the heating was done at  $30^{\circ}\text{C}/\text{min}$  up to  $-50^{\circ}\text{C}$  and the program was adjusted for inclusions to heat at a much slower rate ( $1^{\circ}\text{C}/\text{min}$ ) when the temperature approaches the expected melting temperature, which was estimated based on the freezing temperature of the inclusion.

## 4.8. 3D – analogue reservoir

The generation of a three-dimensional (3D) analogue reservoir of the travertine body is a two-fold process. The model starts with a scaled 3D - model of the quarry. The dimensions and orientations of the quarry walls have been carefully measured and are subsequently drawn in the program SketchUp to get a perfectly scaled representation of the quarry in three dimensions. After this, the reservoir model is constructed based on field- and laboratory data.

The lithotypes that had been indicated on the linedrawings during the field work are carefully indicated in the 3D-SketchUp-model. Each lithotype that is inserted in this model is linked to data from petrophysical analyses. The model is constructed from field observations. The construction of a detailed model was possible thanks to the relatively small size of the quarry and the highly detailed linedrawings.

## 4.9. Upscaling approach

An upscaling approach is applied in the study of porosity. Porosity is studied in a first instance by thin section petrography. Upscaling from the scale of thin section towards the macroscopic scale gives an estimate of the different pore types. For more quantitative data of the porosity (and the permeability), petrophysical techniques are applied on plugs, as explained above. An upscaling approach to look at porosity is required in travertine because of the huge variability in the pore types and the deposits. Porosity is present at a large range of scales, from microporosity to intra- and intergranular porosity to even vugs and cave porosity. Porosity is not the only feature that requires upscaling, but also the fabrics, which are the building components of the travertine tend to be very complex.

A typical example of upscaling in travertine would be the variation from fabrics to lithofacies. One or several fabrics together make up a lithotype. Not each fabric is restricted or linked to one specific lithotype but one lithotype is defined by a specific set of fabrics. In the next step, one or several lithotypes make up a lithofacies. A lithofacies indicates the general depositional conditions. A certain lithotype can occur in several lithofacies. If a certain lithotype only occurs in one specific lithofacies, this lithotype alone can be considered a lithofacies. Finally, a limited set of lithofacies solely based on the mapping of the different textures, can be used to describe the geobody architecture of the entire travertine body,

including information on the depositional environments. This shows that an entire travertine body can be described as an association of a few different textures.



## Chapter 5: Results

The results section approaches the data in a way that they are as much devoid of interpretation as possible. Interpretations and assessment of the reliability of the data are given in the discussion section. The description of the travertine body is given in sections 5.1 and 5.2. With the upscaling strategy in mind, the individual lithotypes are described first, followed by the architecture of the travertine deposit. This is followed by the 3D-reservoir model, in which field data is integrated in with petrophysical and petrographical characteristics. This section is followed by the geochemical analyses, in which the XRD, stable isotope and ICP-OES analyses are treated. Finally, the fluid inclusion results are discussed.

### 5.1. Petrography

A “down-scaling” approach was adopted in the petrographic section. Lithotype description starts at quarry- or sample scale and petrographic detail is increased up to the microscopical analysis. Fifteen lithotypes are recognized in total. Some are of minor importance and are grouped together with other lithotypes. This way the link between macroscopic observations and micro-textures is optimized. This section combines macroscopical observations with traditional, fluorescence and cathodoluminescence microscopical analyses.

#### 5.1.1. Micritic dendrite crust

This lithotype is common in the sloping deposits. At macroscopic scale (Figure 5-1A) dense crusts of bright white to creamy travertine are recognized. Feather-like or fan structures are typical for this lithotype (Figure 5-1B) and they resemble the structures observed by Guo and Riding (1998) and Özkul et al. (2002) in crystalline crusts. On sample scale (Figure 5-1C), small steps can be seen at the end of these ray-structures. These steps have a small elevated rim and a depression behind it. These morphologically resemble the microterraces described by Guo & Riding (1999) and Fouke (2011).

On the microscopical scale, the fan- to featherlike structures consist of dark micritic peloids, organised as dendritic shrubs or “dendrites” (Figure 5-1D to F and 5-2A). The term dendritic shrubs is defined from the branches with small micritic “leaves” or peloids growing from a central micritic strand which branches in the upward direction. The individual dark micritic peloids are surrounded by microsparite crystals. The dendrolites have a height-to-width-ratio larger than 10. This distinguishes them from any microscopical shrubs that are present in other lithotypes. The micritic dendrite fans show undulose extinction under crossed polars. Claes et al. (2015) assign the undulose character to recrystallization.

Upon comparing hand samples with thin sections, the dark peloidal zones in thin section are the whitest on a sample and sparitic zones have a creamy colour. The dark peloids and the associated white colour on sample scale have been recognized by Chafetz and Folk (1984) as bacterial clumps.



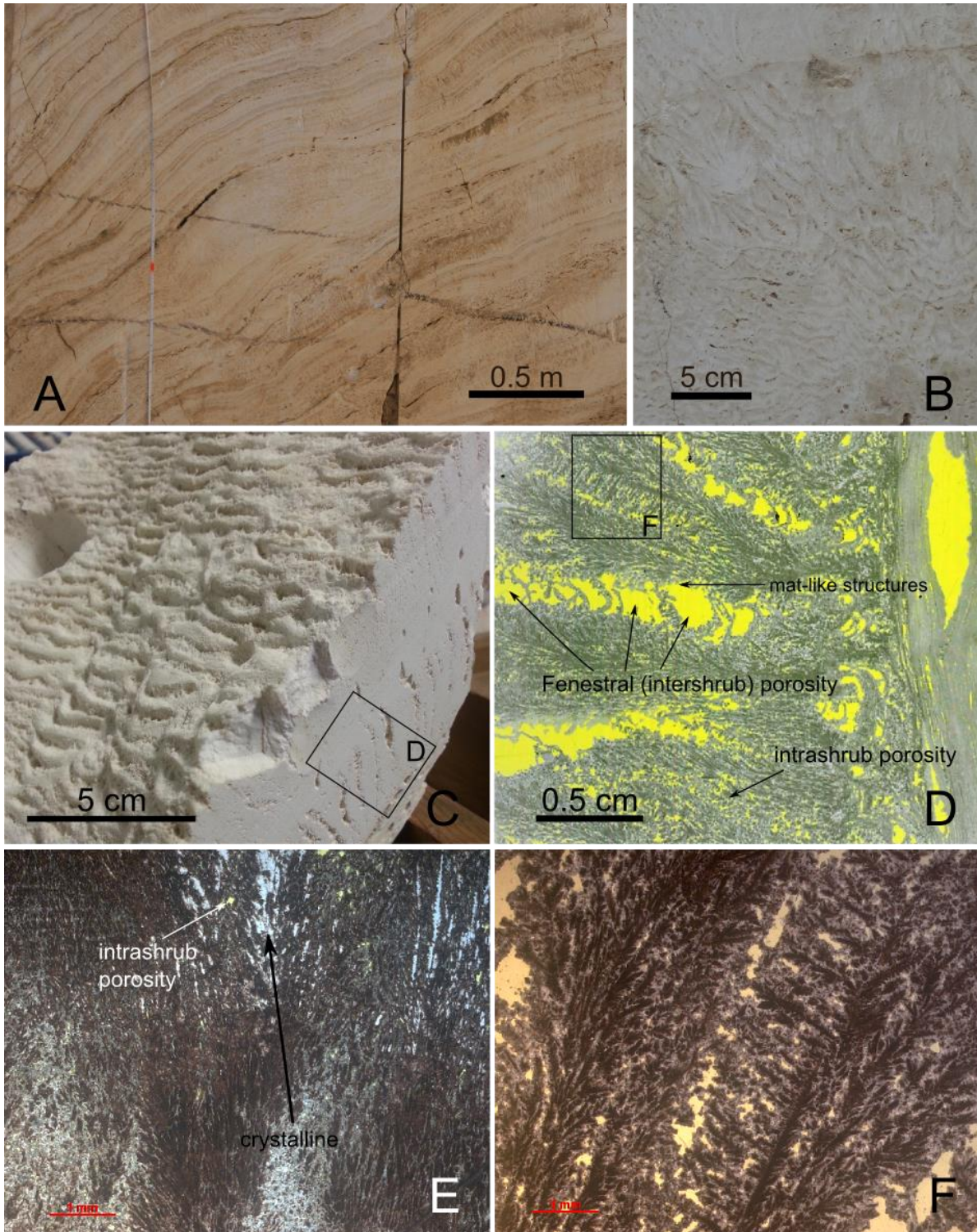


Figure 5-1: Micritic Dendrite Crust. A. Quarry wall containing sloping micritic dendrite shrubs, recognized by dense, brightly white to creamy deposits. B. Detailed quarry wall picture with fan-like appearances. C. Hand sample (AS14NJ030) with microterraces on top. They form the upper stepped boundary of the feather- or fan- structures. D. Thin section scan (PP; AS14NJ030) with dendrite shrubs separated by fenestral pores. E. Microphotograph (PP; AS14NJ029). Crystalline zones (white colour) in between the dendrolites. F. Microphotograph (PP; AS14NJ030). Micritic peloids have a dark brown colour, the surrounding microsparite is grey to white.



The intershrub porosity in between the dendrites are filled with structures resembling microbial mats (section 5.1.3.1), (Figures 5-1C, D and F). These mats are linked to the pools of the microterraces, whereas the dendrite shrubs comprise the rims. The dendrite shrubs are sometimes interrupted by micritic layers. More crystalline fans can develop in between the dendrite shrubs and are related to more densely packed micritic peloids (Figures 5-1E). The crystalline zones in between the micritic dendrite shrubs would be related to increased inorganic precipitation (Chafetz & Folk, 1984). The small (microsparitic) crystals surrounding the micrite peloids likely indicate diagenetic phases in which thermal water could still infiltrate into the deposits which solidified them (Chafetz & Folk, 1984).

Cathodoluminescence shows a purple colour for the micritic peloids, which is characteristic for travertine (Claes et al., 2015). The surrounding microsparitic crystals show no luminescence (Figure 5-2A and B).

The pores in the micritic crust lithotype are mainly microscopical. Intershrub porosity is developed between the dendrites. Intrashrub porosity is frequent in the dendrites but is partially filled by cements

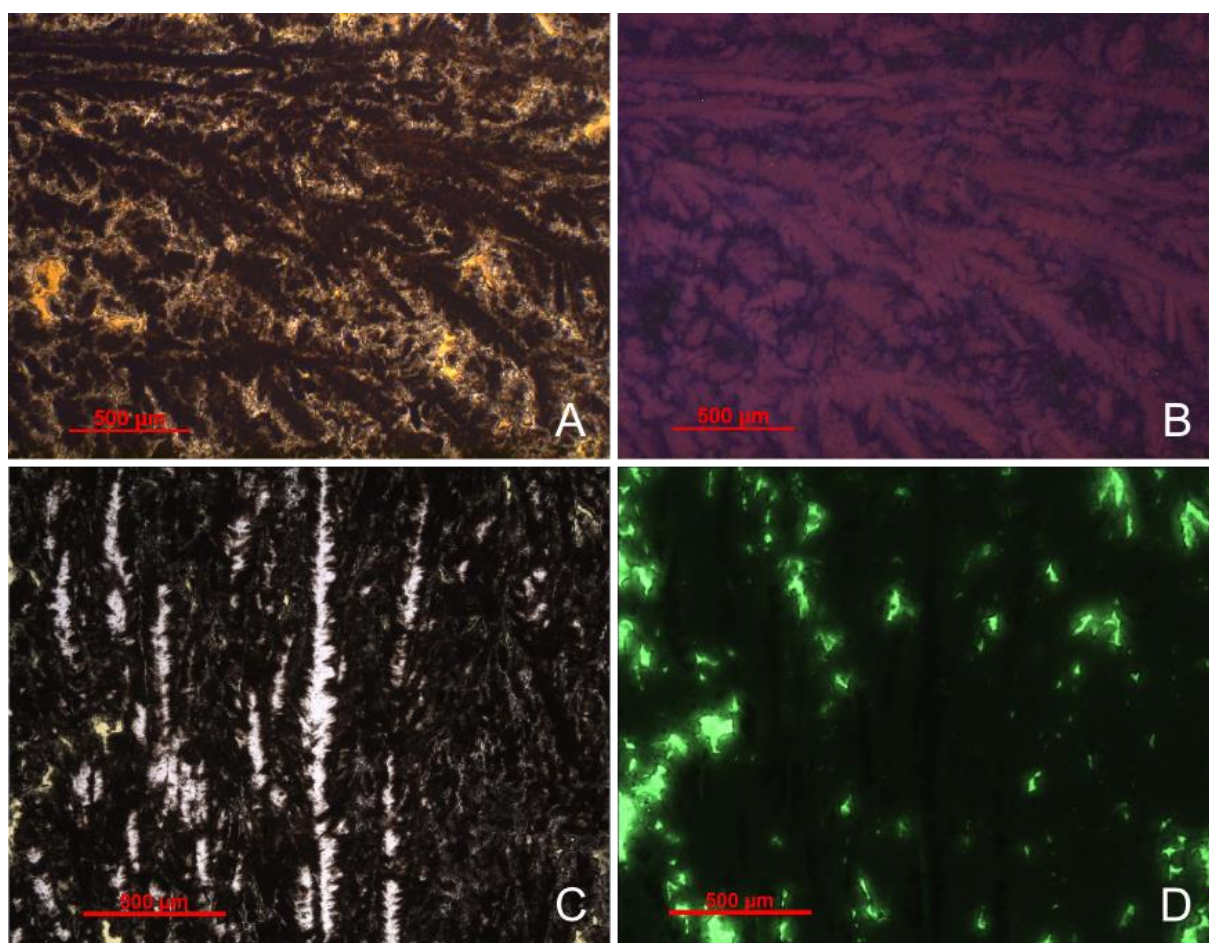


Figure 5-2: Micritic Dendrite Crust. A (PP) and B. Cathodoluminescence of the black peloids is purple and is non-luminescent for the crystals. C (PP) and D. Interpeloidal porosity between the peloids. The crystals are non-fluorescent and the surrounding micrite is slightly fluorescent which indicates microspores.

(Figure 5-2C and D). Within the peloids themselves, which are embedded in a crystal, microporosity is present (Figure 5-2C and D). This porosity could either be created from decay of microorganisms (Chafetz & Folk, 1984) or a porous texture could have developed during precipitation. The microporous zones are slightly fluorescent, indicating their participation in the pore network connectivity. On sample scale, the zones in between the dendritic shrubs are consisting of aligned pores, which corresponds to fenestral porosity (Figure 5-1C). On an even larger scale, the zones between individual pores can be recognized as interlaminar porosity.

### 5.1.2. Peloidal micrite (PM)

This lithotype frequently occurs in steeply sloping deposits in the quarry. Grading of micritic dendrite crusts into peloidal micrite is commonly observed in sloping deposits. The lithotype is described on macroscopical characteristics, like its creamy colour and intershrub porosity (Figure 5-3A and B).

Microscopically, the peloidal micrite lithotype is characterized by black micritic clumps, which also constitute the leaves of the micritic dendrite shrubs. These micritic clumps could either be solitary (Figure 5-3C) or organised as small microscopic shrubs with a height-to-width ratio of 1:1 to 2:1 (Figure 5-3D). The peloids are closely packed and when solitary, they occur encapsulated in a single calcite crystal. When the peloids are organised as small shrubs, they are surrounded by micrite, which is in turn surrounded by microsparite. Cements reduce the pore space and are mainly dogtooth cements. Fluorescent microscopy indicated the presence of mainly intershrub and intrashrub porosity. The black peloids are microporous.

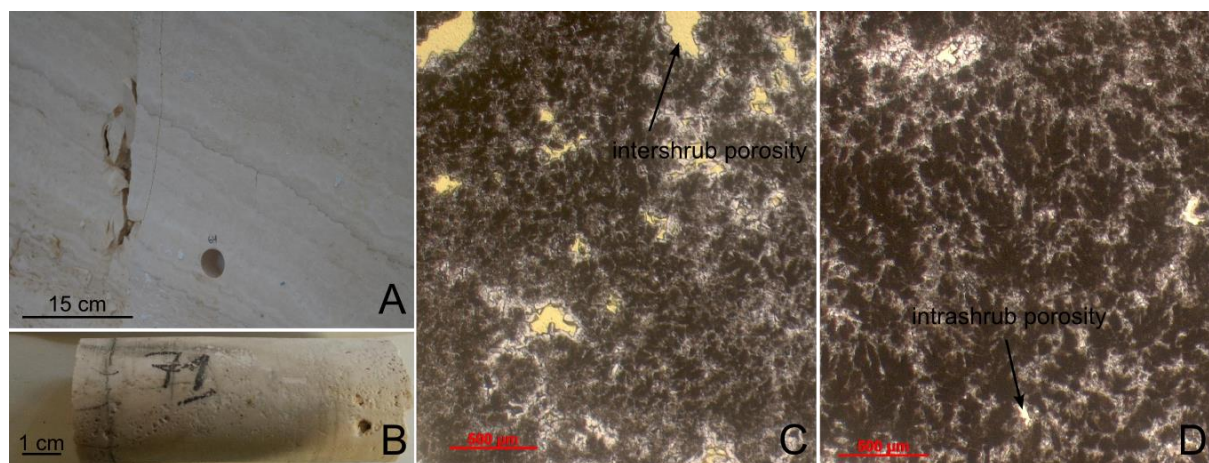


Figure 5-3: Peloidal micrite. A and B. Peloidal micrite on quarry and sample scale. Uniform, creamy coloured deposits with small irregular pores. C. Microphotograph of peloidal micrite. The black micritic clumps are solitary and are surrounded by micrite. D. Microphotograph in which the peloidal micrite has agglutinated.

### 5.1.3. Microbial mats

Microbial mats are a common lithotype in the travertine body. They are recognized from vacuolar, fenestral to interlaminar porosity and a creamy colour. Two types of microbial mats are distinguished,

based on visual characteristics. The first type (Figure 5-4) is the most porous type and is mainly present in smoothly sloping deposits. The second type (Figure 5-6) is less porous, is richer in micrite and is present in flat deposits. The steeper the slope, the more the microbial mats correspond to the first type.

#### 5.1.3.1. *Type I microbial mats (MM I)*

On the macroscopic scale (Figure 5-4A and B) the first type of microbial mats resemble thin layers of creamy coloured travertine with a thickness between one and five millimetres. The layers randomly touch each other, resulting in vacuolar, interlayer porosity. These pores are aligned and can be up to three centimetres in length and up to 1 cm in height (Figure 5-4A and B). Apart from the thin layers and the vacuolar pores, some zones are denser, appearing more micritic.

Layering of the deposits is also observed in the microscopic textures. Individual layers that are recognisable in hand sample are composed of smaller layers with thicknesses varying around 100  $\mu\text{m}$  (Figure 5-4C, D and E). The different layers are recognized by their alternating darker and lighter appearance. The darker layers sometimes contain small dark micritic peloids, which are absent in the lighter layers. The fabrics of the microbial mats are microsparitic and each crystal contains a small dark core (Figure 5-4C, E and F). These cores are likely to be microbial clumps, which have dissolved, resulting in micromouldic porosity. The denser zones are recognized by small micritic dendrite shrubs or solitary black micritic clumps (Figure 5-4D). The zones could be related to the microbial mats which occur with the micritic dendrite crust lithotype.

Reduction of the pore space with dogtooth and dripstone-like cements is common. The dripstone-like cements are preferentially occurring on the bottom pore edge. The cements sometimes have a cloudy dark micritic core. The CL colour of these cores is dull orange (Figure 5-5A and B). The rest of the microbial mat lithotype is characterised by a purple to pink colour which is more pronounced in the dark micritic zones and the cores of the microsparite (Figure 5-5A and B).

Apart from the interlayer-, microbial mouldic- and intraparticle porosity, small micritic zones have micromouldic porosity (Figure 5-5C and D).

#### 5.1.3.2. *Type II microbial mats (MM II)*

The second type of microbial mats is similar to the first one, but appears less porous, denser, with higher micrite content (Figure 5-6A and B). Pores are vacuolar but are smaller (generally < 1 cm) and less elongated. Due to the alignment of the pores and the smaller size, they resemble fenestral porosity. Type II microbial mats are more common than the first type.



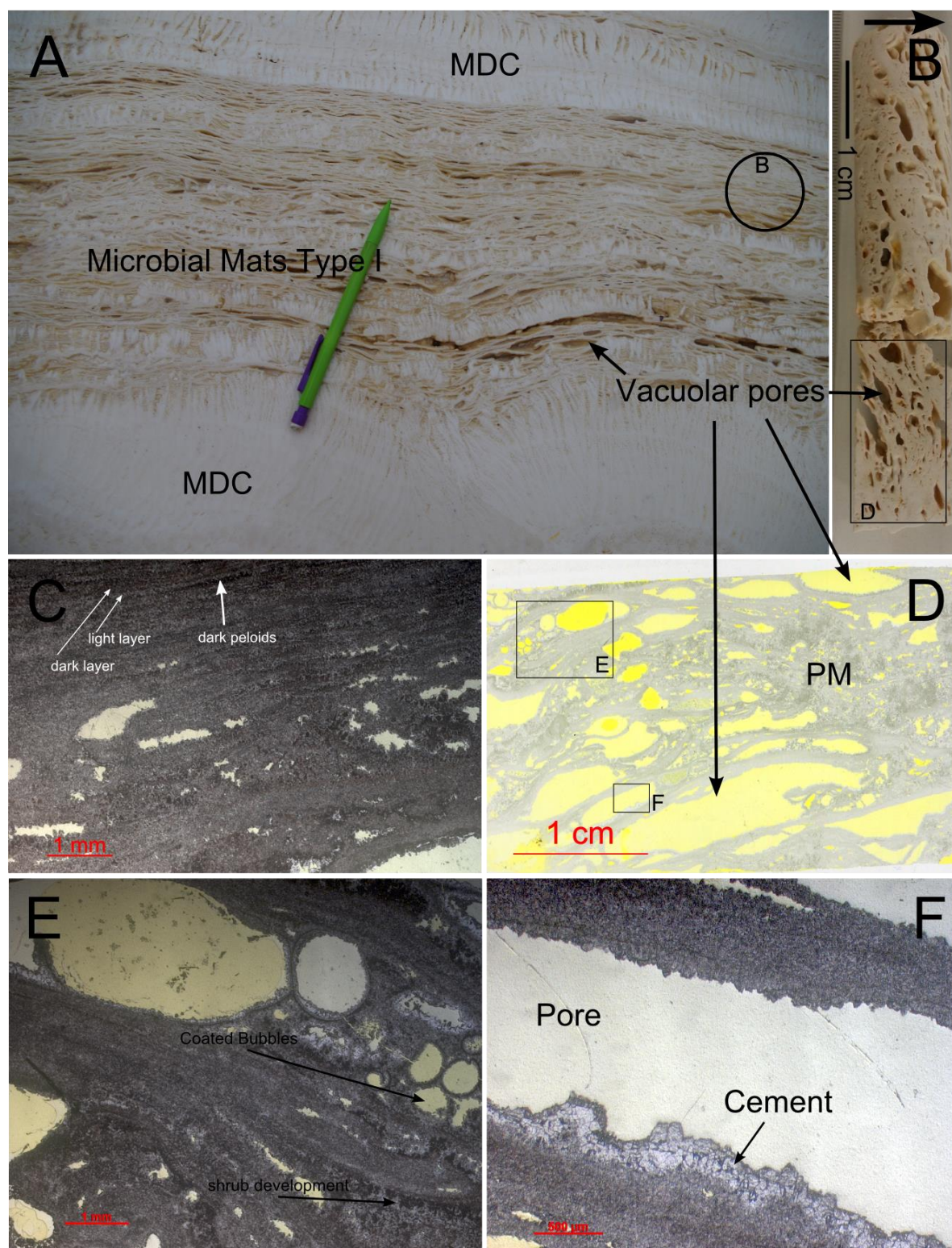


Figure 5-4: Microbial mats type I. A. Macroscopic scale (about 25cm thick). The microbial mats occur together with micritic dendrite crusts (MDC). B. Plug (AS14NJ069). Vacuolar porosity indicated. Black arrow indicates orientation. C. Microphotograph (PP; AS14NJ030) thin layers in microbial mats and peloidal micrite. D. Scan of thin section AS14NJ069. The different shades of yellow are the result of double impregnation. E. Microphotograph (PP; AS14NJ069) thin layering of the microbial mats and the presence of coated bubbles together with the microbial mat. F. Microphotograph (PP; AS14NJ069) of cements located in the lower part of the pore. The cements are absent in the upper part of the pore.



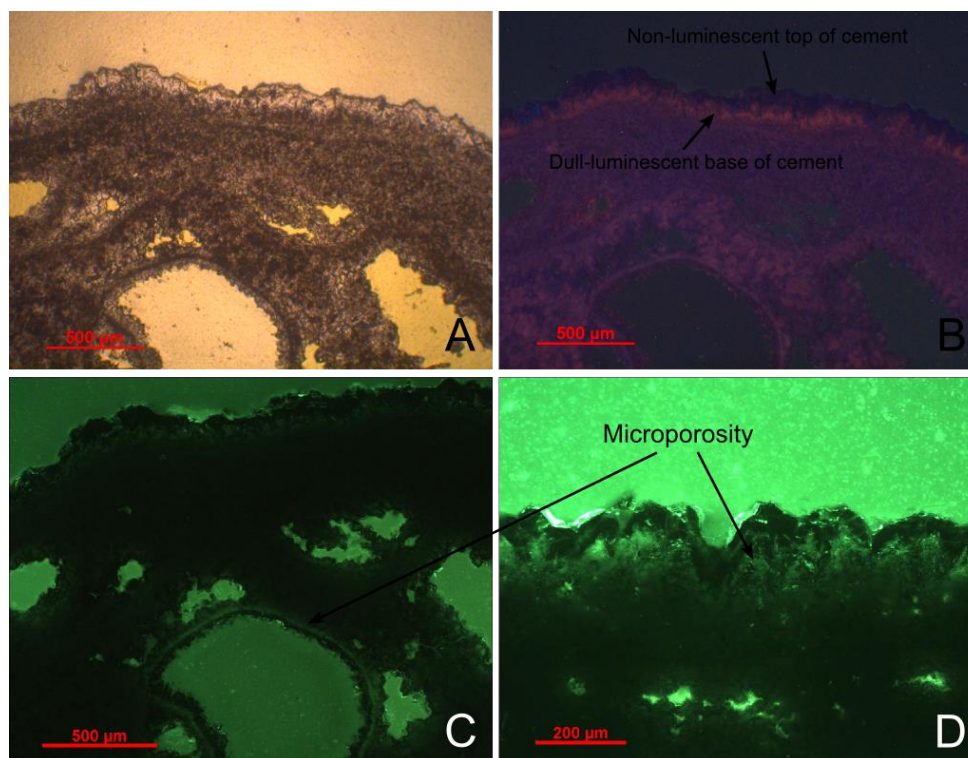


Figure 5-5: Type I microbial mats. A. Microphotograph (PP; AS14NJ069) B. CL, purple luminescent micritic peloids. The lower part of the cements is dull-luminescent, with a non-luminescent top. C. Fluorescence. Micritic zones are microporous, the microsparite is slightly microporous. D. Microporous zones in the cement crystals, detail of C.

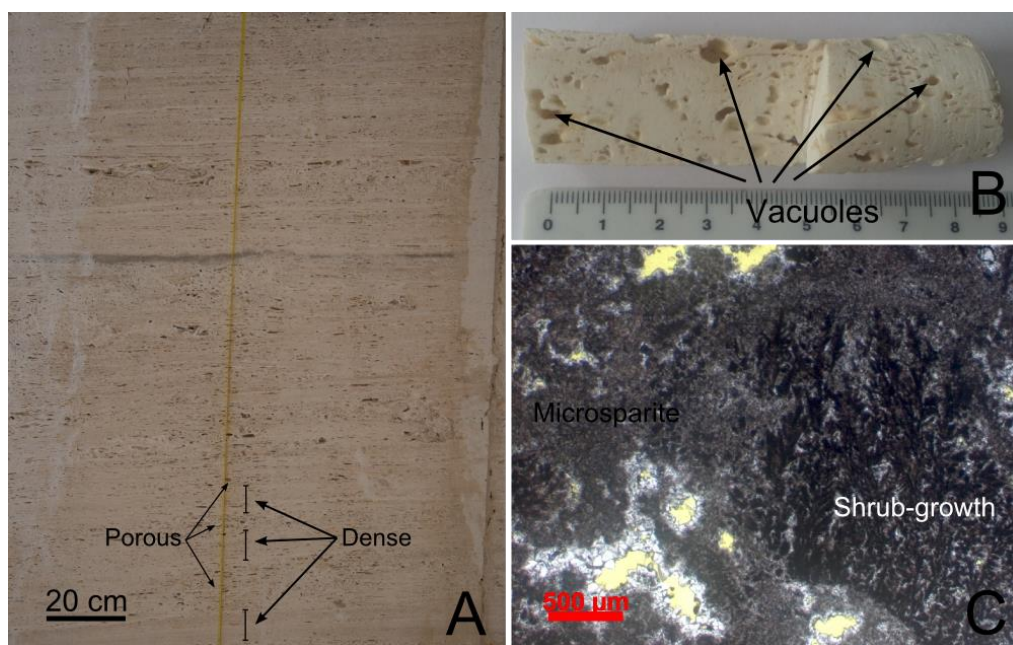


Figure 5-6: Type II microbial mats. A. Macroscale observations indicate that type II microbial mats are less porous, compared to type I mats. The pores are vacuolar. Alternation between more porous and denser horizons is seen. B. Plug (AS14NJ074) with vacuolar pores and denser zones in between them. C. Microphotograph (AS14NJ074). The more porous zones are characterized by grey microsparitic fabrics. There is aggradation of the peloidal micritic shrubs in the dense zones. The pores are reduced with dogtooth cements.

The textures on the microscopic scale are similar to both those of the type I microbial mats and the peloidal micrite. Thinly layered, brownish microsparitic textures are recognized in the proximity of pores. Shrub-like growths of dark micritic peloids occur in the denser zones (Figure 5-6C). These shrubs are sometimes limited to only a few black micritic clumps. The cements are dogtooth cements. The cements are non-luminescent with sometimes a more dull-luminescent horizon.

#### 5.1.4. Erosional horizons

Erosional horizons are recognized by their distinct dark grey colour. Erosional surfaces form during periods in which fluid flow has decreased and subaerial exposure and biological activity were able to influence earlier deposits (e.g.: Guo & Riding, 1998).

On quarry scale, the deposits are grey to dark grey, which contrasts with the creamy white colour of the other lithotypes (Figure 5-7A and B). The horizons often contain fragments or blocks of earlier deposited travertine (i.e. autobrecciation, which means that the earlier created travertine is physically degraded) or from external sources, which results in monomict or polymict breccia, respectively. Only monomict breccia are present in the studied travertine deposit and the source of the breccia is the travertine body itself, which was subjected to diagenetic alteration and erosion during periods of decreased or ceased spring flow (Figure 5-7A). The matrix of the erosional horizons is micritic and no additional structures can be recognized on a macroscopical scale. The porosity of these deposits is vuggy and these pores vary from small holes to large vugs (Figure 5-7B). The erosional horizons are associated with reed growth near the top of the layer (Figure 5-7B). The reed forms large “reed hands”, which are structures composed of hollow tubes that merge together in one point (Soete, 2011). Branching occurs in the upward direction. In situ reed structures indicate suitable conditions for plant growth. Indicating the absence of thermal water, as they form a hostile environment for plant growth ( $T < 30\text{ }^{\circ}\text{C}$  Capezzuoli et al., 2014). Only a few other fossils, like: plant leaves and one gastropod shell, are detected. This indicates that, even though the setting allowed for organisms to be present, colonization was minimal. Cement growth is common in the erosional horizons. Thick bands of cements are recognized in both the reed travertine and in the vugs (Figure 5-7B). On the scale of hand samples, colour varies between different shades of grey, brown and even red. Cements are also visible on plug scale in the smaller vugs (Figure 5-7C and D).

On the microscopical scale, the samples of the erosional horizons are heterogeneous (Figure 5-7E to H). Some of the observations apply to all samples of the erosional horizons: a micritic matrix with siliciclastic minerals (Figure 5-7G and H), vuggy porosity that cuts through certain structures and cementation of these vugs by bladed, dogtooth, equant and even pendant cements (Figure 5-7E to H and 5-9). The siliciclastic grains that are recognized in the thin sections are quartz, muscovite and minor feldspar, biotite and iron-oxides (Figure 5-7G and H). Some samples contain spherulites, which are rounded features consisting of small calcite crystals. An optical effect causes a black cross to be visible



in the crystals under polarizing light (Figure 5-7G). In one sample (AS14NJ005) an ostracod shell was present. The micritic matrix is microporous (Figure 5-8).

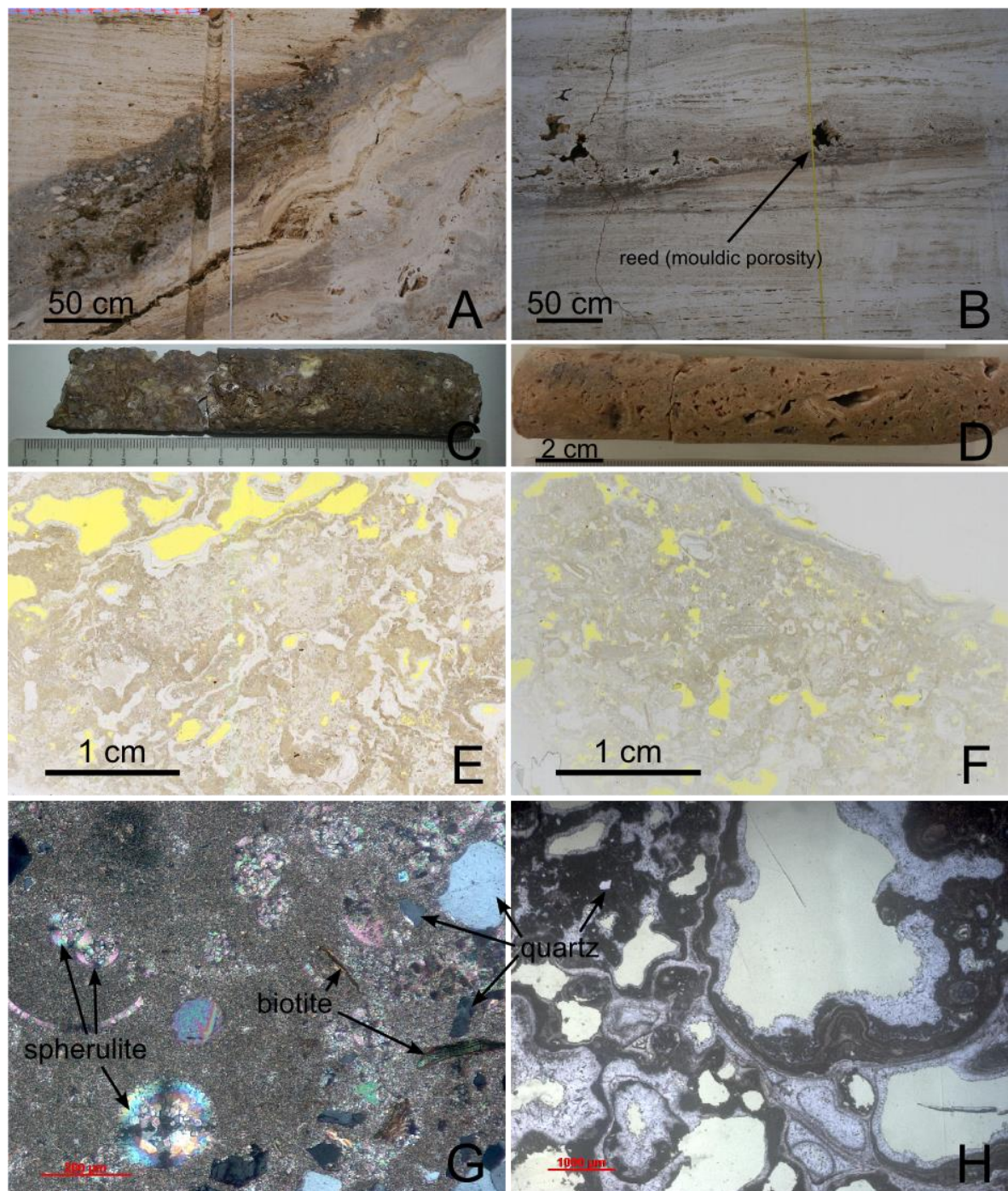


Figure 5-7: Erosional horizons. A. Dark grey erosional surface with monomict fragments, indicating autobrecciation. B. Lighter grey erosional surface with reed moulds and large vugs. The vugs are cemented. C. Plug (AS14NJ042) of a dark grey erosional surface. The white parts are the cements. D. Plug with a brown-reddish colour (AS14NJ006). E and F. Thin section scans (AS14NJ043 (E) and AS14NJ005 (F)), indicating the presence of micrite, vugs and cementation. G. Microphotograph (AS14NJ004) with micritic matrix, siliciclastic grains (quartz and biotite) and spherulites, which are recognized by their round shape, small crystals and the black cross. H. Microphotograph (AS14NJ042) with micritic matrix and bladed, dogtooth and equant cements.



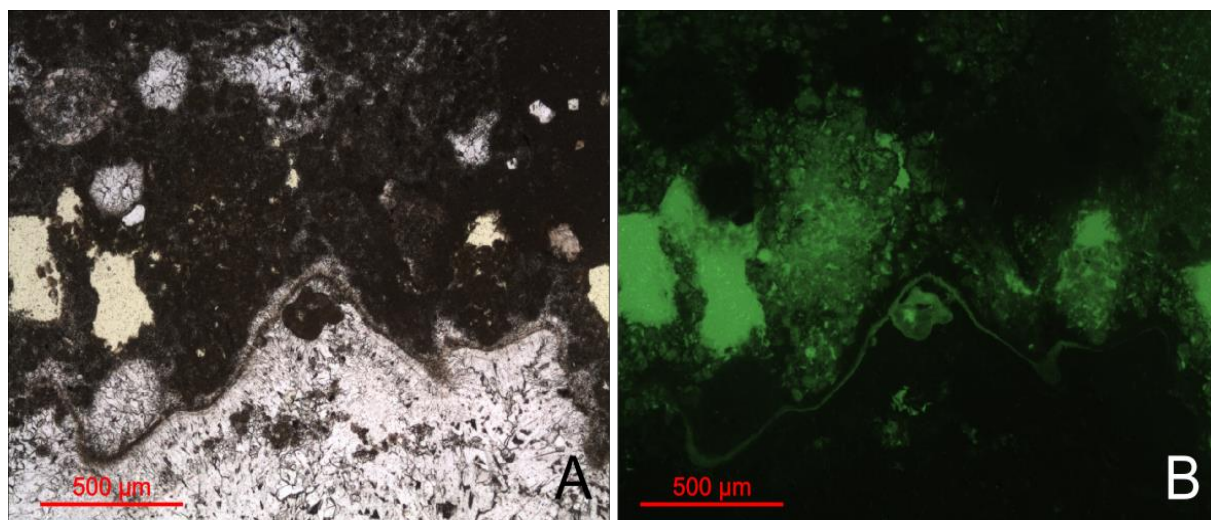


Figure 5-8: Microporosity in the micrite layers marking the erosional horizons (AS14NJ005). A. PP indicates micrite in black and a cemented vug. B. FP, .Some parts in the micrite are clearly more porous than others. The more porous zones are comprised of nodular distributed micrite (pellets), whereas the less porous zone is more uniform.

Cathodoluminescence of the pedogenic horizons is complex (Figure 5-9). The micritic zones are mainly marked by dull luminescence, but some zones are non-luminescent where others show bright luminescence (Figure 5-9B and F). These zones are hard to distinguish in classical microscopy. The zones are indicative for the alternating presence of oxidizing and reducing conditions at the moment of micrite precipitation (Figure 5-9D). Bright luminescence of the micrite is often present at the base of cements (Figure 5-9B and F). The cements show varying luminescence and often typically display the non-bright-dull sequence (Figure 5-9D). This indicates that the cements reflect transition between oxidizing and reducing conditions. Some cement layers are purple or dull luminescent.

### 5.1.5. Microbial laminites

This lithotype is defined by Gandin and Capezzuoli (2014) and is also referred to as puff-pastry. A lot of similarities with their descriptions are observed. In the first instance, these textures were considered paper-thin rafts, due to their straight horizontal outline. The ductility that is shown through draping of the laminites (Figure 5-10B) discerns them from the brittle rafts, as defined by Guo and Riding (1998).

On a macroscopical scale, the deposits show two different textures. The laminites are either straight or curved (Figure 5-10A and B, respectively). At a local disruption in the morphology (e.g. branch of a tree), they drape over the morphology causing them to be curved (Figure 5-10B). When reed is present next to the laminate layers, they curve upwards to the reed, which indicates that the laminate layers are anchored to the reed during decrease in water level or growth of the reed. The deposits are recognized by large and long pores. The high length-to-height ratio of the pores (especially for the straight rafts) discerns them from the pores of the microbial mats lithotype. This difference is used to differentiate the two lithotypes in the field. Macroporosity is mainly interlaminar to framework porosity.

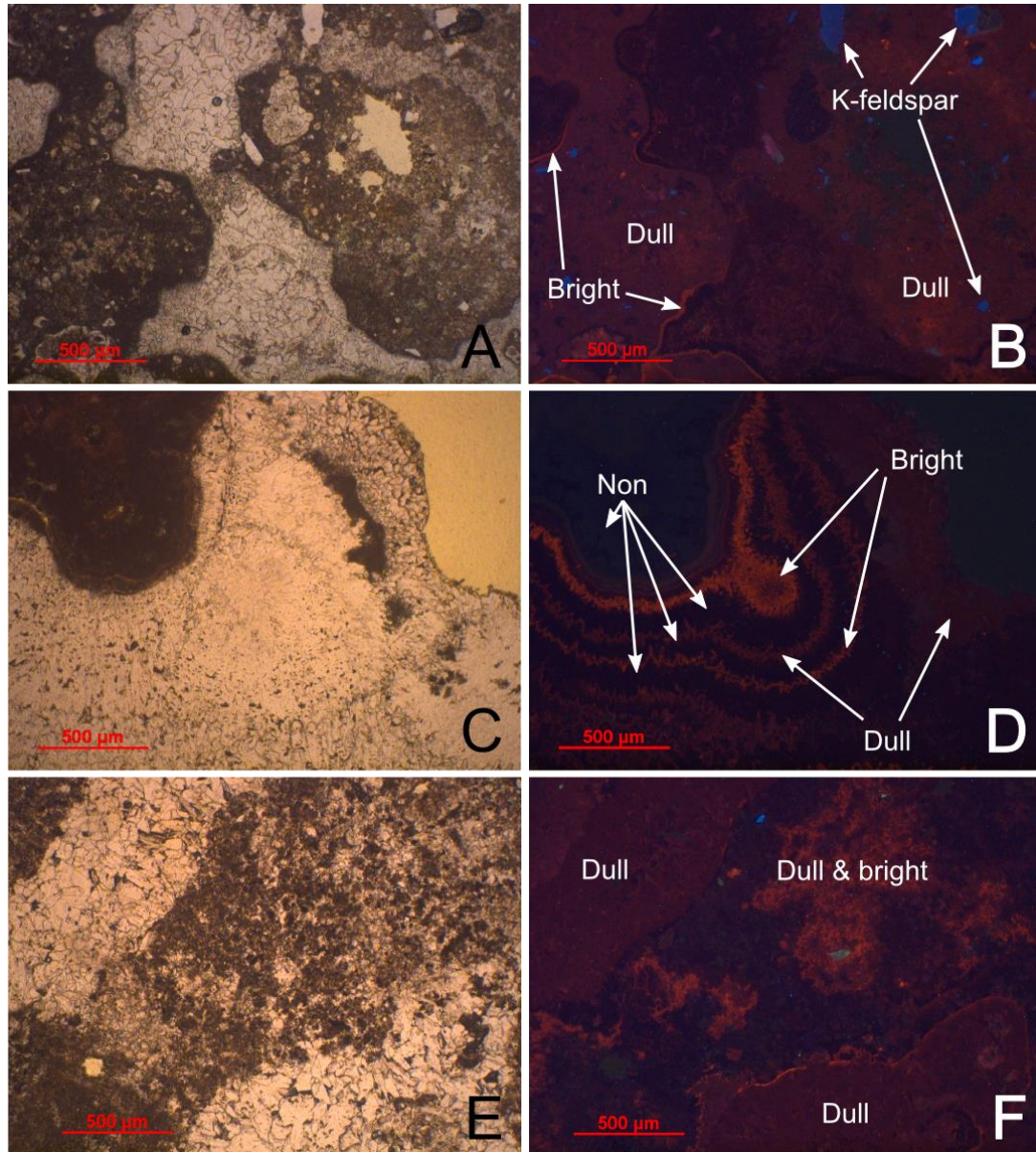


Figure 5-9: Cathodoluminescence in erosional horizons. The left-hand-side pictures show the microphotographs under PP, the right hand-side has the respective images under cathodoluminescence. A-B. Micrite is dull-luminescent with some slightly more brightly luminescent zone. The brightest luminescence is seen at the contact between micrite and cements. Cements are non-luminescent. Notice the blue luminescent K-feldspar grains. C-D. Non-Bright-Dull zonation in pendant cements indicating variation between oxidizing and reducing conditions. E-F. Dull luminescent cements and both non- and bright luminescence in micritic zones.

Reed moulds are commonly present within the microbial laminite lithotype (Figure 5-11). The reed occurs phytoclastic or in growth position. Several types of reed are present and are distinguished based on the thickness of the stems and the extent of branching. Some reed stems occur solitary and others occur grouped together, linked to a root system (Figure 5-11). Almost complete cementation of some of the reed moulds indicates that they were important fluid pathways.



At microscopic scale, the individual laminites are recognized by a thin micritic layer with local micritic cloths (Figure 5-10C - F). The latter sometimes grow upwards, albeit much smaller and less frequently. Both the micritic layer and the cloths are black, resembling microbial clumps (Chafetz & Folk, 1984).

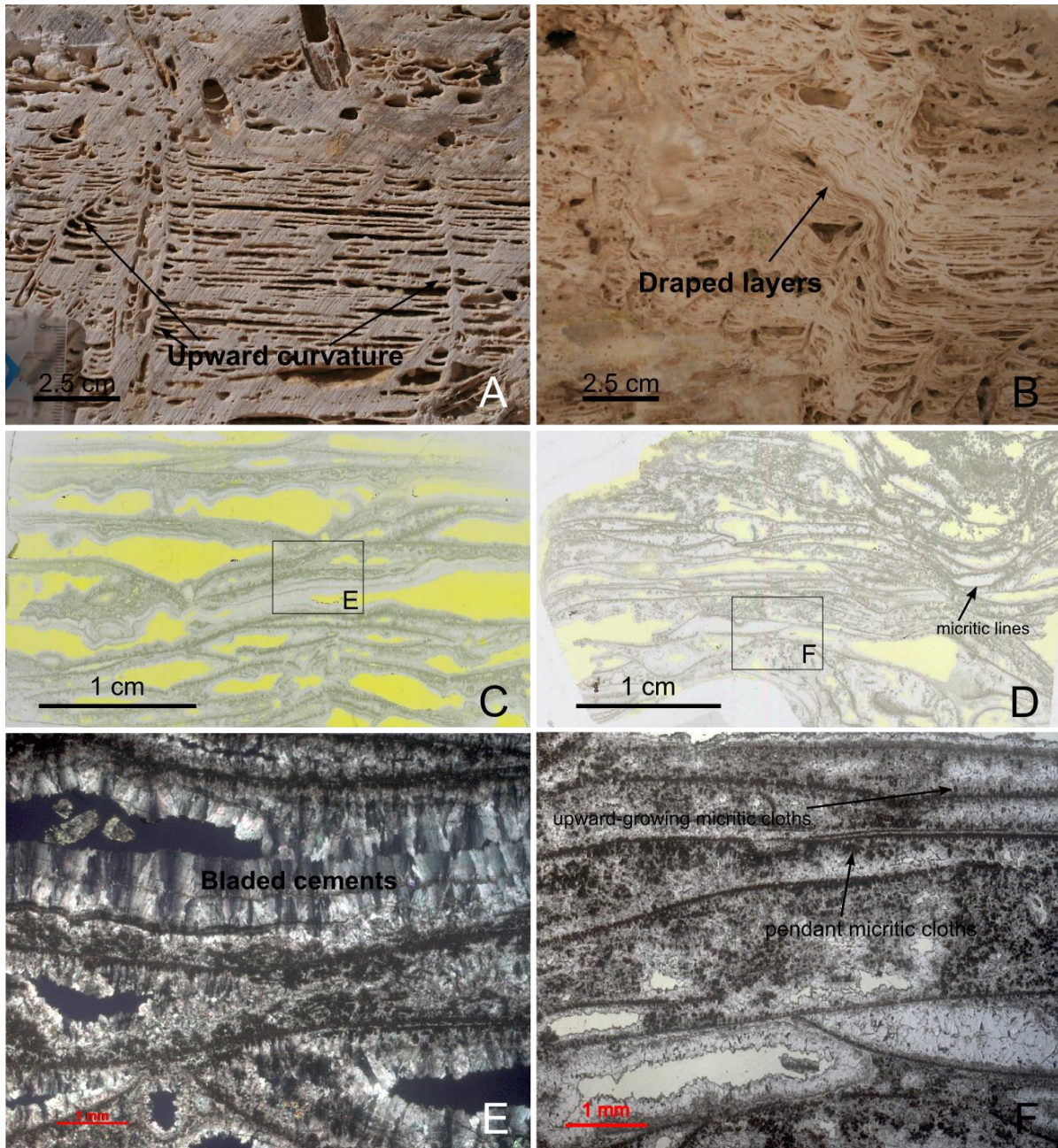


Figure 5-10: Microbial laminites. A. Straight microbial laminites, curving upwards to the thin reed. B. Microbial laminites draping over a local morphological structure. C (AS14NJ009) and D (AS14NJ011). Thin section scans of microbial laminites. E. (XP; AS14NJ009) Large bladed to fan-like crystals grow on the bottom and top edges of the pores in between the laminae. F. (PP; AS14NJ011) thin black micritic layer with small black cloths on the bottom side, indicating the individual laminites.

Greyish micrite surrounds the black micrite concretions. Further away from the dark micrite, cements are present, possessing a dogtooth to bladed fabric. When a pore is entirely cemented, the cements are equant.



Luminescence of the microbial laminites marks the dark micritic layers and dark micritic cloths by their purple luminescence. The micrite is non-luminescent. The cements show variation from non- to bright- to dull-luminescence (Figure 5-12).

Both the macroscopical and microscopical description agree with the definition of “microbial, flat to curled laminites and puff pastry-like fabric”, by Gandin and Capezzuoli (2014). This leads again to the idea that microbes were important in the deposit. According to the latter authors this lithotype is deposited in very shallow pools in which micrite accumulates on thin films of bacterial colonies at the pool bottom.

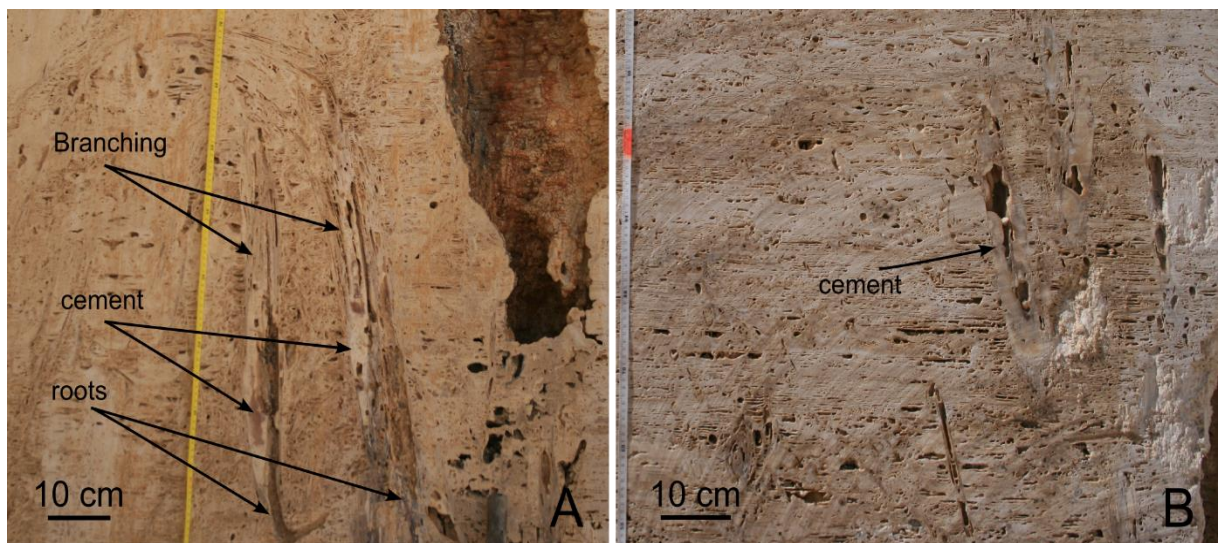


Figure 5-11: Reed moulds: A. Two large moulds of reed. They display narrow spaced upward branching. The lower part of the mouldic structure are probably the roots. B. A few solitary small reed strands and large, cemented reed moulds (right part of the picture).

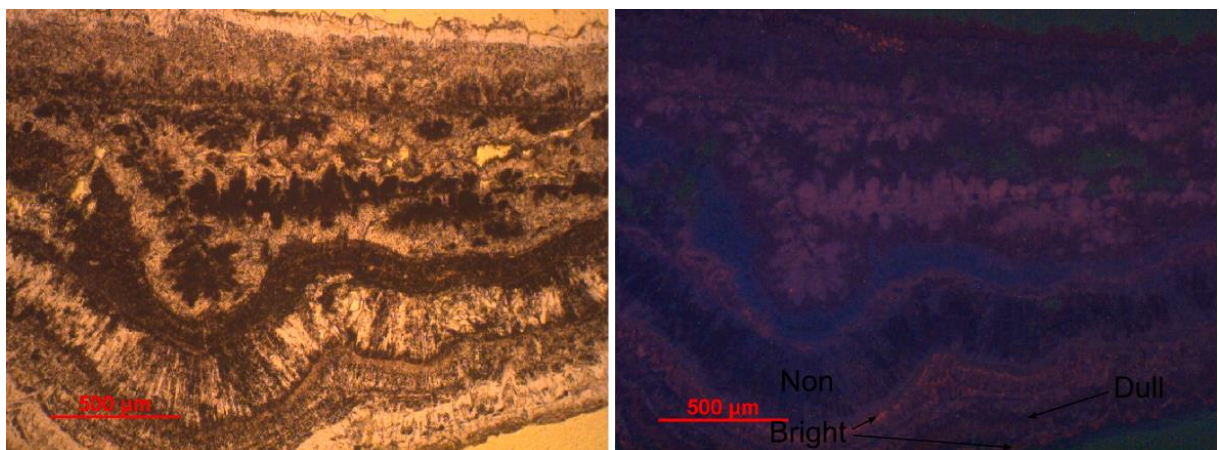


Figure 5-12: Cathodoluminescence in the microbial laminite travertine is mainly marked by purple luminescence in the black micritic zones. The cements vary between non- to bright- and dull luminescent.

### 5.1.6. Crystalline crust

The crystalline crust lithotype is named after Guo and Riding (1998). The lithotype is characterised by an alternation of thin crystalline and micritic layers (Figure 5-13A to C), but rarely occurs in the investigated travertine body. The micritic layers are porous whereas the crystalline layers are dense.

On microscopical scale, the crystalline layers can also be subdivided in two different types. The first type is dendrolitic or fan-like and resembles shrubs, referred to as “ray-crystals” by Chafetz and Guidry (1999)(Figure 5-13D). The ray crystals are crystalline and devoid of black micritic clumps. The second morphology recognised in the crystalline layers is composed of bladed crystals (Figure 5-13D, E and F). The bladed crystal layers occur in voids in the micritic horizons. The crystals occupied the entire pore surface and grew inward, indicating that the crystals formed after pore formation (Figure 5-13E). Cathodoluminescence shows indeed that these crystals are formed afterwards under changing redox conditions, which is reflected in non-, bright- and dull luminescence appearances (Figure 5-13G). The micrite can be subdivided in micrite and microsparite.

These authors attribute the crystals to inorganic precipitation. The crystalline crust lithotype is linked to a high energy environment and can be recognized by its fan-crystals (Chafetz & Folk, 1984; Gandin & Capezzuoli, 2014).

### 5.1.7. Banded travertine

The banded travertine lithotype consists of veins that vertically crosscut the layered travertine. Bands in these dense veins have colours varying from white-translucent to brown (Figure 5-14A to D).

Thin section study of the banded travertine focussed on the different colours of bands in the vein and the contact between the banded and the layered travertine. Textures of the vein travertine vary in function of macroscopical colour. White to translucent parts are characterised by thin needle crystals, which generally grow unidirectional or in fan-like structures (Figure 5-14E to I). The brownish part contains large unidirectional crystals (Figure 5-14I). All crystals are commonly characterized by a length-to-width-ratio over 10:1. The white bands are clearly indicative of very fine needle-crystals that could indicate the presence of aragonite. The centres of the needle fans are similar to spherulites, due to optical effects that cause a black cross to be present in the centre of the fan (Figure 5-14G).

A greyish layer separates the travertine veins from the layered travertine. Between this thin layer and the banded travertine, featherlike crystals can be seen on macroscopic scale (Figure 5-15A). Microscopically, these structures have an aragonitic matrix as seen from the needle-like crystals (Figure 5-15B). The pores are cemented with dogtooth to equant calcite cements (Figure 5-15B).



The vein travertine can also be called “banded palisade crystals” (Gandin & Capezzuoli, 2014). They are related to conduits that feed fissure ridges (Altunel & Hancock, 1993; De Filippis et al., 2012; Gandin & Capezzuoli, 2014).

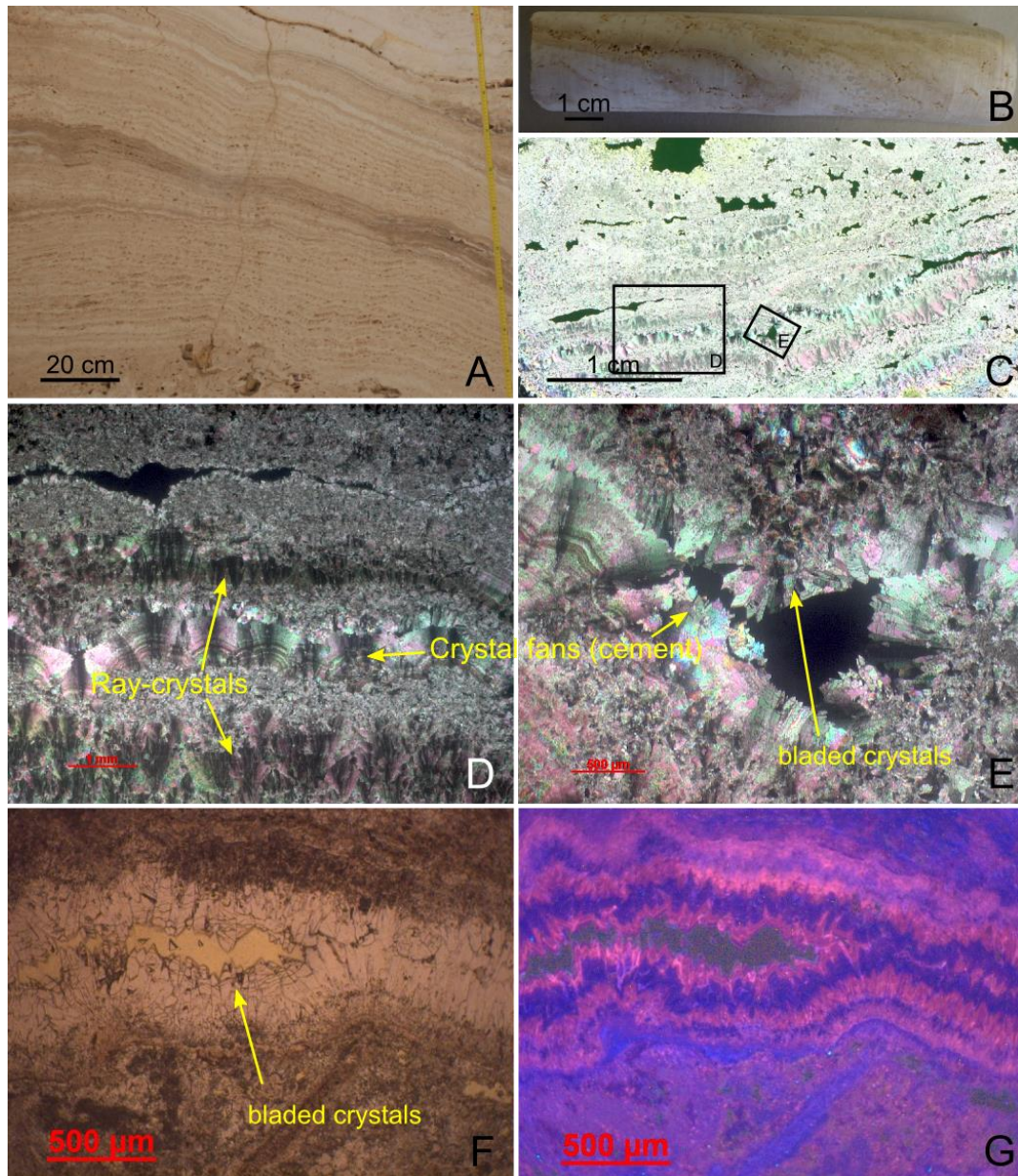


Figure 5-13: Crystalline crust. A. Macro-scale, showing the alternation of micritic and crystalline layers. B. Plug scale (AS14NJ025): alternation of crystalline layer, which contains translucent crystals, and micrite. C. Thin section scan (XP; AS14NJ025) Alternation between crystalline and micritic layers. D. Microphotograph (XP; AS14NJ025) with ray-crystals and bladed crystals (middle cement layer). The latter are arranged like fans. E. Detailed microphotograph (XP) of the bladed crystals, growing from both sides of the pore, suggesting post-depositional growth of the cements. F and G. Cathodoluminescence microphotograph of the cements, showing dull and non-luminescent layers (CL picture is overexposed).



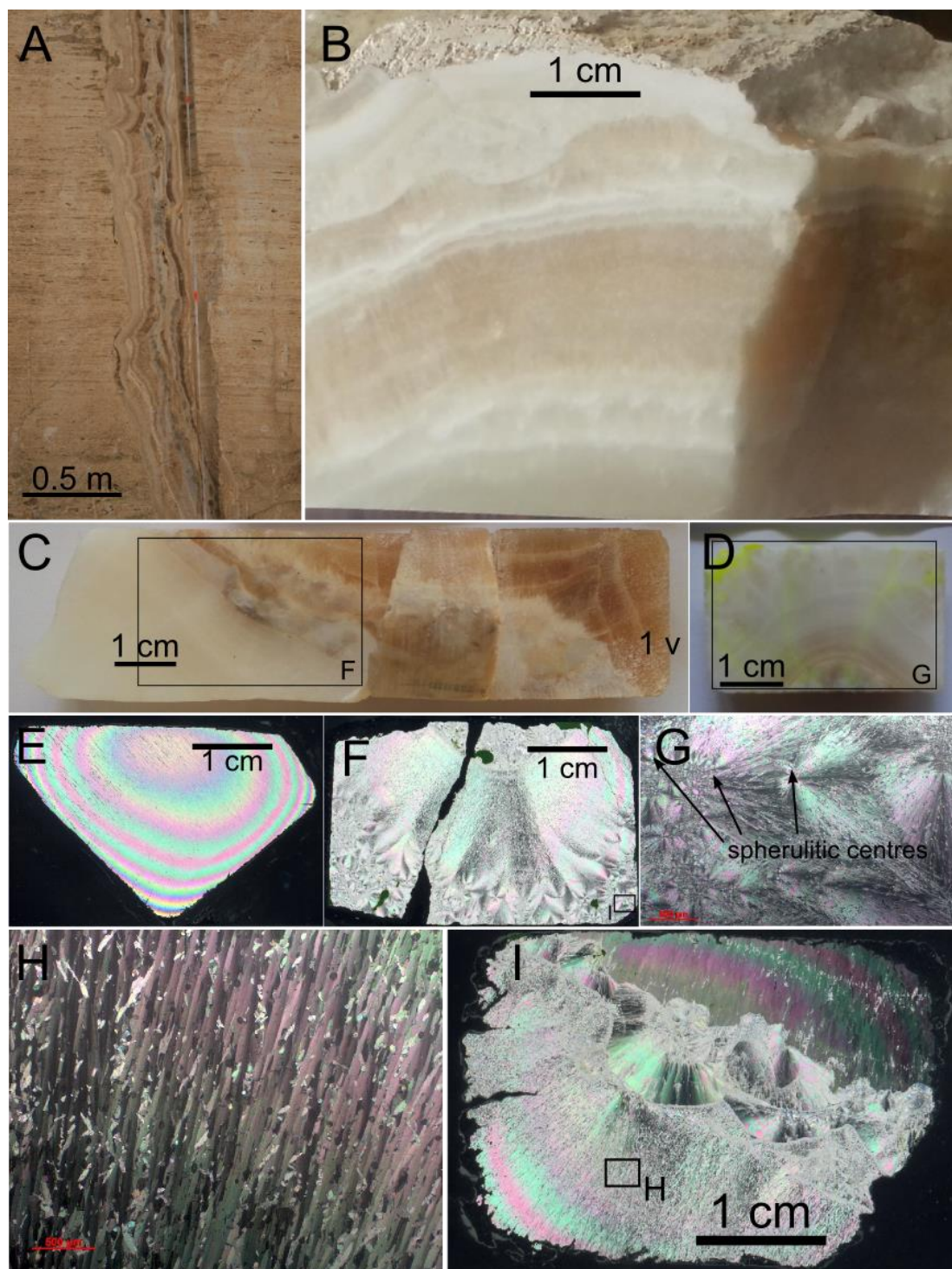


Figure 5-14: Vein travertine. Scale bars of figures B, C, D, E, F and G are 1 cm. A. Banded travertine in relation to the surrounding layered travertine. B. Sample of the banded travertine (AS14NJ019). Several cement bands can be recognized and colour varies from brown to white and translucent. C. Plug of banded travertine (AS14NJ001) with several cement bands. D. Plug (AS14NJ100) indicating white a white band in connection to translucent cements. E. Thin section scan (XP; AS14NJ003) of white cement, showing a uniform texture. F. Fans of needle crystals with their central part resembling spherulites, recognized by a black cross. G. Thin section scan (XP; AS14NJ100) with needle crystals growing into fans. H. Needle crystals in banded travertine. I. Thin section scan (XP; AS14NJ001) with different cement bands. The middle cement bands show fan-crystals.

### 5.1.8. Exotic lithotypes

A few lithotypes that were observed during the field campaign appear only sporadically throughout the travertine body. These lithotypes are not neglected in the analysis, as even small features can have a significant impact on the depositional as well as the reservoir model. The lithotypes of concern here are coated bubbles, paper-thin rafts, unconsolidated micrite and pisoids (radial shrubs).

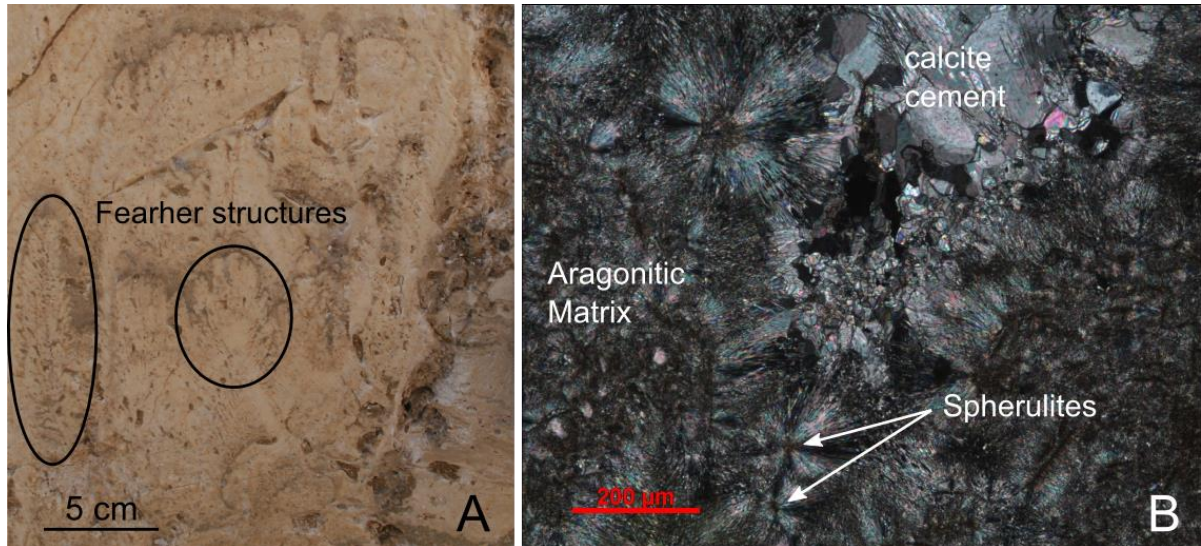


Figure 5-15: Feather crystals near vein travertine. A. Feathers are encircled. B. Microphotograph (XP; AS14NJ015) of the feather structures. The matrix consists of needle crystals and the cements in the pores are calcite.

#### 5.1.8.1. Coated bubbles

The coated bubbles occur in small lenticular pockets in between the microbial laminites. The bubbles macroscopically resemble actual fossil gas bubbles (Figure 5-16A).

In the microscopic analysis, the fabrics of the coated bubble travertine shows similarity with the microbial laminites. The bubbles have a black micritic rim with inwards growing crystals (Figure 5-16B). These crystals make up an equant to bladed fabric. The dark micritic concretions that grew on the microbial laminites are also present on the outer rim of the bubbles. The small zone in between the dark micrite rim and the crystals consists of less dense micrite.

The name coated bubbles is a regularly used term for deposits in which gas bubbles are coated by a calcite rim. They are observed in both active and fossil systems (Chafetz & Folk, 1984; Fouke, 2011; Guo & Riding, 1998; Özkul et al., 2002). The actual gas bubbles are expected to be of microbial origin (Gandin & Capezzuoli, 2014). Chafetz and Folk (1984) describe that the gas bubbles are coated by a microbial film, which is also expected here as a black micritic rim is described.



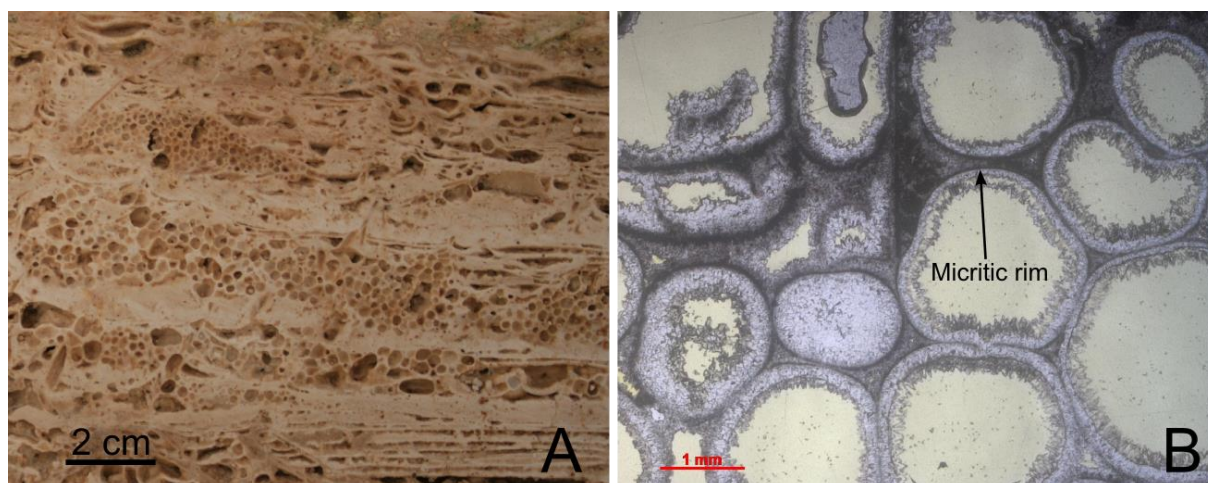


Figure 5-16: Coated bubbles. A. Macroscale. The coated bubbles occur together with the microbial laminites, they occur as small pockets of concentrated bubbles. B. Microphotograph (PP; AS14NJ007). The black micritic rim and inward growing crystals are characteristic.

#### 5.1.8.2. Shrubs

This lithotype describes morphologies, which macroscopically resemble shrubby plants. The shrub lithotype is a less common lithotype in this travertine body. The occurrence of the shrubs is restricted to the small depressions in small terraced deposits (Figure 5-17A).

The shrubs in this lithotype are larger than those of preceding lithotypes and can be recognized macroscopically (Figure 5-17B, C and D). They have a lower height-to-width ratio, which is 5:1, compared to the long microscopically recognised dendrites. The shrubs have a creamy colour with whiter and browner zones. The white colour is restricted to the internal part of the shrubs, whereas the browner colour forms an envelope around it.

At microscopic scale, the shrub morphology is less recognizable. The inner parts of the shrubs are composed of micritic pellets, which are up to 1 mm in diameter, or of small dark micritic peloids organised as shrubs on a microscopic scale (Figure 17E to I). The micritic pellets are variably lighter or darker. Crystals surrounding the micrite are microsparitic calcite and when occurring close to a pore, they have dogtooth-like appearance. The alternation of micrite and sparite is also recognized by Chafetz and Guidry (1999) in what they classify as “bacterial shrubs” even though they noticed the shrub morphology on a microscopical scale as well.

Cathodoluminescence shows, like for the other dark micritice, pink to purple luminescence. The cements immediately adjacent to the micrite are non-luminescent. More towards the pores these cements have a dull orange luminescence.

Figure 5-17E to G shows the vertical variation from bottom to top of one shrub. A variation from more sparitic and less dense micrite towards almost entirely micritic is marked from top to bottom. The shrubs

are also microscopically recognized in Figure 5-17F and G. If the micrite is indeed linked to microbial activity (e.g.: Chafetz & Folk, 1984; Chafetz & Guidry, 1999), this sequence shows increasing microbial influence to the top of the shrubs.

The shrubs are morphologically the same to those defined at the extensive flat deposits in Tivoli (Chafetz & Folk, 1984; Chafetz & Guidry, 1999; De Filippis et al., 2013b; Pentecost, 2005) and those at Rapolano Terme in the Shrub Flat Depression lithotype (Guo & Riding, 1998). The shrubs in this travertine body are restricted to small pools and flat deposits. This observation agrees with the shrubs being restricted to calm settings. The waters generally have a high temperature and dissolved H<sub>2</sub>S (Fouke, 2011). A relation to paper-thin rafts (Figure 5-17B and C) indicates calm pool conditions (Guo & Riding, 1998; Özkul et al., 2002).

#### 5.1.8.3. *Paper-thin (microbial) raft*

The paper-thin raft, calcite ice or “hot ice” lithotype is defined by several authors (Fouke, 2011; Gandin & Capezzuoli, 2014; Guo & Riding, 1998; Özkul et al., 2002; Pentecost, 2005). In general, these rafts can remain intact if the pool would desiccate and the rafts have the time to settle. They could break if the water surface is disturbed (Guo & Riding, 1998). In this travertine body, broken rafts were only observed in relation to the shrub lithotype (Figure 5-18A).

In microscopic section, the paper-thin rafts look similar to the microbial laminites (Figure 5-18B). The centre of the raft is marked by a black micritic line. At the bottom of this line there are black micritic cloths or tooth-like protuberances, sensu Gandin and Capezzuoli (2014). Both the black micritic line and the cloths resemble the microbial laminite fabrics, although they are much denser and more pronounced for the paper-thin rafts. This lithotype is referred to as “Microbial rafts” by Gandin and Capezzuoli (2014).

Paper-thin rafts are deposited at the water surface in low-energy environments, like pools. The paper-thin rafts are linked to the pools of small terraces which provides an additional argument to assume low energy environment (Guo & Riding, 1998).

#### 5.1.8.4. *Unconsolidated micrite*

This lithotype has only been recognised once, in a twenty centimetres thick layer (Figure 5-18C). The name “unconsolidated micrite” is used here since the layer is poorly cemented. Pieces come off easily. The sample is considered micritic because of the macroscopical absence of textures.

On a microscopical scale, the fabrics of this lithotype are small shrubs, made up of black peloids, even though this is barely recognisable (Figure 5-18D). The fabrics are altered and weathered which causes the texture to be only faintly visible. The unconsolidated micrite deposit could be considered as an

erosional surface in which the original fabrics can still be recognized. No secondary cements are present and porosity is vuggy.

#### 5.1.8.5. *Pisoids*

Pisoids are small sphere-like bodies (3D) that are seen as circles (2D) in the deposit (Figure 5-18E). In this travertine body, the pisoids are limited to thin layers related to flat deposits of the type II microbial mats. The pisoids sometimes grow into small shrubs within the flat deposits.

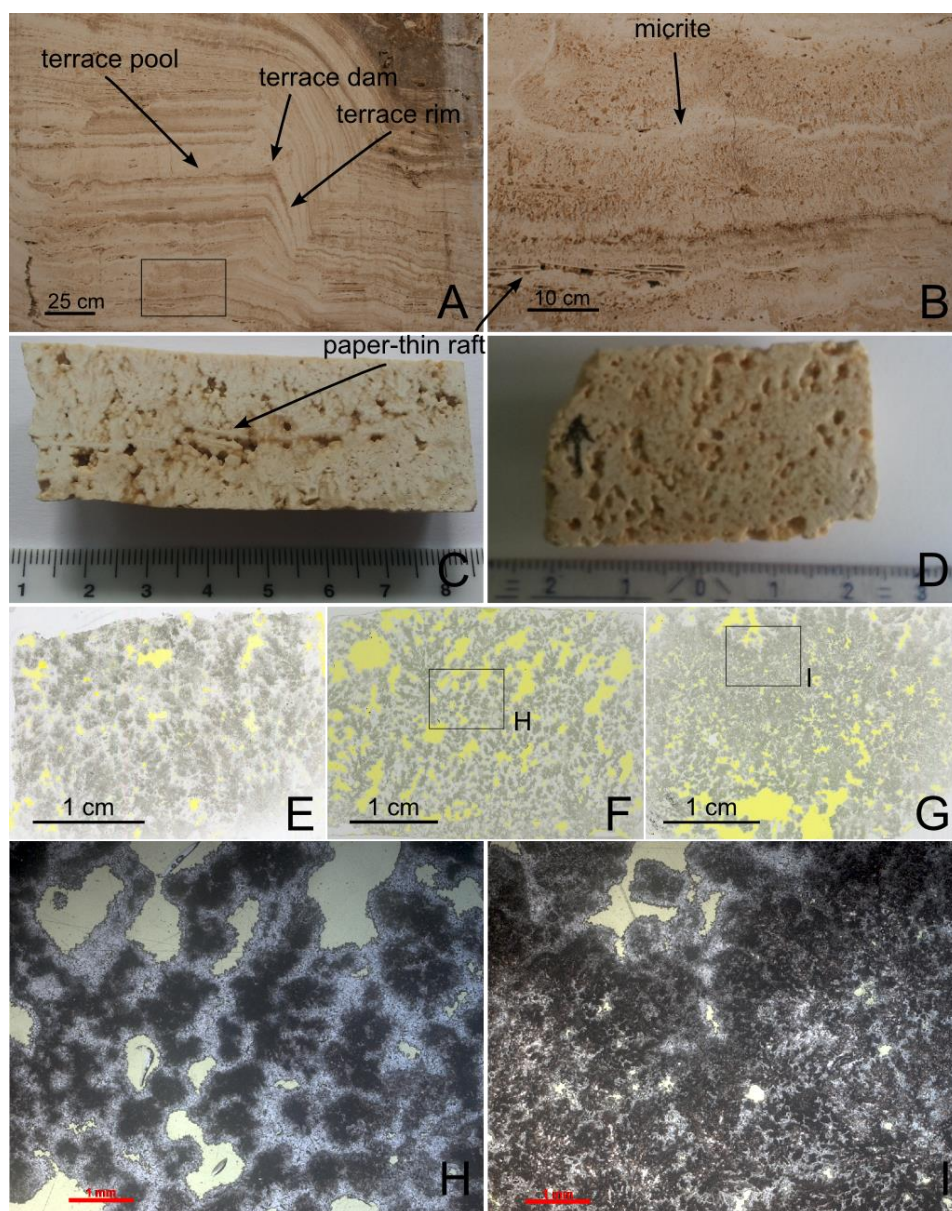


Figure 5-17: Shrub lithotype. A. Shrub lithotype is related to the pools of terraces. B. Two shrub levels on top of each other, separated by a micritic layer. C. Shrubs associated with paper-thin rafts (AS14NJ021). D. Plug (AS14NJ022) Shrubs are recognised by small leaves. E – G: (E: AS14NJ021; F: AS14NJ022; G: AS14NJ023) vertical section of shrubs from lowest to upper part with increase in black micritic clumps and decrease of sparite. H. Microphotograph (PP; AS14NJ022) of shrubs showing the micritic pellets covered by sparite. I. (PP; AS14NJ023) Microphotograph of the upper part of the vertical section of shrubs. Black micritic shrubs prevail.



On the microscopical scale, the pisoids are comprised of a small nucleus, rimmed by black peloidal micrite. The peloidal micrite is organised as small micro-shrubs, which grow radially away from the nucleus (Figure 5-18F).

Such pisoids are described as “bacterial pisoids” or “bacterial pisoliths” in Folk and Chafetz (1983), Chafetz and Folk (1984) and Guo and Riding (1998). They form another indication of the bacterial or microbial influence in this travertine deposit. Pisoids can be formed in a variety of settings, but are most

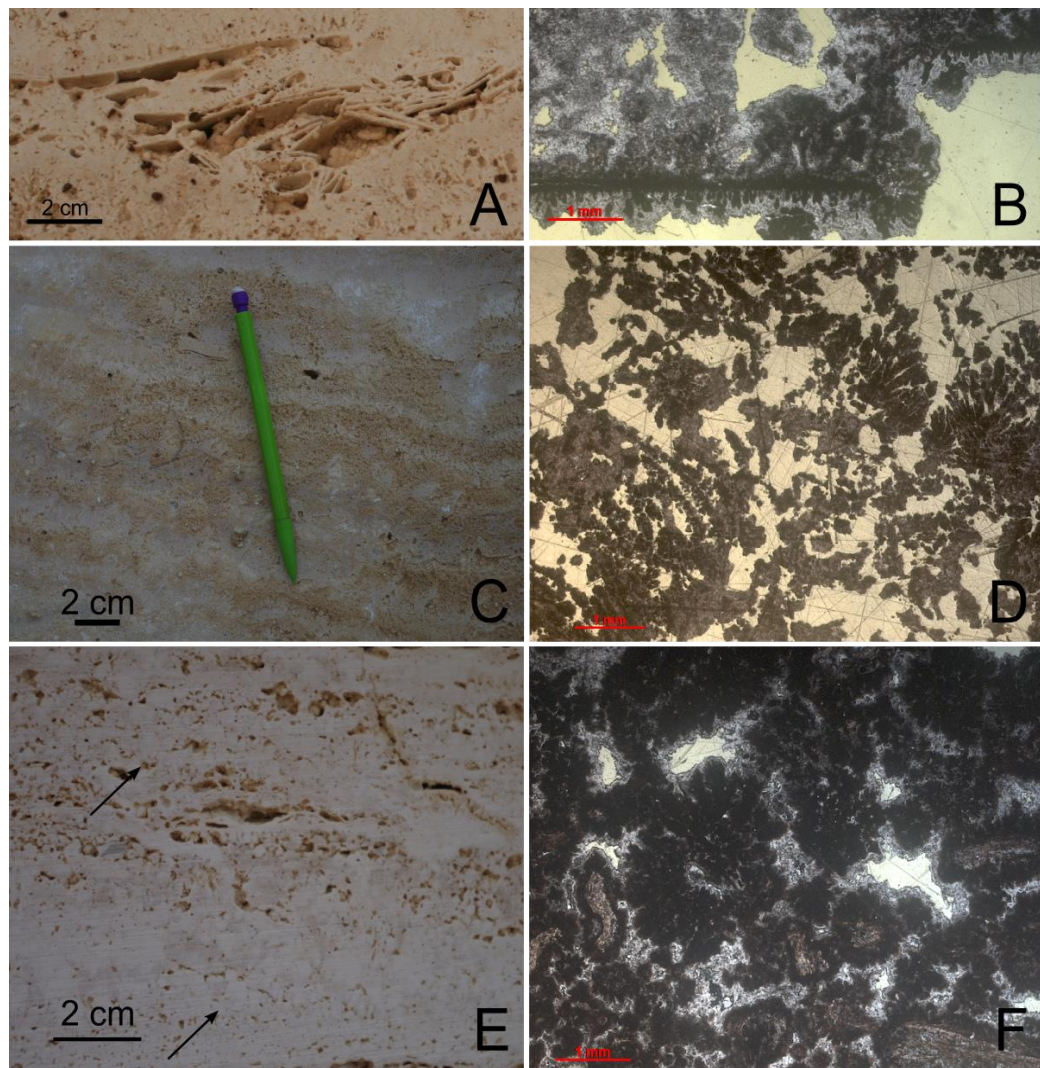


Figure 5-18: Exotic lithotypes. A. Broken paper-thin (microbial) rafts on macroscale. B. Microphotograph (PP; AS14NJ020) of a paper-thin raft. Note the thick micritic line in the centre of the raft and the tooth-like micritic cloths on the bottom. C. Unconsolidated micrite on macroscopic scale. The wall had been wet and the porous micrite is retaining the water. D. Microphotograph (PP; AS14NJ066) of unconsolidated micrite. The fabrics consist of micritic dendrite shrubs which have been significantly altered to micrite. E. Pisoids on macroscopic scale, occurring in distinct layers. F. Microphotograph of the pisoids (PP; AS14NJ017). The pisoids are recognized as radial shrubs that sometimes clearly have a clast in the centre.

commonly related to either calm pool settings or to an area of increased agitation due to water falling from a terrace rim or at the base of waterfalls.

### 5.1.9. Fossil cave fill

This peculiar structure has been observed in the field and cannot be assigned to any of the other lithotypes (Figure 5-19). The structure is described as a fossil cave, based on a few observations that indicate a karstic origin: i.e. a triangular shape with the apex towards the top (Figure 5-19A), the presence of both fossil leaves and gastropods (Figure 5-19C and D), dripstone morphologies (Figure 5-19A) and breccia.

The fossil cave is made up of two different parts, separated by dense deposits that resemble veins, comparable to banded travertine (Figure 5-19A). At both sides of the veins, more porous deposits are present, which resemble layered travertine (Figure 5-19A). A horizontal cross-section, created by excavation activities, was observed on the quarry floor and reveals circular features (Figure 5-19B). These features consist of alternating denser and more porous zones, similar to the rest of the travertine-like fossil cave fill. The circular features could be cross-sections of structures that morphologically resemble dripstones.

On a microscopic scale, the deposits are generally marked by a high amount of vuggy porosity. The fabrics consist of either micrite or more crystalline shrubs (Figure 5-19F). Micritic deposits sometimes have a very dark colour, which could indicate microbial influence (Chafetz & Folk, 1984). The shrubs in these deposits are dark micritic and crystalline shrubs (Figure 5-19E and F, respectively). The crystalline shrubs show clear extinction and their slightly dark brown colour indicates a not entirely inorganic precipitation mechanism (Chafetz & Guidry, 1999). The crystalline shrubs are deposited perpendicular to the substrate instead of growing upwards as usual for shrubs. The shrubs do not branch upwards but are rather composed of thick “leaves” that grow from the base to the top. Black micritic peloids are seen in the dark micritic shrubs, but are rare for the crystalline shrubs in which they are embedded in a crystal, which is in agreement with Chafetz and Folk’s (1984) observations. All deposits show layered textures. Shrub-like textures that occur laterally on the same level are all interrupted at the same point by micritic layers (Figure 5-19E). Even the more crystalline shrubs are alternating with micritic porous zones (Figure 5-19F). These highly porous samples contain cements in some instances, varying from dogtooth to bladed cements.

The textures at the border of the fossil cave fill resemble erosional horizons, but are bordering the entire fill. The layer has a grey colour and a micritic matrix with large vugs that have been cemented by dogtooth, equant and bladed crystals (Section 3.2.6.; Figure 5-19H). There is a minor presence of quartz in the samples. Micritization is deduced from cathodoluminescence in the micrite from certain structures



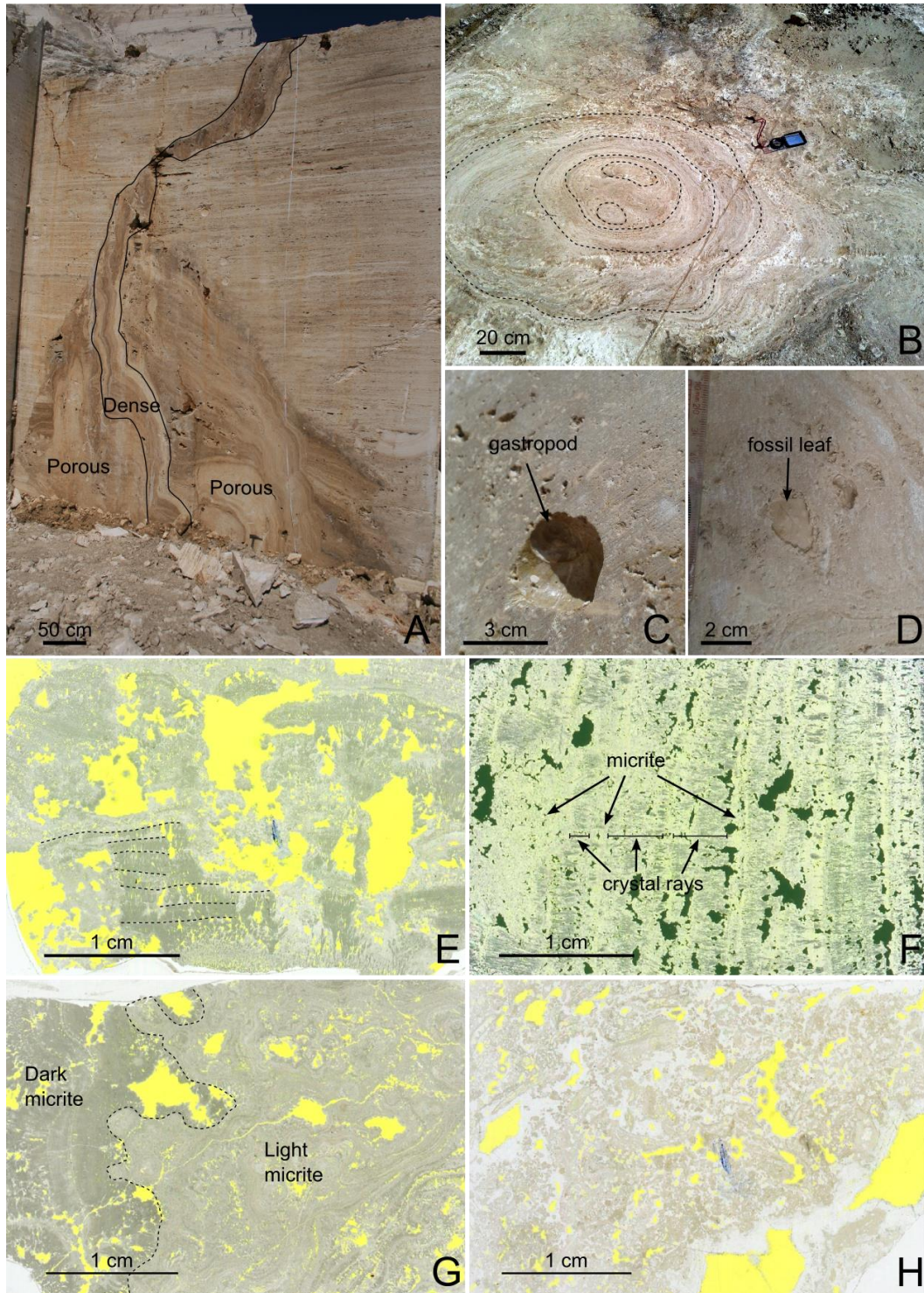


Figure 5-19: Fossil cave deposits. A. Fossil cave. Dense band is discernible in the middle of the structure. Both to the right and to the left, more porous travertine is present. B. Floor right next to the wall of A is marked by circular features. C. Fossil gastropod. D. Fossil leaf. E. Thin section scan (PP; AS14NJ045) the lower part are dark, crystalline shrubs stacked in layers. F. Thin section scan (XP; AS14NJ052). The crystal-ray shrubs are layered and are separated by porous, micritic layers. G. Thin section scan (PP; AS14NJ054). The left side is marked by dark micrite and the middle and the right side consists of lighter micrite. H. Thin section scan (PP; AS14NJ056). Grey horizon at the border of the fossil cave, marked by a micritic matrix, vuggy pores and cements.



in the micrite that are brightly luminescent in contrast to the rest of the dull-luminescent micritic matrix (Figure 5-20B). The brightly luminescent structures have distinct shapes, possibly related to its pre-micritization state. The cements are mainly non-luminescent with sometimes bright- and dull-luminescent layers (Figure 5-20A and B). The luminescence in other samples is black for the micritic parts and dull for cements (Figure 5-20C and D). The samples of the vein in the centre of the fossil cave fill (Figure 5-19A) show bright to dull luminescence, suggesting reducing conditions (Figure 5-20E and F).

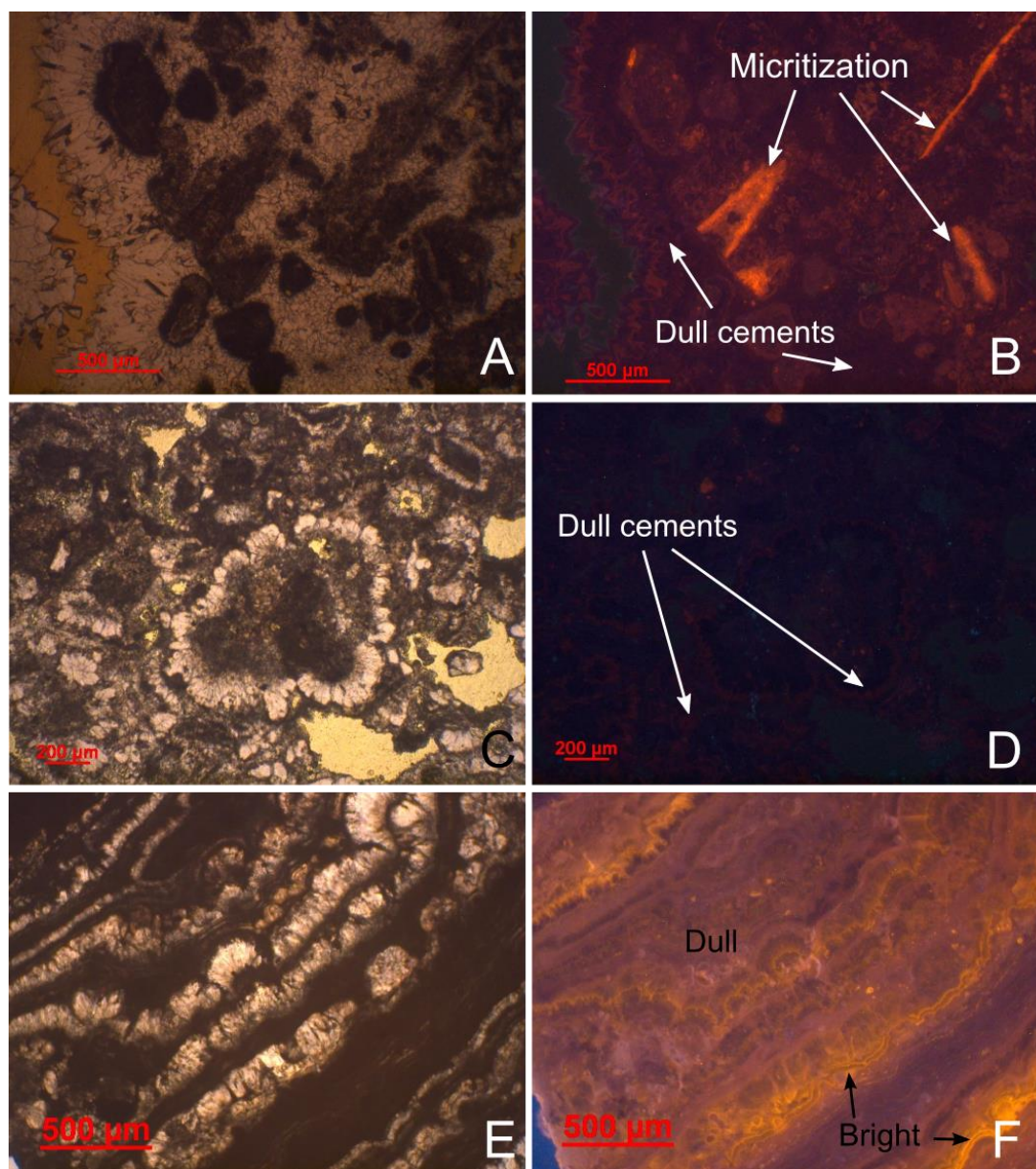


Figure 5-20: Cathodoluminescence in fossil cave. A and B. (AS14NJ056) Sample of the border of the fossil cave. Micrite is both dull and bright luminescent. The bright parts are micritized textures. The cements are dull luminescent. C and D. (AS14NJ060). The micrite is non-luminescent and the cements are dull luminescent. E and F. (AS14NJ057) Sample of the dense veins. The crystals are dull to bright luminescent. The majority is dull luminescent, indicating reducing conditions.

### 5.1.10. White cements

Some white or translucent cements are discovered inside pores of certain deposits (Figure 5-21A). In thin section, the white cements are composed of needle-like crystals (Figure 5-21B). They are present in a variety of deposits. The translucent cements occur as thick rims in some vuggy pores or sometimes in interlayer porosity. These have not been examined in petrography. The white cements are non-luminescent.

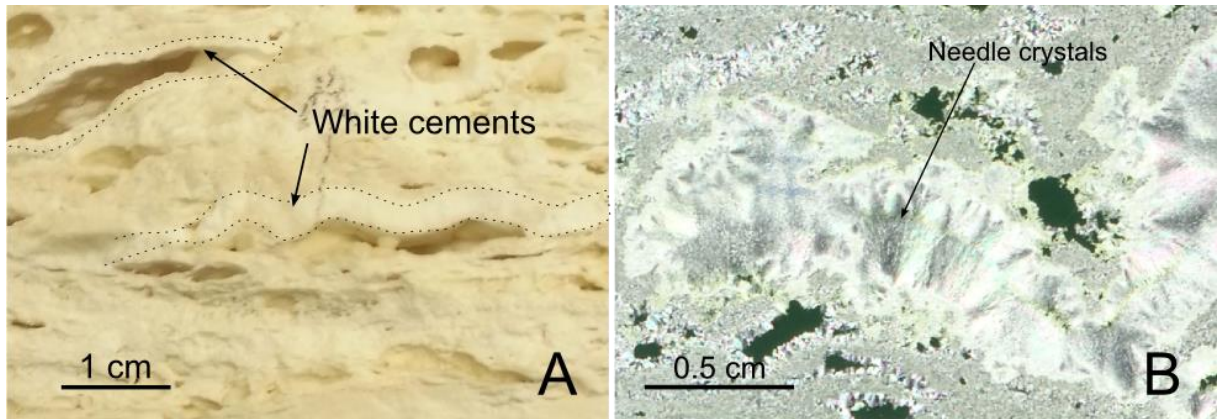


Figure 5-21: White cements in sample (A; AS14NJ032) and in thin section (B; AS14NJ098). The needle crystals grow from the top and the bottom of the pore towards the centre.

## 5.2. Travertine architecture

This section treats several types of field data, like lithologs, linedrawing, lithotype variations, different lithofacies and structural data. These data are required to unravel the travertine architecture. A geological map of the surrounding area has been created which is present in Appendix 2.

### 5.2.1. Lithologs and image analysis

For assessment of the vertical variation in the travertine body, lithologs are generated. The lithologs are based on field characteristics like textures and porosity. The porosity was estimated in the field and is complemented with point-counting analyses on terrain photographs. An example of a litholog is given in Figure 5-22, the other lithologs are given in Appendix 2, together with the point-counting data.

### 5.2.2. Linedrawings, lithotype variation and lithofacies

The small scale of the quarry allowed to carry out detailed mapping of the lithotype variation in the field on pictures of quarry walls. An example of a linedrawing is given in Figure 5-23, the other linedrawings are given in Appendix 2. The linedrawings form the base for the 3D reservoir model and are also used in determination of paleo-fluid flow, based on the slope of the deposits.

The relation between the slope of the layers and the variation of the lithotypes allows assessment of the lithofacies. Six lithofacies are described, based on the field relations:



- The sloping lithofacies is marked by lateral transition of type I microbial mats towards micritic dendrite crust, which ultimately grades into peloidal micrite. The transition between the lithotypes is marked by interfingering of the layers.
- Flat pool lithofacies are marked by type II microbial mats with thin layers of pisoids growing into shrubs of maximum 1 cm high. The deposits are rather porous and rich in micrite.

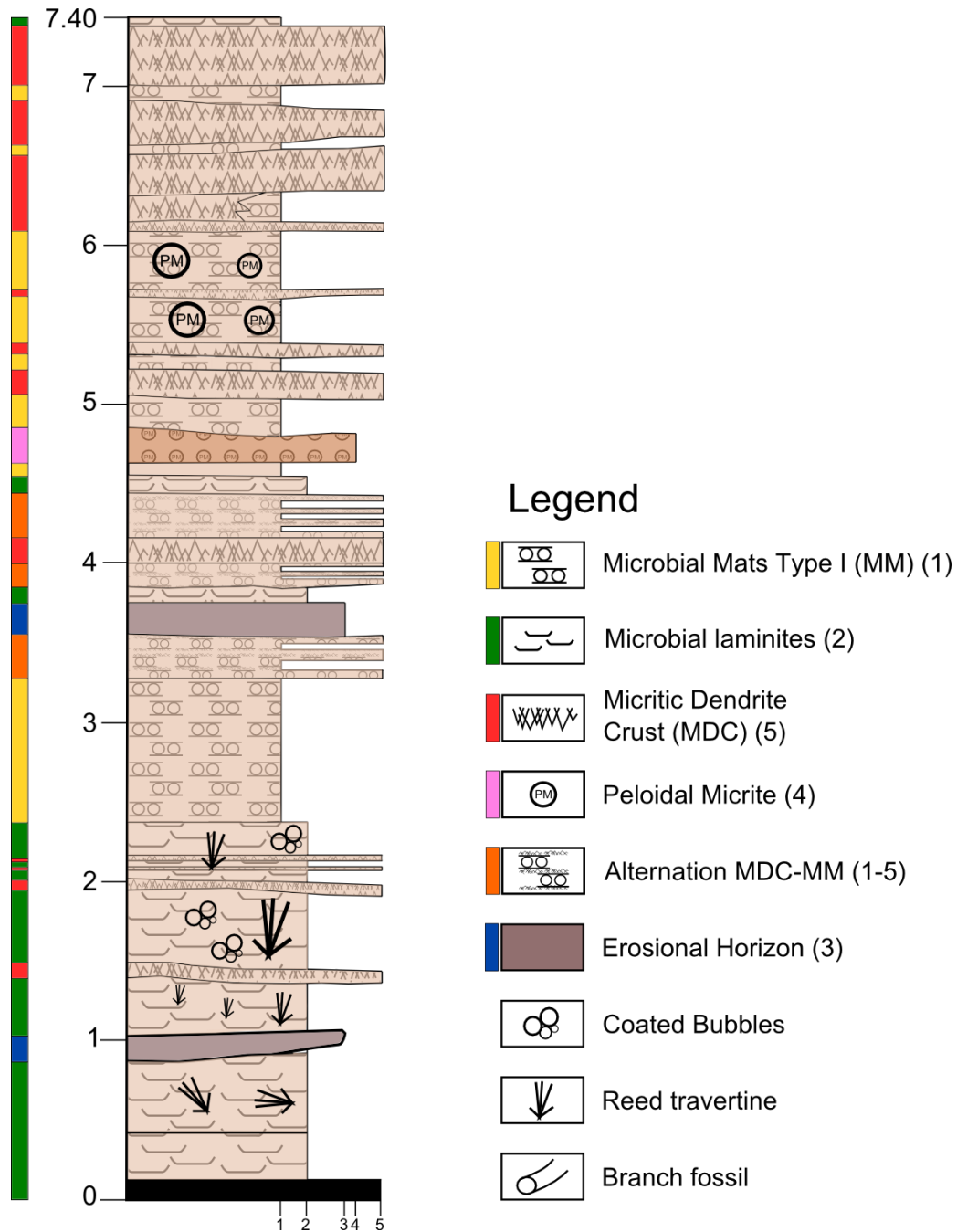


Figure 5-22: Example of a litholog. Variation in lithotypes in the vertical sense can be seen. This litholog shows variation of reed travertine towards deposits dominated by microbial mats followed by domination by micritic dendrite shrubs.

- Reed lithofacies: This lithofacies mainly contains the microbial laminites and the coated bubbles. These two lithotypes occur together with reed moulds. The layering of this lithofacies is flat.
- Terrace lithofacies: Small terraces are recognized by flat deposits with slightly elevated rims followed by steeply sloping deposits, which are linked to the terrace pools, rims and slopes, respectively (Fouke, 2011; Guo & Riding, 1998). The pools are characterised by shrubs and the rims and slopes by micritic dendrite crusts (Figure 5-17). This lithofacies is uncommon in this travertine deposit.
- Erosional horizons: This lithofacies can be draped over any other lithofacies and the next layers are usually onlapping. They indicate phases of the absence of spring waters, whereas the onlapping layers indicate the following phase in spring activity.
- Waterfall lithofacies: The waterfall deposits are recognized by almost vertical layering of micritic dendrite crusts or crystalline crusts. The sub-vertical deposits have a height of up to 20m. No samples could be taken from this lithofacies due to safety reasons. This impedes defining the details of this lithofacies with certainty.

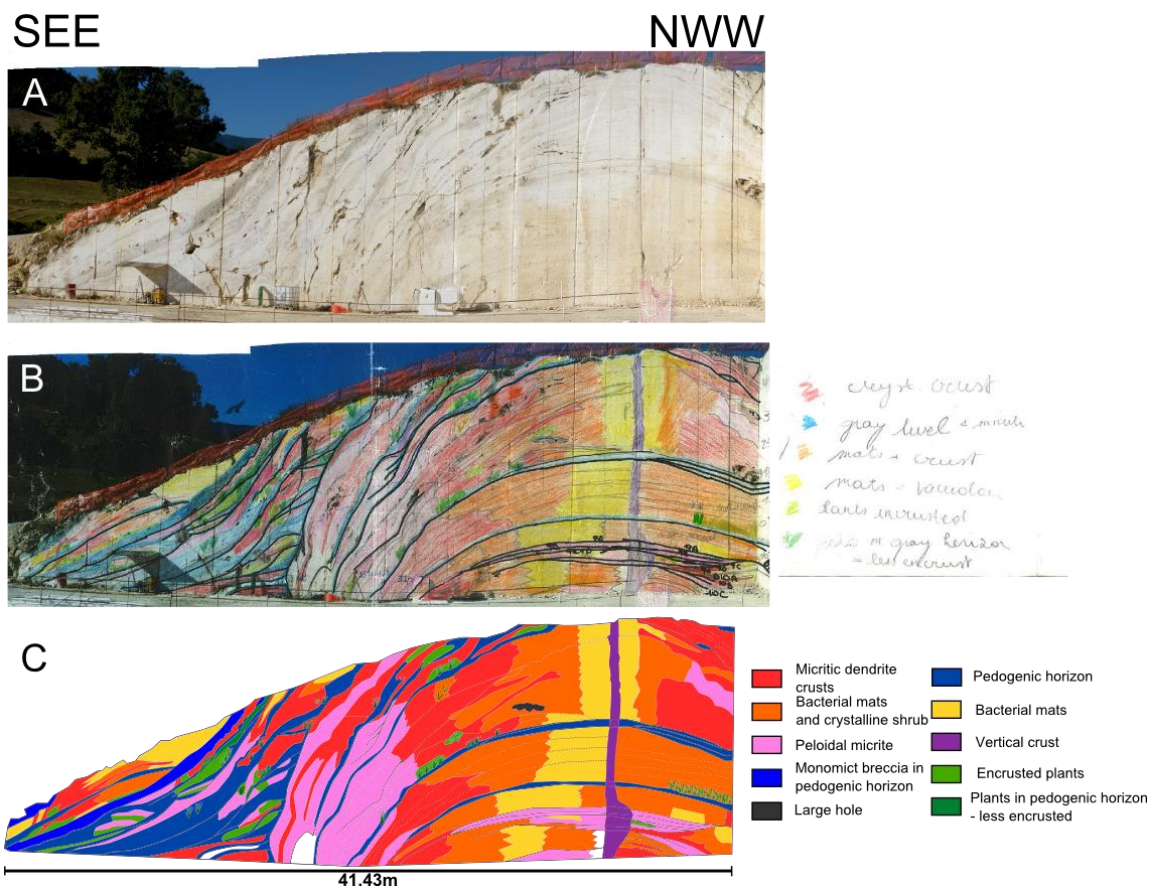


Figure 5-23: Example of a linedrawing. A. Original photograph created by merging several photos together. B. Field drawing: linedrawing (thick black lines) and lithotype variation. C. Digitized linedrawing.

Based on the lithotype variations and onlapping and/or offlapping relations, several depositional bodies are defined (Figure 5-24). Each body marks a certain morphology at a certain moment in time. Each body indicates a further phase in the evolution of the travertine system, thus indicating variation through time. Bodies 2 and 3 are interfingering, indicating that the deposition of those bodies was simultaneous with fluids coming from different directions. The bodies are used to investigate whether variation through time of certain parameters exists (e.g. stable isotopes, section 3.5.1). Seven bodies could be differentiated (Figure 5-24). The main paleoflow directions are determined based on the slope of the layers. The paleoflow directions vary throughout the depositional history (Figure 5-25). The lower bodies have two opposite flow directions, with the main one directed towards the valley. The upper

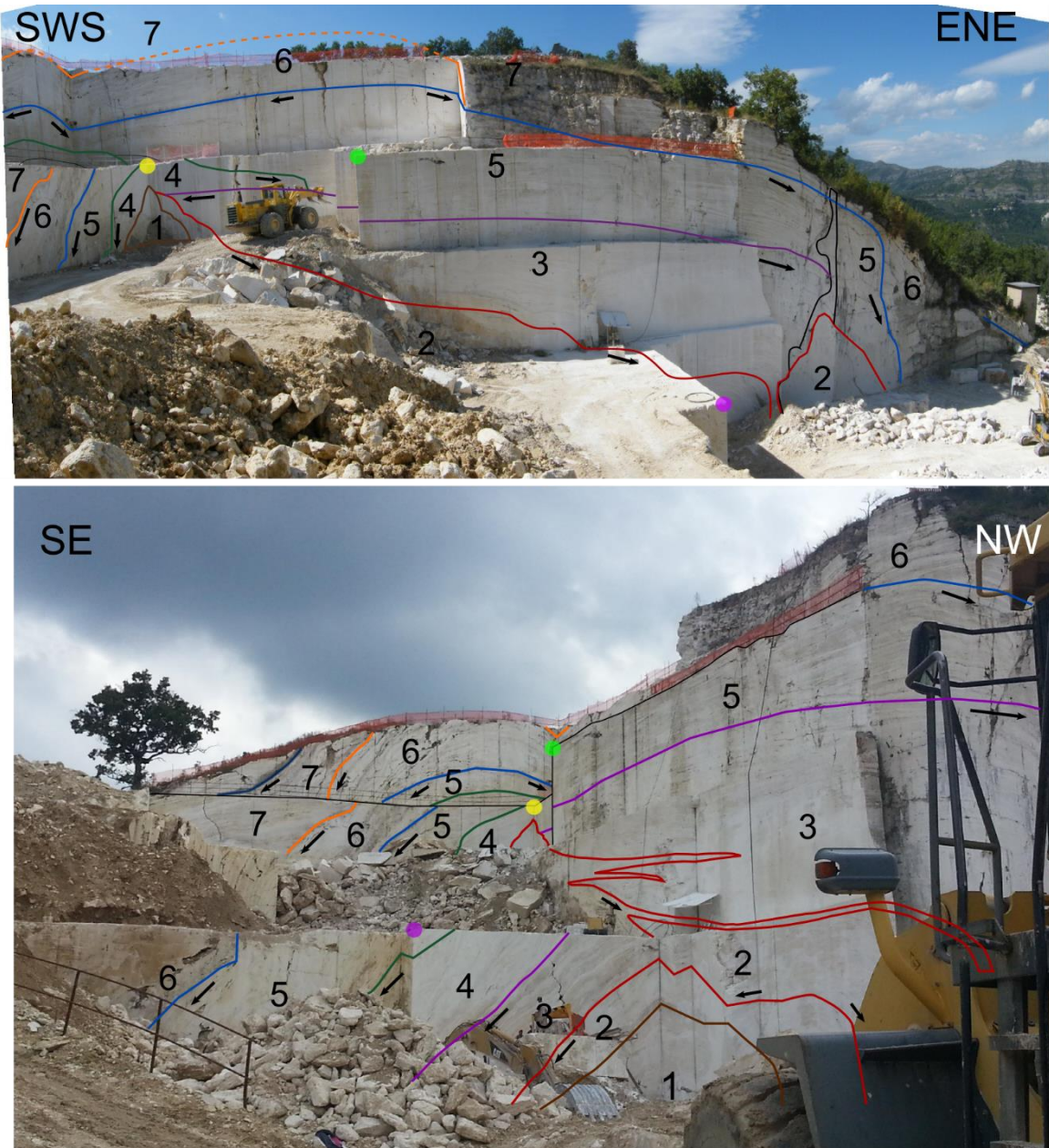


Figure 5-24: The seven different bodies of the travertine system indicated on photos taken at different angles, the coloured dots are reference points, they are also indicated on a map in figure 25. Bodies 2 and 3 are interfingering.



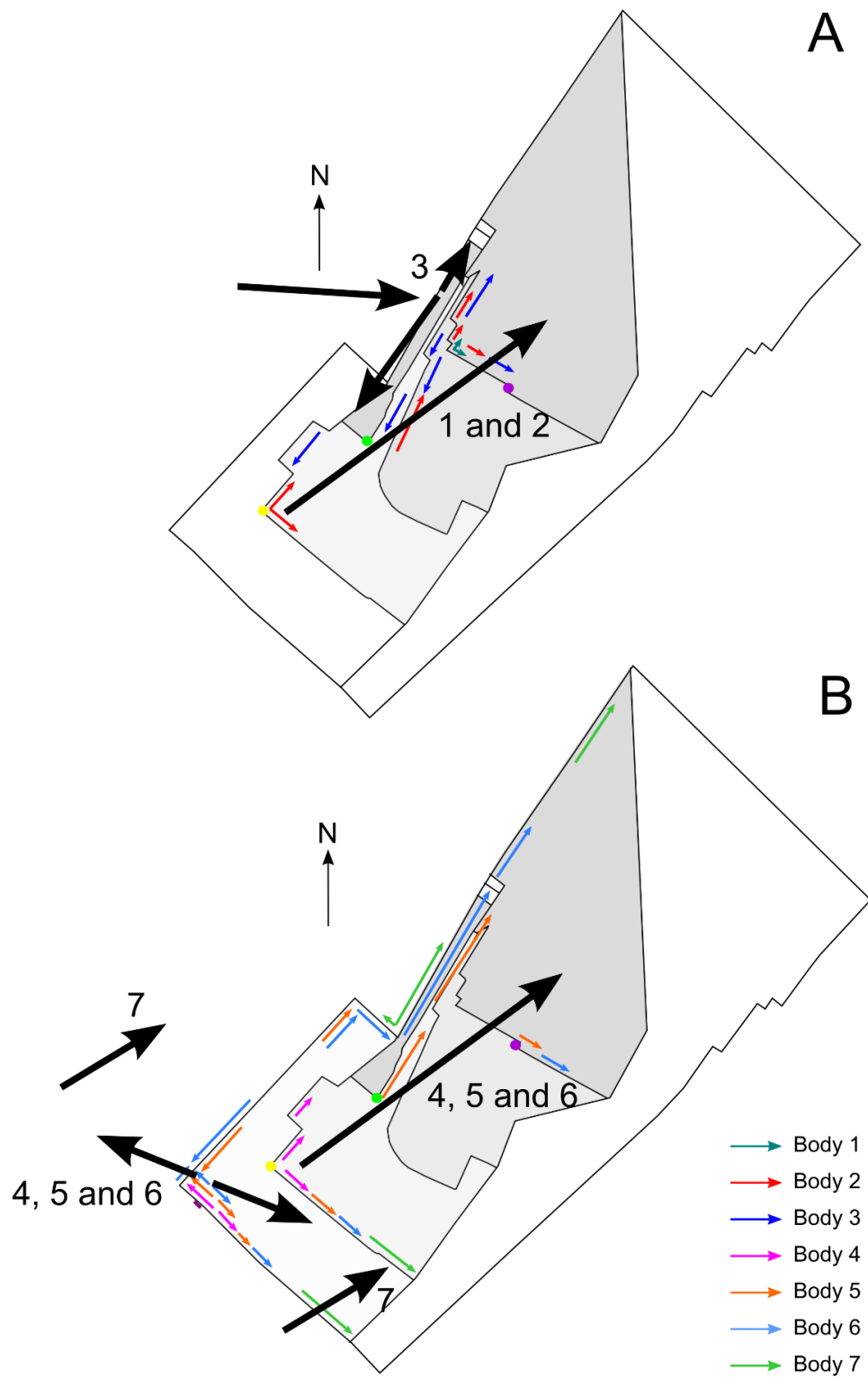


Figure 5-25: Paleoflow directions. The coloured arrows indicate the slopes of the layers in linedrawings. The black arrows are the inferred paleoflow directions. The numbers with the black arrows indicate which bodies show this fluid flow direction. The three coloured dots indicate the same points as figure 24.

bodies indicate flow in two directions, moving away from a central vein. The paleoflow in the direction of the valley remains present.

### 5.2.3. Structural data

The dip direction and dip of fractures that are present in the travertine body are measured in the field. Two types of fractures are discerned, those with and without mineralization (Figure 5-26). The fractures without such mineralization show two different dip directions, but most have a dip direction/dip of approximately 50/85. This value is an average of a limited dataset, so should be treated with caution. Data in Appendix 4.

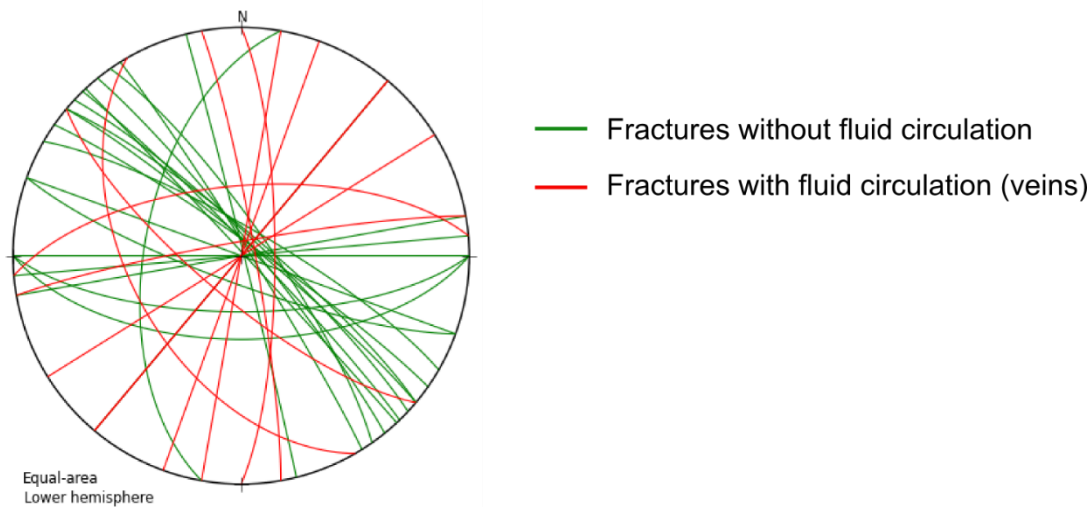


Figure 5-26: Structural data based on field observations. The green lines indicate fractures without evidence of fluid circulation. The red lines indicate fractures containing calcite veins, which indicate fluid circulation.

## 5.3. Three-dimensional analogue reservoir characterization

A 3D representation of the reservoir analogue is constructed from the lithotype distribution noted from field data (Figure 5-27). This data is integrated with the petrophysical data and the observations of the pore types, as explained in section 5.1. (Figure 5-28). The presented data consists of averages of the porosity and the Empirical Klinkenberg permeability. The grain densities are included in the petrophysical data as they provide a relative estimate for the amount of microporosity within the grains. The 3D reconstruction is limited to those lithotypes that can be backed by data for the porosity and the permeability. Just like in a lot of reservoir studies, some lithotypes have measurements for only one or two samples. Data usually has a large spread, even within one specific lithotype (Figure 5-28 and 5-29). To investigate the difference between vertical and horizontal permeability, three vertical plugs are taken in the micritic dendrite crusts and the type I microbial mats. The majority of the data is related to 22 horizontal plugs. The vertical permeability is slightly higher than the horizontal permeability in the

micritic dendrite shrubs and lower for the type I microbial mats (Figure 5-28 and 5-29). Data on the porosity and permeability in Appendix 4.

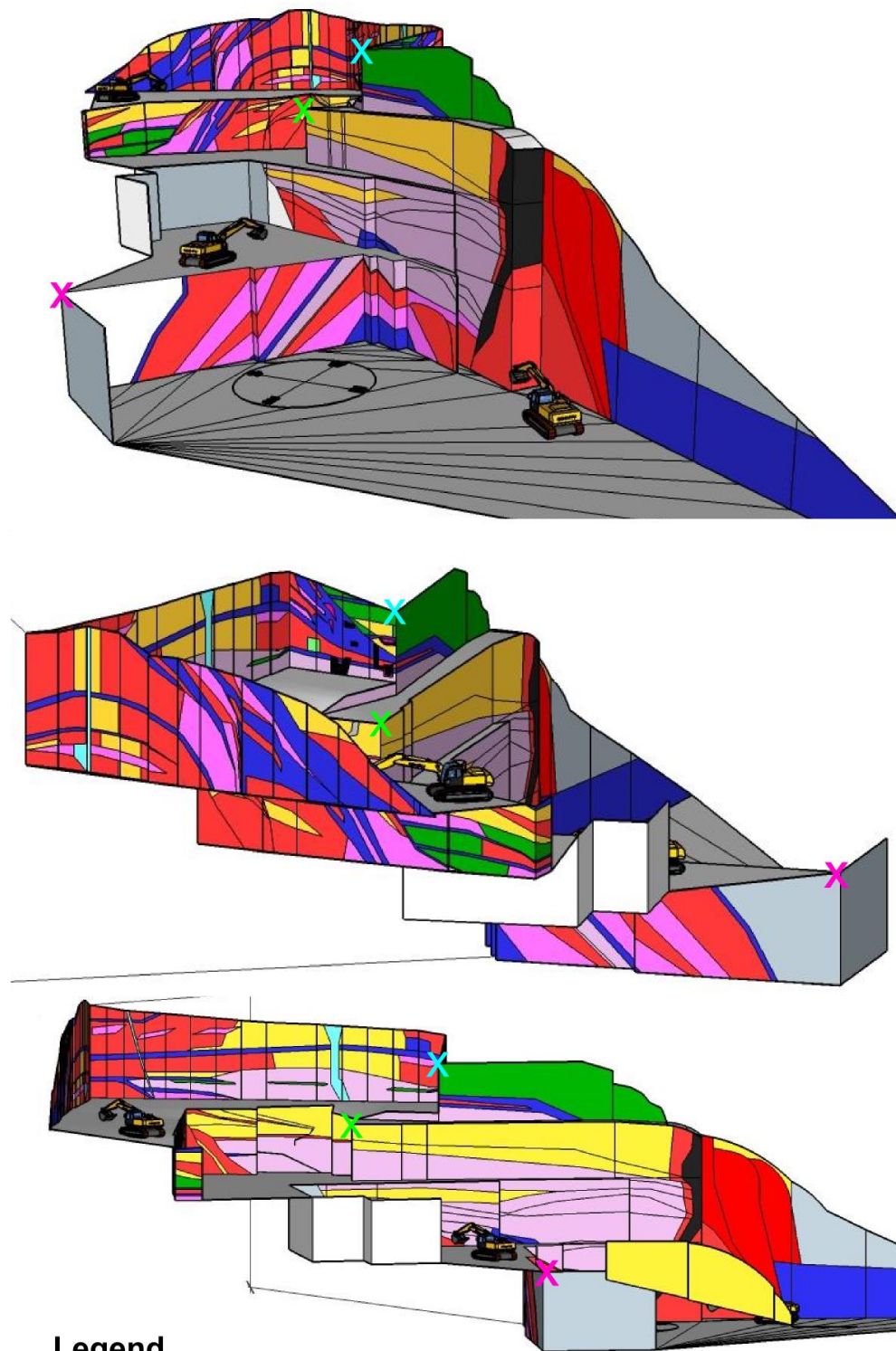


Figure 5-27: Three-dimensional reservoir model generated in SketchUp, excavator for scale. (scale length: 11.48m, width: 3.24m). The total height is approximately 40 m, the length 125 m and the width 35 m.

<b>Micritic Dendrite Shrubs</b>		Std. Dev.	Amount of Samples	<b>Porosity types</b>	<b>Diagenesis</b>
Porosity	6.7 %	2.38	5	IESP	Cements? Minor
Hor. permeability	0.8 mD	0.56	3	IASP	Cement types? Dogtooth
Ver. Permeability	4.71 mD	4.42	2	MP	
Vuggy?	No			FE	
Grain Density	2.58 g/mL	0.01	5	IL	Dissolution? No
<b>Peloidal Micrite</b>		Std. Dev.	Amount of Samples	<b>Porosity types</b>	<b>Diagenesis</b>
Porosity	12.8 %	1.06	3	IESP	Cements? Minor
Hor. permeability	23.10 mD	15.55	3	IASP	Cement types? Dogtooth
Ver. Permeability	/ mD	/	/	MP	
Vuggy?	No				
Grain Density	2.59 g/mL	0.01	3		Dissolution? No
<b>Microbial mats: Type I</b>		Std. Dev.	Amount of Samples	<b>Porosity types</b>	<b>Diagenesis</b>
Porosity	26.8 %	4.49	3	MP	Cements? Yes
Hor. permeability	4.71 mD	4.52	2	IASP	Cement types? Dogtooth
Ver. Permeability	0.34 mD	/	1	IL	Bladed (minor)
Vuggy?	Yes			FW	
Grain Density	2.61 g/mL	0.01	3		Dissolution? No
<b>Microbial mats: Type II</b>		Std. Dev.	Amount of Samples	<b>Porosity types</b>	<b>Diagenesis</b>
Porosity	11.7 %	1.55	2	MP	Cements? Minor
Hor. permeability	0.07 mD	0.02	2	IASP	Cement types? Dogtooth
Ver. Permeability	/ mD	/	/	FP	
Vuggy?	Y/N			IL	
Grain Density	2.61 g/mL	0.02	2		Dissolution? No
<b>Erosional surfaces</b>		Std. Dev.	Amount of Samples	<b>Porosity types</b>	<b>Diagenesis</b>
Porosity	23.2 %	4.95	2	MP	Cements? Yes
Hor. permeability	98.56 mD	98.44	2	BM	Cement types? Dogtooth
Ver. Permeability	/ mD	/	/	PBM	Bladed
Vuggy?	Yes			SP	Equant
Grain Density	2.67 g/mL	0.00	2	EV	Dissolution? Yes
<b>Microbial laminites</b>		Std. Dev.	Amount of Samples	<b>Porosity types</b>	<b>Diagenesis</b>
Porosity	23.6 %	2.04	5	MP	Cements? Yes (thick isopachous rims)
Hor. permeability	34.3 mD	53.04	5	PBM	Cement types? Dogtooth
Ver. Permeability	/ mD	/	/	IL	Bladed
Vuggy?	Yes			FW	Equant
Grain Density	2.6 g/mL	0.02	5		Dissolution? No
<b>Crystalline crust</b>		Std. Dev.	Amount of Samples	<b>Porosity types</b>	<b>Diagenesis</b>
Porosity	8.1 %	2.89	2	MP	Cements? Yes
Hor. permeability	101.2 mD	46.94	2	SP	Cement types? Bladed
Ver. Permeability	/ mD	/	/	IL	
Vuggy?	No			SV	
Grain Density	2.6 g/mL	0.03	2		Dissolution? Maybe
<b>Vein</b>		Std. Dev.	Amount of Samples	<b>Porosity types</b>	<b>Diagenesis</b>
Porosity	0 %	/	0	IEP	Cements? /
Hor. permeability	0 mD	/	0	Fr	Cement types? /
Ver. Permeability	0 mD	/	0		
Vuggy?	No				
Grain Density	/ g/mL	/	0		Dissolution? /
<b>Shrubs</b>		Std. Dev.	Amount of Samples	<b>Porosity types</b>	<b>Diagenesis</b>
Porosity	20.3 %	/	1	IASP	Cements? Minor
Hor. permeability	5552 mD	/	1	BM	Cement types? Dogtooth
Ver. Permeability	/ mD	/	/	FW	
Vuggy?	Yes			IESP	
Grain Density	2.65 g/mL	/	1		Dissolution? No
<b>Unconsolidated micrite</b>		Std. Dev.	Amount of Samples	<b>Porosity types</b>	<b>Diagenesis</b>
Porosity	36.9 %	/	1	BM	Cements? No
Hor. permeability	253 mD	/	1	EV	Cement types? /
Ver. Permeability	/ mD	/	/	TV	
Vuggy?	Yes			MP	
Grain Density	2.65 g/mL	/	1		Dissolution? Yes

Figure 5-28: Data used in the reservoir model. Abbreviation of porosity types, next page.



Porosity types	Abbreviations
Intershrub porosity	IESP
Intrashrub porosity	IASP
Interparticle porosity	IEP
Separate Vugs	SV
Biomouldic	BM
Plant Biomouldic	PBM
Microporosity	MP
Shelter porosity	SP
Erosional vuggy porosity	EV
Touching Vugs	TV
Fenestral Porosity	FE
Framework Porosity	FW
Fracture Porosity	Fr
Interlaminar Porosity	IL
Cave Porosity	Cave

Figure 28 (cont.): Abbreviations for porosity types.

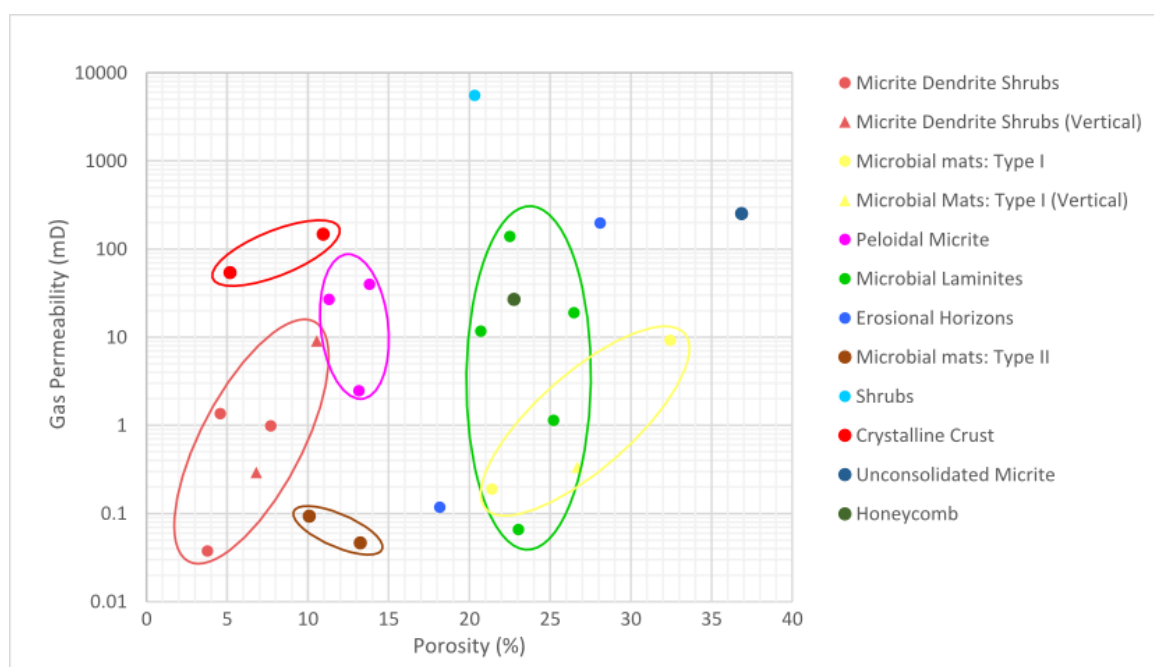
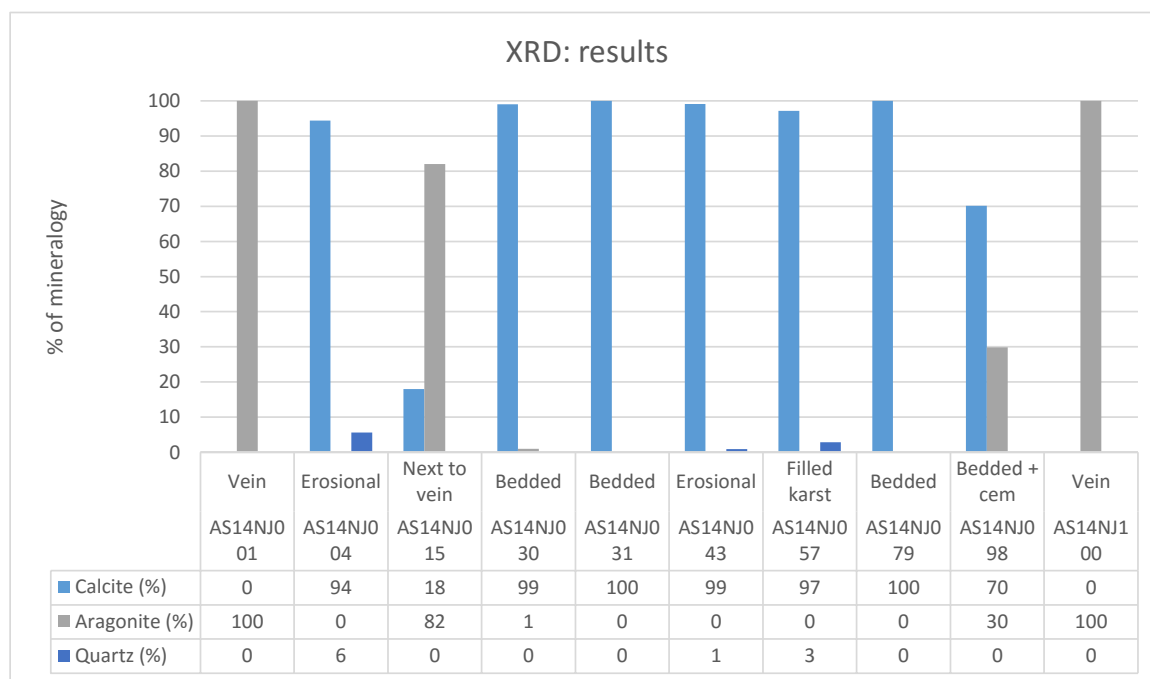


Figure 5-29: Petrophysical data. Each lithotype still has a lot of spread. One vertical plug for the micritic dendrite crusts shows higher permeability, compared to the other data of that lithotype.

## 5.4. Geochemistry and mineralogy

### 5.4.1. XRD-analysis

XRD-analysis of 10 samples reveals varying mineralogy for different lithotypes (Figure 5-30). The sampling approach of the XRD-analysis focussed on the determination of the mineralogy of the banded



*Figure 5-30: Results of XRD analysis. A general lithological classification is indicated here, as this already gives information in how the different mineralogies are spread throughout the system. The classification distinguishes between: veins (= banded travertine), layered travertine and erosional horizons. The “filled karst” sample is also a sample from a vein.*

travertine, compared to the layered travertine. The resulting mineralogy does not reflect the bulk of the travertine body. The results show that the mineralogy of the banded travertine veins, compared with the layered travertine differs entirely (Figure 5-30). The banded travertine, samples AS14NJ001 and AS14NJ100, show a 100% aragonitic mineralogy. Sample AS14NJ015, which is adjacent to the vein, contains feather structures and was probably in contact with the paleosurface through a fracture (indicated by e.g. fossil leaves), is mainly aragonitic (82%) with a small calcite component. This mineralogy was expected from petrography, as the sample has an aragonitic matrix cemented by calcite. The layered travertine, which correspond to samples AS14NJ030, AS14NJ031 and AS14NJ079, consist of 100% calcite. The erosional horizons, AS14NJ004 and AS14NJ043, both consist out of pure calcite and a minor amount of quartz (Figure 5-30). Muscovite and feldspar grains are observed with microscopy within both samples, but are not detected by XRD. Sample AS14NJ057 has similar mineralogy to the erosional horizons. This sample, however, is considered a vein in the fossil cave. Sample AS14NJ098 is selected to determine the mineralogy of its white cements, which have needle-like crystals. The analysis of this sample is on bulk, so both the travertine and the cements are included. The amount of calcite (70.14%) and aragonite (30.86%), in combination with petrographical observations, suggest that the cements are dominantly aragonitic and the matrix is mainly calcite (Figure 5-30). These results of the XRD-analysis are not representative for the entire travertine deposit as the veins only comprise 0.5% of the travertine system.

### 5.4.2. Stable oxygen and carbon isotopes

Forty samples have been analysed for oxygen and carbon isotopes (Figure 5-31; Appendix 4). The analysis has been done while assuming all samples are calcitic. XRD-results proved that vein and cement samples are aragonitic. This mineralogical difference is important as the analysis and its calculations depend on the fractionation between the acids and the carbonate, which is different for aragonite and calcite. This effect is however recalculated. Notice also that not all of the analysed samples are taken from the San Pietro quarry. One sample comes from another small nearby quarry, which had a vein with  $\delta^{18}\text{O} = -8.57\text{‰}$  and  $\delta^{13}\text{C} = 7.82\text{‰}$ . Another sample comes from veins in the calcareous marly substrate rock as these veins could possibly be linked to the travertine system. This sample displays values for  $\delta^{18}\text{O} = -2.44\text{‰}$  and  $\delta^{13}\text{C} = -0.02\text{‰}$ , which are close to a marine carbonate signature. The samples of San Pietro quarry are linked to the bodies in which they were situated (Figure 5-24; Section 5.3 and in Appendix 2). The layered travertine, samples of erosional horizons excluded, has an average  $\delta^{18}\text{O}$  value of  $-10.95\text{‰}$  with minimal and maximal values of  $-12.27\text{‰}$  and  $-9.26\text{‰}$ , respectively and  $\delta^{13}\text{C} = 8.48\text{‰}$  with minimum of  $7.75\text{‰}$  and maximum of  $11.01\text{‰}$ . When the erosional horizons are included in the layered travertine, the average values change to  $-10.89\text{‰}$  for  $\delta^{18}\text{O}$  and  $8.18\text{‰}$  for  $\delta^{13}\text{C}$  and the minimum value of  $\delta^{13}\text{C}$  decreases to  $2.68\text{‰}$ . No actual evolution is present between the signatures of the different bodies. The samples of the different bodies plot within one group (Figure 5-31). The interbody variation is smaller than the intrabody variation. The interbody difference is mainly seen in variation of  $\delta^{18}\text{O}$ , thus is probably related to the temperature. The samples of the sixth depositional body have a slightly deviating signature of  $\delta^{18}\text{O}$  between  $-10.71\text{‰}$  and  $-9.26\text{‰}$  and  $\delta^{13}\text{C}$  between  $9.31\text{‰}$  and  $11.01\text{‰}$  which is higher than the other 5 bodies. This is related to the slope of approximately  $60^\circ$ , compared  $10$  to  $30^\circ$  for the other bodies. The banded travertine (veins) have an average  $\delta^{18}\text{O}$  of  $-11.90\text{‰}$  and  $7.79\text{‰}$  for  $\delta^{13}\text{C}$ . Four samples are selectively chosen to represent diagenetic phases, which are present as cements in samples or as separate crystalline horizons within the deposits. Three of the samples are aragonitic and form two separate sets of data (Figure 5-31). The first consists of two samples and has an average signature of  $\delta^{18}\text{O} = -12.20\text{‰}$  and  $\delta^{13}\text{C} = 6.61\text{‰}$ . The third sample has a signature of  $\delta^{18}\text{O} = -11.34\text{‰}$  and  $\delta^{13}\text{C} = 7.17\text{‰}$ . The final cement sample has a calcite mineralogy and has a signature of  $\delta^{18}\text{O} = -11.34\text{‰}$  and  $\delta^{13}\text{C} = 7.17\text{‰}$ , which is the same as the aragonitic sample of the second set. Samples of the fossil cave fill are included in the stable isotope analysis. The signature of the veins have an average signature of  $-7.56\text{‰}$  for  $\delta^{18}\text{O}$  and  $14.01\text{‰}$  for  $\delta^{13}\text{C}$ , which is an exceptionally high value. The travertine inside the fossil cave has a signature similar to the rest of the travertine body with average  $\delta^{18}\text{O} = -10.99\text{‰}$  and  $\delta^{13}\text{C} = 8.77\text{‰}$ .

The correlation coefficient of the  $\delta^{18}\text{O}$ - $\delta^{13}\text{C}$  results is 0.35 for the 23 samples of the layered travertine without the sample of the erosional horizon with lower  $\delta^{13}\text{C}$  (AS14NJ004). The coefficient is 0.46 when the diagenetic cements and the vein travertine are added, resulting in 32 samples.

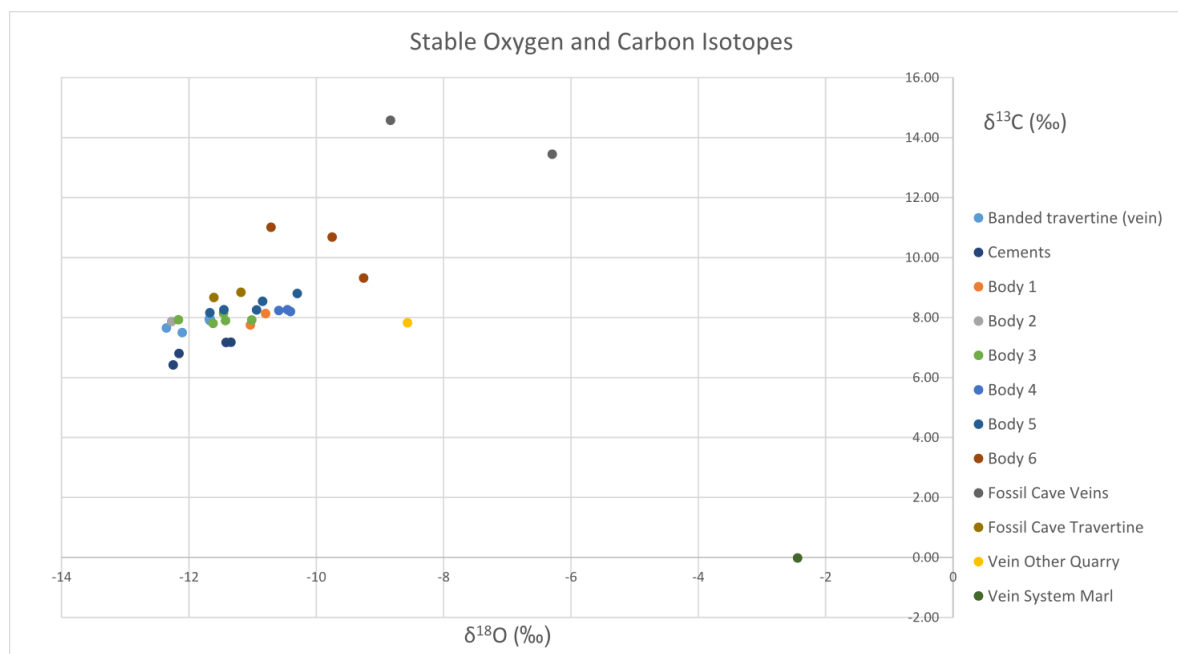


Figure 5-31: Results of stable oxygen and carbon isotopes. The samples of the layered travertines are separated into six separate bodies, which indicate the evolution through time.

### 5.4.3. Stable strontium isotopes

The strontium isotopes have been analysed for 7 sample of the travertine body, of which one sample comes from the banded travertine. The other two samples are taken from potential host rock carbonates, of which one is from marly limestone, outcropping at the Tronto river (Acquasanta Group; Miocene). All the data of the travertine body varies between 0.70790 and 0.70795, with an average of 0.70791. The variation of 0.0005 is small enough to assume that all the deposits are from the same fluid source and no variation in fluid origin was present throughout deposition. The full dataset, with standard errors is given in Appendix 4.

The marly limestone of the Acquasanta Group (Miocene) has a  $^{87}\text{Sr}/^{86}\text{Sr}$ -ratio of 0.70838. This value is significantly higher than the values of the travertine. The veins in the Miocene marl (Acquasanta group) have a  $^{87}\text{Sr}/^{86}\text{Sr}$ -ratio of 0.70862. These veins are thus not related to the formation of the travertine body and rather record the composition of the marl host rock in which they occur.

### 5.4.4. ICP-OES

The ICP-OES results are given in Appendix 4. The samples for the analysis are chosen to infer whether differences between different lithotypes exists. The samples come from erosional horizons, aragonitic vein travertine, layered travertine and the fossil cave fill in which both veins and layered travertine are sampled. The different lithotypes of the layered travertine cannot be differentiated, based on their geochemical composition. The other groups that have been sampled can be differentiated from the

layered travertine. Erosional horizons (AS14NJ004, AS14NJ006, AS14NJ042 and AS14NJ043) are enriched in Al, Ba, Fe, K, Mg, Mn, Na, P and Ti compared to the other samples, related to a higher non-carbonate content. The vein samples that cross-cut the layered travertine (AS14NJ001, AS14NJ002 and AS14NJ019) are significantly enriched in Sr and depleted in Fe, Mg and S compared to the average signature in the travertine body. Here the aragonitic composition can explain these differences. These veins have slightly elevated values for Al, Ba and P in comparison to the layered travertine. Vein samples of the fossil cave (AS14NJ044 and AS14NJ057) are enriched in S and Na, like the erosional horizons. The porous travertine in the fossil cave has a signature similar to the layered travertine of the quarry.

A statistical analysis in R has been performed. The different samples got different numbers during this analysis, which are used in figures (Table 5-1). The analysis in R is used to check if the different types of travertine can be recognized by cluster analysis and to investigate which elements define the difference(s). The elemental composition provides information on the mineralogy and possibly environmental parameters.

*Table 5-1: Link of the number (N°), used in the figures and the sample number. The type of travertine is indicated with each sample number.*

N°	SAMPLE	TYPE	N°	SAMPLE	TYPE	N°	SAMPLE	TYPE
1	AS14NJ001	Vein	7	AS14NJ029	Layered	13	AS14NJ044	Karst Vein
2	AS14NJ002	Vein	8	AS14NJ030	Layered	14	AS14NJ052	Filled Karst
3	AS14NJ004	Erosional	9	AS14NJ031	Layered	15	AS14NJ057	Karst Vein
4	AS14NJ006	Erosional	10	AS14NJ042	Erosional	16	AS14NJ063	Layered
5	AS14NJ019	Vein	11	AS14NJ043	Erosional	17	AS14NJ072	Layered
6	AS14NJ022	Layered	12	AS14NJ045	Filled karst	18	AS14NJ079	Layered

In first instance, a bivariate analysis with untransformed data is done to discern clusters based on a few elements. The data can be visually grouped into three groups (Figure 5-32). Both the erosional horizons and the aragonitic veins can be distinguished from the geochemical data. The layered travertine and the samples of the fossil cave fill often group together, but the bivariate analysis produced clusters that are not solid. The vein travertine is mainly recognized by its higher Sr-value. The erosional horizons are also discerned from the rest of the group. A matrix of all possible bivariate plots (with CLR-transformed data) is given in Appendix 4. Visual clustering of the data in plots of this matrix also produces inconsistent groups. In the further analysis, multivariate analysis is performed to provide more meaningful clusters of data.



The data of the ICP-OES measurements does not have a normal distribution, so transformation of the data is required for meaningful statistics. Transformation is also required because compositional data is used, which is interdependent. Transformation is done both taking a logarithm of 10 and a centred log-function. CLR-transformation provides the most normally distributed data and is therefore used in the statistical analyses.

The data will be grouped into clusters by cluster-analysis. The clustering of the data is tested by different types of clustering (hierarchical, representative-based, fuzzy-clustering; Appendix 4). Five different types of travertine were analysed. A function in R, NbClust analyses what amount of cluster will give the most reliable clusters. For an amount of three clusters, the results are the most solid. The three main groups of the samples are recognised by the cluster analysis. More or less similar groups were discerned in the bivariate analysis, but those groups were inconsistent. The cave travertine is clustered together with the layered travertine, as was done in the bivariate analysis, with the exception of one sample, AS14NJ054. The clusters are presented in Table 5-2.

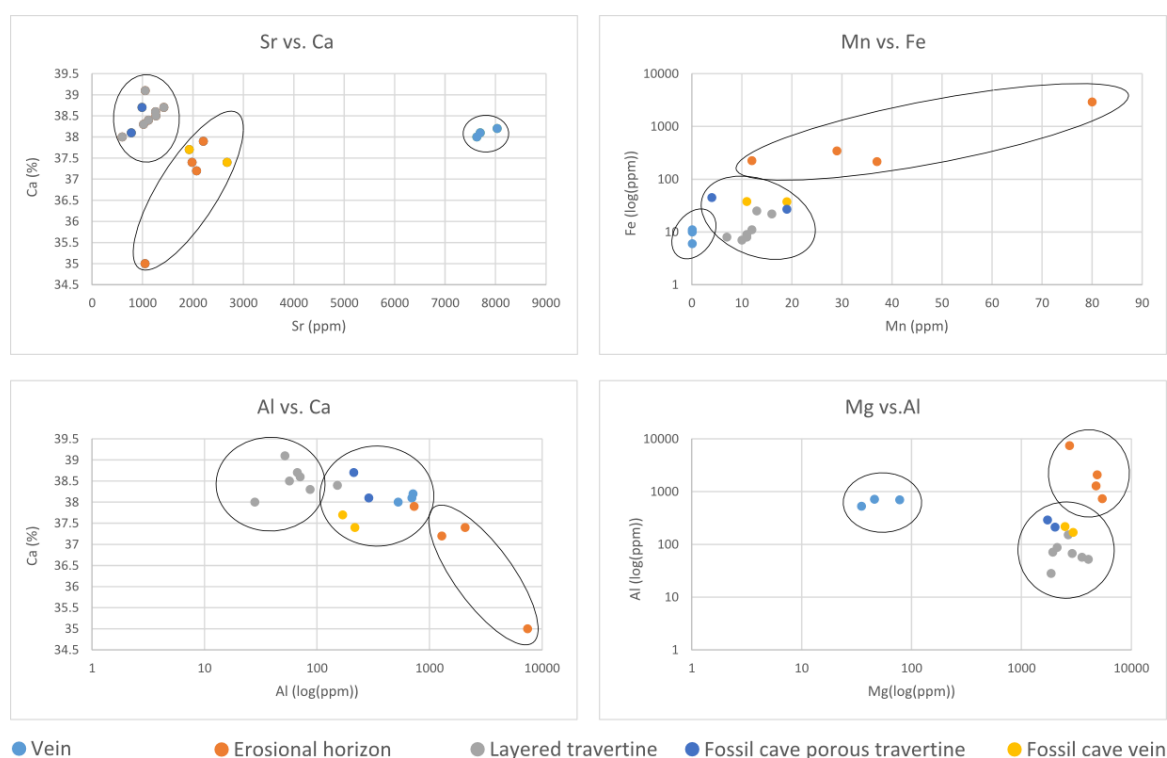


Figure 5-32: Bivariate analysis on four examples of scatterplots. In most instances three groups are discerned. These groups are not the same, but the erosional horizons commonly do cluster together. The data is not transformed apart from the logarithmic plotting in the graphs.

Table 5-2: Results of representative based clustering to three clusters. The travertine types that had been defined before are indicated with abbreviations (V: Vein, E: Erosional horizon, L: Layered travertine, FCP: Porous travertine of the fossil cave, FCV: Veins of the fossil cave). The clusters more or less represent the give types.

SAMPLE	TYPE	CLUST	SAMPLE	TYPE	CLUST	SAMPLE	TYPE	CLUST
AS14NJ001	V	1	AS14NJ029	L	3	AS14NJ044	FCV	3
AS14NJ002	V	1	AS14NJ030	L	3	AS14NJ052	FCP	2
AS14NJ004	E	2	AS14NJ031	L	3	AS14NJ057	FCV	3
AS14NJ006	E	2	AS14NJ042	E	2	AS14NJ063	L	3
AS14NJ019	V	1	AS14NJ043	E	2	AS14NJ072	L	3
AS14NJ022	L	3	AS14NJ045	FCP	3	AS14NJ079	L	3

Correlation between elements is tested by hierarchical clustering of CLR-transformed data (Figure 32) and by correlation matrices (Appendix 4). Mg, S and Sr are elements that vary together and are elements related to the carbonate phase and K, Al and Na, which are linked to clay content, vary together as well. The Pearson correlation coefficients indicate which elements correlate the most. The correlation is tested on all data together. The highest positive correlations are seen for Mn and Mg ( $r_{\text{Mg-Mn}} = 0.90$ ), Sr and P ( $r_{\text{Sr-P}} = 0.81$ ) and Sr and Na ( $r_{\text{Sr-Na}} = 0.72$ ). The highest negative correlations are: Mn and P ( $r_{\text{Mn-P}} = -0.88$ ), Mg and Al ( $r_{\text{Mg-Al}} = -0.86$ ) and Na and Mn ( $r_{\text{Na-Mn}} = -0.84$ ).

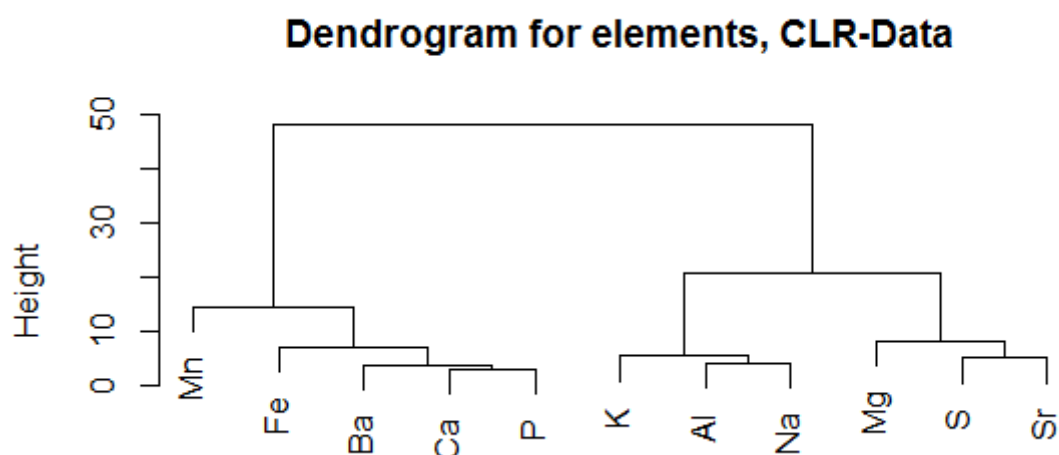


Figure 5-33: Dendrogram of an inverted dataset to cluster elements. Dendrogram is generated from CLR-transformed data.

Variation between the clusters is governed by several elements, which is seen from a Principle Component Analysis (Figure 5-34). The most important variation between the clusters is given by the first component (Comp. 1; explains 64.9 % of variance) and the second component explains an additional 26.4 % of the variance. The PCA-analysis shows which elements are responsible for the different clusters. The first cluster is mainly based on elevated Sr and Al and low Mg and Mn contents

(Figure 5-34). This is related to the aragonitic mineralogy of these samples. The second group is mainly separating itself from the others by a high Fe (and K) and a low Ca content, which are elements, typically related to detrital material. The third group has no specific elements linked to them (Figure 5-34). The elements that are mentioned above for each group are not the only governing elements, but they are the most important in differentiating the different groups.

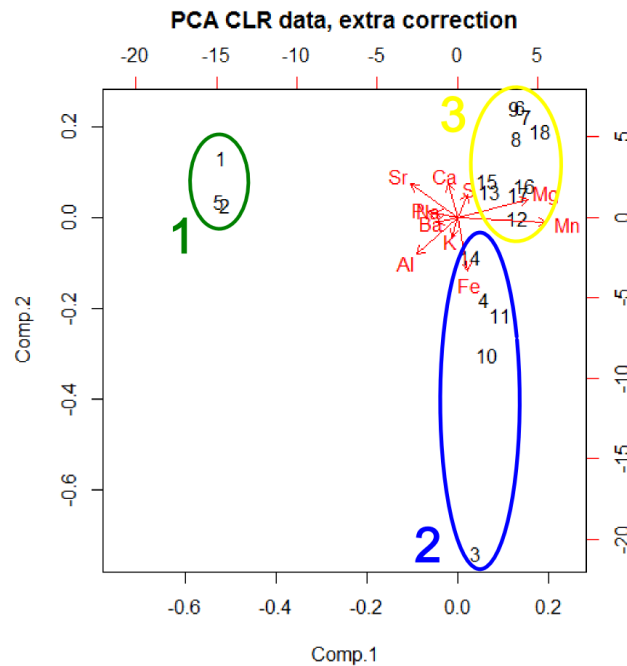


Figure 5-34: PCA analysis with CLR-transformed data. The groups of the representative-based, three cluster analysis are indicated with ellipses.

## 5.5. Fluid inclusions

### 5.5.1. Petrography

Six wafers have been prepared and analysed, but only two wafers contain sufficiently large inclusions for microthermometric analysis. The studied wafers (AS14NJ001 and AS14NJ019) contain both crystals and fluid inclusions that are sufficiently large. These samples are both from banded travertine veins in the upper part of the quarry. The other wafers are either too micritic (AS14NJ029) or contain crystals that are needle-like (AS14NJ016, AS14NJ044 and AS14NJ057). A basic petrographical analysis is done on wafers AS14NJ044 and AS14NJ057, as they both contain few very small monophase inclusions. Both samples are taken from brown layers in the veins. The Fluid Inclusion Assemblage (FIA)-method of Goldstein and Reynolds (1994) is applied during petrography but did not prove to be successful during the measurements as each FIA contained a maximum of only three fluid inclusions.

Fluid inclusions are sparse and often too small with sizes below  $3 \times 3 \mu\text{m}$ . Many inclusions are elongated and have a long and a short axis, of which the long axis is parallel to the growth direction. The short axis is often too small ( $< 3 \mu\text{m}$ ) to analyse the fluid inclusions.

A classification of the fluid inclusions is based on the characteristics of shape and the liquid-to-vapour-ratio of the inclusions (Figure 5-35). The fluid inclusion content is not incorporated in the classification as the different fluids are found in inclusions with similar shapes. There are both monophasic (liquid or vapour) and two-phase inclusions. All-liquid inclusions are recognized by a slightly pinkish colour which distinguishes them from the glue which is remaining after sample preparation. Two-phase inclusions are inclusions with a vapour bubble, in addition to liquid. The inclusions have a variable bubble size (Section 3.6.2). Inclusions without any liquid are recognised as dark grey to black inclusions and are not treated in this research. The content of the vapour phase is unknown and could either be a gas under pressure or a diffuse gas. The petrographical analysis is only done after cooling the samples at  $-18^\circ\text{C}$  for two weeks to overcome metastability in monophasic inclusions. No extra bubbles are generated during this cooling.

- Type I (monophasic): This inclusion type comprises long but thin ( $< 2$  to  $3 \mu\text{m}$ ) inclusions. The inclusions are usually situated between two separate crystals or along the crystal cleavage planes (Figure 5-35 A, B and D).
- Type II (monophasic): Triangular inclusions usually embedded along crystals. The triangles are isosceles triangles, but sometimes occur as almost equilateral triangles (Figure 5-35 C and D). Type II inclusions also include inclusions with a diamond or rhomb shape.
- Type III (monophasic): These inclusions have a random shape and are not belonging to the preceding two types of monophasic inclusions (Figure 5-35D).
- Type IV (two-phase): These inclusions have, like type II inclusions, a triangular to diamond or rhomb shape, but they are two-phase (Figure 5-35E).
- Type V (two-phase): This fluid inclusion type comprises inclusions that contain a “tail” or a microfracture at the boundary of the inclusion (Figure 5-35F). The inclusions can either have a random shape or be lenticular in shape. The lenticular shape is related to the microfracture.
- Type VI: These inclusions are dark grey (Figure 5-35A and B) and are empty or contain a vapour phase. These inclusions can have different shapes.

Wafers AS14NJ044 and AS14NJ057 are only analysed by petrography. They contain a few, small ( $< 3 \times 3 \mu\text{m}$ ) monophasic inclusions. These samples are not used for microthermometric analysis as the inclusions are too sparse and too small for stretching.

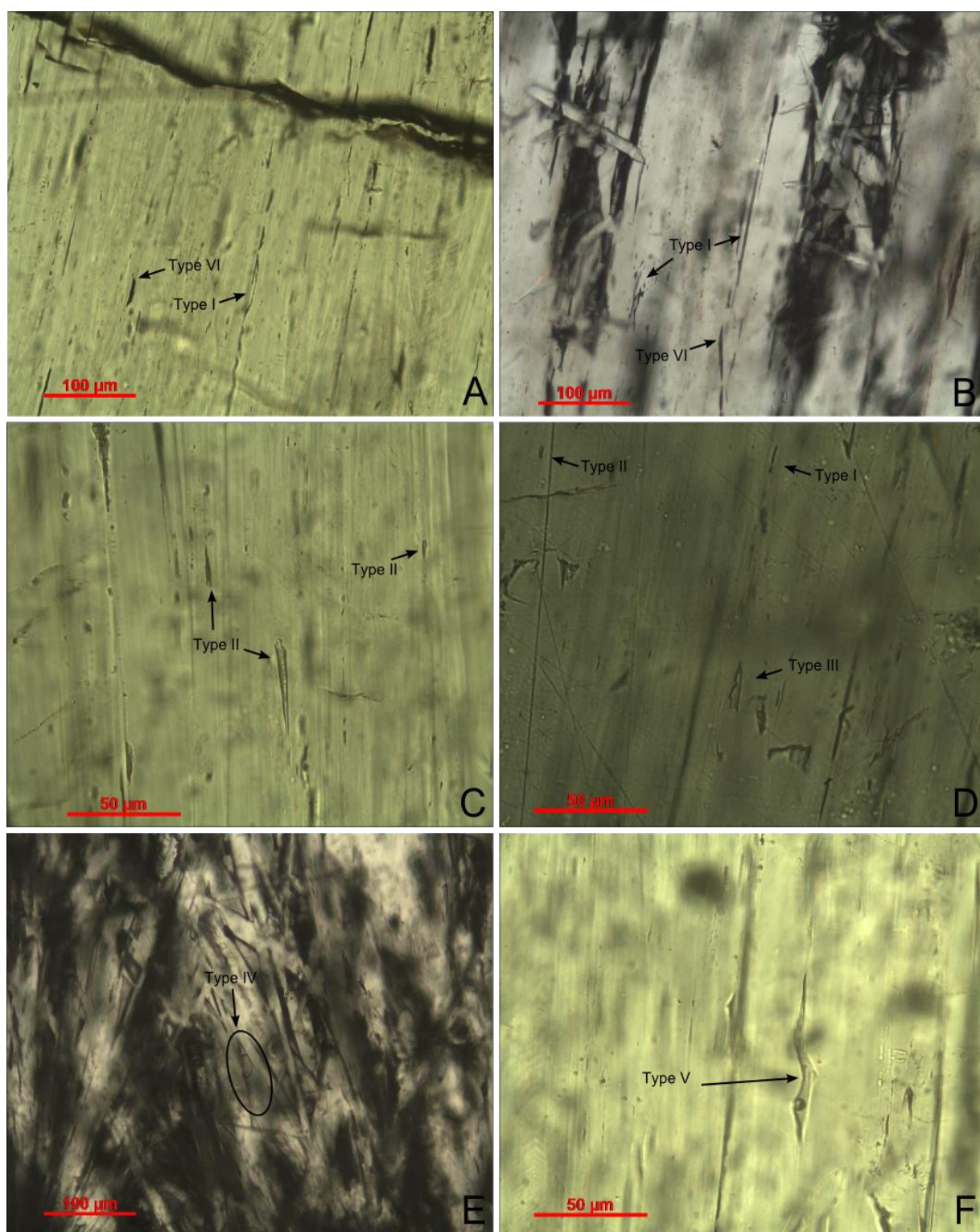


Figure 5-35: Fluid inclusion types. A & B. Type I inclusion are long and small, Type VI inclusion is empty or 100% vapour and is recognized by the black colour. C. Type II inclusions have a triangular shape and are monophasic. D. Type III inclusions are monophasic and have a shape that cannot be assigned to types I and II. E. Type IV are triangular two-phase inclusions. F. Type V inclusions show small fractures at their extremities and contain two phases. The shown inclusion is deformed.



All studied inclusions are primary and there is no evidence of the secondary generation of inclusions. The long axis of the fluid inclusions of the type I, II and IV inclusions is parallel to the long axis of the calcite crystals which argues in favour of a primary origin (Figure 5-35A to D; Goldstein & Reynolds, 1994; Verhaert et al., 2004). The other inclusion types (III and V) can also be considered of primary origin as primary fluid inclusions in calcite or aragonite can have any shape. The long axis is parallel to the crystal cleavage which is an additional argument for a primary origin of the inclusion (Figure 5-34 D and F; Goldstein & Reynolds 1994).

Several of the fluid inclusions are altered after deposition. Evidence for this is necking-down of the inclusions (Figure 5-36 B) or the deformation of the fluid inclusion (Figure 5-35F). Deformation is also seen on the scale of the crystals by small en-echelon fractures (Figure 5-36A). Deformation of easily deformable aragonite crystals could influence the fluid inclusions by generating microfractures near the inclusions (Kerrich, 1976; Roedder, 1984). The fractures have not healed in the present samples and are still present at the rim of the fluid inclusions (e.g. type V fluid inclusions; Figure 5-35F). The existence of a microfracture is an indication that the fluid inclusions possibly leaked (Goldstein & Reynolds, 1994; Kerrich, 1976; Roedder, 1984). This is further discussed in section 6.

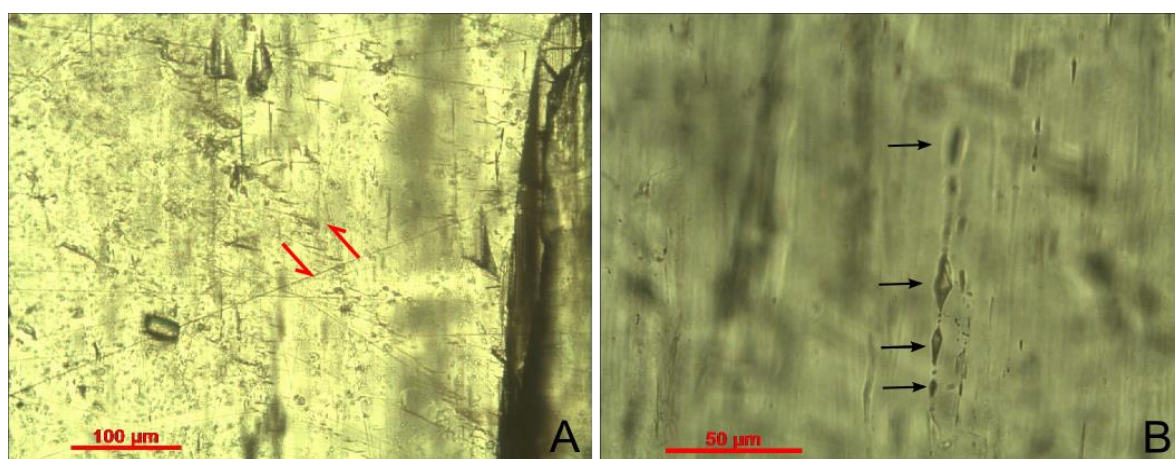


Figure 5-36: A. Deformation structures in the crystals. These small fractures indicate en echelon fracturing with the indicated directions of deformation. B. Necking down of an inclusion.

### 5.5.2. Microthermometry data

Each wafer is broken into smaller chips (5 x 5 mm) for the microthermometric analysis. During the petrographical analysis, chips are selected based on their suitability for microthermometry or not, which is determined on the presence of sufficient two-phase inclusions (> 1 per chip). Chips that contain too much micrite or those that contain small crystals are discarded. Identification of the fluid inclusions is done in the microthermometry chamber. Both samples (AS14NJ001 and AS14NJ019) are from similar vein bands. As FIA's do not yield additional information, the fluid inclusions are studied as if they are from one cement generation. Homogenization temperatures are measured before freezing to avoid the

influence of stretching on homogenization temperatures. Calibration of the microthermometry instrument is done by the analysis of four different fluid inclusion standards. Fitting a plot of the measured melting temperatures versus the theoretical melting temperatures gives following calibration formula:

$$T_{real}(^{\circ}C) = 0.9742 * T_{measured}(^{\circ}C) + 0.1596$$

The actual calibration curve and data are given in Appendix 4. A total of 50 fluid inclusions have been analysed (data in Appendix 4) but not each inclusion has data for first- and/or final melt ( $T_{fm}$  and  $T_m$ , respectively). The final melt was measured in 25 inclusions, the first melt was measured in another 23 inclusions of which 18 correspond to the same inclusions as for  $T_m$ .

The final melting temperature data is distributed into two groups (Figure 5-37). One group has final melting temperatures close to 0 °C whereas the other group has a final melting temperature of ice at around -29.5 °C (Figure 5-37). This indicates the presence of two different fluids in the inclusions.  $T_{fm}$  data are close to the  $T_m$  for most of the inclusions. Fluids with the  $T_m$  close to 0 °C have a  $T_{fm}$  between -0.4 and -0.7 °C, which indicates that the fluids are almost pure H<sub>2</sub>O. The  $T_{fm}$  for the inclusion with a  $T_m$  of approximately -29.5°C is for most inclusions varying between -29.9 °C and -31.9 °C. One of these inclusions was sufficiently large for more detailed measurements and had a  $T_{fm}$  of -48.9 °C, a final melt of hydrohalite ( $T_{m,HH}$ ) at -30.5 °C and the final melt of ice at -29.3°C. This inclusion is the only inclusion in which  $T_{m,HH}$  could be accurately measured. The  $T_{fm}$  is lower compared to the other inclusions and implies that the actual first melt was not recorded for the other inclusions. The measured  $T_{fm}$  could have been the  $T_{m,HH}$  for these inclusions, but this is uncertain. The first type of fluids is

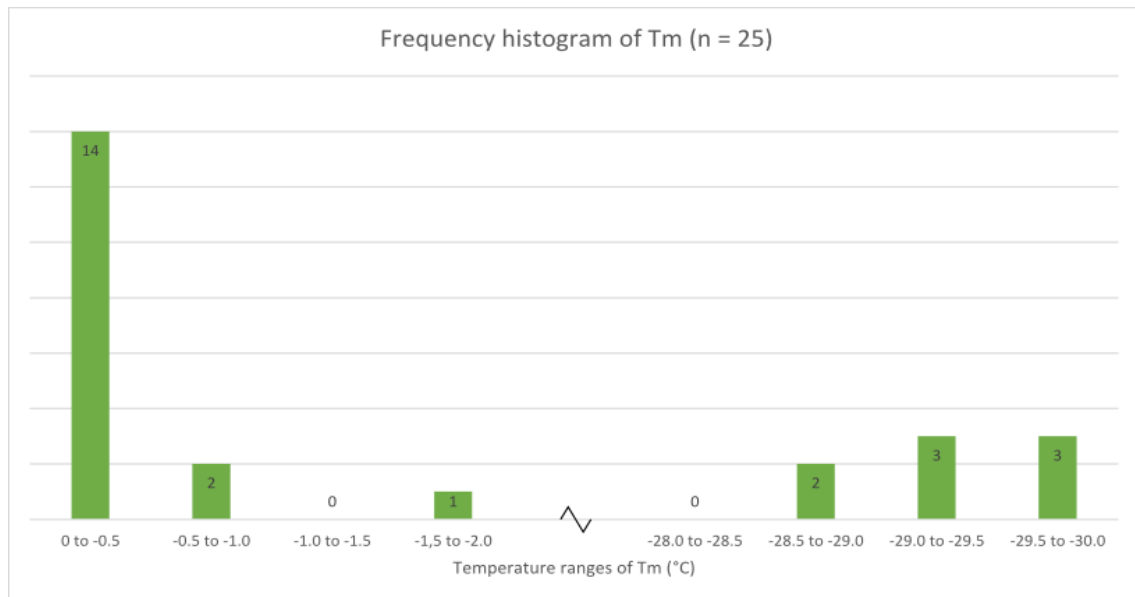


Figure 5-37: Frequency histogram of the final melting temperatures. Two groups of temperatures are noted. The first group has final melting temperatures close to 0°C whereas the second group is close to -29.5°C.

meteoric to slightly saline with a  $T_m$  close to  $0^\circ\text{C}$ . The other type has a low melting temperature and is highly saline.

Homogenization temperatures have been measured for 19 fluid inclusions but only two inclusions homogenized below  $110^\circ\text{C}$ . During the heating run, no change in the size of the bubble size is noted for the inclusions that did not homogenize. Two inclusions homogenized to all-liquid inclusions at  $61^\circ\text{C}$  and  $65^\circ\text{C}$ . Both inclusions contain saline fluids.

During petrography, a variable bubble size is noted. An estimate of the percentage of the fluid inclusion occupied by vapour is noted for 40 of the analysed two-phase inclusions (Figure 5-38). Vapour content ranges between 5 and 80% but most inclusions have a vapour content close to 20%. The entirely gaseous inclusions are not incorporated.

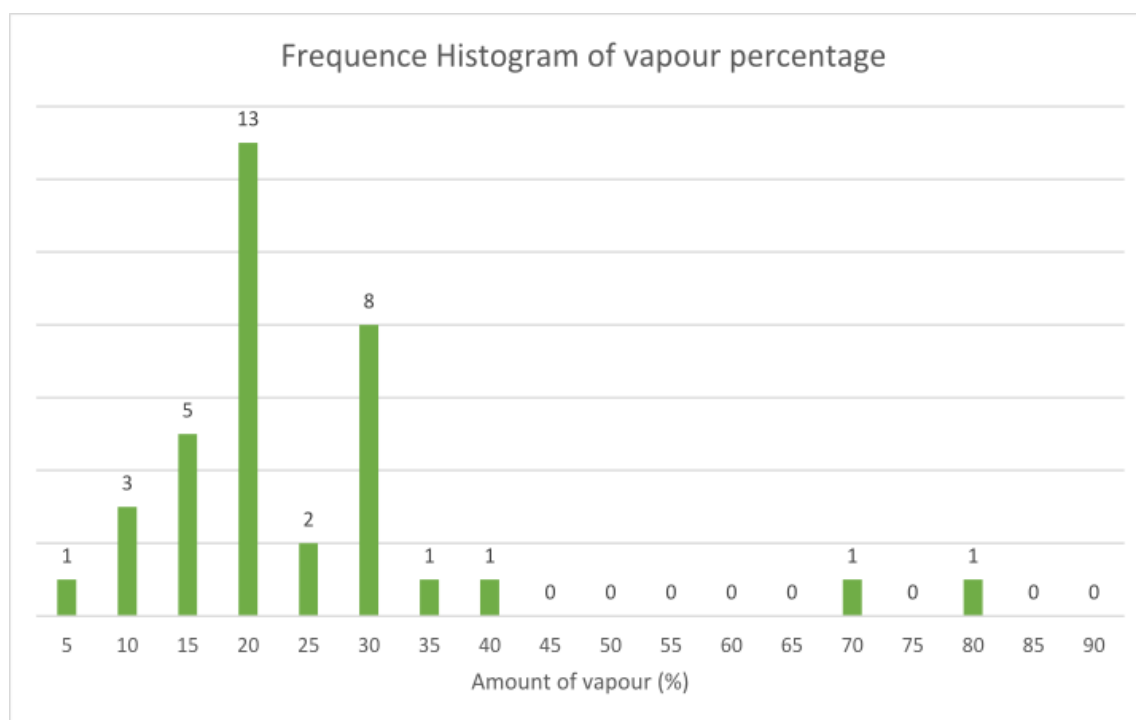


Figure 5-38: Vapour content in measured fluid inclusions in percentages. Variable vapour content is observed, but most of the inclusions have a bubble that makes up 15 to 30% of the inclusion.

### 5.5.3. Salinity of fluids

The microthermometric analysis indicates the presence of two types of fluids of which one had a first and final melt close to  $0^\circ\text{C}$  and the other has a  $T_{fm}$  of  $-48.9^\circ\text{C}$  and a  $T_m$  close to  $-29.5^\circ\text{C}$ . A  $T_{fm}$  below  $0^\circ\text{C}$  and a  $T_m$  close to  $0^\circ\text{C}$  indicates fluids that are almost pure  $\text{H}_2\text{O}$  (Roedder, 1984). The fluid composition can be approached by a  $\text{H}_2\text{O}$ - $\text{NaCl}$  model composition (Goldstein & Reynolds, 1994) of which the salinity can be determined, based on the formula by Bodnar (1993):

$$\text{Salinity (wt\%)} = 0.00 + 1.78\theta - 0.0442\theta^2 + 0.000557\theta^3$$

- $\Theta$  = depression below 0.0°C, this is expressed in absolute values.

Salinities of the fluids with  $T_m$  varying between 0.0°C and -0.5°C (and -1.6°C for one inclusion) is between 0 and 0.88 eq. wt% NaCl (up to 2.74 eq. wt% NaCl when the -1.6°C value is taken into account).

The second type of fluid is marked by low melting temperatures, indicating the presence of divalent cations. Goldstein and Reynolds (1994) suggest to approach aqueous fluid inclusions with a  $T_{fm}$  below -40°C by H<sub>2</sub>O-NaCl-CaCl<sub>2</sub> fluid composition. A first melt of -48.9°C fits this recommendation. As carbonates precipitated from the fluids Ca<sup>2+</sup> is most likely an important cation in the fluid system. Salinity and the NaCl/(NaCl+CaCl<sub>2</sub>)-ratio can be approached by graphical plotting the data on a ternary diagram (Figure 5-39). Determination of the NaCl/(NaCl+CaCl<sub>2</sub>)-ratio requires data for  $T_{m,HH}$ , which is only measured in one inclusion. With  $T_{m,HH}$  at -30.5°C and  $T_{m,ice}$  varying between -29.7 and -28.8°C, salinity varies between 26.0 and 25.5 wt% salinity, with a NaCl/(NaCl+CaCl<sub>2</sub>)-ratio of 0.38, calculated from the graph given by Goldstein and Reynolds (1994 and references therein). The diagram given in Shepherd et al. (1985 and references therein) results in slightly different data, with a salinity of approximately 26.5 wt%, distributed as 20 wt% CaCl<sub>2</sub> and 6.5 wt% NaCl, giving a NaCl/(NaCl+CaCl<sub>2</sub>)-ratio of 0.25. Both the diagrams give approximately the same results for salinity but different results for the NaCl/(NaCl+CaCl<sub>2</sub>)-ratio.

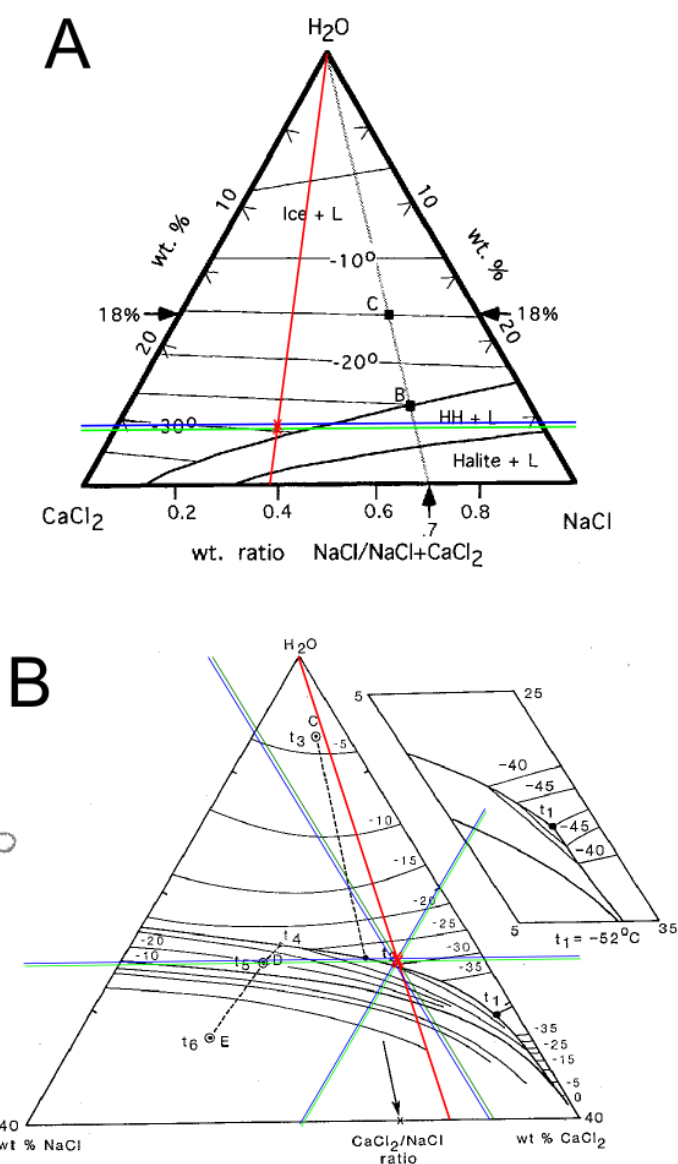


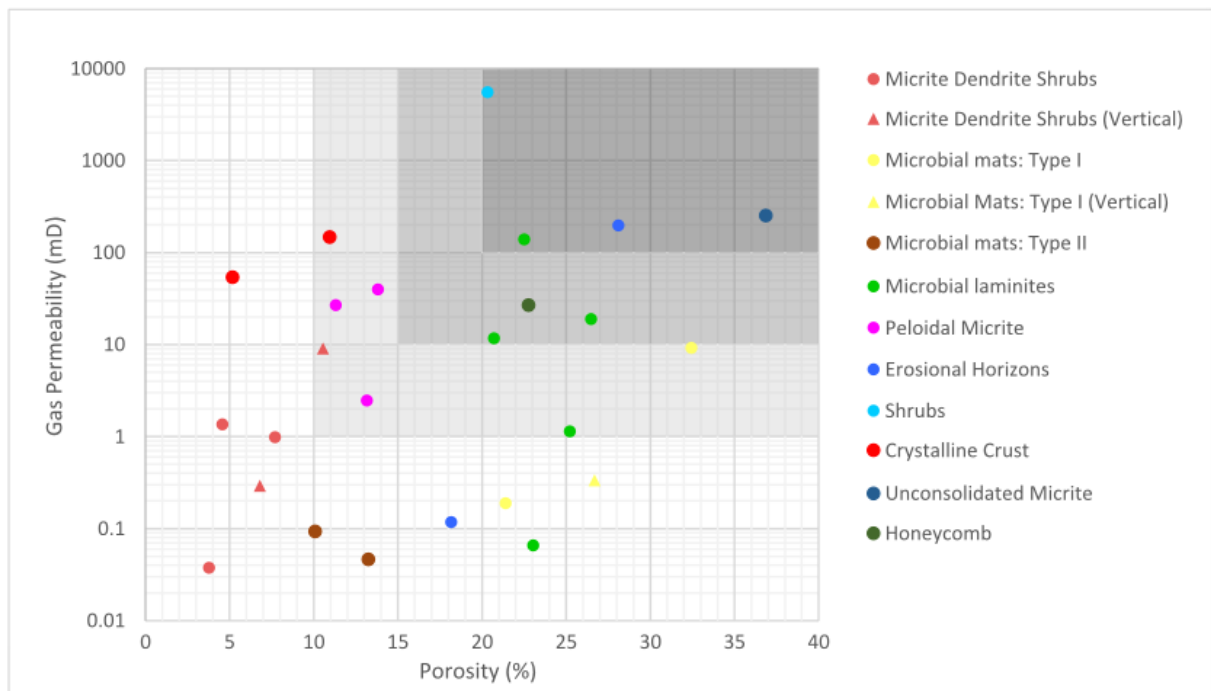
Figure 5-39: Graphical determination of the salinity of  $\text{H}_2\text{O}$ - $\text{NaCl}$ - $\text{CaCl}_2$  inclusions. The red lines connect the apex of the triangle (at  $\text{H}_2\text{O}$ ) with the  $T_{m, \text{HH}}$ . The  $T_m$  is indicated on this line with a red cross. The green lines indicated the lower temperature of  $-29.7^\circ\text{C}$ , whereas the blue lines indicate the  $T_m$  of  $-28.8^\circ\text{C}$ . Both the green and the blue lines show almost the same salinities. A. The diagram given in Goldstein and Reynolds (1994). B. The diagram given in Shepherd et al. (1985) with data from Borisenko (1977).



## Chapter 6: Discussion

### 6.1. Three-dimensional reservoir model

A three-dimensional reservoir model is constructed from field data, petrophysical data and petrographical descriptions. The petrophysical data is linked to the classification of Levorsen (1954) for reservoirs (Figure 6-1), which ranks the reservoir quality from fair to very good. This is an old classification, but it is nonetheless applied to the data as it provides a simple framework to assess reservoir quality. The actual permeability and porosity values of reservoirs that are exploited are probably lower due to increase in technology and the values will vary along with the oil price. The 3D-model, which is based on lithotype variation, is adjusted to indicate reservoir qualities. A reservoir



Reservoir quality	Porosity (%)	Permeability (mD)
Very good	25 - 20	1000 - 100
Good	20 - 15	100 - 10
Fair	15 - 10	10 - 1
Less suitable	< 10	< 1

Figure 6-1: Categories of reservoir qualities according to Levorsen (1954). The ranges of porosity and permeability are indicated on the petrophysical data. In this respect, the different lithotypes are linked to their respective reservoir quality.

quality was assigned to each lithotype based on its average petrophysical values (Figure 6-2). The adaptation of the model provides 3D insight in the reservoir quality.

The shrubs and unconsolidated micrite are considered very good reservoir rocks. Both these lithotypes are marked by large interpeloidal and vuggy porosity and only have minor extra cementation. Their distribution is limited to only 0.21 % of the total quarry wall surfaces (Appendix 4). They do not significantly contribute to the total reservoir quality. The microbial laminites are the only lithotype that would make a good quality reservoir and comprises 5.42 % of the total exposed quarry surfaces. The good quality of this lithotype is linked to large framework porosity and good interconnectivity. Not all samples of the microbial laminites have good reservoir qualities, which indicates a lot of variation, even within one lithotype. Field observations show the presence of large moulds of reed in this lithotype, which is not present in the plugs. The reed moulds are often cemented, indicating they were preferential fluid pathways. The total porosity and permeability of this lithotype can be higher than deduced from plug petrophysical data alone because the large reed moulds are missed in the samples. The Representative Elementary Volume is not reached during sampling, causing extra variability. Fair reservoir quality is seen for peloidal micrite and the erosional horizons, which are both widely distributed and add up to 20.61 % of the total exposed surface. The peloidal micrite is marked by interpeloidal porosity and microporosity. Even though the porosity of this lithotype is not considered high, the samples are sufficiently permeable to achieve fair reservoir quality. The erosional horizons are considered fair reservoir quality as the two samples that have been analysed are spread between very good and non-reservoir quality. Due to this spread and the low amount of samples, the fair reservoir quality is a generalization based on the average values. The large differences between the samples of erosional horizons are linked to the amount of dissolution and cementation. The sample of very good quality contains reworked micrite with large vuggy porosity and cementation is limited. The other sample contains small, cemented vugs and its porosity is mainly microporosity, which explains the rather low permeability. More samples of erosional horizons should be sampled for more reliable results that assess the variability. Petrophysical understanding of this lithotype is important as one horizon can span large distances and connect several other lithotypes. In a hydrocarbon reservoir, such a layer could be, if it contains sufficiently high reservoir quality, a preferential path for hydrocarbon migration. The preceding approach indicates that 73.77 % of the travertine deposit is characterised by less suitable reservoir quality. For some of these lithotypes the reservoir quality is underestimated because average values of the petrophysical data are used. These lithotypes contain some samples that actually plot within the three reservoir quality categories, but that are not represented individually because of the generalisation approach that was followed.

It is suggested that a petrophysical analysis should either be performed on more samples to assess the spread in the data within each lithotype or that it should be performed on core samples (i.e. 4 inch).

Larger samples would smoothen out the small scale variability, which complicates the petrophysical interpretation of plugs measurements. The data could also be better interpreted with Computerized Tomography (CT), which allows to investigate the relation between porosity and pore types.

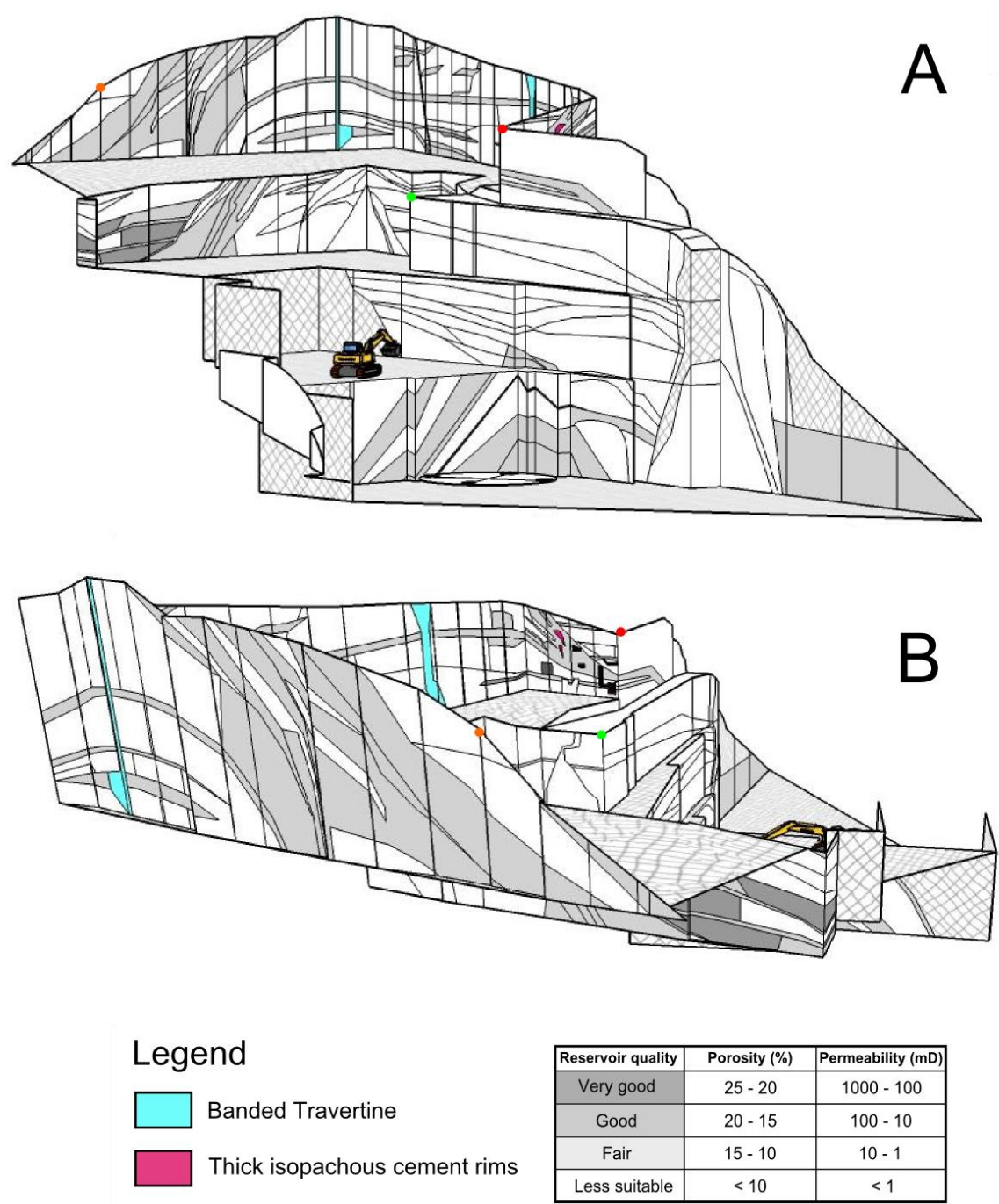


Figure 6-2: Reservoir model with the grey scales linked to the classification of Levorsen (1954). The main fraction of the travertine body consists of non-reservoir quality material. Cave porosity is indicated in black.

The difference between vertical and horizontal permeability has been assessed by analysing three plugs sampled perpendicular to the layering. This approach did not produce significantly different results from the horizontal measurements, apart from those of the micritic dendrite crust, in which both a vertical and

horizontal plug is taken from the same sample. The permeability is 10 times higher for the vertical plug. This implies that cross-layer flow in a possible reservoir is more likely than along-layer flow for the micritic dendrite crusts. The higher permeability is explained by the large pores, in between and parallel to the dendrites in the lithotype.

Fractures are cutting through the entire travertine body (Appendix 4 and 6-3). Open fractures would provide permeable pathways in a possible hydrocarbon reservoir. Fracture porosity connects the more permeable lithotypes to each other, across the non-reservoir rocks which have a minor contribution to the reservoir. The analysed fractures are almost vertical and most are parallel to each other. A structural study of the quarry indicated the presence of “staircase fractures” which are related to gravitational sliding (Maggi et al., 2015). Such fractures can briefly become layer-parallel along the boundary of different lithotypes, before crosscutting them. The staircase fractures have not been studied in this research. A similar process of gravitational sliding is proposed for the analysed fractures, based on the observation that they are perpendicular to the slope of the layers, thus also the paleo-slope. Fractures are also important as they provide pathways for fluids that dissolve the travertine. Cave porosity is sometimes generated along fractures.

Pores that are larger than those on sample and thin section scale are not quantitatively studied. The pores are certainly present, which is evident from vug and cave porosity. Additional point-counting analyses on quarry walls could provide a way to assess this porosity types. Cave porosity is indicated in the 3D-reservoir analogue (Figure 6-2).

The banded travertine vein observed in the upper level (Figure 6-2) forms an entirely impermeable horizon. The vein separates the travertine body in two separated hydrological systems. This compartmentalisation has to be taken into account when drilling complex travertine hydrocarbon reservoirs.

If this travertine body would be a hydrocarbon reservoir in the subsurface, the best approach to exploit it would be through horizontal drilling to allow for exploitation through the impermeable barrier (banded travertine). The fractures would be major pathways to connect the permeable lithotypes. Since most fractures are more or less parallel, it is beneficial to do the horizontal drilling perpendicular to the fault direction (i.e. perpendicular to paleoslopes). This approach is only applicable for deposits on slopes as the fractures have a gravitational origin.

Projecting this travertine body into the subsurface reservoir environment, it can be expected that during dissolution or decarbonation of limestones, extra porosity is generated. These limestones could provide additional targets for oil exploration.

## 6.2. Fluid characterization

Characterization of the fluids involved in travertine precipitation is based on the study of stable isotopes ( $\delta^{18}\text{O}$ ,  $\delta^{13}\text{C}$  and  $^{87}\text{Sr}/^{86}\text{Sr}$ ), cathodoluminescence and fluid inclusion analysis. The first step in the analysis of the precipitating fluids is the characterization of the fluids that emerged at the spring orifice. The next section characterizes the further evolution of the fluids after emergence from the spring. The final part of the fluid characterization treats the diagenetic fluids involved in cement precipitation.

### 6.2.1. Spring water

The fluids that emerge at the spring are trapped inside the aragonite crystals of the banded travertine. Analysis of primary fluid inclusions indicates the presence of two different fluids in the conduit during crystal precipitation. One has a high salinity with values between 25.5 and 26.5 wt% with a  $\text{NaCl}/(\text{NaCl}+\text{CaCl}_2)$ -ratio of 0.25 or 0.38, depending on the method used to unravel the ratio. The other fluid has a low salinity varying between 0.0 and 0.88 eq. wt% NaCl, with one inclusion at 2.74 eq. wt% NaCl. The bulk isotopic composition of these samples is -12.05 ‰ for  $\delta^{18}\text{O}$  and 7.70 ‰ for  $\delta^{13}\text{C}$ .

The fluid inclusions that have been analysed are two-phase inclusions and a few artificially stretched mono-phase inclusions. A downside of the analysis is that no distinction between two phase and stretched monophase inclusions was made in the results. Uncertainty remains concerning the origin of the vapour bubble in the two-phase inclusions as variable vapour-to-liquid ratios are noted and no homogenization is achieved for most inclusions. Bubbles can be generated through several mechanisms: trapping of the inclusion with subsequent separation in two phases (liquid and vapour) upon cooling and depressurization, heterogeneous trapping at high- or low temperatures and post-depositional generation of a bubble by leakage (Goldstein & Reynolds, 1994; Roedder, 1984; Van Den Kerkhof & Hein, 2001). The first mechanism would lead to inclusions with a constant vapour-to-liquid-ratio in which the homogenization temperature can be analysed by heating the inclusion. The resulting liquid and gas phase are under pressure. Heterogeneous trapping could result from boiling or immiscible fluids at high-temperatures or from trapping in the vadose zone at low temperatures, both resulting in variable vapour-to-liquid ratios with gas at atmospheric pressure (Goldstein & Reynolds, 1994; Van Den Kerkhof & Hein, 2001; Verhaert et al., 2004). Finally, leakage of fluids during fluid inclusion modifications could result in variable vapour content through deformation of crystals and fluid inclusions. This mechanism will not influence all inclusions (Goldstein & Reynolds, 1994). The mechanism of trapping in the vadose zone can be disregarded, as the depositional setting is phreatic. Homogeneous trapping is unlikely to be a creation mechanism for bubbles in these fluid inclusions as most inclusions do not homogenize and do not have constant vapour-to-liquid ratios. Two inclusions, however, do homogenize and are the only analysed inclusions which could possibly have a bubble created by homogeneous trapping. The remaining options for the other inclusions are heterogeneous trapping and leaking. Heterogeneous trapping would result from boiling fluids but leakage has more compelling arguments for the bubble



generation. Arguments for this process are: microfractures at fluid inclusions (Figure 5-35F) and the absence of bubble shrinkage upon heating to 110 °C, suggesting that the bubble content is not in relation to the fluid phase (Goldstein & Reynolds, 1994; Roedder, 1984; Shepherd et al., 1985; Van Den Kerkhof & Hein, 2001). Additional tests can be performed to provide certainty as suggested in Goldstein and Reynolds (1994). The inclusions would be crushed while the samples are emerged in oil. If the bubble would expand, it indicates that gas was present in the inclusion and it was under pressure. If the bubble would keep the same size, a gas at low pressure must have been present in the bubble, suggesting heterogeneous trapping. If the oil would disappear into the bubble, leakage is indicated.

The temperature of the upwelling fluids can be constrained by  $T_h$  measurements and by calculation of the formation temperature from stable isotopes.  $T_h$  is only measured in two inclusions at 61 and 65 °C. This temperature constrains the upper limit of the temperature, if these inclusions have not leaked. The monophase inclusions did not show metastability after cooling them to -18 °C for two weeks, suggesting trapping below 50 °C (Goldstein & Reynolds, 1994). This defines the maximal temperature of all inclusions in AS14NJ044 and AS14NJ057 which only contain monophase inclusions. The stable oxygen value of the veins is taken from bulk samples and is -12.05 ‰ V-PDB. The formula for the calculation of the temperature from oxygen isotopes is (Craig, 1965):

$$T = 16.9 - 4.2(\delta^{18}O_c - \delta^{18}O_w) + 0.13(\delta^{18}O_c - \delta^{18}O_w)^2$$

With:

- $\delta^{18}O_c$  = the stable oxygen isotopic value of the carbonate
- $\delta^{18}O_w$  = the stable oxygen isotopic composition of the actual precipitating fluids.

The  $\delta^{18}O_w$ -value of currently emerging spring waters is -9.36 ‰ V-SMOW (Minissale et al., 2002). This results in a calculated temperature of 29.1 °C which is significantly lower than the measured  $T_h$ . The inaccuracies, inherent to using this equation, arise from: (i) it is an empirical formula for marine carbonates, (ii) the  $\delta^{18}O_w$ -value indicates the present day composition, which could differ from the prevailing conditions and (iii) degassing induced isotope fractionation at the moment of aragonite precipitation. The calculated temperatures and  $T_h$  provide, respectively, the lower and upper limit for the temperature range. Upwelling fluids probably ranged between 29.1 and 65 °C. This is comparable to present day temperatures at the Acquasanta springs, which seasonally vary between 21.9 and 43.4 °C. The  $T_h$  is recorded in the highly saline fluids, which indicates that these are formed at the upper limit of the temperature range. The low salinity fluids have probably formed at lower temperatures.

The composition of these fluids can provide a possible indication of their origin. Low salinity fluids have a salinity varying between meteoric and marine water. These fluids could be the result of mixing

of meteoric and saline fluids or from water-rock interactions (Baccar & Fritz, 1993; Verhaert, 2006; Verhaert et al., 2004). Because no actual range of salinities varying between two values is seen, the mixing hypothesis is less plausible. Fluid-rock interaction can occur during subsurface migration of the fluids. Fluid migration probably occurs by shallow, regional topographically driven flow from the nearby Monte Vettore area towards the Acquasanta area (Figure 6-3). The meteoric fluids undergo fluid-rock interactions and are charged in ions that cause minor salinity increase.

The high salinity fluids are rich in  $\text{CaCl}_2$  compared to  $\text{NaCl}$  and can have a variety of sources, like osmotic effect of clays through which fluids migrate or the dissolution of evaporite deposits (Verweij, 1993). The most likely explanation for increase in salinity is the dissolution of the Triassic evaporites in the sedimentary succession. Anhydrite could dissolve at high pressure conditions at a depth of approximately 3 to 4 km (Cardello & Doglioni, 2015; Newton & Manning, 2005). The fluids that dissolve the anhydrite are probably deeply circulating brines that could be formational fluids or meteoric fluids that migrated through faults of the fold and thrust belt. The original fluids are more likely to be meteoric due to the highly negative stable oxygen isotopes ( $-12.05\text{‰}$ ). Upward migration could be enabled by tectonically driven fluid flow (Verhaert et al., 2009; Verweij, 1993) or by thermally driven flow (Menichetti, 2008). The  $T_h$  of  $65\text{ °C}$  is an indication for a deep-seated origin of the fluids. A depth of approximately 3 to 4 km would suggest temperatures of approximately  $110$  to  $140\text{ °C}$  when assuming a geothermal gradient of  $30\text{ °C/km}$ . The drop in temperature could be explained by cooling of the fluids, by conduction through the rock matrix (Menichetti, 2008). Mixing with shallow fluids (e.g.: El Desouky et al., 2015) is disregarded as no mixing trends are seen in the data. The presence of sulphur in currently active springs is noted by a strong sulphuric smell. This could be a minor, but additional argument to indicate anhydrite dissolution into  $\text{H}_2\text{S}$  and  $\text{SO}_2$  for creation of the fluids (Newton & Manning, 2005). The high amount of  $\text{Ca}^{2+}$  compared to  $\text{Na}^+$  is then related to the dissolution of anhydrite and possible fluid-rock interactions.

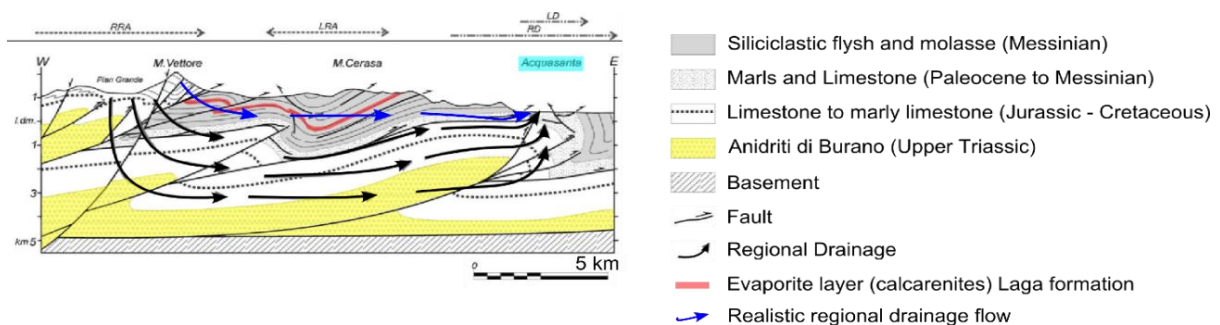


Figure 6-3: Fluid flow model of Menichetti (2008) indicating topographically driven flow of the Monte Vettore area, indicated with blue arrows. The black arrows are from the model, suggested by Menichetti (2008), in which fluid flow is thermally driven.

Other studies at Acquasanta mention the co-existence of deeply and shallow meteoric circulating water. Due to a spring water composition, with both  $\text{Ca}^{2+}$  and  $\text{SO}_4^{2-}$ , these researches already proposed deeply circulating waters near the anhydrite deposits, similar to the proposed model in this research (Galdenzi et al., 2010; Madonna et al., 2005; Menichetti, 2008; Nanni & Vivalda, 2005).

Both the low and high salinity fluids are observed in primary inclusions, making it difficult to discern which of the two fluids was responsible for the precipitation of the travertine cements. The two fluid types are not linked to distinct cement bands as both wafers are considered to be of the same vein.

Additional crush-leach analysis could provide more information on the composition of the fluid inclusions. This could provide more information on the fluid-rock interaction involved in the genesis of both fluid types. A more detailed fluid inclusion analysis on a larger set of samples of the banded travertine could provide more information on the relation of the fluids to certain bands of cement.

The fluid inclusion analysis determines the source of the fluids, but does not yet indicate the source of the carbonate in the fluids. This can be done with stable carbon isotope analysis. The vein has an average signature of  $\delta^{13}\text{C}_{\text{trav}} = 7.70 \text{ ‰}$ , giving a calculated fluid signature of  $\delta^{13}\text{C}_{\text{fluid}} = -1.26 \text{ ‰}$  (Panichi & Tongiorgi, 1976), which can be used to determine the source of the carbon. Figure 6-4 shows the possible sources of  $\text{CO}_2$  and the fractionation processes that affect the  $\delta^{13}\text{C}$ -signatures. The  $\delta^{13}\text{C}$ -data of the vein deposits plots close to thermal decarbonation at  $90 \text{ °C}$  which is a process commonly related to travertine generation (Claes et al., 2015; El Desouky et al., 2015; Pentecost, 2005 & 1995). Organic sources of  $\text{CO}_2$  can be disregarded as the  $\delta^{13}\text{C}_{\text{fluid}}$ -value is too high. The  $\text{CO}_2$  could have a magmatic origin, which is often proposed for Turkish travertine (Claes et al., 2015; El Desouky et al., 2015; Kele et al., 2011). No evidence can be given for this case study that supports the latter hypothesis. Madonna et al. (2005) pointed to the influence of magmatic processes, based on geochemical and gravimetric data. This hypothesis can however not be confirmed from other data like measured carbon isotopes and helium isotopes, analysed from the thermal springs by Minissale et al. (2002). The  $^3\text{He}/^4\text{He}$ -ratio of the Acquasanta Terme thermal spring is 0.07 which is close to an average crustal  $^3\text{He}/^4\text{He}$  value of 0.05 (Minissale et al., 2002). These values do not support a mantle origin, making the hypothesis of magmatic  $\text{CO}_2$  less likely. The  $\text{CO}_2$  in the fluids is probably only derived from thermal decarbonation.

Caution is required with regard to the preceding interpretations as isotope data are from bulk analyses. The fluid inclusions record two fluids which were both involved in the precipitation processes of the travertine. It is uncertain whether the isotopic composition of aragonite precipitated by both or one of these fluids match. The interpretation of thermal decarbonation is the most probable, but influence of other  $\text{CO}_2$ -sources can be hidden in the signature.

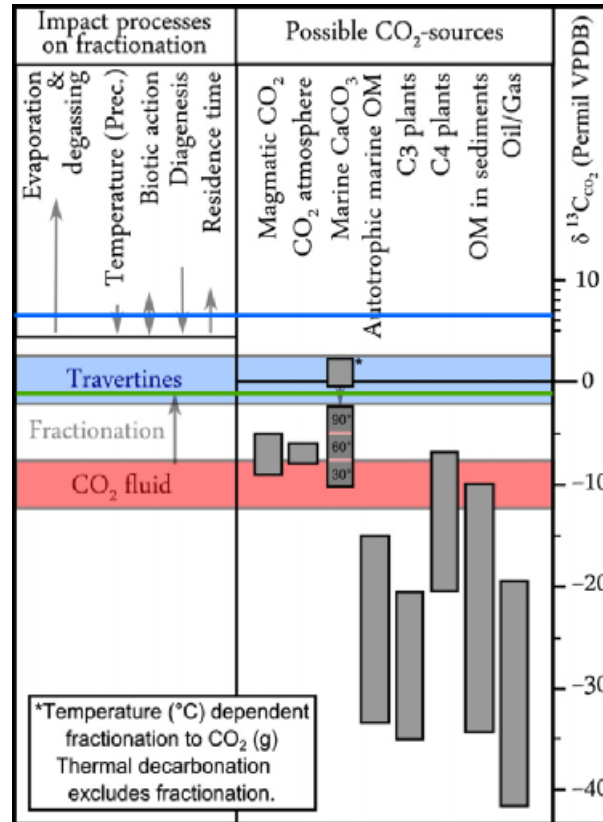


Figure 6-4: Carbon sources and processes that influence the  $\delta^{13}\text{C}$ -signature. The fractionation from the  $\text{CO}_2$  in the fluid to the travertine deposit is determined based on the formula of Panichi and Tongiorgi (1976) (Claes et al., 2015). The  $\delta^{13}\text{C}_{\text{CO}_2}$  of the travertine vein is indicated with a green line. The  $\delta^{13}\text{C}_{\text{CO}_2}$  of the veins in the fossil cave is indicated with a blue line.

Strontium isotopes may provide additional information that can help to determine which rocks are decarbonated or dissolved and loaded the spring water with carbonate. The entire travertine body records the same  $^{87}\text{Sr}/^{86}\text{Sr}$ -ratio of  $0.70791 \pm 0.0004$  on average, indicating an unchanged source throughout the evolution of the travertine body. No Sr-isotope data of the actual formations in the stratigraphy from the Acquasanta region is present in the literature. Therefore, a different approach is applied. The only available data are the measured  $^{87}\text{Sr}/^{86}\text{Sr}$  ratios of the Miocene marly limestone and the calcite veins occurring in the Miocene marls, of 0.70838 and 0.70862, respectively. These rocks are of the Acquasanta group (Koopman, 1983). For the other formations, data of the Sr-isotope stratigraphy from McArthur et al (2001) is used (Figure 6-5). This approach plots the analysed data on a plot of the marine  $^{87}\text{Sr}/^{86}\text{Sr}$ -ratio through time and gives possible constraints to the age of the dissolved rocks because no fractionation occurs during dissolving of the carbonates and precipitation of the travertine. Three different ages are possible for the given  $^{87}\text{Sr}/^{86}\text{Sr}$ -ratio. These ages are Paleogene, Middle-Triassic and Permian. The latter is excluded as no carbonate rocks older than Triassic are present between the dissolved anhydrites and the surface. The parent rocks of the travertine are expected to be of Triassic age as the younger Paleogene rocks are outcropping at the surface and temperature would be lower than

90 °C at which carbonation is occurring. These rocks are part of the Burano formation, which also contains anhydrite layers (Koopman, 1983).

Thermal decarbonation of the limestone either happened at a temperature close to 90 °C or degassing had an important influence on the carbon signature during formation of the banded travertine veins. The effect of degassing most likely influenced the signature but this is expected to be of subordinate importance on the carbon signature in the phreatic conditions of the vein. This implies a decarbonation temperature of >90 °C, which is in agreement with temperatures of 110 °C, derived from a geothermal gradient of 30 °C/km.

Vein samples of the fossil cave have  $\delta^{13}\text{C}_{\text{trav}} = 13.44$  and  $14.58$  ‰, which implies a  $\delta^{13}\text{C}_{\text{CO}_2}$  of 5.63 and 6.99 ‰, respectively (Panichi & Tongiorgi, 1976). This value is significantly higher from the other veins or any other sample in the deposit (Figure 6-4). No possible source for such high carbon isotopic values is found in figure 6-4 and such high values are unrecorded in travertine research. The samples that record this signature are bright- to dull luminescent. A few hypotheses for the high carbon signatures are suggested. The first hypothesis would be extensive boiling, which would increase both  $\delta^{18}\text{O}$  and  $\delta^{13}\text{C}$  through effervescence of a vapour phase. This hypothesis can be refuted, based on the fluid inclusions that record temperatures below 50°C. Another hypothesis is the influx of methane bearing water, in which methane is provided by methanogenesis by bacterial mediation (Whiticar, 1999). The  $\text{CO}_2$  has a positive  $\delta^{13}\text{C}$  (> 10‰) and can be incorporated in calcite. Neither of these suggested hypotheses can be proven but they provide plausible processes for such a high  $\delta^{13}\text{C}$ -signature.

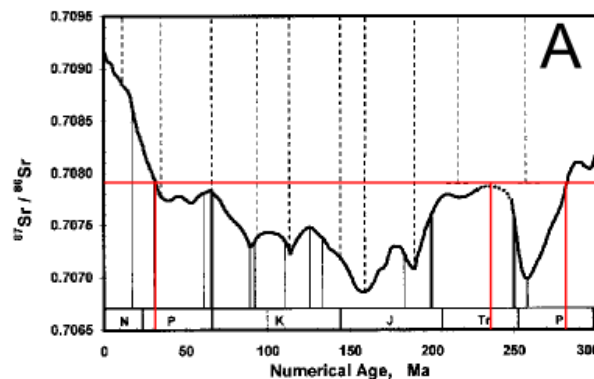


Figure 6-5: Determination of the age of the source rocks. Three different ages are possible from the  $^{87}\text{Sr}/^{86}\text{Sr}$ -ratio of 0.70791. As the Paleogene rocks are outcropped at the surface it is less likely that they have dissolved. Therefore the Triassic carbonates, which are interbedded with the Jurassic evaporites (Anhydriti di Burano), are the most likely candidates.

Minissale (2002) published lower  $\delta^{13}\text{C}$ -signatures for the travertine deposits in Acquasanta Terme. It is however uncertain which of the deposits was sampled as Acquasanta Terme has three different stratigraphic levels of travertine deposits. It is possible that the fluids responsible for the lower terraces are different of those that precipitated the studied travertine due to decreased influence of deep waters. The lower  $\delta^{13}\text{C}$ -signature could be reflecting such a change.



The banded travertine consists of pure aragonite and the layered travertine of pure calcite. This difference is probably related to the temperature and pressure drop upon emergence from the spring. Pentecost (2005) reported that a quick decrease in temperature can induce calcite precipitation.

### 6.2.2. Fluid evolution after emergence from the spring

After emerging from the spring, subaerial exposure will alter the fluid composition and temperature will decrease with increasing distance from the spring. As the fluids cannot be studied directly, the deposits are analysed as a proxy. This section will look into processes inducing variations in isotope and geochemical signatures.

The stable isotope data of the layered travertine groups together, with the exceptions of three data points belonging to the deposits of the sixth depositional body. The main group, which is the layered travertine apart from those three data points, has  $\delta^{18}\text{O}$  between -12.27 and -10.30 ‰ (average = -11.13 ‰) and  $\delta^{13}\text{C}$  between 7.04 and 9.15 ‰ (average = 8.13 ‰). No significant trends are seen between the isotope data of the different bodies, which makes it impossible to draw conclusions regarding the variations in isotopic composition through time. Slightly increased values for both oxygen and carbon isotopes compared to the banded travertine are noted. The differences are 1.08 and 0.43‰ for oxygen and carbon isotopes, respectively. The increase in  $\delta^{18}\text{O}$  suggests that the most important differentiation process is a temperature drop (Gonfiantini et al., 1968). The increase in  $\delta^{13}\text{C}$  suggests additional degassing (Claes et al., 2015; Kele et al., 2011; Pentecost, 2005). A possible hypothesis for the deviant data of the sixth body can be related to additional turbulence by steeper slopes (60°) compared to the slopes of other samples (at 20-30°), causing degassing and possibly a decrease in temperature.

Samples of the erosional horizons plot within the group of the layered travertine, with the exception of one sample (AS14NJ004). This sample has a lower  $\delta^{13}\text{C}$ , at 2.68‰ and a less depleted  $\delta^{18}\text{O}$ , at -8.94‰. The latter  $\delta^{18}\text{O}$ -signature could be explained by a lower temperature of the fluids or the influence of rain water (Guo & Riding, 1998). A decrease in  $\delta^{13}\text{C}$  is typically linked to increased organic influence (e.g.: Kele et al., 2011). The other samples would then record less influence of organic influence.

From the trace element geochemical data, three different clusters are discerned through cluster and PCA analysis. These clusters agree with the occurrence of three types of deposits, i.e. banded- and layered travertine and erosional horizons. The samples of the fossil cave are clustered with the layered travertine, apart from one sample that is clustered with the erosional surfaces. The banded travertine can be differentiated from the other samples by its high amount of Sr. This is linked to the aragonitic mineralogy of the veins, which contains more Sr compared to the calcite (Pentecost, 2005). The erosional horizons are marked by significantly higher magnesium and lower calcium, but also higher Fe, Al, Ti, Mn, P, K, and Na. Especially AS14NJ004, of which the stable isotopes also deviated, is enriched in these elements. These elements are related to detrital influx in these deposits. Minerals that give rise to these element

concentrations are iron-oxides (Fe and Ti), biotite/muscovite (K, Al, Fe and Mg), feldspars (Na, Al and K), etc. The layered travertine shows no outstanding data.

The ICP-OES analysis was not able to characterise the different lithotypes in the layered travertine, but was able to discern the erosional and vein travertine. The analysis can be used as a fast way to check the mineralogy of a large amount of samples. The technique should still be complemented with XRD data of the siliciclastic fraction whenever those minerals should be determined quantitatively. Notice however that the siliciclastic minerals cannot be discerned from bulk XRD-analysis.

### 6.2.3. Diagenetic fluids

Data for characterization of diagenetic fluids comes from stable isotope signatures and CL analysis, which are both performed on cements.

Fluids that precipitated the cements of the layered travertine deposits are formed from thermal water flowing through the pores. The water that is actively precipitating travertine through water runoff over the travertine body is also present in the pores of the near-surface underlying. Water flows through these pores and the lower flow velocity, could generate cements. This process is recognized from the cements in microbial mats. The latter cements are only occurring in the bottom part of the pores, indicating that the pores are not always entirely filled. This process of cementation explains why both oxidizing and more reducing conditions are recognized within the cement generations. The oxidizing conditions indicate periods at which the pores were not entirely filled by fluids. The more reducing conditions indicate moments in which the pores are entirely filled or deeper burial of the deposits beneath the active surface. Both processes suggest decreased availability of oxygen, resulting in reducing conditions. The process of water flowing through the earlier created fabrics is considered an important process in the solidification of the travertine. This process induces extra inorganic precipitation, which stabilizes the sediments quickly.

The XRD analysis and the stable isotopes indicate that the cement samples have an aragonitic composition and that the stable isotopes have values, similar to those of the banded travertine. The similarity in mineralogy and isotopic composition could indicate that the fluids that flow through the body do not cool significantly and the effect of degassing is less pronounced. The higher temperature conditions are recognized from the aragonitic mineralogy.

### 6.2.4. Fossil cave fluids

The waters causing precipitation of the porous travertine are thermal waters that infiltrate the cave through fractures. This hypothesis comes from the similarity of the stable isotopic- and elemental composition and fabric texture, compared to the rest of the layered travertine. The resulting deposits are morphologically similar to dripstones, but are created through processes, similar to travertine deposition

(e.g. degassing, microbial influence, etc.). The black micrite of the samples in thin sections is dense which could be an indication for the influence of microbes (Chafetz & Folk, 1984).

### 6.3. Depositional history

The depositional history can be determined based on the onlapping and offlapping relationships of the layers, combined with the lithotypes present in the depositional body (Figure 6-9). The lithotypes are grouped into lithofacies which are related to certain environmental settings as described in Veysey et al. (2008).

The sloping lithofacies can be linked to higher energy water flow and subaerial precipitation of travertine from a thin sheet of water. Transition of type I microbial mats to micritic dendrite crusts to peloidal micrite could be related to higher energy of water flow caused by increasingly steeper slopes. The microbial mats are only located in the upper, flatter areas of the sloping lithofacies and are related to shallow water conditions (Gandin & Capezzuoli, 2014). When slopes become steeper, the mats grade into micritic dendrite crusts, which form microterraces. Such terraces are commonly observed on steep (up to subvertical) slopes at active travertine depositions (Chafetz & Folk, 1984; Fouke, 2011; Guo & Riding, 1999). The crusts grade into peloidal micrite lithotype. The microscopic shrubs occurring in the peloidal micrite are however smaller, indicating that growth was more often interrupted, related to the faster flow and decreased water depth of the spring waters. The peloidal micrite defined in this research is different from peloidal micrite in other studies. It rather consists of small dendrolitic to arborescent (lower height-to-width ratio) shrubs, in contrast to the long dendrolites of the micritic dendrite crusts and it is not occurring as separate crusts.

The flat lithofacies consists of type II microbial mats and pisoids or radial shrubs (microbial or “bacterial” pisoids; Folk & Chafetz, 1983). Shrubs are also seen microscopically, in the denser micritic parts and macroscopically as small shrubs of up to 1 cm high. The growth of shrubs is related to shallow pool conditions and water in which only bacteria can grow. Such water is too hot and too rich in  $H_2S$  for any other organism to grow (Chafetz & Folk, 1984; Chafetz & Guidry, 1999; Fouke et al., 2000; Guo & Riding, 1994). The flat lithofacies is related to extensive pools with alternation between deeper (< 2 m) and shallower conditions, indicated by growth of shrubs and microbial mats, respectively. These pools are filled with hot, chemically harsh water, rich in  $H_2S$ .

The reed lithofacies consists of microbial laminites and reed moulds, deposited in very shallow pans in which microbial colonies excrete EPS and trap micrite (Gandin & Capezzuoli, 2014). The presence of reed indicates that the water is less hostile, compared to the chemically harsh water of the flat lithofacies.

The terrace lithofacies consists of the shrub lithotype in the pools and micritic dendrite crusts at the rims of the pools. The shrubs are indicative for calm conditions within the pool. The spring water must have

had a sufficiently high temperature and  $H_2S$  to allow shrub growth. The rims of the terraces contain microterraces, like the terraces described by Guo and Riding (1999). The terrace lithofacies is not common in this travertine body.

Erosional horizons are related to periods with low or no spring water discharge, which leads to subaerial exposure of the previously deposited travertine. An erosional phase is usually coincident with a change in the depositional environment and thus lithofacies. Reed moulds and their related shelter porosity are commonly present at the top of the erosional horizons. Reed grows in conditions with less thermal water. The water present during erosional phases is probably meteoric water from direct rainfall.

The waterfall lithofacies consists of subvertical crystalline crust deposits with a height of up to 20 m. Reed moulds and shelter porosity is present in the deposit, indicating that the fluids have sufficiently cooled to host anything other than bacteria (Capezzuoli et al., 2014).

All the deposits of the layered travertine are linked to at least partial microbial origin through analogy with Chafetz and Folk (1984), which identify black peloids as microbial clumps. Additional similarity with the microbial mats, microbial laminites and microbial paper-thin rafts described by Gandin and Capezzuoli (2014) is a further indication for microbial origin of the deposits.

The banded travertine in the upper part of the quarry is a paleo-pathway for spring waters. The fluid inclusions confirm the presence of high-temperature fluids. Two of such veins, with palisade crystals (*sensu* Gandin & Capezzuoli, 2014), are analysed. Two hypotheses for the relation of the veins to each other can be proposed. The first hypothesis is that the two veins represent two different point-sources. The second hypothesis states that the two veins represent the same fluid conduit of a fissure ridge. Evidence for the former hypothesis can be found based on the lenticular occurrence of the deposits in the upper part of the quarry (Figure 6-6A). This could indicate that fluids come from both sources and meet there, causing the creation of lenses.

There is however more evidence for the hypothesis in which the two veins represent the fissure of a fissure ridge, implying that the veins form one connected fracture (Figure 6-7). The most compelling evidence for their connection is the strike of N40E, for both veins. Despite the difference in thickness of the veins on the quarry wall, a continuous thickness is seen when the veins are connected in 3D (Figure 6-7). The fissure even slightly thins towards the vein that appears thickest in the quarry wall (on the NW wall). This thickness variation can be attributed to the orientation of the quarry walls, which cross-cut the vein. The deposits dip down from each of the veins onwards (Figure 6-7). Other field evidence is the similarity of the deposits, at both sides of the vein, to the profile of a cross-cut fissure ridge exemplified in De Filippis et al. (2012) or De Filippis and Billi (2012) (Figure 6-8A and B). The lenticular deposits, used as an argument for two point-sources are likely deposits of small subordinate flows of thermal waters, generated from individual small mounds on the fissure (Figure 6-6B; Brogi &

Capezzuoli, 2009; Guo & Riding, 1999). Also geochemical signatures indicate similar formational waters. The stable isotopes have similar values ( $\delta^{18}\text{O} = -12.20$  vs.  $-11.67$  ‰ and  $\delta^{13}\text{C} = 7.57$  vs  $7.93$  ‰). The geochemical composition of both veins belongs to the same statistical cluster. The preceding arguments are indications that a fissure ridge system developed in relation to these veins.

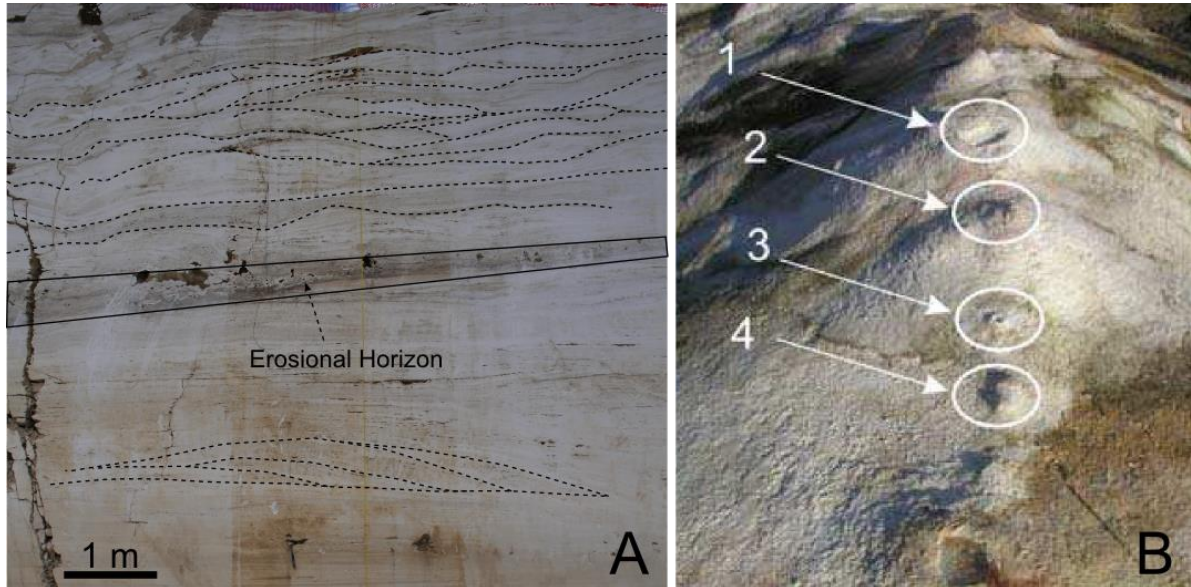


Figure 6-7: Lenticular layering of the travertine deposits. This can be related to either fluid flow from two sources that meet at this location or it could be related to flow from different small-scale (few cm) travertine mounds on the fissure ridge (B) (Brogi & Capezzuoli, 2009).

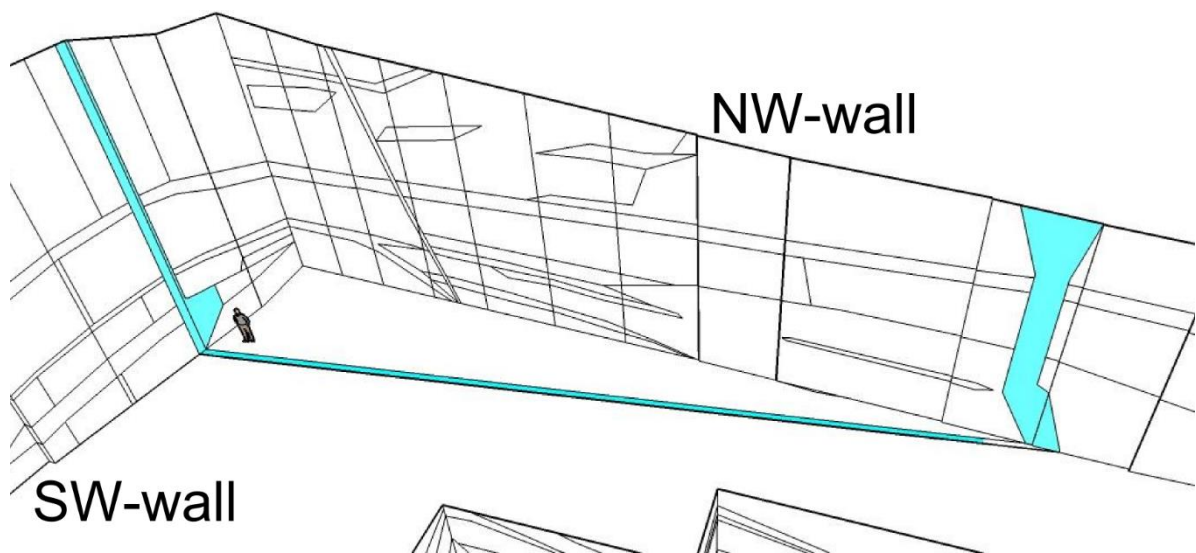


Figure 6-6: Connecting both veins of the quarry in 3D shows a fracture with an almost constant thickness. The layered travertine dips downwards, away from both veins. Man for scale.

The depositional history can be reconstructed based on the environmental interpretation of the different lithofacies. The depositional history starts off with subaerially precipitated travertine and is marked by steep slopes (Figure 6-9A and G). This body is interfingering with deposits of another body (Figure 6-9B). At the base of the interfingering deposits, both deposits are subaerial and slopes are oriented in



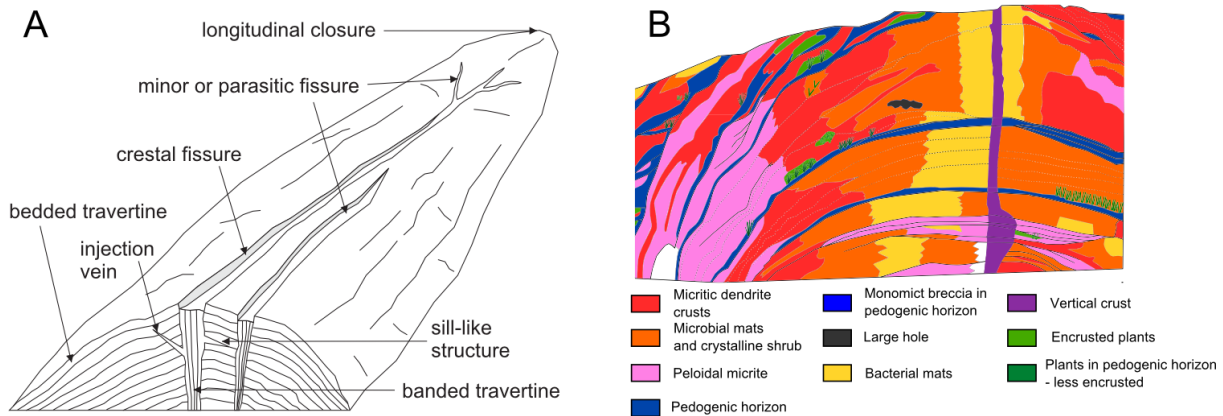


Figure 6-8: Fissure ridge. A. Schematic representation of a fissure ridge by De Filippis et al. (2012). The cross-section looks very similar to the deposits noted in the linedrawing from San Pietro quarry (B).

opposite directions (Figure 6-9B). This indicates two different springs that were alternatingly active or it could indicate two different primary flow paths. The latter is also seen in active travertines in which the primary flow can shift its flow path (Fouke, 2011; Kele et al., 2011). The simultaneous activity of several point-sources is also possible along a fault (De Filippis et al., 2013b). The interfingering deposits grade towards subaqueous deposits for the third body, while the other body remains subaerial, with steep slopes (Figure 9B). This indicates a contrasting depositional style. The water of the shallow pool conditions, indicated by the flat lithofacies is contained by a morphological high, created during subaerial conditions (second body). The influence of this dam is seen from the distribution of the flat deposits of the third body, which are only recorded at one side of the deposits of the second body (Figure 6-9F and J).

The next phase in the deposition indicates progradation of the fissure (Figure 6-9C, D, E, H and I). The fourth depositional body has a small extent and has sloping deposits on one side and more smoothly sloping deposits on the other side, on top of the earlier precipitated flat deposits (Figure 6-9C and H). The influence of the fissure ridge is seen from the arc shaped deposits close to the banded travertine although the top arc is not yet coinciding with the vein (Figure 6-9H and I). The progradation of the fissure becomes more pronounced in the following depositional bodies (Figure 6-9I). The tops of the arcs, described by the layered deposits, coincide with the vein (Figure 6-9I). The deposits record the presence of a steeply sloping part of the fissure ridge at one side and a shallow pool, recognised from the flat lithofacies (Figure 6-9D, E and I). The pool can be considered morphologically similar to a large terrace. The rim of the terrace is marked by waterfalls (Figure 6-9B - F). The final deposits, which downlap and onlap on the fissure ridge slopes, mark decreasing temperature and cessation of the spring water flow (Figure 6-9F and J). The decreased temperature is seen from growth of reed travertine in the

microbial laminites. The cessation of spring water discharge is inferred from thick erosional horizons and autobrecciation of the travertine body.

The vein crosscuts the layered travertine but did not preserve precipitates of the transitional stage, in which the outflowing spring water starts to form layered travertine. De Filippis et al. (2012, 2013a) linked this observation to alternating deposition of layered and banded travertine, following a crack and seal model, in which the banded travertine is precipitated during the sealing phase. The subsequent crack phase can be caused by increasing pressure, for example during wet climatic conditions (De Filippis et al., 2013a) or from faulting activity (Brogi & Capezzuoli, 2009). Water is emerging from the fissure during this period, thus depositing the layered travertine.

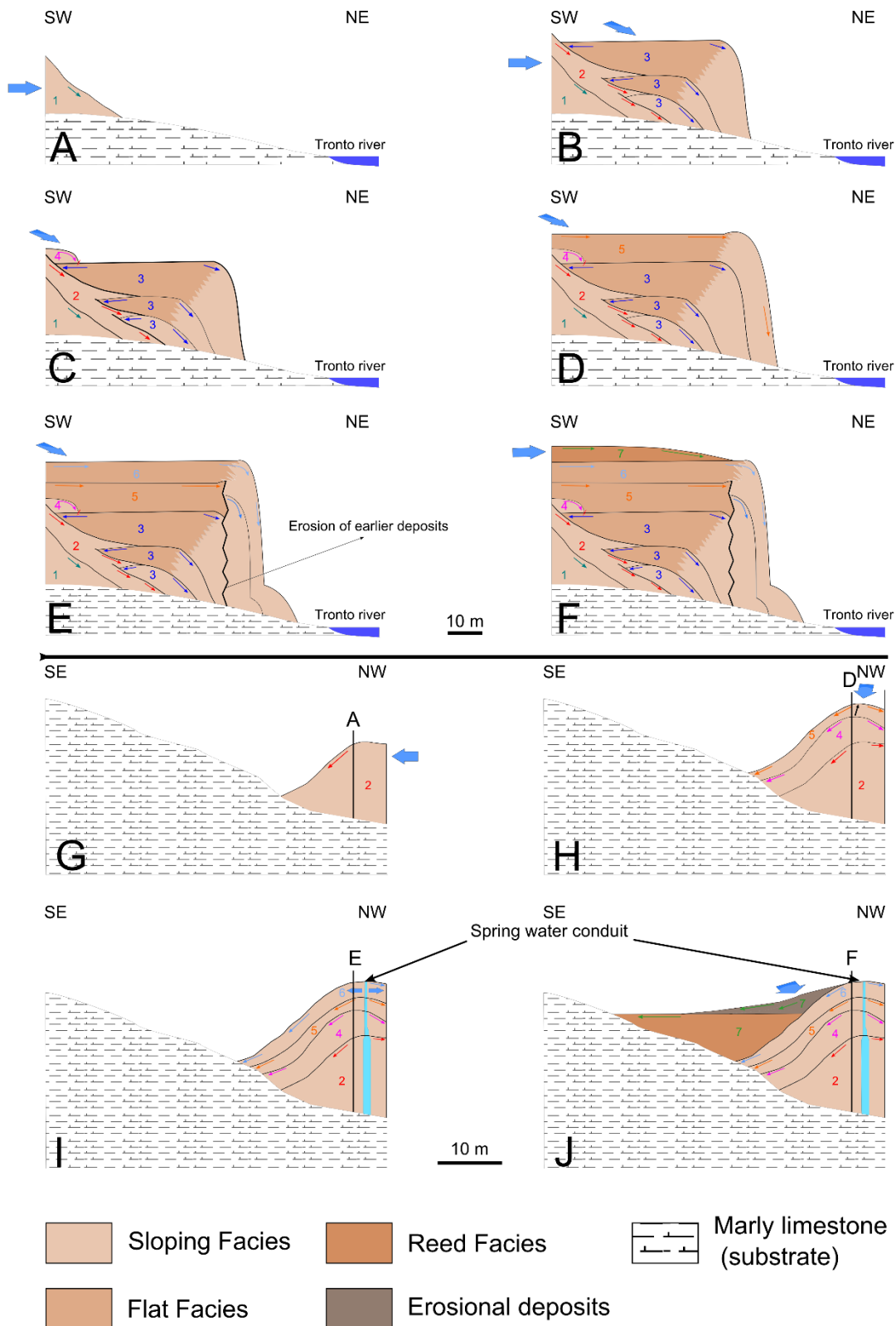


Figure 6-9: Depositional model. The thick blue arrows indicate the estimated location of the spring. A to F. Evolution of the travertine deposition along a NE-SW cross-section. In A and B, two different springs are discerned, which are thought to be individual point-sources. D to E record the deposits of the fissure ridge phase F indicates downlapping of the reed facies. G to J illustrates the evolution along a NW-SE cross-section. From H to J, the fissure ridge stage is recorded. The fissure is propagating in H and is responsible for precipitation during I. F and J show cessation of the system by development of the reed facies and erosional deposits.

## Chapter 7: Conclusion

The goal of this research was to construct a 3D reservoir model, characterize the fluids responsible for precipitation and develop a depositional model of the studied Acquasanta Terme travertine body.

Fourteen different lithotypes are characterized by petrographical analysis, of which the ten most important lithotypes are further analysed to characterise their reservoir properties. These ten studied lithotypes are micritic dendrite crusts, peloidal micrite, microbial mats (two types), erosional surfaces, microbial laminites, crystalline crust, banded travertine veins, shrubs and unconsolidated micrite. Porosity and permeability show large variation within each lithotype group, indicating the complexity of the rock types. Characterization of the reservoir quality with the reservoir classification of Levorsen (1954) indicated that only 0.21 % of the entire carbonate body can be considered very good quality, 5.42 % is good quality and 20.61 % of fair quality, leaving another 73.77 % of the deposit as non-reservoir quality. It is realised that this classification is outdated with current technology, but it provides a solid framework. The actual exploited reservoir characteristics are dependent on the actual oil and gas prices. Fractures that crosscut the travertine form permeable pathways that connect the permeable and porous lithotypes. The vein that separates the travertine deposits in two compartments forms a vertical impermeable barrier. The constructed 3D model, based on detailed descriptions, records the complexity of the studied travertine deposit and indicates the challenges that can be faced in exploitation of such a reservoir. Horizontal drilling, perpendicular to the main fracture strike and crosscutting the vein would be the optimal scenario for exploitation of a similar travertine body.

Fluid characterization of the original spring waters based mainly on analysis of fluid inclusions and isotope geochemistry records the presence of two different fluid types in the vein samples. The first fluid is a meteoric fluid with salinities of 0.0 to 0.88 wt%, with one higher value at 2.74 wt%. From the low salinity and the geomorphological situation in the area, it is concluded that these fluids are meteoric fluids that infiltrated in the M. Vettore area, 10 km away from the area of study. They underwent fluid-rock interactions during gravitationally-driven regional fluid flow. The second fluid is highly saline with a  $\text{H}_2\text{O}-\text{NaCl}-\text{CaCl}_2$  composition and a total salinity between 25.5 and 26.5 wt% and is richer in  $\text{CaCl}_2$  compared to  $\text{NaCl}$ , with a  $\text{NaCl}/(\text{NaCl}+\text{CaCl}_2)$ -ratio of 0.25 or 0.38. The high amount of  $\text{CaCl}_2$  and homogenization temperatures of  $>60^\circ\text{C}$  indicate that the fluids are derived from dissolution of deeply circulating brines in the Burano Formation (Triassic), which contains both anhydrites and carbonates. Data of  $\delta^{18}\text{O} = -12.05\text{‰}$  indicates a meteoric origin of these deeply circulating brines, which have infiltrated through faults of the thrust-and-fold belt. Additional  $\delta^{13}\text{C}$  and  $^{87}\text{Sr}/^{86}\text{Sr}$  analyses indicate that the Triassic carbonates of the Burano Formation are decarbonated and dissolved at temperatures  $> 90^\circ\text{C}$ . The fluids however have cooled before reaching the surface. The presence of other fluids in the system is recorded from veins in fossil cave deposits, present in the travertine body. These fluids record the influence of bacterial methanogenesis.

After emerging from the spring, the fluids are subjected to subaerial processes, like temperature decrease, degassing, etc. which are recorded in the stable oxygen and carbon isotopes, which increase on average 1.08 ‰ for  $\delta^{18}\text{O}$  and 0.43 ‰ for  $\delta^{13}\text{C}$ . The dominantly calcitic mineralogy of the travertine deposits is different from the aragonite of the vein deposits and is governed by the difference in temperature and pressure between phreatic and subaerial conditions. The diagenetic fluids in the travertine system are spring waters that flow through the previously deposited travertine. They both solidify the earlier precipitated cements and create both calcitic and aragonitic cement in the pores.

Six different lithofacies have been defined for unravelling the depositional history. The sloping lithofacies records subaerial deposits of slope angles in between 10 and 60 °, which are precipitated from a thin sheet of water. A more specific type of sloping deposits are the waterfall deposits, which form subvertical layers of travertine that may reach heights up to 20 m. The flat lithofacies records deposition in a subaqueous environment, with recorded alternation between shallow and deeper phases (< 2 m). Reed lithofacies records subaqueous deposition in very shallow pans, with cooler and chemically less harsh waters than the flat lithofacies. Terrace deposits are considered a separate lithofacies, but only have a minor extent. Erosional horizons record phases in which spring water was absent and subaerial processes affected the travertine.

The depositional history is marked by two different depositional styles. The first recorded deposits indicate subaerial precipitation, resulting in steep morphologies. These deposits are interfingering with subaqueous deposits. The interfingering layers indicate deposition of two sources or primary flow paths. Subsequently, a pronounced fissure ridge phase is responsible for deposition and results in precipitation of steeply sloping deposits in one sector of the ridge and flat, subaqueous deposits in the other. The fissure ridge is recognized from a central fissure that has been excavated. Layered travertine deposits slope down in both directions away from the fissure. The final deposits record cooling of the system, by an increase in phytoclastic deposits and cessation of spring activity, by thick erosional horizons.



## Chapter 8: Future research

Additional research of this travertine body could further focus on a more extensive study of the fluid inclusions. The data of the fluid inclusions of the crystallized fluid conduits could be compared with data of fluid inclusions in cements. The latter would require additional sampling of thick cement layers, which are noted in relation to large vugs and mouldic porosity. The fluid characterization could also be expanded to veins, exposed in other (abandoned) quarries in the neighbourhood of San Pietro quarry.

Petrophysical characterization can be expanded by creating a larger dataset or by analysing cores, instead of plugs as they would likely smooth out a large fraction of the variability. Computerized Tomography would provide additional characterization of pore networks and its linkage to permeability.

The Acquasanta Terme area proved to be an interesting study area for depositional processes and the resulting deposits in travertine. This research focussed on the upper travertine level of the three Acquasanta Terme travertine levels. The other travertine levels are interesting to be studied as well, just like the travertine deposits in the area of Ascoli Piceno and Civitella del Tronto.

It is, for example, possible to examine the relation between the isotopes of the different deposits. Minissale et al. (2002) and Minissale (2004) noted carbon isotopes for the travertine deposits with values as much as 11‰ lower than those measured in the San Pietro quarry (7.70 ‰ vs 6.35 ‰). Even within the deposits of the studied quarry, there was a difference between 7.70 and 14.58 ‰. These different isotopic values probably represent different fluids, recorded on a scale of just 1000 m. The processes behind the different sources could be interesting to unravel.

Additional research in the area would also be interesting in the context of reservoir analogue studies. Travertine can be found within an area of approximately 250 km<sup>2</sup> (not continuous) between Acquasanta Terme and Ascoli Piceno. The deposits of Acquasanta Terme are linked to different tectonic structures compared to those of Ascoli Piceno (Boni & Colacicchi, 1966). It could be interesting to analyse the linkage of travertine deposition to tectonic structures and its evolution through time could be of interest. During dissolution of carbonates in the subsurface to enrich the spring waters in Ca<sup>2+</sup> and CO<sub>3</sub><sup>2-</sup>, extra porosity is created which could provide an additional target for hydrocarbon or geothermal reservoirs. A large framework, in the interest of the oil industry, can be provided through a multidisciplinary approach of tectonics, travertine distribution and the fluid origin.

The area presents a variety of different types of continental carbonates which could improve scientific knowledge on the relationship of these different types of continental carbonates. In this research a fissure ridge with flat, sloping and waterfall deposits has been analysed. A reconnaissance study of the area presents a multitude of different continental carbonate deposits. The abandoned travertine quarry on Colle San Marco near Ascoli Piceno shows “travitufa” deposits next to more sloping deposits. The area

in between Acquasanta Terme and Ascoli Piceno (Colle San Nicola) has both lacustrine carbonate deposits, tufa deposits and travertine deposits. Civitella del Tronto deposits consists of lacustrine deposits at the foot of the mountain and layered bryophyte to plant-rich deposits at the top. The abandoned quarries close to Cava San Pietro show different travertine lithofacies, whereas deposits closer to the river resemble more tufa-like deposits. At present there are even some tufa bodies developing along the Tronto River.

## Chapter 9: References

- AAPG. (2014). Porosity. Retrieved April 7, 2015, from <http://wiki.aapg.org/Porosity>
- ALTUNEL, E., AND HANCOCK, P. L. (1993). Morphology and structural setting of Quaternary travertines at Pamukkale, Turkey. *Geological Journal*, 28(3-4), 335–346.
- ALTUNEL, E., AND HANCOCK, P. L. (1996). Structural attributes of travertine-filled extensional fissures in the Pamukkale Plateau, Western Turkey. *International Geology Review*, 38, 768–777.
- ANDERSEN, M. A., DUNCAN, B., AND MCLIN, R. (2013). Core Truth in Formation Evaluation The nature of subsurface exploration forces oil and gas companies to investigate. *Oilfield Review*, 25(2), 16–25.
- ARTONI, A. (2013). The Pliocene-Pleistocene stratigraphic and tectonic evolution of the Central sector of the Western Periadriatic Basin of Italy. *Marine and Petroleum Geology*, 42, 82–106.
- BACCAR, M. BEN, AND FRITZ, B. (1993). Geochemical modelling of sandstone diagenesis and its consequences on the evolution of porosity. *Applied Geochemistry*, 8(3), 285–295.
- BARCHI, M. R., AND MIRABELLA, F. (2009). The 1997–98 Umbria–Marche earthquake sequence: “Geological” vs. “seismological” faults. *Tectonophysics*, 476(1-2), 170–179.
- BARGAR, K. E. (1978). Geology and thermal history of Mammoth Hot Springs, Yellowstone National Park, Wyoming. *Geological Survey Bulletin*, 1444, 1–55.
- BASKARAN, M. (2012). *Handbook of environmental Isotope Geochemistry*. Berlin, Heidelberg: Springer-Verlag.
- BATES, R. L., AND JACKSON, J. A. (1987). *Glossary of Geology* (Third Edit). Alexandria, Virginia: American Geological Institute.
- BEASLEY, C. J., FIDUK, J. C., BIZE, E., BOYD, A., FRYDMAN, M., ZERILLI, A., DRIBUS, J. R., MOREIRA, J. L. P., AND CAPELEIRO PINTO, A. C. (2010). Brazil’s Presalt Play. *Oilfield Review*, 22(3), 28–37.
- BIGI, S., CASERO, P., AND CIOTOLI, G. (2011). Seismic interpretation of the Laga basin; constraints on the structural setting and kinematics of the Central Apennines. *Journal of the Geological Society*, 168(1), 179–190.
- BIGI, S., CONTI, A., CASERO, P., RUGGIERO, L., RECANATI, R., AND LIPPARINI, L. (2013). Geological model of the central Periadriatic basin (Apennines, Italy). *Marine and Petroleum Geology*, 42, 107–121.
- BOCCALETTI, M., NICOLICH, R., AND TORTORICI, L. (1990). New data and hypothesis on the development of the Tyrrhenian basin. *Palaeogeography, Palaeoclimatology, Palaeoecology*, 77, 15–40.
- BODNAR, R. J. (1993). Revised equation and table for determining the freezing point depression of H<sub>2</sub>O-NaCl solutions. *Geochimica et Cosmochimica Acta*, 57(3), 683–684.

- BONI, C., AND COLACICCHI, R. (1966). I travertini della Valle del Tronto: giacitura, genesi e cronologia. *Memorie Della Società Geologica Italiana*, 5, 315–339.
- BORISENKO, A. S. (1977). Study of the salt composition of solutions of gas-liquid inclusions in minerals by the cryometric method. *Soviet Geology and Geophysics*, 18, 11–19.
- BORSATO, R., JONES, W., GREENHALGH, J., MARTIN, M., AND ROBERSON, R. (2012). South Atlantic Conjugate Margin: An Exploration Strategy, 30(December), 79–84.
- BRASIER, A. T. (2011). Searching for travertines, calcretes and speleothems in deep time: Processes, appearances, predictions and the impact of plants. *Earth-Science Reviews*, 104(4), 213–239.
- BROGI, A., AND CAPEZZUOLI, E. (2009). Travertine deposition and faulting: the fault-related travertine fissure-ridge at Terme S. Giovanni, Rapolano Terme (Italy). *International Journal of Earth Sciences*, 98, 931–947.
- BROGI, A., CAPEZZUOLI, E., ALÇİÇEK, M. C., AND GANDIN, A. (2014). Evolution of a fault-controlled fissure-ridge type travertine deposit in the western Anatolia extensional province : the Çukurbağ fissure-ridge ( Pamukkale , Turkey ), 171.
- CALAMITA, F., SATOLLI, S., SCISCIANI, V., ESESTIME, P., AND PACE, P. (2011). Contrasting styles of fault reactivation in curved orogenic belts: Examples from the central Apennines (Italy). *Bulletin of the Geological Society of America*, 123(5), 1097–1111.
- CAPEZZUOLI, E., GANDIN, A., AND PEDLEY, M. (2014). Decoding tufa and travertine (fresh water carbonates) in the sedimentary record: The state of the art. *Sedimentology*, 61(1), 1–21.
- CAPOZZI, R., ARTONI, A., TORELLI, L., LORENZINI, S., OPPO, D., MUSSONI, P., AND POLONIA, A. (2012). Neogene to Quaternary tectonics and mud diapirism in the Gulf of Squillace (Crotone-Spartivento Basin, Calabrian Arc, Italy). *Marine and Petroleum Geology*, 35(1), 219–234.
- CARDELLO, G. L., AND DOGLIONI, C. (2015). From Mesozoic rifting to Apennine orogeny: The Gran Sasso range (Italy). *Gondwana Research*, 27, 1307–1334.
- CHAFETZ, H. S., AND FOLK, R. L. (1984). Travertines: Depositional morphology and the bacterially constructed constituents. *Journal of Sedimentary Petrology*, 54(1), 289–316.
- CHAFETZ, H. S., AND GUIDRY, S. A. (1999). Bacterial shrubs , crystal shrubs , and ray-crystal shrubs : bacterial vs . abiotic precipitation. *Sedimentary Geology*, 126(1), 57–74.
- CHIOCCHINI, U., AND CIPRIANI, N. (1989). The composition and provenance of the Tortonian and Messinian turbidites in the context of the structural evolution of the Central Apennines along the “Ancona-Anzio” line. *Sedimentary Geology*, 63(1-2), 83–91.
- CLAES, H. (2011). *Petrology of the travertine quarry “ECE” Denizli basin , Turkey with emphasis on micro-porosity*. Unpublished Master's Thesis, KU Leuven.
- CLAES, H., SOETE, J., VAN NOTEN, K., EL DESOUKY, H., MARQUES ERTHAL, M., VANHAECKE, F., ÖZKUL, M., AND SWENNEN, R. (2015). Sedimentology, three-dimensional geobody reconstruction and carbon

dioxide origin of Pleistocene travertine deposits in the Ballık area (south-west Turkey). *Sedimentology*.

- CRAIG, H. (1965). Measurement of oxygen isotope paleotemperatures. In E. Tongiorgi (Ed.), *Stable Isotopes in Oceanographic Studies and Paleotemperatures* (pp. 161–182). Pisa: CNR Lab. Geol. Nucl.
- D'AGOSTINO, N., MANTENUTO, S., D'ANASTASIO, E., AVALONE, A., BARCHI, M., COLLETTINI, C., RADICIONI, F., STOPPINI, A., AND FASTELLINI, G. (2009). Contemporary crustal extension in the Umbria–Marche Apennines from regional CGPS networks and comparison between geodetic and seismic deformation. *Tectonophysics*, 476(1-2), 3–12.
- DANDEKAR, A. Y. (2013). *Petroleum Reservoir Rock and Fluid Properties* (Second). Boca Raton: Taylor & Francis Group.
- DE FILIPPIS, L., ANZALONE, E., BILLI, A., FACCENNA, C., PONCIA, P. P., AND SELLA, P. (2013a). The origin and growth of a recently-active fissure ridge travertine over a seismic fault, Tivoli, Italy. *Geomorphology*, 195, 13–26.
- DE FILIPPIS, L., AND BILLI, A. (2012). Morphotectonics of fissure ridge travertines from geothermal areas of Mammoth Hot Springs (Wyoming) and Bridgeport (California). *Tectonophysics*, 548-549, 34–48.
- DE FILIPPIS, L., FACCENNA, C., BILLI, A., ANZALONE, E., BRILLI, M., OZKUL, M., SOLIGO, M., TUCCIMEI, P., AND VILLA, I. M. (2012). Growth of fissure ridge travertines from geothermal springs of Denizli Basin, western Turkey. *Geological Society of America Bulletin*, 124(9-10), 1629–1645.
- DE FILIPPIS, L., FACCENNA, C., BILLI, A., ANZALONE, E., BRILLI, M., SOLIGO, M., AND TUCCIMEI, P. (2013b). Plateau versus fissure ridge travertines from Quaternary geothermal springs of Italy and Turkey: Interactions and feedbacks between fluid discharge, paleoclimate, and tectonics. *Earth-Science Reviews*, 123, 35–52.
- DEGROS, M. (2013). *Sedimentological-Petrological Study and Reservoir Characterization of the Budakalász Travertine Carbonates (Buda Mountains, Hungary)*. Unpublished Master's Thesis, KU Leuven.
- DEVOTI, R., ESPOSITO, A., PIETRANTONIO, G., PISANI, A. R., AND RIGUZZI, F. (2011). Evidence of large scale deformation patterns from GPS data in the Italian subduction boundary. *Earth and Planetary Science Letters*, 311(3-4), 230–241.
- DI BENEDETTO, F., MONTEGROSSI, G., MINISSALE, A., PARDI, L. A., ROMANELLI, M., TASSI, F., DELGADO HUERTAS, A., PAMPIN, E. M., VASELLI, O., AND BORRINI, D. (2011). Biotic and inorganic control on travertine deposition at Bullicame 3 spring (Viterbo, Italy): A multidisciplinary approach. *Geochimica et Cosmochimica Acta*, 75(16), 4441–4455.
- DI FRANCESCO, L., FABBI, S., SANTANTONIO, M., BIGI, S., AND POBLET, J. (2010). Contribution of different kinematic models and a complex Jurassic stratigraphy in the construction of a forward model for the Montagna dei Fiori fault-related fold (Central Apennines, Italy). *Geological Journal*, 45(January), 489–505.



- DOGLIONI, C., MERLINI, S., AND CANTARELLA, G. (1999). Foredeep geometries at the front of the Apennines in the Ionian Sea (central Mediterranean). *Earth and Planetary Science Letters*, 168, 243–254.
- DREYBRODT, W., LAUCKNER, J., ZAIHUA, L., SVENSSON, U., AND BUHMANN, D. (1996). The kinetics of the reaction  $\text{CO}_2 + \text{H}_2\text{O} \rightarrow \text{HCO}_3^-$  as one of the rate-limiting steps for the dissolution of calcite in the system  $\text{H}_2\text{O}-\text{CO}_2-\text{CaCO}_3$ . *Geochimica et Cosmochimica Acta*, 60(96), 3375–3381.
- EL DESOUKY, H., SOETE, J., CLAES, H., ÖZKUL, M., VANHAECKE, F., AND SWENNEN, R. (2015). Novel applications of fluid inclusions and isotope geochemistry in unravelling the genesis of fossil travertine systems. *Sedimentology*, 62(1), 27–56.
- FACCENNA, C., BECKER, T. W., LUCENTE, F. P., JOLIVET, L., AND ROSSETTI, F. (2001). History of subduction and back-arc extension in the Central Mediterranean. *Geophysical Journal International*, 145(3), 809–820.
- FACCENNA, C., PIROMALLO, C., CRESPO-BLANC, A., JOLIVET, L., AND ROSSETTI, F. (2004). Lateral slab deformation and the origin of the western Mediterranean arcs. *Tectonics*, 23.
- FACCENNA, C., SOLIGO, M., BILLI, A., DE FILIPPIS, L., FUNICIELLO, R., ROSSETTI, C., AND TUCCIMEI, P. (2008). Late Pleistocene depositional cycles of the Lapis Tiburtinus travertine (Tivoli, Central Italy): Possible influence of climate and fault activity. *Global and Planetary Change*, 63(4), 299–308.
- FOLK, R. L., AND CHAFETZ, H. S. (1983). Pisoliths (pisoids) in Quaternary travertines of Tivoli, Italy. In T. M. Peryt (Ed.), *Coated Grains* (p. 655). Berlin, Heidelberg: Springer-Verlag.
- FORD, T. D., AND PEDLEY, H. M. (1996). A review of tufa and travertine deposits of the world. *Earth-Science Reviews*, 41(3-4), 117–175.
- FOUKE, B. W. (2011). Hot-spring Systems Geobiology: abiotic and biotic influences on travertine formation at Mammoth Hot Springs, Yellowstone National Park, USA. *Sedimentology*, 58(1), 170–219.
- FOUKE, B. W., FARMER, J. D., DES MARAIS, D. J., PRATT, L., STURCHIO, N. C., BURNS, P. C., AND DISCIPULO, M. K. (2000). Depositional facies and aqueous-solid geochemistry of travertine-depositing hot springs (Angel Terrace, Mammoth Hot Springs, Yellowstone National Park, U.S.A.). *Journal of Sedimentary Research. Section A, Sedimentary Petrology and Processes : An International Journal of SEPM (Society for Sedimentary Geology)*, 70(3), 565–585.
- FRANCIS, P., AND OPPENHEIMER, C. (2004). *Volcanoes* (Second). Oxford: Oxford university press.
- G20. (2015). Pamukkale, Turkey. Retrieved April 18, 2015, from <https://g20.org/pamukkale-turkey/>
- GALDENZI, S., COCCHIONI, F., FILIPPONI, G., MORICHETTI, L., SCURI, S., SELVAGGIO, R., AND COCCHIONI, M. (2010). The sulfidic thermal caves of Acquasanta Terme (central Italy). *Journal of Cave and Karst Studies*, 72(1), 43–58.
- GANDIN, A., AND CAPEZZUOLI, E. (2014). Travertine: Distinctive depositional fabrics of carbonates from thermal spring systems. *Sedimentology*, 61(1), 264–290.

- GOLDSTEIN, R., AND REYNOLDS, J. (1994). *Systematics of Fluid Inclusions in diagenetic minerals*. SEPM Short Course (31).
- GONFIANTINI, R., PANICHI, C., AND TONGIORGI, E. (1968). Isotopic disequilibrium in travertine deposition. *Earth and Planetary Science Letters*, 5, 55–58.
- GUEGUEN, E., DOGLIONI, C., AND FERNANDEZ, M. (1997). Lithospheric boudinage in the Western Mediterranean back-arc basin. *Terra Nova*, 9, 184–187.
- GUIDO, D. M., AND CAMPBELL, K. A. (2012). Diverse subaerial and sublacustrine hot spring settings of the Cerro Negro epithermal system (Jurassic, Deseado Massif), Patagonia, Argentina. *Journal of Volcanology and Geothermal Research*, 229–230, 1–12.
- GULIA, L., AND WIEMER, S. (2010). The influence of tectonic regimes on the earthquake size distribution: A case study for Italy. *Geophysical Research Letters*, 37, 1–7.
- GUO, L., AND RIDING, R. (1994). Origin and diagenesis of Quaternary travertine shrub fabrics, Rapolano Terme, central Italy. *Sedimentology*, 41, 499–520.
- GUO, L., AND RIDING, R. (1998). Hot-spring travertine facies and sequences , Late Pleistocene , Rapolano Terme , Italy. *Sedimentology*, 45, 163–180.
- GUO, L., AND RIDING, R. (1999). Rapid facies changes in Holocene fissure ridge hot spring travertines , Rapolano Terme , Italy. *Sedimentology*.
- HANCOCK, P. L., CHALMERS, R. M. L., ALTUNEL, E., AND ÇAKIR, Z. (1999). Travitonics: Using travertines in active fault studies. *Journal of Structural Geology*, 21(8-9), 903–916.
- HARRISON, R. D., ELLIS, H., JENKINS, H. D. B., BRIERLEY, A. W., DAWSON, B. E., DUDENEY, A. W. L., HARRIS, J., STOKES, B. J., VOKINS, M. D. W., AND WENHAM, E. J. (2010). *Revised Book of Data*. (H. Ellis, Ed.) (Twenty-sev). Essex: Pearson Education Limited.
- HIATT, E. E., AND PUFAHL, P. K. (2014). Cathodoluminescence petrography of carbonate rocks: a review of applications for understanding diagenesis, reservoir quality and pore system evolution. In *Mineralogical Association of Canada Short Course* (Vol. 45, pp. 75–96).
- HOEFS, J. (2009). *Geochemistry* (Sixth). Berlin: Springer-Verlag.
- HONLET, R. (2013). *Sediment-petrological study and reservoir characterization of travertine carbonates in Rapolano Terme, Italy*. Unpublished Master's Thesis, KU Leuven.
- KANDIANIS, M. T., FOUKE, B. W., JOHNSON, R. W., VEYSEY, J., AND INSKEEP, W. P. (2008). Microbial biomass: A catalyst for CaCO<sub>3</sub> precipitation in advection-dominated transport regimes. *Bulletin of the Geological Society of America*, 120(3-4), 442–450.
- KELE, S., DEMÉNY, A., SIKLÓSY, Z., NÉMETH, T., TÓTH, M., AND KOVÁCS, M. B. (2008). Chemical and stable isotope composition of recent hot-water travertines and associated thermal waters, from Egerszalók, Hungary: Depositional facies and non-equilibrium fractionation. *Sedimentary Geology*, 211(3-4), 53–72.

- KELE, S., ÖZKUL, M., FÓRIZS, I., GÖKGÖZ, A., BAYKARA, M. O., ALÇİÇEK, M. C., AND NÉMETH, T. (2011). Stable isotope geochemical study of Pamukkale travertines: New evidences of low-temperature non-equilibrium calcite-water fractionation. *Sedimentary Geology*, 238(1-2), 191–212.
- KERRICH, R. (1976). Some Effects of Tectonic Recrystallisation on Fluid Inclusions in Vein Quartz. *Contributions to Mineralogy and Petrology*, 59, 195–202.
- KOBAN, C. G., AND SCHWEIGERT, G. (1993). Microbial origin of travertine fabrics: two examples from Southern Germany (Pleistocene Stuttgart travertines and Miocene Riedöschingen travertine). *Facies*, 29, 251 – 264.
- KOOPMAN, A. (1983). Detachment tectonics in the Central Apennines, Italy. *Geologica Ultraiectina: Mededelingen van Het Instituut Voor Aardwetenschappen Der Rijksuniversiteit Te Utrecht*, 30, 1–155.
- KRUMBEIN, W. E. (1979). Calcification by bacteria and algae. In P. A. Trudinger & D. J. Swaine (Eds.), *Biogeochemical cycling of Mineral-forming Elements* (pp. 47–68). New York: Elsevier.
- LAPIDES, D. N. (1978). *McGraw-Hill Encyclopedia of the Geological Sciences*. (D. N. Lapedes, S. P. Parker, J. Weil, & E. J. Fox, Eds.). New York: McGraw-Hill Book Company.
- LEEMAN, W. P., DOE, B. R., AND WHELAN, J. (1977). Radiogenic and stable isotope studies of hot-spring deposits in Yellowstone National Park and their genetic implications. *Geochemical Journal*, 11, 65–74.
- LEVORSEN, A. I. (1954). *Geology of Petroleum*. San Fransisco: W.H. Freeman and company.
- LOTTAROLI, F., MECIANI, L., AND ANDREOTTI, P. (2012). West Africa Presalt Exploration : Background and Perspective of the West African “Tupi” myth. *GCS SEPM*, 460–468.
- LU, G., ZHENG, C., DONAHOE, R. J., AND LYONS, W. B. (2000). Controlling processes in a CaCO<sub>3</sub> precipitating stream in Huanglong Natural Scenic District , Sichuan , China. *Journal of Hydrology*, 230, 34–54.
- MADONNA, R., SIGNANINI, P., CREMA, G., SABATINO, B. DI, RAINONE, M. L., AND NUNZIO, A. DI. (2005). The Geothermal Area of Acquasanta Terme ( Central Italy ): Main Characteristics and an Attempt of Field Evaluation. In *Proceedings World Geothermal Congress* (pp. 1–8).
- MAGGI, M., CIANFARRA, P., SALVINI, F., AND LIMA, C. (2015). Fracture architecture and the role of lamination-related mechanical anisotropy in the Acquasanta Terme travertine deposits ( Central Italy ) . *Geological Society of America Bulletin*, 1–18.
- MANATSCHAL, G., AND BERNOULLI, D. (1999). Architecture and tectonic evolution of nonvolcanic margins: Present-day Galicia and ancient Adria. *Tectonics*, 18(6), 1099–1119.
- MENICHETTI, M. (2008). Assetto strutturale del sistema geotermico di Acquasanta Terme (Ascoli Piceno). *Rendiconti Online Societa Geologica Italiana*, 1, 118–122.
- MINISSALE, A. (2004). Origin, transport and discharge of CO<sub>2</sub> in central Italy. *Earth-Science Reviews*, 66(1-2), 89–141.

- MINISSALE, A., KERRICK, D. M., MAGRO, G., MURRELL, M. T., PALADINI, M., RIHS, S., STURCHIO, N. C., TASSI, F., AND VASELLI, O. (2002). Geochemistry of Quaternary travertines in the region north of Rome (Italy): structural, hydrologic and paleoclimatic implications. *Earth and Planetary Science Letters*, 203(2), 709–728.
- MITCHELL, R. S. (1985). *Dictionary of Rocks*. New York: Van Nostrand.
- NANNI, T., AND VIVALDA, P. (2005). The aquifers of the Umbria-Marche Adriatic region : relationships between structural setting and groundwater chemistry. *Bollettino Della Società Geologica Italiana*, 124(3), 523–542.
- NEWTON, R. C., AND MANNING, C. E. (2005). Solubility of anhydrite, CaSO<sub>4</sub>, in NaCl-H<sub>2</sub>O solutions at high pressures and temperatures: Applications to fluid-rock interaction. *Journal of Petrology*, 46(4), 701–716.
- ÖZKUL, M., VAROL, B., AND ALÇİÇEC, C. (2002). Depositional environments and petrography of denizli travertines. *Mineral Res. Expl. Bull.*, 13–29.
- PANICHI, C., AND TONGIORGI, E. (1976). Carbon Isotopic Composition of CO<sub>2</sub> from Springs, Fumaroles, Mofettes and Travertines of Central and Southern Italy: A preliminary prospection method of geothermal area. *Proceedings of the 2nd U.N. Symposium on the Development and Use of Geothermal Energy, San Francisco, 20–29 May 1975*.
- PEDLEY, H. M., AND ROGERSON, M. (2010). *Tufas and Speleothems: Unravelling the Microbial and Physical Controls*. London: Geological Society of London.
- PEDLEY, M. (2009). Tufas and travertines of the Mediterranean region: A testing ground for freshwater carbonate concepts and developments. *Sedimentology*, 56, 221–246.
- PENTECOST, A. (1995). Geochemistry of carbon dioxide in six travertine-depositing waters of Italy. *Journal of Hydrology*, 167, 263–278.
- PENTECOST, A. (2005). *Travertine*. London: Springer-Verlag.
- PENTECOST, A., AND VILES, H. (1994). Überblick über und Neubewertung der Travertinklassifizierung. *Géographie Physique et Quaternaire*, 48(3), 305.
- RIDING, R. (2000). Microbial carbonates: The geological record of calcified bacterial-algal mats and biofilms. *Sedimentology*, 47(SUPPL. 1), 179–214.
- RODUIT, N. (2002-2007). JMicroVision: Image analysis toolbox for measuring and quantifying components of high-definition images. Version 1.2.2. Retrieved May 7, 2015, from <http://www.jmicrovision.com>
- ROEDDER, E. (1984). *Reviews in Mineralogy: Volume 12: Fluid inclusions*. (P. H. Ribbe, Ed.). Mineralogical Society of America.
- ROYDEN, L., PATACCA, E., AND SCANDONE, P. (1987). Segmentation and configuration of subducted lithosphere in Italy: an important control on thrust-belt and foredeep-basin evolution. *Geology*, 15(August), 714–717.

- SANI, F., DEL VENTISETTE, C., MONTANARI, D., COLI, M., NAFISSI, P., AND PIAZZINI, A. (2004). Tectonic evolution of the internal sector of the Central Apennines, Italy. *Marine and Petroleum Geology*, 21, 1235–1254.
- SANTANTONIO, M., AND CARMINATI, E. (2011). Jurassic rifting evolution of the Apennines and Southern Alps (Italy): Parallels and differences. *Bulletin of the Geological Society of America*, 123(3), 468–484.
- SCHIEFERDECKER, A. A. G. (1959). *Geological Nomenclature*. Royal Geological and Mining Society of The Netherlands.
- SCISCIANI, V., AGOSTINI, S., CALAMITA, F., PACE, P., CILLI, A., GIORI, I., AND PALTRINIERI, W. (2014). Positive inversion tectonics in foreland fold-and-thrust belts: A reappraisal of the Umbria–Marche Northern Apennines (Central Italy) by integrating geological and geophysical data. *Tectonophysics*, 637, 218–237.
- SCISCIANI, V., TAVARNELLI, E., AND CALAMITA, F. (2002). The interaction of extensional and contractional deformations in the outer zones of the Central Apennines, Italy. *Journal of Structural Geology*, 24, 1647–1658.
- SHARP, I., VERWER, K., FERREIRA, H., SNIDERO, M., MACHADO, V., HOLTAR, E., SWART, R., MARSH, J., GINDRE, L., PUIGDEFABREGAS, C., AND FEHERSKOV, M. (2012). Pre- and Post-Salt Non Marine Carbonates of the Namibe Basin. In *AAPG Annual Convention and Exhibition* (p. 1). Long Beach, California.
- SHEPHERD, T. J., RANKIN, A. H., AND ALDERTON, D. H. M. (1985). *A Practical Guide to Fluid Inclusion Studies*. California: University of California.
- SMEKENS, T. (2013). *Sedimentpetrological study and reservoir characterization of travertine carbonates near Süttő (Gerecse Mountains , Hungary )*. Unpublished Master's Thesis, KU Leuven
- SOETE, J. (2011). *Facies-development in the travertine quarry “FABER”. Sedimentology, diagenesis and macroporosity characterization*. Unpublished Master's Thesis, KU Leuven.
- STEIGER, R. H., AND JÄGER, E. (1977). Subcommission on geochronology: Convention on the use of decay constants in geo- and cosmochronology. *Earth and Planetary Science Letters*, 36(3), 359–362.
- TERRA, J. G. S., SPADINI, A. R., FRANÇA, A. B., SOMBRA, C. L., ZAMBONATO, E. E., JUSCHAKS, L. C. DA S., ARIENTI, L. M., ERTHAL, M. M., BLAETH, M., FRANCO, M. P., MATSUDA, N. S., CARRAMAL DA SILVA, N. G., MORETTI JUNIOR, P. A., D’AVILA, R. S. F., SCHIFFER DE SOUZA, R., TONNETTO, S. N., COUTO DOS ANJOS, S. M., SILVA, C. V., AND WINTER, W. R. (2010). Classificações clássicas de rochas carbonáticas. *B. Geoci. Petrobras, Rio de Janeiro*, 18(1), 9–29.
- TORSAETER, O., AND ABTAHI, M. (2000). *Experimental Reservoir Engineering Laboratory Work Book*. Department of Petroleum engineering and Applied Geophysics.
- VAN DEN KERKHOF, A. M., AND HEIN, U. F. (2001). Fluid inclusion petrography. *Lithos*, 55(1-4), 27–47.
- VAN DER PLAS, L., AND TOBI, A. C. (1965). Reliability of point counting results; reply. *American Journal of Science*, 263, 87–90.



- VANDEWIJNGAERDE, W. (2012). *Reservoir characterization including LiDAR analysis of a travertine reservoir analogue : The Ballik case study ( SW Turkey )*. Unpublished Master's Thesis, KU Leuven.
- VERHAERT, G. (2006). *Normal Fault Architecture and Related Fluid Flow in Carbonate Rocks*. Doctorate Thesis, KU Leuven.
- VERHAERT, G., MUCHEZ, P., KEPPENS, E., AND SINTUBIN, M. (2009). Fluid impact and spatial and temporal evolution of normal faulting in limestones . A case study in the Burdur- Isparta region ( SW Turkey ). *Geologica Belgica*, 12, 59–73.
- VERHAERT, G., MUCHEZ, P., SINTUBIN, M., SIMILOX-TOHON, D., VANDYCKE, S., KEPPENS, E., HODGE, E. J., AND RICHARDS, D. A. (2004). Origin of palaeofluids in a normal fault setting in the Aegean region. *Geofluids*, 4(4), 300–314.
- VERWEIJ, J. M. (1993). Chapter 2: Groundwater flow in sedimentary basins. In *Hydrocarbon Migration Systems Analysis* (p. 273). Amsterdam: Elsevier.
- VEYSEY, J., FOUKE, B. W., KANDIANIS, M. T., SCHICKEL, T. J., JOHNSON, R. W., AND GOLDENFELD, N. (2008). Reconstruction of Water Temperature, pH, and Flux of Ancient Hot Springs from Travertine Depositional Facies. *Journal of Sedimentary Research*, 78(2), 69–76.
- WALTERS, R. J., ELLIOTT, J. R., D'AGOSTINO, N., ENGLAND, P. C., HUNSTAD, I., JACKSON, J. A., PARSONS, B., PHILLIPS, R. J., AND ROBERTS EDINBURGH, G. (2009). The 2009 L'Aquila earthquake (central Italy): A source mechanism and implications for seismic hazard. *Geophysical Research Letters*, 36, 1–7.
- WHITCAR, M. J. (1999). Carbon and hydrogen isotope systematics of bacterial formation and oxidation of methane. *Chemical Geology*, 161(1-3), 291–314.
- WRIGHT, V. P. (2012). Lacustrine carbonates in rift settings: the interaction of volcanic and microbial processes on carbonate deposition. *Geological Society, London, Special Publications*, 370(1), 39–47.



## Chapter 10: Appendices

The most important appendices are presented in this chapter. Additional images are added on a DVD as this allows for a clearer view on the figures and allows zooming. These figures are not necessary to understand the text, but are made for this research and actively used to come up with the proposed reservoir analogue. Reference to the DVD will be made where it is needed.

### Appendix 1: Methodology background

#### 1.1. Cathodoluminescence

During a cathodoluminescence study, electrons of atoms are excited to a higher energetic level. They will fall back to their original state in one or separate steps, during which a photon is emitted. The photon will have a certain wavelength, which is determined by the amount of energy between the two energy levels (Figure 10-1). The difference in wavelengths for different minerals results in a different luminescence colour. The amount of energy between the levels of excitation (or the wavelength) depends on a variety of factors. The most important factor is the presence of trace elements in the crystal lattice (e.g.:  $\text{Mn}^{2+}$ ,  $\text{Fe}^{2+}$ , REE, etc.). Other factors, which are of minor importance are distorted crystal surfaces, cracks, lattice defects due to abnormally sized or ionized atoms, etc. (Dorobek & Watkinson, 1988; Machel, 1985). Factors affecting luminescence are classified in two groups. The first group are intrinsic factors, of which crystal defects are an example. Electron transitions are determined by the gap in between the valence and conduction band, which are crystal dependent parameters. The other group are extrinsic factors, which are mainly the (effects of) impurity ions and trace elements (Gucsik, 2009). Extrinsic factors are usually the most important.

The presence of trace elements is the most important cause for luminescence of crystals. These trace elements could act as activators, quenchers (inhibitors) and sensitizers (Hiatt & Pufahl, 2014; Machel, 1985; Pierson, 1981). An activator (e.g.  $\text{Mn}^{2+}$  and REE) makes the luminescence brighter, whereas a quencher (e.g.  $\text{Fe}^{2+}$ ,  $\text{Ni}^{2+}$  and  $\text{Co}^{2+}$ ) tends to dim or extinguish the luminescence. Sensitizers do neither

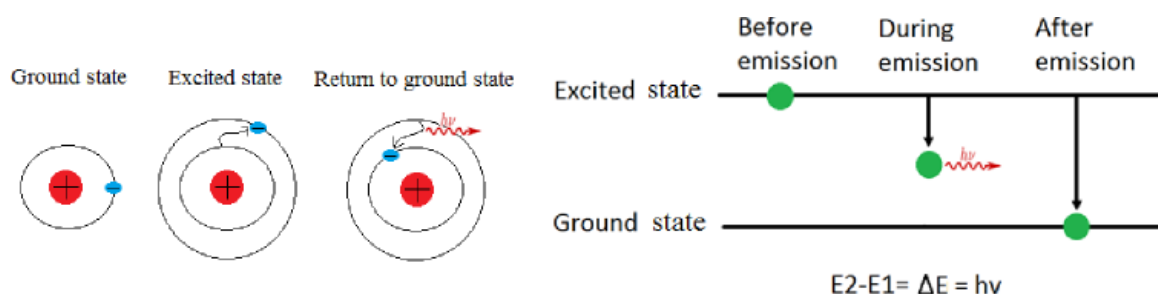


Figure 10-1: Excitation of an atom and subsequent drop to ground state, during which a photon, with a characteristic wavelength, is emitted ( $\lambda = c/\nu$ , with  $c$  = the speed of light,  $\nu$  = the frequency, which is determined by the difference between the two energetic levels). Excitation is caused by bombardment with a highly energetic electron beam. Figure from Soete (2011)

of these things, but they “sensitize” or facilitate the effect of the activators. Examples of such sensitizers are  $\text{Pb}^{2+}$  and  $\text{Ce}^{3+}$  (Hiatt & Pufahl, 2014). The most important activator in carbonate minerals is  $\text{Mn}^{2+}$  and the most important quencher is  $\text{Fe}^{2+}$ . The presence of these two elements is often used to determine the redox conditions (Eh) of the fluids that precipitated the studied minerals as both these elements have different redox-potentials (Barnaby & Rimstidt, 1989; Hiatt & Pufahl, 2014). Different redox conditions will result in non-luminescent, bright-luminescent and non-luminescent minerals indicating oxidizing (i.e. atmospheric or vadose), slightly reducing (i.e. phreatic) and reducing conditions, respectively (Figure 10-2). This sequence indicates the change of  $\text{Mn}^{2+}/\text{Fe}^{2+}$ -ratio with changing Eh and shows that  $\text{Mn}^{4+}$  is more easily reduced, compared to  $\text{Fe}^{3+}$  (Barnaby & Rimstidt, 1989; Hiatt & Pufahl, 2014).

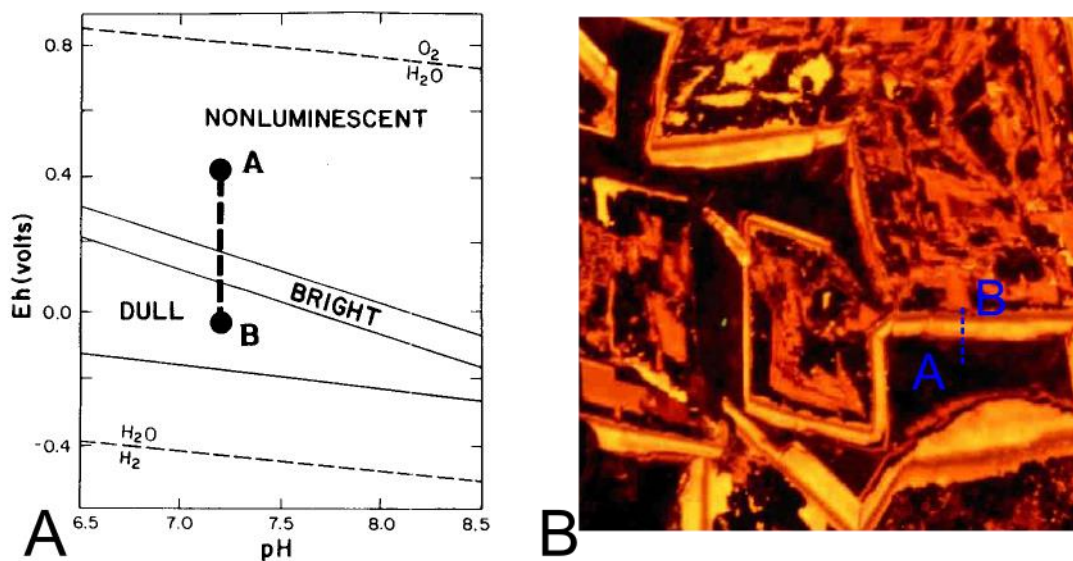


Figure 10-2: Variation in cathodoluminescence in varying redox-conditions. A. colour variation in function of pH and Eh. More oxidizing conditions will cause non-luminescent cements ( $\text{Mn}^{2+}$  and  $\text{Fe}^{2+}$  are both absent), with decreasing Eh (less oxygen and more reducing conditions) will lead to bright ( $\text{Mn}^{2+}$  in cements, but no  $\text{Fe}^{2+}$ ) and ultimately to dull ( $\text{Mn}^{2+}$  and  $\text{Fe}^{2+}$  both in cements). B. Illustration of non – bright – dull sequence in calcite cements.

## 1.2. X-Ray Diffraction

The X-rays that are sent to the sample will be scattered by the electrons of the atoms that comprise the crystals in more or less random spherical directions, as they make the electrons oscillate and send out secondary X-rays themselves. A lot of energy will be lost due to absorption. For crystals in a sample the main zones of scattering are the crystal planes because electrons are more concentrated here. The spherically scattered X-rays will interfere with each other. The resulting interference pattern is measured as it is characteristic to the crystal structure and thus to the mineralogy. When a powder sample of randomly oriented crystals is studied, the interference pattern is called a “diffractogram” (Waseda et al., 2011). The mineralogy can be determined by calculation of the distance that two crystal

planes are away from each other ( $d$ ), based on Bragg's equation of which the wave length ( $\lambda$ ) and the angle (known as  $2\theta$ ) are known (Figure 10-3; Klein & Dutrow, 2007; Waseda et al., 2011):

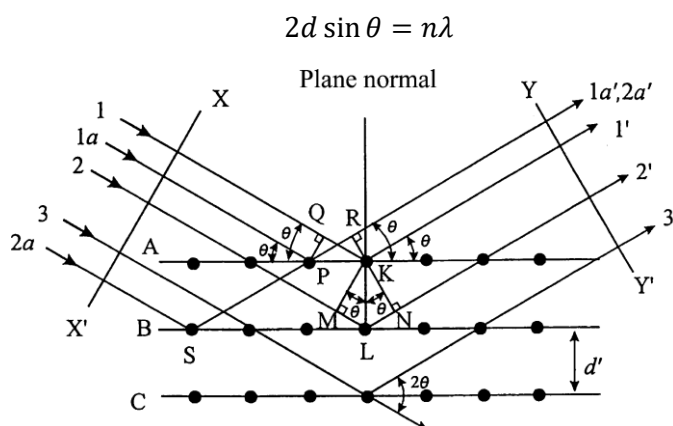


Figure 10-3: Illustration of Bragg's equation. The distance between two crystal lattices is given by  $d$  and the angle of incidence is given by  $\theta$ . Figure from Waseda et al. (2011)

### 1.3. Stable isotopes

Isotopes are atoms that have the same amount of protons, but with a different amount of neutrons. The core of the atoms consists out of a certain amount of neutrons and protons. The amount of protons determines the atomic number, which is dependent on the element. The amount of proton and neutrons combined gives the atomic mass, which can vary due to variation in the amount of neutrons. Isotopes are atoms with the same atomic number but a different atomic mass. Even though the different isotopes of one element behave in the same way, the small difference in mass results in differences in bonding and kinetics (Baskaran, 2012). An examples of this is photosynthesis, in which the light carbon-isotopes are favoured as they more easily participate in the reaction. Stable isotopes are isotopes from elements that do not undergo radioactive decay. They can be added to the system through decay of other elements, but they will not decay themselves.

### 1.4. ICP-OES (Inductively Coupled Plasma Optical Emission Spectroscopy)

Analysis is done with a VARIAN ICP-OES spectrometer of the 700 series. In this machine the sample solution is delivered into a nebulizer in which the sample is atomized and introduced in a plasma flame with temperatures of 8000°C. This temperature excites all the elements, causing them to emit light. The emitted light has a wavelength, specific to the element. The emitted light of all the different atomic species is send to a diffraction grid, which resolves the light into a spectrum. The diffracted light is amplified and collected per wavelength. The intensity is compared with standards to obtain the concentration of the measured element in the sample. The concentration is finally recalculated to reflect the concentration of the elements in ppm ( $\mu\text{g/g}$ ) and of  $\text{Ca}^{2+}$  in percentages.



## Appendix 2: Field work

The field work consisted of several types of data gathering. The appendix will show the figures that are created from field data.

### 2.1. Lithologs

Twelve lithologs are created in total, two of which are shown here (Figure 10-4 and 10-5). The other lithologs are on the DVD. A point-counting analysis was performed on field photographs to assess the porosity quantitatively. This allowed for correct lithologs, in which porosity variation is shown (Table 10-1). It is assumed that all pictures are sufficiently large to be analysing a Representative Elementary Volume.

	Porosity	Counts	Std. Dev
Micritic Dendrite Shrubs	14.00	250	2.19
	25.60	250	2.76
	13.43	350	1.82
Microbial mats type I	37.33	300	2.79
	27.60	250	2.83
Microbial mats type II	26.00	250	2.77
	28.40	250	2.85
Erosional horizon	21.60	250	2.60
	23.20	250	2.67
Crystalline crust	18.50	400	1.94
Microbial laminites	33.20	250	2.98
	24.80	250	2.73
Shrubs	43.60	250	3.14
	32.86	Object extraction	
	22.33		

Table 10-1: Point-counting data of field photographs.

### 2.2. Linedrawing

Linedrawings have been drawn on the field and they form the basis of the 3D model. One other example is given in this appendix and the other ones are on the DVD (Figure 10-6).

### 2.3. Geological map

A geological map of the area close to the quarry has been constructed during the field work. The map records the three travertine levels of Acquasanta Terme (Figure 10-7).

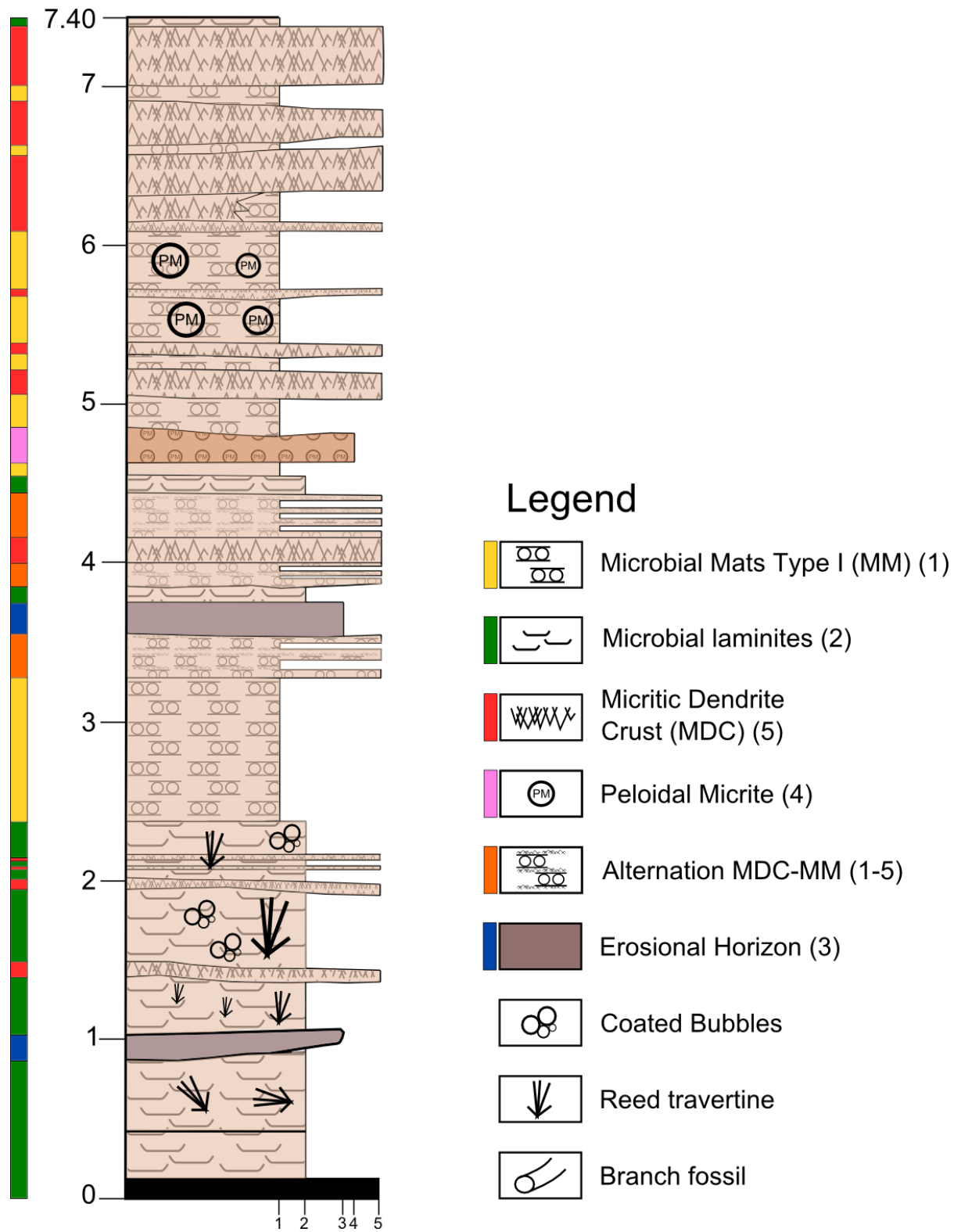


Figure 10-4: Litholog with variation from microbial laminites towards interfingering microbial mats and micritic dendrite crusts.

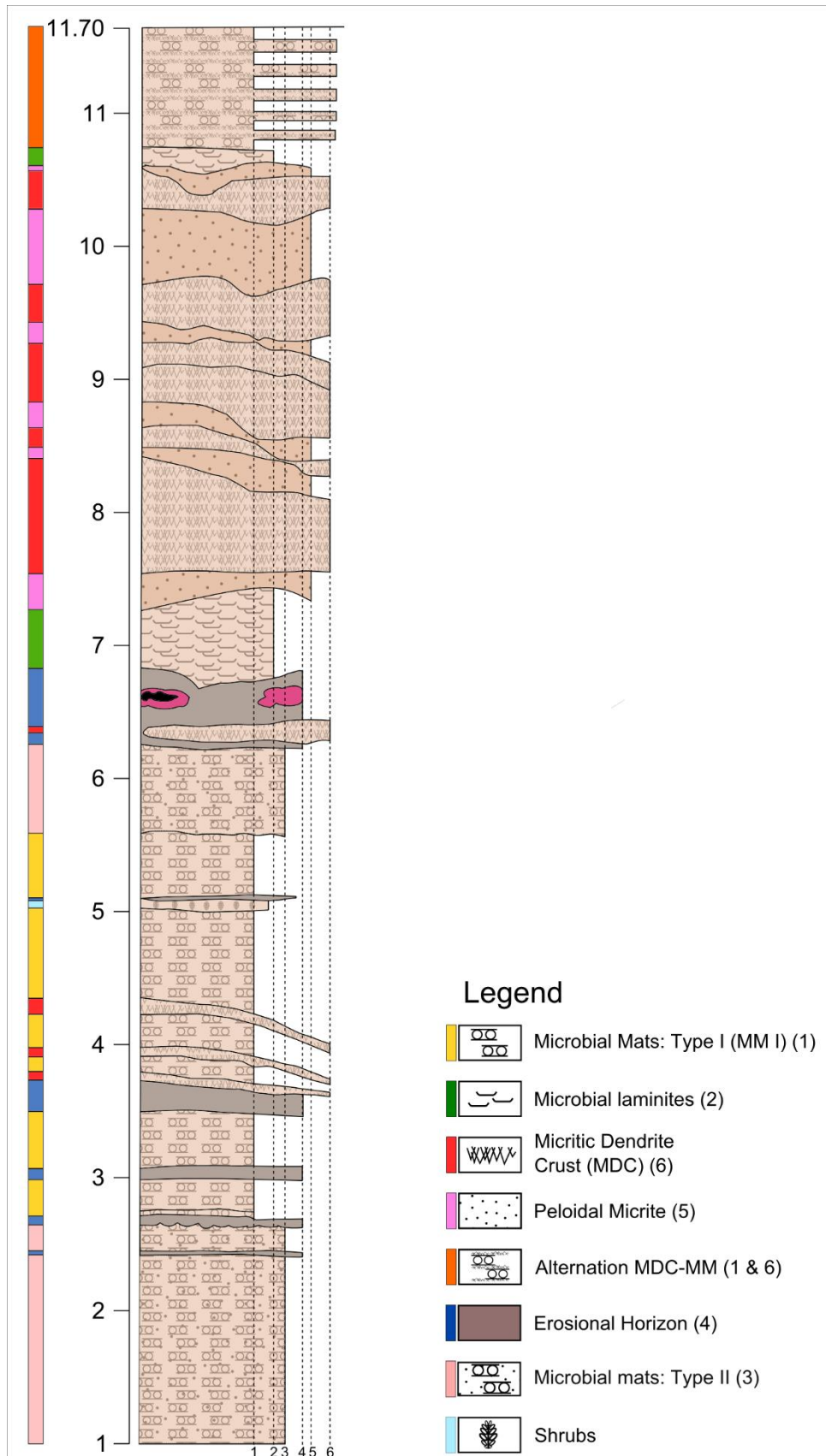


Figure 10-5: More complex example of a litholog. The dip of the layers is indicated in the litholog. Gradation from type II microbial mats (flat lithofacies) to lenticular deposits (sloping lithofacies) is seen from this litholog.

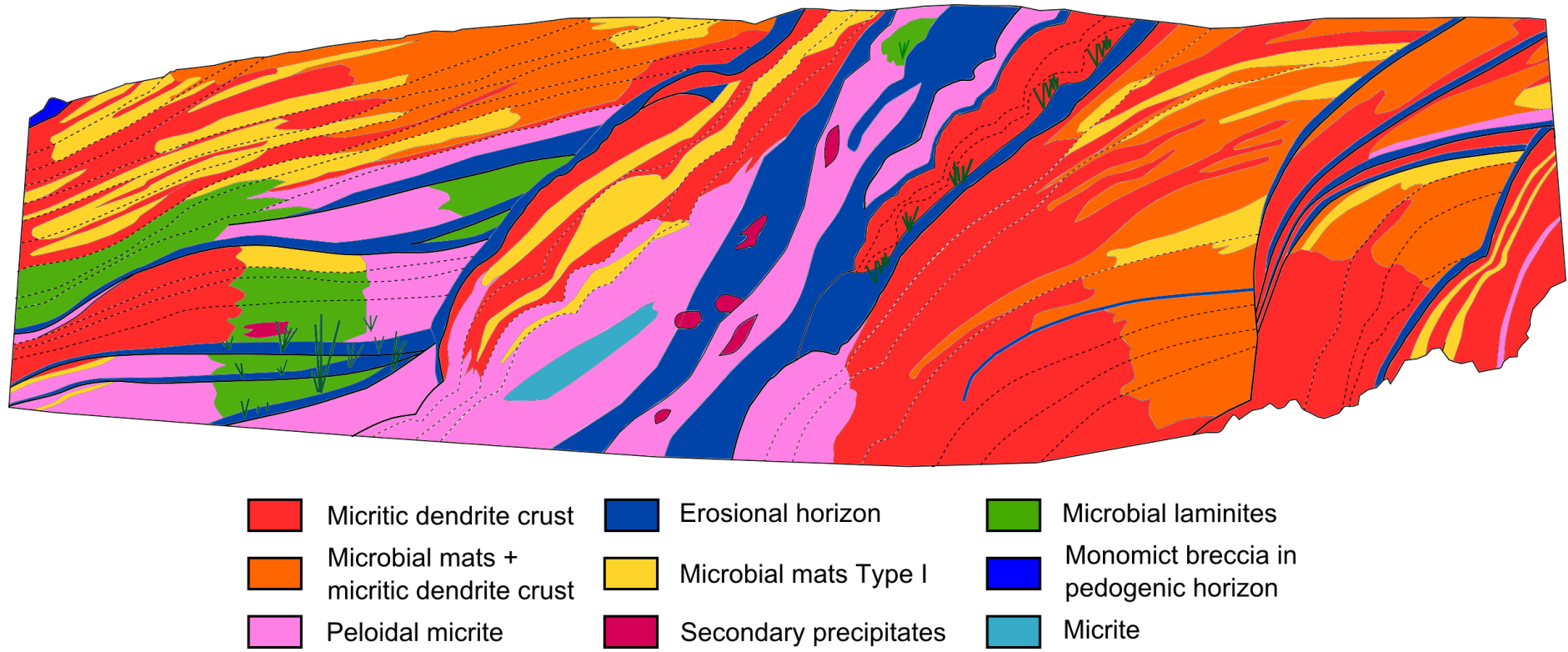
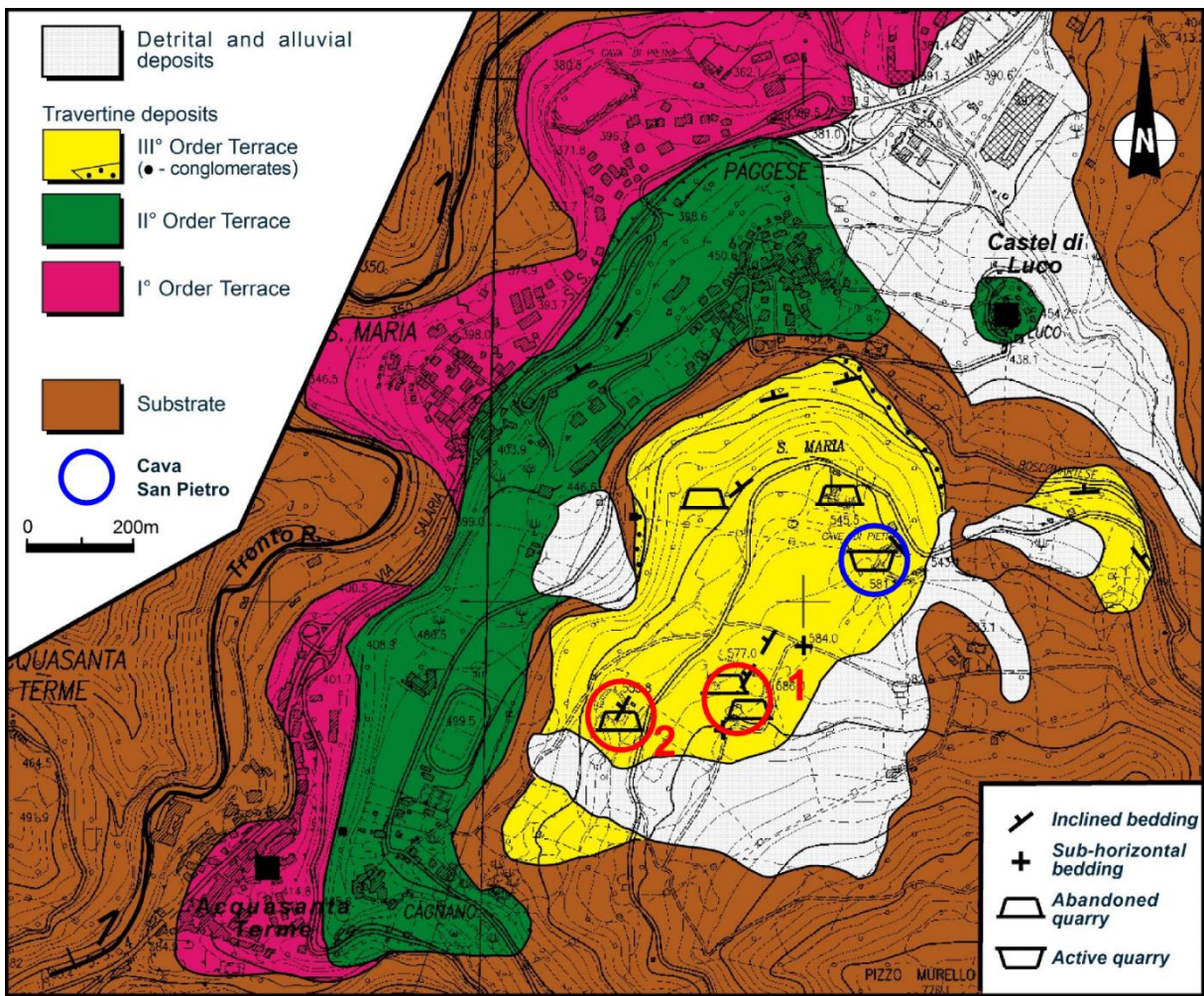


Figure 10-6: Example of a linedrawing of the south-western wall on the second level of the quarry.





*Figure 10-7: Geological map of the Acquasanta travertine bodies in the proximity of Cava San Pietro (blue circle), where the research has been conducted. This quarry is situated in the upper travertine body of the Acquasanta travertines. The oldest travertines are topographically the highest. The youngest travertine terrace (I° order terrace) is located closest to the Tronto River. The abandoned quarries in which samples are taken are indicated with red circles.*

## Appendix 3: Samples

Samples are taken from the following walls (Figure 10-8). The sample numbers are indicated on the photographs of the walls individually and these photographs are added to the DVD. The seven different depositional bodies that are discerned are indicated on these figures. This way, the samples are linked to their depositional body. A table with all the samples with the performed techniques is given at the end of this section (Table 10-2).

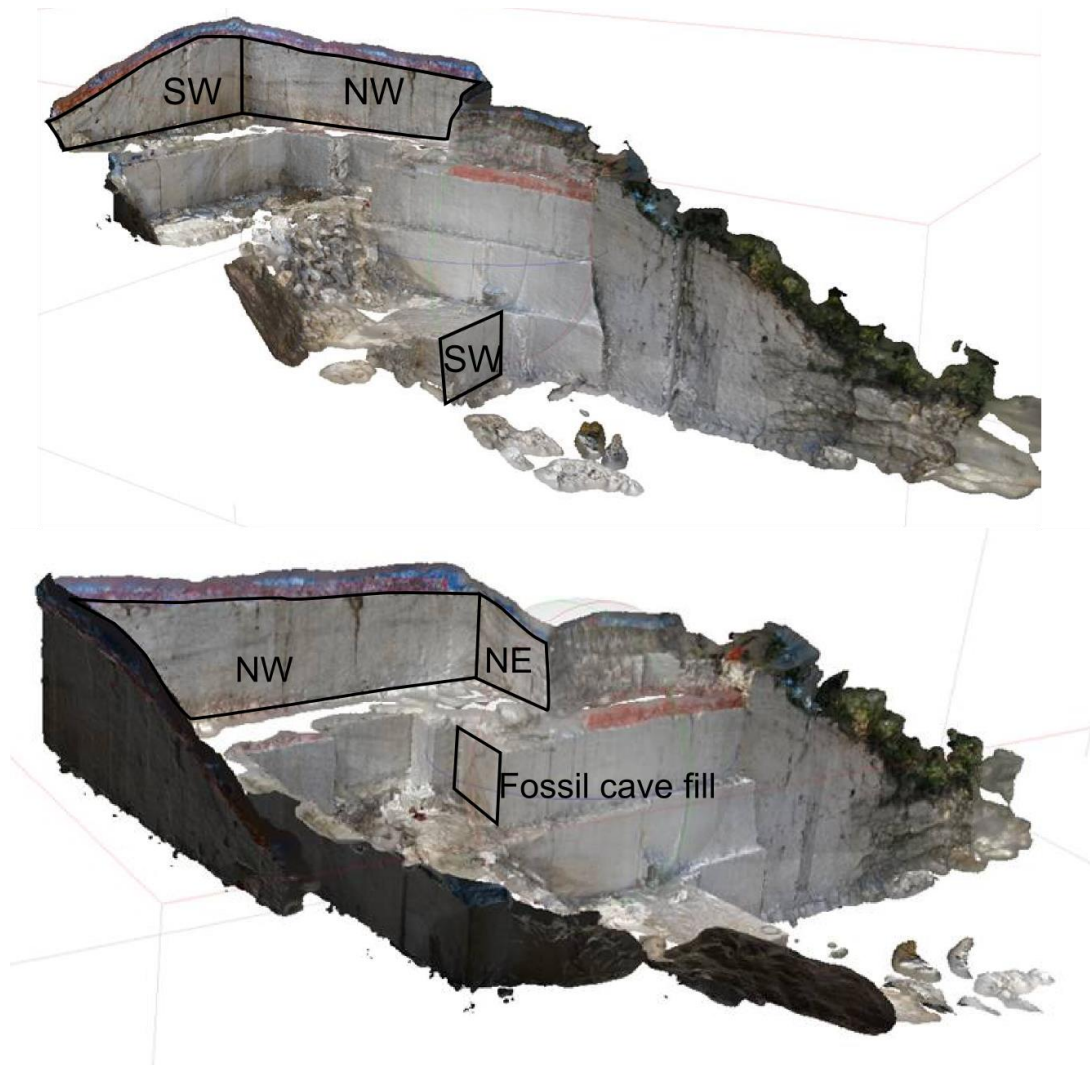


Figure 10-8: 3D representation from photogrammetry. The different walls along which samples are taken are indicated.

### 3.1. Sample description

#### 3.1.1. NE wall (upper level)

- 6: Black horizon. Grey-brownish colour. Micritic. Dissolution forms vuggy pores with secondary precipitation. Also contains small white fragments.



- 7: Coated bubbles and curved laminites.
- 8: Sampled for the bubbles. Also contains curved laminites (no mats, as these would give more vacuolar pores). Possibly secondary precipitation on laminites and in a bubble. Brownish horizon at top of the plug.
- 9: Laminites, vacuolar porosity.
- 10: Laminites between reed. The sample is most likely curved laminite with a crystalline part. This could be primary (thermal) or secondary (karstic) precipitates. The lower part contains small fragments, part of erosional horizon?
- 11: curved microbial laminites.
- 12: laminites, rafts and coated bubbles.
- 13: Micritic dendrite crusts at rim of terrace.
- 14: There is a darker colour present which could be part of an erosional horizon. It contains some irregular holes, with possibly some secondary precipitation. Contact with overlying dendrite shrubs or peloidal micrite. Might also be a transitional zone lithotype. Pisoids?
- 17: large core: contains mats/laminites, micrite and possibly small shrubs. Contains pisoids.
- 18: core: micrite in lower part. Also contains small secondary precipitates (tufted erected structures). Contains part of a vein.
- 20: Shrubs on raft.
- 21-23: Vertical section of shrubs, three samples on top of each other. They become gradually denser (less porous) towards the top.

### 3.1.2. SW wall (upper level)

- 1: vertical crust, five layers and alternation white, translucent and brown.
- 2: vertical crust from vein, brown.
- 3: vertical crust, white.
- 4: sample of erosional layer, records the connection with micrite. White fragments in the grey part of the sample.
- 15: core taken next to vertical vein and is taken from feather crystals. Sample contains leaves.
- 16: core from travertine vein.
- 24: core from crystalline crust (alternation brownish micrite and white micrite).
- 25: alternation micrite and crystalline layers → crystalline crust.
- 26: alternation micrite and crystalline crust → crystalline crust.
- 27: crystalline crust.
- 28: peloidal micrite adjacent to crystalline crust. PM contains some larger vuggy pores, parallel to layers.

- 29: Core in crystalline crust. Alternation with peloidal micrite and dendrite shrubs is seen.
- 30: large block with micritic dendrites and microterraces.
- 31: core of micritic dendrite crusts.
- 32: core with microbial mats.
- 42: grey horizon, sample is micritic and has grey colour.
- 43: grey horizon, very dark colour of sample, compared to 42.
- 97: From the possible “thrombolytic structures” on the upper level. This is the upper part. Looks all rather vuggy.
- 98: From same structure. It looks micritic with dissolution vugs, which are later filled with white cements.
- 99: Horizontal section in vertical crust. Is broken in several pieces. Each piece contains one layer of the crust.
- 100: Vertical crust. A crystal growing in another direction, compared to the main growth direction is present in the sample.

#### 3.1.3. NW wall (upper level)

- 5: Grey horizon, contains white fragments.
- 19: vertical crust material from the large vein.

#### 3.1.4. Second level: Block

- 33: Stalactite from block.

#### 3.1.5. NE wall (second level) with fossil cave

- 44: (Wall) Vein with thin layers with different colours.
- 45: (Wall) Primary precipitation of dendrite shrubs?
- 46: (Wall) Brownish horizon underneath the crystalline crust. Is this similar to soil formation? It appears to consist of small internal, whiter layers.
- 47: (Wall) vein sample.
- 48: (Wall) plant fragments.
- 49: (Wall) hard to sample because of softness, resembles bryophytes.
- 50: (Floor) core of a circle, horizontal layers.
- 51: (Floor) crystalline and porous parts are alternating.
- 52: (Floor) Core of one of the small circles. Parallel lines. Rather high porosity, but small pores.
- 53: (Floor) In circular structure. Dense layers (with several sublayers) alternated by very porous layer. Is this the side of a stalacmite.
- 54: (Floor) Brownish lower part. Whiter, more crystalline upper part. Comes from floor.

- 55: (Floor) Colour is greyish. Some small fractures occur. Are these leaves? Secondary precipitation also appears to be present. Appears very dense, maybe crystalline.
- 56: (Floor) Upper part is brown, with irregular pores. Also smaller angular white fragments occur. The lower part is lighter and seems rather crystalline. Pores are rather irregular as well. Resembles erosional horizons.
- 57: Part of vein.
- 58: Same as 49 (same layer): Looks rather crystalline.
- 59: Sample contains two different colours. On one side it is rather brown. It contains small dissolution holes, with even secondary precipitation.
- 60: Sample in very dark colour, with alternating small layers. Appears to consist of crystals. Is this thermal or meteoric?

### 3.1.6. NW wall (lower level): fallen wall

The wall on which the samples are taken was just excavated. This allowed for sampling a vertical section.

- 62: Vacuolar, mats
- 63: Dendrite crust + vacuolar pores (mats).
- 64: Peloidal Micrite.
- 65: Dendrite crust adjacent to microterrace near peloidal micrite (like sample 30).
- 66: Very porous sample, micritic, not well cemented.
- 67: micritic dendrite crust is main lithotype, but a more porous zone could be micritic (peloidal micrite).
- 68: feather crystals: possible honeycomb structure.
- 69: Mats and vacuolar pores.
- 70: Mats, vacuolar porosity.
- 71: Peloidal micrite, brownish colour, porous.
- 72: Micritic dendrite crust and mats (not very porous).
- 73: Peloidal micrite and dendrite crust.
- 74: Mats with a cement layer.
- 75: Sample is taken in dendrite crusts, but porosity could indicate it is peloidal micrite.
- 76: Dendrite crust, transition to peloidal micrite.
- 77: Sample is micritic. Lower part appear to be mats, based on the vacuolar pores. Microbial mats type II

- 78: Sample on top of block: Part consists of dendrite crust, the other part is bacterial mats. Are these grading into each other?
- 79: Sample on top of block: Mainly dendrite crust and peloidal micrite.
- 80: Clear crystals from a vein, in between the layered travertine. Are these aragonite?

### 3.1.7. *Abandoned quarry 1*

Vein is parallel to bedding. This suggests that overburden must have been present because the high pressurized fluids would probably break overlying rocks if no overburden is present.

- 81: Main vein. Contains both white and the brown layers.
- 82: This one only contains the brown vein. Has several different colours and a small part of the host material.
- 83: Very dark micritic material. The many vuggy pores point at dissolution. Secondary precipitation is present in here, but is very rare.
- 84: Second dark brown vein material, not a lot is left. Also contains host rock which is micritic with a lot of pores.
- 85: Brown vein, close to where it joins with the white vein. Very dark brown layers. Small amount of host material is present.
- 86: Consists mainly of peloidal micrite. Also contains some pores which are round and seem long. Could it be part of a branch/root? Or maybe some reed? It is near to the dark horizon, which just overlies it, so are possible.
- 87: Peloidal micrite. In this example it is clear that a branch is present.
- 88: vertical section of vein by drilling a block. A lot of different colours appear.

### 3.1.8. *Abandoned quarry 2: sloping environment*

- 89: resembles steeply sloping microbial mats or dendrite crust. The plug itself look like steep sloping mats, but the pores are stretched and not high. Peloidal Micrite also present, based on a more brownish colour.
- 90: Originally described as mats with peloidal micrite. This seems to be correct but white circular structures appear to be a horizontal section of shrubs. Also honeycomb structure appears to be present between branches of a shrub.
- 91: Micritic dendrite shrubs
- 92: Sloping microbial mats. There appears to be secondary precipitation in the vacuolar pores.
- 93: Crystals similar to vertical crust, without the thin layers. Probably infill of a small vug. Different colours are present: brown, white, translucent.

- 94: Sample appears to be consisting of micritic (peloidal?) material. Two different colours are present. Dissolution is the clearest in the light brown part.

### 3.1.9. *Extra:*

- 34: (Along road near quarry) Veins in marl.
- 35: Pisoids.
- 36: (Colle San Nicola) continental lacustrine carbonates. These are micritic.
- 37: (Colle San Nicola) Uncertain what it is, carbonate.
- 38: (Colle San Nicola) Chips from basal conglomerate, underlying a travertine body. Appear micritic.
- 39: Phytoclastic rich rock. Resembles tufa. Bryophytes are present, which could indicate system being a tufa.
- 40: (Delphinos house; Civitella del Tronto) Resembles plants, are these reeds/plants/bryophytes/algae-mosses/...?
- 41: (Along Tronto river) Marly limestone with veins.
- 61: (Along Tronto river) active tufa.
- 95: Tronto river: piece of marine limestone.
- 96: Bryophytes of Colle San Nicola.

[illegible]





## Appendix 4: Data and Tables

### 4.1. Structural data

Dip	Dip Dir	type	notes
220	75	fracture	evidence of circulation with mm-thick, white veins
240	50	fracture	evidence of circulation with mm-thick, white veins
280	55	fracture	open, probably gravitative
180	70	fracture	filled with fine material
130	90	vertical conduit	evidence of circulation with mm-thick, white veins
180	60	fracture	filled with fine material
130	90	vertical conduit	evidence of circulation with mm-thick, white veins
220	25	fracture	open, low angle, probably gravitative
40	82		Large system of syntethic fractures, coalescent with the first one (130NE82) with offlapping relation. Some are circulated, some are opened.
58	87		
55	80		
47	89		
51	85		
43	83		
46	86		
76	89	fracture	filled with fine material
180	90	fracture	opened
200	90	fracture	opened, 20cm wide
175	90	fracture	opened, 20cm wide
80	85	vertical conduit	
110	90	vertical conduit	
355	65	fracture	opened, small evidences of circulation, speleothems
350	85	fracture	opened, small evidences of circulation, speleothems
148	90	fracture	opened, small evidences of circulation, speleothems
90	78	fracture	opened, small evidences of circulation, speleothems
170	90	fracture	opened
160	20	fracture	open, low angle, probably gravitative
130	90	fracture, lateral to a vertical conduit	opened, with Fe-Ox circulation, karstic evidence
100	90	vertical conduit	opened
30	90	fracture	opened, gravitative
120	85	fracture	opened, gravitative
162	80	fracture	opened, gravitative
205	90	fracture	opened, gravitative, filled with soil material
210	60	fracture	opened, gravitative, filled with soil material
40	85	fracture	opened, 10cm wide
200	80	fracture	opened, 5cm wide
30	80	fracture	opened, 5cm wide
35	85	fracture	opened, with speleothems

Table 10-2: Data of the fractures in the travertine body

## 4.2. Petrophysical data

Sample Number	Lithotype	Ambient He Porosity	Gas Horizontal Permeability	Emp. Klink. Hor. Perm.	Grain Density	Remarks
		(% of Vb)	(mD)	(mD)	(g/ml)	
NJ06	Erosional	18.2	0.19	0.12	2.66	Vuggy
NJ07	Micr. Laminites	22.5	150	139	2.59	Vuggy
NJ08	Micr. Laminites	25.2	1.61	1.14	2.61	Vuggy
NJ10	Micr. Laminites	23.1	0.11	0.07	2.60	Vuggy
NJ12	Micr. Laminites	26.5	22.9	19.0	2.58	Vuggy
NJ18	Micr. Laminites	20.7	14.5	11.7	2.55	Vuggy
NJ22	Shrub	20.3	5674	5552	2.65	Vuggy
NJ24	Dendr. Crust	3.8	0.06	0.04	2.58	
NJ27	Cryst. Crust	5.2	61.7	54.3	2.58	
NJ28	Cryst. Crust	10.9	159	148	2.64	
NJ30	Dendr. Crust	7.7	1.40	0.99	2.58	
NJ31	Dendr. Crust (v)	10.5	11.4	9.12	2.56	
NJ32	Micr. Mats I	26.7	0.51	0.34	2.63	Accupyc, Vuggy
NJ42	Erosional	28.1	209	197	2.67	Vuggy
NJ62	Micr. Mats I	21.4	0.30	0.19	2.61	Vuggy
NJ63	Micr. Mats II	13.2	0.08	0.05	2.62	Vuggy
NJ66	Uncons. Micr.	36.9	264	253	2.56	
NJ69	Micr. Mats I	32.4	11.6	9.22	2.60	Vuggy
NJ70	Micr. Mars II	22.8	31.9	27.0	2.60	Vuggy
NJ71	Pel. Micrite	13.8	46.2	40.0	2.60	
NJ72	Pel. Micrite	13.2	3.33	2.47	2.60	
NJ73	Pel. Micrite	11.3	31.7	26.8	2.57	
NJ76	Dendr. Crust	4.6	1.90	1.36	2.58	
NJ77	Micr. Mars II	10.1	0.15	0.09	2.59	
NJ79	Dendr. Crust	6.8	0.44	0.29	2.60	

Table 10-3: Petrophysical data. The empirical Klinkenberg permeability is used in this research.

### 4.3. Geochemical data and statistical analysis

The patterns of the XRD-analysis are on the DVD. Data itself is in Results section 5.4.

		Lithology	d13C permil V-PDB	d18O permil V-PBD	d13C of CO <sub>2</sub>
					Panichi & T
1	AS14NJ001	Banded travertine	7.65	-12.35	-1.32
2	AS14NJ003	Banded travertine	7.50	-12.11	-1.50
3	AS14NJ019	Banded travertine	7.95	-11.68	-0.96
4	AS14NJ019	Banded travertine	7.95	-11.67	-0.96
5	AS14NJ019	Banded travertine	7.90	-11.67	-1.02
6	AS14NJ044	Fossil Cave (Vein)	14.58	-8.84	6.99
7	AS14NJ057	Fossil Cave (Vein)	13.44	-6.29	5.63
8	AS14NJ045	Fossil Cave (Bedded Trav.)	8.84	-11.18	0.11
9	AS14NJ050	Fossil Cave (Bedded Trav.)	8.67	-11.61	-0.10
10	AS14NJ034	Veins in marly limestone	-0.02	-2.44	N/A
11	AS14NJ069	Microbial Mats: Type I	7.80	-11.62	-1.14
12	AS14NJ032	Microbial Mats: Type I	8.20	-10.41	-0.66
13	AS14NJ012	Reed Travertine (microb. laminites)	8.16	-11.67	-0.71
14	AS14NJ007	Reed Travertine (coated bubbles)	8.26	-11.45	-0.59
15	AS14NJ022	Shrubs	8.25	-10.94	-0.59
16	AS14NJ030	Micritic Dendrite Crust	8.26	-10.45	-0.59
17	AS14NJ030	Microbial Mats: Type I	8.23	-10.59	-0.62
18	AS14NJ070	Micritic Dendrite Crust	7.92	-11.01	-1.00
19	AS14NJ014	Micritic Dendrite Crust	8.46	-10.78	-0.35
20	AS14NJ063	Micritic Dendrite Crust	7.75	-11.04	-1.20
21	AS14NJ067	Micritic Dendrite Crust	7.87	-12.27	-1.06
22	AS14NJ072	Micritic Dendrite Crust	8.13	-10.80	-0.74
23	AS14NJ079	Peloidal Micrite	7.93	-12.16	-0.99
24	AS14NJ080	Cements (Diagenetic)	6.42	-12.25	-2.80
25	AS14NJ071	Peloidal Micrite	8.14	-11.46	-0.73
26	AS14NJ056	Fossil Cave (Erosional Layer)	8.80	-10.19	0.07
27	AS14NJ004	Erosional Horizon	2.68	-8.94	-7.28
28	AS14NJ005	Erosional Horizon	7.04	-11.68	-2.05
29	AS14NJ006	Erosional Horizon	9.15	-10.85	0.48
30	AS14NJ042	Erosional Horizon	7.78	-10.83	-1.17
31	AS14NJ005	Cements (Diagenetic)	7.17	-11.42	-1.90
32	AS14NJ033	Cements (Stalactite)	6.80	-12.16	-2.34
33	AS14NJ085	Abandoned Quarry: Vein	7.82	-8.57	-1.11
34	AS14NJ032	Cements (Diagenetic)	7.17	-11.34	-1.89
35	AS14NJ025	Crystalline Crust	11.01	-10.71	2.71
36	AS14NJ028	Peloidal Micrite	9.31	-9.26	0.68
37	AS14NJ018	Reed Travertine (microb. laminites)	8.54	-10.84	-0.25
38	AS14NJ029	Micritic Dendrite Crust	10.68	-9.75	2.32
39	AS14NJ031	Micritic Dendrite Crust	8.80	-10.30	0.06
40	AS14NJ077	Microbial Mats: Type II	7.90	-11.42	-1.02

Table 10-4: Stable oxygen and carbon isotope data. The values of  $\delta^{18}\text{O}$  for veins are already recalculated due to their aragonitic mineralogy.

Lithotype	Surface (Quarry Walls) (m <sup>2</sup> )	Percentage of exposed quarry walls
Micritic Dendrite Crust	899.84	26.37
Peloidal Micrite	267.71	7.84
Microbial Mats: Type I	719.9	21.09
Microbial Mats: Type II	713.52	20.91
Microbial Laminites	184.54	5.41
Crystalline Crust	162.38	4.76
Erosional Horizons	435.55	12.76
Veins (Banded)	23.16	0.68
Shrubs	1.49	0.04
Unconsol. Micrite	4.6	0.13
<b>Total</b>	<b>3412.69</b>	<b>100.00</b>

Table 10-5: Total surface of each lithotype as exposed in the quarry. These are the exact amounts of the reservoir analogue.

Sample No	Sample	Lithology	Sr 87/86	% Std Err
NJ1	AS14NJ034	Veins in marl	0.70862	0.0013
NJ2	AS14NJ041	Marly Limestone	0.70838	0.0014
NJ5	AS14NJ003	Banded	0.70790	0.0016
NJ4	AS14NJ063	Layered	0.70791	0.0015
NJ3	AS14NJ079	Layered	0.70794	0.0014
NJ6	AS14NJ029	Layered	0.70791	0.0013
NJ7	AS14NJ032	Layered	0.70790	0.0015
NJ8	AS14NJ030	Layered	0.70790	0.0015
NJ9	AS14NJ013	Layered	0.70795	0.0012

Table 10-6: <sup>87</sup>Sr/<sup>86</sup>Sr data.

Sample	Ca	Al	As	Ba	Co	Cr	Cu	Fe	K	Li	Mg	Mn	Na	Ni	P	Rb	S	Sr	Ti	V	Zn
LOQ (U)*	1	15	5	2	1	5	1	5	15	1	10	2	80	1	15	5	50	15	1	2	2
	%	µg/g	µg/g	µg/g	µg/g	µg/g	µg/g	µg/g	µg/g	µg/g	µg/g	µg/g	µg/g	µg/g	µg/g	µg/g	µg/g	µg/g	µg/g	µg/g	µg/g
N-1	38.1	698	<5	37	<1	<5	<1	6	67	1	78	<2	762	<1	135	<5	1538	7695	1	<2	<2
N-2	38.0	526	<5	22	<1	<5	<1	11	74	<1	35	<2	411	<1	47	<5	717	7630	2	<2	<2
<b>N-4</b>	<b>35.4</b>	<b>7526</b>	<b>&lt;5</b>	<b>281</b>	<b>&lt;1</b>	<b>10</b>	<b>3</b>	<b>2942</b>	<b>2409</b>	<b>5</b>	<b>2775</b>	<b>81</b>	<b>1585</b>	<b>4</b>	<b>133</b>	<b>19</b>	<b>2038</b>	<b>1067</b>	<b>306</b>	<b>9</b>	<b>10</b>
<b>NJ-4</b>	<b>34.5</b>	<b>7391</b>	<b>&lt;5</b>	<b>293</b>	<b>&lt;1</b>	<b>8</b>	<b>3</b>	<b>2877</b>	<b>2363</b>	<b>4</b>	<b>2693</b>	<b>79</b>	<b>1542</b>	<b>4</b>	<b>130</b>	<b>16</b>	<b>1957</b>	<b>1034</b>	<b>310</b>	<b>8</b>	<b>9</b>
N-6	37.9	732	<5	28	<1	<5	<1	224	388	3	5441	12	878	<1	49	<5	7052	2208	28	<2	<2
N-19	38.2	713	<5	29	<1	<5	<1	10	77	<1	46	<2	491	<1	71	<5	813	8033	2	<2	<2
N-22	39.1	52	<5	10	<1	<5	<1	8	85	<1	4067	7	347	<1	19	<5	3436	1055	1	<2	<2
N-29	38.5	57	<5	11	<1	<5	<1	9	89	<1	3558	11	332	<1	17	<5	3196	1268	<1	<2	<2
N-30	38.6	71	<5	13	<1	<5	<1	11	44	<1	1926	12	149	<1	19	<5	2267	1258	<1	<2	<2
N-31	38.7	67	<5	14	<1	<5	<1	7	87	2	2899	10	321	<1	17	<5	3711	1424	<1	<2	<2
N-42	37.4	2077	<5	46	<1	<5	<1	345	487	6	4880	29	879	<1	97	<5	7332	1983	57	<2	<2
N-43	37.2	1287	<5	36	<1	<5	<1	216	404	2	4774	37	1047	<1	79	<5	9527	2071	35	<2	<2
N-45	38.7	212	<5	12	<1	<5	<1	27	85	<1	2024	19	223	<1	27	<5	2152	990	2	<2	<2
N-44	37.7	169	<5	20	<1	<5	<1	34	148	2	2949	11	471	<1	57	<5	3840	1925	3	<2	<2
N-52	38.1	289	<5	12	<1	<5	<1	45	106	2	1726	4	202	<1	33	<5	1729	778	5	<2	<2
<b>N-57</b>	<b>37.3</b>	<b>217</b>	<b>&lt;5</b>	<b>39</b>	<b>&lt;1</b>	<b>&lt;5</b>	<b>&lt;1</b>	<b>25</b>	<b>300</b>	<b>3</b>	<b>2501</b>	<b>19</b>	<b>986</b>	<b>&lt;1</b>	<b>37</b>	<b>&lt;5</b>	<b>8275</b>	<b>2680</b>	<b>3</b>	<b>&lt;2</b>	<b>&lt;2</b>
<b>NJ-57</b>	<b>37.5</b>	<b>216</b>	<b>&lt;5</b>	<b>39</b>	<b>&lt;1</b>	<b>&lt;5</b>	<b>&lt;1</b>	<b>24</b>	<b>296</b>	<b>3</b>	<b>2481</b>	<b>18</b>	<b>980</b>	<b>&lt;1</b>	<b>40</b>	<b>&lt;5</b>	<b>8265</b>	<b>2673</b>	<b>3</b>	<b>&lt;2</b>	<b>&lt;2</b>
<b>N-63</b>	<b>38.5</b>	<b>85</b>	<b>&lt;5</b>	<b>18</b>	<b>&lt;1</b>	<b>&lt;5</b>	<b>&lt;1</b>	<b>22</b>	<b>37</b>	<b>1</b>	<b>2117</b>	<b>16</b>	<b>114</b>	<b>&lt;1</b>	<b>27</b>	<b>&lt;5</b>	<b>1268</b>	<b>1028</b>	<b>&lt;1</b>	<b>&lt;2</b>	<b>&lt;2</b>
<b>NJ-63</b>	<b>38.1</b>	<b>88</b>	<b>&lt;5</b>	<b>18</b>	<b>&lt;1</b>	<b>&lt;5</b>	<b>&lt;1</b>	<b>21</b>	<b>37</b>	<b>&lt;1</b>	<b>2105</b>	<b>15</b>	<b>111</b>	<b>&lt;1</b>	<b>29</b>	<b>&lt;5</b>	<b>1238</b>	<b>1015</b>	<b>&lt;1</b>	<b>&lt;2</b>	<b>&lt;2</b>
N-72	38.4	152	<5	10	<1	<5	<1	25	59	<1	2667	13	190	<1	24	<5	2104	1119	2	<2	<2
N-79	38.0	28	<5	10	<1	<5	<1	8	21	<1	1861	11	84	<1	17	<5	703	601	<1	<2	<2

Table 10-7: ICP-OES data. Some samples are analysed double to define the analytical precision.



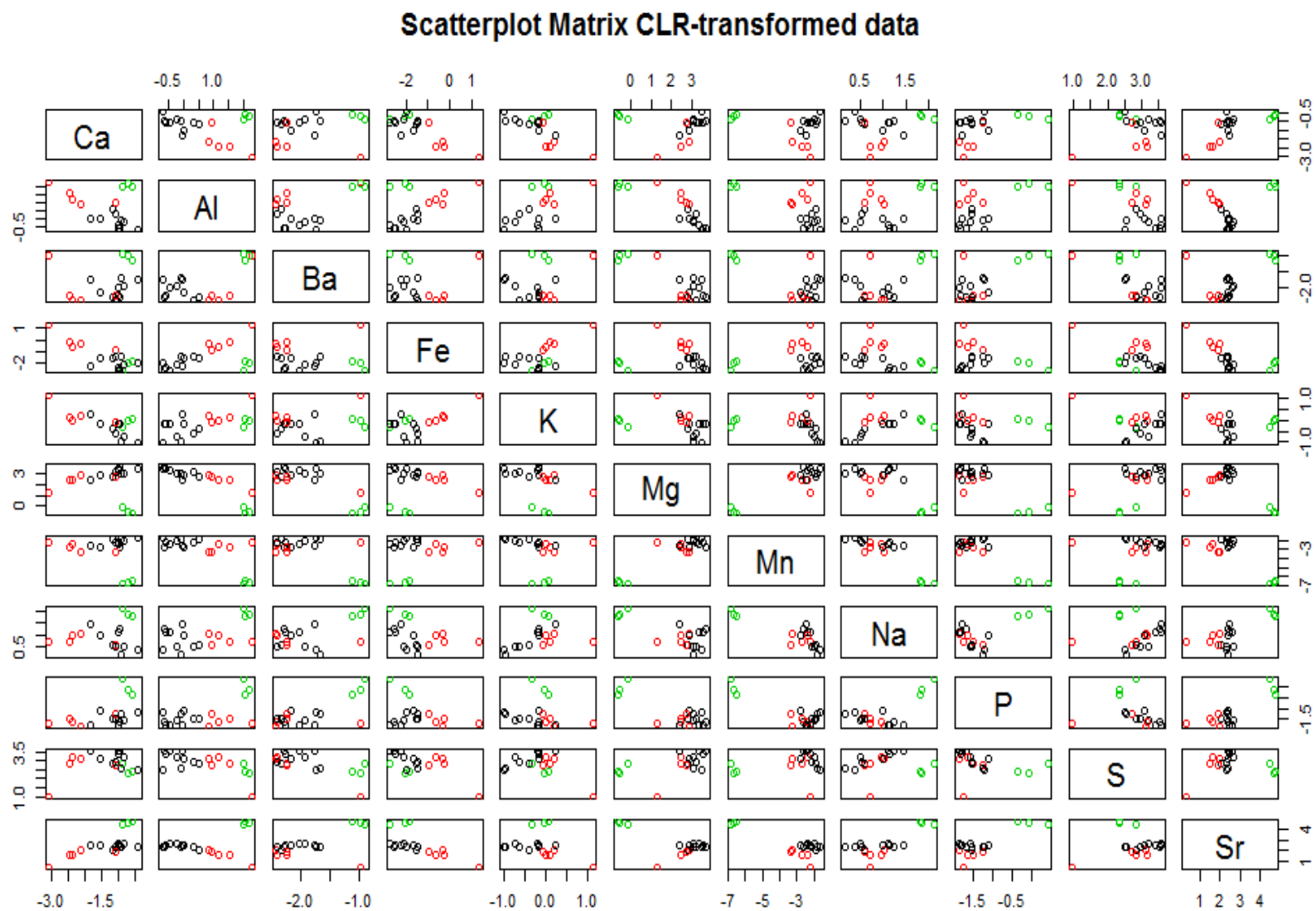
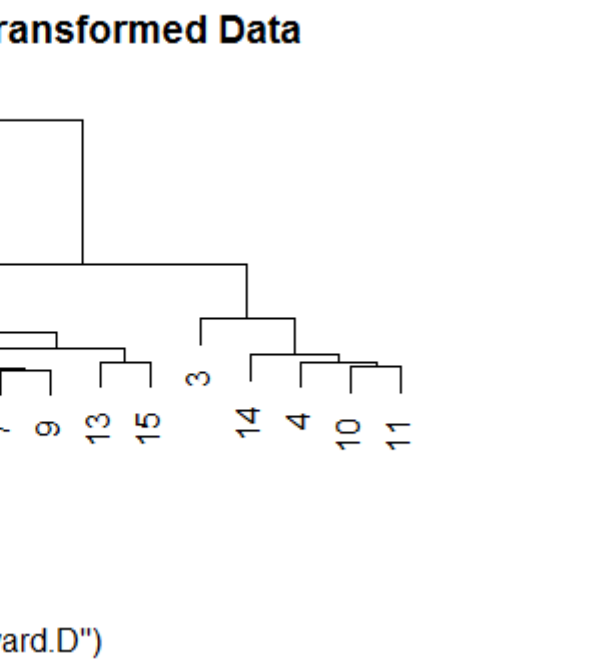
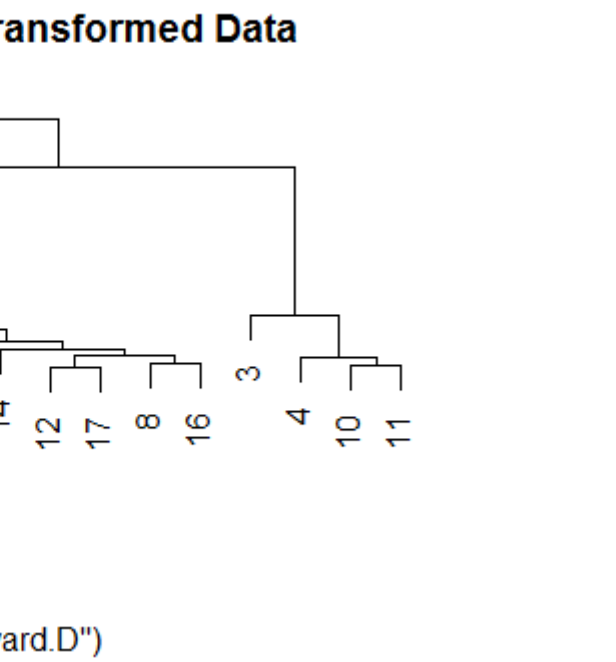


Figure 10-9: Scatterplot matrix of geochemical data transformed by the Centred Logarithmic Ratio transformation. The colours in this figure reflect the three clusters created by representative-based clustering.

Clustering type	Hierarchical				Representative-based				Fuzzy	
Transformation	Log		CLR		Log		CLR		Log	CLR
Cut-height	5	10	5	10						
AS14NJ001	1	1	1	1	1	1	1	1	1	1
AS14NJ002	1	1	1	1	1	1	1	1	1	1
AS14NJ004	2	2	2	2	2	4	2	2	2	2
AS14NJ006	3	2	3	2	2	4	2	2	2	2
AS14NJ019	1	1	1	1	1	1	1	1	1	1
AS14NJ022	4	3	4	3	3	3	3	3	3	3
AS14NJ025	4	3	4	3	3	3	3	3	3	3
AS14NJ030	4	3	4	3	3	2	3	4	3	3
AS14NJ031	4	3	4	3	3	3	3	3	3	3
AS14NJ042	3	2	3	2	2	4	2	2	2	2
AS14NJ043	3	2	3	2	2	4	2	2	2	2
AS14NJ044	5	3	4	3	3	3	3	4	3	3
AS14NJ045	4	3	4	3	3	2	3	3	3	3
AS14NJ052	4	3	3	2	3	2	2	2	3	1
AS14NJ057	5	3	4	3	3	3	3	3	3	3
AS14NJ063	4	3	4	3	3	2	3	4	3	3
AS14NJ072	4	3	4	3	3	2	3	4	3	3
AS14NJ079	4	3	4	3	3	2	3	4	3	3

Table 10-8: Table showing the clusters of different methods. Representative-based clustering with the CLR transformed dataset of three different clusters is used in the research. The three clusters are considered more likely because of a function in R analyses the optimal amount of clusters. A small amount of clusters is suggested due to small amount of samples. These clusters agree with the hierarchical clustering of CLR-transformed data.



sters are defined by cutting the tree at a given height.

## 4.4. Fluid inclusion calibration and data

### 4.4.1. Calibration of the Linkam stage

Table 10-9: Data for calibration. The theoretical temperature is the temperature at which melting (or first melt in the case of NaCl-H<sub>2</sub>O inclusions) is supposed to occur in inclusions with the composition of these artificially created wafers and fluid inclusions. The measured temperature is lower in all instances.

	CO <sub>2</sub>	NaCl – H <sub>2</sub> O	KCl	H <sub>2</sub> O
<b>Theoretical temperature</b>	-56.6°C	-21.2°C	-10.7°C	0.0°C
<b>Measured temperature</b>	-58.3°C	-21.9°C	-11.0	-0.3°C

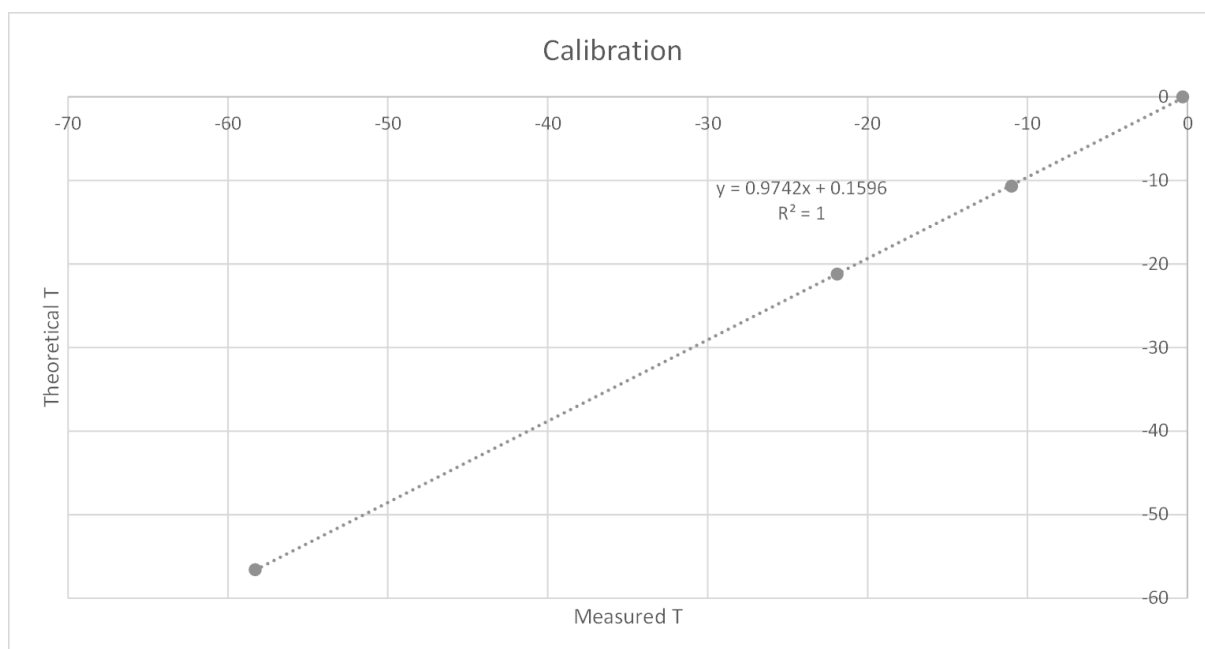


Figure 10-11: Calibration curve. The measured data of the reference samples is plotted against the actual temperature.

AS14NJ001							
Measurement	Vapour %	Tfm (°C)	Tm (°C)	Th (°C)	Salinity (wt%)	Tfreeze (°C)	Extra
1	20			> 110		-41.6	
2	22.5	-0.6	-0.2	> 110	0.36	-40.5	
3	/	-0.7	-0.3	> 110	0.54	-40.0	
4	/		-0.5		0.90		
5	45	-48.9	-29.3	> 110		-84.7	Tm,hh = -30.5
6				> 110			
7	25					-41.0	
8	20	-0.4	-0.2		0.36	-41.0	
9		-0.4	-0.1		0.18		
10	20		-0.1		0.18		
11		-0.6				-41.0	
12	15						
13		-3.1	-1.6		2.96		
14	15	-4.0				-41.7	
15	20	-1.2	-0.5		0.90		
16			-0.2		0.36		
17			-0.3		0.54		
18	30		-0.2		0.36		
19	20		-0.3		0.54		
20	20						
21	25						
22	30		0.0			-47.0	
23	17.5						
24	20	-0.7	-0.4	> 110	0.72	-41.7	
25	30	-1.1		> 110			
26	20			> 110			
27	12.5			> 110			
28	5			> 110			
29	35	-33.7	-28.8	> 110			
30	30			> 110			
AS14NJ019							
Measurement	Vapour %	Tfm (°C)	Tm (°C)	Th (°C)	Salinity (wt%)	Tfreeze (°C)	Extra
31	20	-30.7	-29.4	> 110		-114.0	
32	20	-29.9	-29.6	61		-113.0	
33	20	-0.6	-0.2		0.36		
34	15	-31.9	-29.1	65		-112.3	
35	30					-40.0	
36	30	-0.1	0.0				
37	20						
38	15	-31.2	-29.0			-96.5	
39		-0.3				-41.5	
40		-30.3	-29.7			-115.0	
41	25						
42	20			> 110			
43	10			> 110			
44	30	-29.9	-28.9				
45	10					-112.0	
46	40	-31.2	-29.1			-112.0	
47	20	-29.9	-29.1			-114.0	
48	27.5	-0.4	-0.3		0.54		
49	70						
50	80						
Amount	40	23	25				
Average	25.52631579	-14.23958333	-11.01481481				
St.Dev	14.09738095	16.06646987	13.95120342				

Table 10-10: Fluid inclusion data. The fluid inclusions are indicated per sample but they are interpreted as a unity.





AFDELING GEOLOGIE  
Celestijnenlaan 200 E, bus 2408  
3000 LEUVEN, BELGIË  
tel. + 32 16 32 64 60  
fax + 32 16 32 29 80  
[www.kuleuven.be](http://www.kuleuven.be)

